

Piperine Derivatives as Modulators of Amyloid-Beta ($A\beta$) Aggregation

by

Shirley Wang

A thesis

presented to the University of Waterloo

in fulfillment of the

thesis requirement for the degree of

Master of Science

in

Pharmacy

Waterloo, Ontario, Canada, 2023

© Shirley Wang 2023

Author's Declaration

I hereby declare that I am the sole author of this thesis. This is a true copy of the thesis, including any required final revisions, as accepted by my examiners.

I understand that my thesis may be made electronically available to the public.

Abstract

Alzheimer's Disease (AD) is a life-changing neurodegenerative disease that progresses in stages and currently has no effective cure. More than 597,000 Canadians suffer from AD. Symptoms of late-stage AD are severe and include memory loss, apathy, depression, and psychosis, resulting in large burdens for caregivers and the economy. A major factor leading to AD is the aggregation of a protein known as amyloid- β ($A\beta$). However, most pharmacotherapies for AD provide only symptomatic relief and target other pathways. The recently approved monoclonal antibodies (mAbs) are the only disease-modifying therapies targeting $A\beta$ peptide aggregation in AD that are available in the US. Limitations of mAb therapies include high-cost for patients, high manufacturing costs and resource-intensive parenteral administration. In this regard, the current study focused on the development of novel anti-amyloid small molecules based on piperine, derived from the black pepper plant, that was reported to enhance cognition. Advantages of small molecule AD therapeutics include being highly scalable and applicable to non-invasive routes of drug administration. A library of 13 piperine derivatives were designed, synthesized, and evaluated as potential inhibitors of $A\beta$ 42 aggregation. The experiments carried out include i) developing chemistry reaction conditions to synthesize the target compounds, ii) compound characterization by analytical chemistry, iii) determining their inhibition activity toward $A\beta$ 42 aggregation by fluorescence aggregation kinetics studies and transmission electron microscopy, iv) computational modeling studies in the $A\beta$ 42 model to understand the binding interactions of lead compounds and v) cell viability studies in mouse hippocampal HT22 cells. The structure activity relationship (SAR) studies led to the identification of three piperine derivatives **4a** (R = pyrrolidine), **4b** (R = thiomorpholine) and **4c** (R = morpholine) as the lead compounds with inhibition ranging from

35-48 % (at 10 μM). The results were also confirmed by electron microscopy studies which demonstrated the ability of these compounds to reduce A β 42 aggregation. Molecular docking studies in the A β 42 pentamer model show that the terminal acyl substituents play a major role in stabilizing the A β 42 pentamer assembly by interacting at the amyloidogenic interface consisting of the C- and N-terminal residues. This prevents further self-assembly and aggregation. Cell culture assays in HT22 mouse hippocampal cells showed that the lead compounds **4a**, **4b** and **4c** were not toxic (cell viability >90 %, at 25 μM). This is the first study that reports the discovery of novel piperine based compounds as direct inhibitors of A β 42 aggregation. Overall, the results obtained from this thesis provide valuable insights in the design, development, and application of novel small molecules to study and treat AD.

Acknowledgements

I would like to express my sincere gratitude for my supervisor, Dr. Praveen P. Nekkar Rao for allowing me to work in his lab, and for providing consistent support and generous dedication of time to help me grow as a scientist over the past two years. Many thanks also go out to my thesis committee; Dr. David Edwards and Dr. Shawn Wettig for their time and inputs which helped me gain new insights about my research project and how to produce high-quality results. Additionally, I would like to thank Avro Life Science for giving me the flexibility and opportunity to pursue this Master of Science in Pharmacy degree part-time while continuing to work at the company. The financial support has been a crucial part of my successes during this time, and I am deeply grateful. Another instrumental part of my successes during my Master's degree include the support for my lab-mates at the Nekkar lab. The number of times each of you have showed your kindness and uplifted me in times of need are priceless and I appreciate all of your hard work and motivation. Lastly, I would like to thank my lovely family, friends and life-partner for constantly providing me with continued support and reminding me about the importance of work-life balance during my academic ventures. All my successes would not have been possible without each and every one of you.

Table of Contents

Author's Declaration.....	ii
Abstract.....	iii
Acknowledgements.....	v
List of Figures.....	i
List of Schemes.....	v
List of Tables.....	v
List of Abbreviations.....	vii
Chapter 1: Introduction to Alzheimer's Disease.....	1
1.1 Alzheimer's Disease - Background and Statistics.....	1
1.2 Pathophysiology of Alzheimer's Disease.....	3
1.2.1 The Cholinergic Hypothesis.....	3
1.2.2 The Tau Hypothesis.....	5
1.2.3 The Amyloid Beta (A β) Hypothesis.....	6
1.2.3.1 Non-amyloidogenic APP Processing.....	9
1.2.3.2 Amyloidogenic APP Processing.....	10
1.2.3.3 Post-processing Fates of A β Peptides.....	16
1.2.4 Other Hypotheses for Pathological Routes to AD.....	22
1.3 AD Risk Factors.....	24
1.4 Advances in AD Therapeutics: Present and Past.....	26
1.5 Piperine Background.....	31
Chapter 2: Objectives and Hypothesis.....	34
Chapter 3: Methodology.....	41
3.1 Synthetic Chemistry.....	41
3.2 Aggregation Kinetics Fluorescence Assay Methodology.....	47
3.3 Transmission Electron Microscopy (TEM) Studies Methodology.....	49
3.4 Molecular Docking Studies Methodology.....	50

3.5 Cytotoxicity Assay Methodology	52
Chapter 4: Results and Discussion	54
4.1 Synthesis of Piperine Derivatives 4a-m	54
4.2 Aggregation Kinetics Assay	55
4.3 TEM Analysis of A β 42 co-incubated with Piperine Derivatives 4a, 4b and 4c	61
4.4 In Silico Studies of 4a-c Docked into the A β 42 Pentamer Model.....	62
Chapter 5: Conclusion and Future Directions	71
Chapter 6: Experimental	75
6.1 Chemistry	75
6.1.1 Synthesis and Characterization (NMR and LC-MS)	76
6.2 Aggregation Kinetics Assay	85
6.3 TEM Studies	88
6.4 Computational Modelling Studies	89
6.5 Cell Culture Assays.....	90
References	95
Appendix A - Supplementary Analytical and Experimental Data	122
A1. NMR spectra for compounds 4a-m	122
A2. HR-MS data for compounds 4g, 4i, 4j, 4l, and 4m	139
A3. LC-MS trace for compounds 4a-m	143
A4. Additional aggregation kinetics plots for piperine derivatives 4d-m and 3	148

List of Figures

- Figure 1.** Canada’s forecasted number and ages of people over the age of 65 that will have dementia in 2033. Image adapted from the Alzheimer’s Society of Canada..... 2
- Figure 2.** Projected out of pocket (A) and direct care (B) costs associated with dementia care for the Canadian economy. Bars indicate the number of patients accounted for and the proportion of two age brackets (65+ and 40-64 years old). Note that panel B figures do not account for out-of-pocket costs. Figure adapted from Alzheimer Society of Canada 2
- Figure 3.** AD patient brains exhibit a significantly lower amount of ACh and cholinergic neurogenesis compared with a healthy brain, shown by a decrease in number of ACh neurotransmitters present during axonal transport and within the synaptic cleft. Dysfunctional cholinergic neurons result from deficits in receptor expression (nAChR and mAChR), shown in this figure by a decrease in color vibrancy 3
- Figure 4.** Dissociation of aberrantly phosphorylated tau proteins results in microtubule disintegration and neurodegeneration. NFT formation may also occur, sticking to the outer neuron and reducing signal transmission abilities of affected neurons 6
- Figure 5.** Amyloidogenic cleavage of the APP by β - and γ - secretases within the neuronal membrane releases extracellular $A\beta$ monomers which may aggregate to form neurotoxic oligomers. Oligomers of $A\beta$ may cause cell death by binding various receptors or inducing dyshomeostasis via pore formation..... 8
- Figure 6.** Schematic of non-amyloidogenic APP processing (EC = Extracellular Space, IC = Intracellular Space). The pink segment represents the 40/42 amino acid residue long $A\beta$ peptide, known for its neurotoxic effects. Once cleaved by α -secretase, it is released..... 10
- Figure 7.** Schematic of amyloidogenic APP processing 12
- Figure 8.** Mechanism of action (panels 1-6) for BACE-1 proteolysis of the APP between amino acid residues Met596 and Asp597. Note that extracellular and intracellular domains are not shown in this schematic. Red colored bonds and text are representative of the substrate (APP), blue represents water molecule(s) and black text represents the amino acid residues in the BACE-1 active site participating in hydrolysis 14
- Figure 9.** $A\beta$ step-wise aggregation process into senile plaques. After $A\beta(42/40)$ is released via the β -secretase cleavage, it undergoes self-assembly to produce soluble aggregates with varying degrees of toxicity. These soluble aggregates further assemble into insoluble fibrils in a β -pleated sheet conformation, resulting in disruption of the synapses ability to transmit signals ultimately causing neuronal death. Figure adapted from Safura et al..... 17

Figure 10. Amino acid sequence of A β 42, folded into a β -sheet conformation. Ala42 and Arg5 are key residues involved in the enhanced stabilization of the β -hairpin structure of A β 42 relative to A β 40 peptides 18

Figure 11. Schematic of the various mechanisms by which A β oligomers are hypothesized to induce neurotoxicity. There are two main hypotheses used to describe A β oligomer toxicity; i) the bilayer insertion hypothesis, and ii) the receptor hypothesis which both induce a plethora of toxic pathways including Ca²⁺ dyshomeostasis, tau hyperphosphorylation, mitochondrial dysfunction, reactive oxygen species formation, decreases in ATP generation, impaired transport of brain-derived neurotrophic factor (BDNF), hyperactivity of Ca²⁺/calmodulin-dependent phosphatase calcineurin (CaN), and ultimately neuronal apoptosis. Known A β oligomer binding receptors shown in this diagram include the previously mentioned PrP^c, NMDAR, causing Ca²⁺ dyshomeostasis and other receptors that cause tau hyperphosphorylation: α -Amino-3-hydroxy-5-methyl-4-isoxazolepropionic acid receptor (AMPA), β 2-adrenergic receptor (β 2-AR), p75 neurotrophin receptor (p75NTR) and α 7-nicotinic acetylcholine receptor (α 7nAChR). Figure adapted from Huang et al. 21

Figure 12. Piperine and its structural isomers. A = piperine, B = isopiperine, C = chavicine, D = isochavicine..... 33

Figure 13. Key pharmacophores in curcumin, and resveratrol. These planar molecules have similar functional groups (aromatic and alkene moieties) to piperine and this planarity is a key feature that we hypothesize to play a role in its bioactivity against A β aggregation..... 34

Figure 14. Proposed piperine derivatives 4a-m. Precursor molecule, piperic acid (3) will also be included in the scaffold for comparison of activity. Reaction conditions: (C) Methyl Piperate, 1:1 ratio of 2 M NaOH to methanol (MeOH), 70 °C, 3 h. (D) Oxalyl chloride, piperic acid, dry dichloromethane (DCM), dimethyl formamide DMF (cat.), Ar (g), 0 °C to rt. over 3 h, then dropwise addition of amine to reconstituted reaction mixture in dry DCM, stir overnight at rt. (18 h) 36

Figure 15. Panel A: 3D diagram of A β 42 pentamer model (pbd id: 5KK3) with piperine nested within the KLVFFA seeding region. All simulated interactions with residues are shown via green dotted lines. Panel B: 2D interaction map of piperine docked in A β 42 pentamer model. Hydrophobic interactions such as pi-alkyl and alkyl-alkyl interactions are displayed in pink dotted lines whereas van der Waals interactions are displayed by green spheres representing the interacting amino acid residues..... 39

Figure 16. Conformational change of ThT upon binding to β -sheets of A β fibrils causes the C-C bond to lock, resulting in a fluorescence maxima shift 47

Figure 17. Flow diagram demonstrating the order of operations for the A β 42 aggregation kinetics assay. Under physiological conditions at pH 7.4 and 37 °C, the A β 42 aggregates form mature fibrils which are bound by ThT fluorophores and produce an increase in fluorescence, indicative

of relative amounts of fibril formation per well. Note that the experimental lag phase may be shorter than displayed due to rapid aggregate formation of A β 42..... 49

Figure 18. Schematic of colorimetric changes that occur upon WST-8 entry into the mitochondria of a cell due to metabolism by mitochondrial dehydrogenases into the orange WST-8 formazan intermediate. This change is detected using a UV-Vis spectrophotometer at 450 nm 53

Figure 19. Panels A and B display the aggregation kinetics experimental results when 10 μ M of A β 42 was incubated with **4a** and **4b** respectively. Compounds were tested at 1, 5, 10, and 25 μ M, pH 7.4 phosphate buffer and monitored over 24 hours at 37 $^{\circ}$ C. ThT fluorescence was determined using an excitation and emission λ of 440 and 490 nm respectively. The data presented are an average of three independent experiments (n = 3). ThT = Thioflavin T control fluorescence, BG = Background compound fluorescence 58

Figure 20. The aggregation kinetics experimental results when 10 μ M of A β 42 was incubated with **4c**. **4c** was tested at 1, 5, 10, and 25 μ M, pH 7.4 phosphate buffer and monitored over 24 hours at 37 $^{\circ}$ C. ThT fluorescence was determined using an excitation and emission λ of 440 and 490 nm respectively. The data presented are an average of three independent experiments (n = 3). ThT = Thioflavin T control fluorescence, BG = Background compound fluorescence 59

Figure 21. The aggregation kinetics experimental results when 10 μ M of A β 42 was incubated with piperine. Piperine was tested at 1, 5, 10, and 25 μ M, pH 7.4 phosphate buffer and monitored over 24 hours at 37 $^{\circ}$ C. ThT fluorescence was determined using an excitation and emission λ of 440 and 490 nm respectively. The data presented are an average of three independent experiments (n = 3). ThT = Thioflavin T control fluorescence, BG = Background compound fluorescence .. 59

Figure 22. Panels A and B display the aggregation kinetics experimental results when 10 μ M of A β 42 was incubated with MB and RVT respectively. Compounds were tested at 1, 5, 10, and 25 μ M, pH 7.4 phosphate buffer and monitored over 24 hours at 37 $^{\circ}$ C. ThT fluorescence was determined using an excitation and emission λ of 440 and 490 nm respectively. The data presented are an average of three independent experiments (n = 3). ThT = Thioflavin T control fluorescence, BG = Background compound fluorescence 60

Figure 23. The micrograph presented in panel A represents the morphology of the 10 μ M A β 42 fibril control and panel B shows the ThT control well after 24 hours of incubation at 37 $^{\circ}$ C. Panels C-G represent A β 42 aggregate morphology in the presence of resveratrol, piperine, and **4a-c** respectively (10 μ M each) 62

Figure 24. Panels A and B: Compound **4a** docked into A β 42 pentamer model (pdb id: 5KK3) full view (A) and zoomed into binding site (B) with green dotted lines representing intermolecular interactions. Panel C: 2D schematic of intermolecular interactions colored by interaction type. Pink = alkyl interactions, green = van der Waals interactions, purple = pi-sigma interaction. Hydrogen atoms were removed for clarity 63

Figure 25. Panels A and B: Compound **4b** docked into A β 42 pentamer model (pdb id: 5KK3) full view (A) and zoomed into binding site (B) with green dotted lines representing intermolecular

interactions. Panel C: 2D schematic of intermolecular interactions colored by interaction type. Pink = alkyl interactions, green = van der Waals interactions, purple = pi-sigma interaction. Hydrogen atoms were removed for clarity 64

Figure 26. Panels A and B: Compound **4c** docked into A β 42 pentamer model (pdb id: 5KK3) full view (A) and zoomed into binding site (B) with green dotted and solid lines representing intermolecular interactions. Panel C: 2D schematic of intermolecular interactions colored by interaction type. Pink = alkyl interactions, green = van der Waals interactions. Hydrogen atoms were removed for clarity 65

Figure 27. Panels A and B: Piperine docked into A β 42 pentamer model (pdb id: 5KK3) full view (A) and zoomed into binding site (B) with green dotted lines representing intermolecular interactions. Panel C: 2D schematic of intermolecular interactions colored by interaction type. Pink = alkyl interactions, green = van der Waals interactions. Hydrogen atoms were removed for clarity 67

Figure 28. Cell viability data from the CCK-8 cytotoxicity assay. The lead compounds **4a-c** were evaluated at 10 μ M (dotted coloured bars) and 25 μ M (solid-coloured bars) while the controls RVT and PPN were tested at 25 μ M. Data reported represents the average \pm s.d (n = 3) based on three independent experiments 70

Figure 29. Potential modifications to the current lead template of this thesis (**4a**) that are hypothesized to improve A β 42 binding potential..... 73

Figure 30. Cell counting workflow for determination of cell concentration. Panel A: Hemocytometer and zoomed view of grid for counting cells manually. Cells within all four white quadrants are counted and boundary touching cells are only counted on the left and topmost borders to avoid over counting. Panel B: Stepwise description of concentration calculation after cells are counted..... 92

Figure 31. A schematic of the 96-well plate layout for the cell culture studies. Legend: UT = Untreated control, A β = A β 42 control (10 μ M), A10 = Compound **4a** (10 μ M), A25 = Compound **4a** (25 μ M), B10 = Compound **4b** (10 μ M), B25 = Compound **4b** (25 μ M), C10 = Compound **4c** (10 μ M), C25 = Compound **4c** (25 μ M), P25 = Piperine (25 μ M), R25 = Resveratrol (25 μ M). 94

Figure S1. Additional aggregation kinetics data from the remaining piperine derivatives that were not included in the top three piperine derivatives. Panels A-K show the experimental results from 10 μ M of A β 42 incubated with compounds 4d-m and 3 respectively. All compounds were tested at 1, 5, 10, and 25 μ M into the wells under physiological conditions (pH 7.4 phosphate buffer) and monitored over 24 hours at 37 $^{\circ}$ C. Detection of ThT fluorescence was done using an excitation and emission λ of 440 and 490 nm respectively. These results represent an average of two independent assays (n = 3) 149

List of Schemes

- Scheme 1.** Summary of reaction schemes used to synthesize piperine derivatives (**4a-m**) and precursor molecules (**2** and **3**). (A) Toluene, 130 °C reflux, 5 h. (B) Piperonal, lithium hydroxide (LiOH), dry tetrahydrofuran (THF), 70 °C reflux, 8 h, Ar (g). (C) Methyl Piperate, 1:1 ratio of 2 M NaOH to MeOH, 70 °C, 3 h. (D) (COCl)₂, piperic acid, dry dichloromethane (DCM), dimethyl formamide DMF (cat.), Ar (g), 0 °C to rt. over 3 h, then dropwise addition of amine to reconstituted reaction mixture in dry DCM, stir overnight at rt. (18 h). R groups for final piperine derivatives are displayed in Figure 14..... **41**
- Scheme 2.** Panel A is the overall Michaelis-Arbuzov reaction scheme where triethyl phosphite is coupled to 4-bromo-butenoate. Panel B shows the mechanism of the Michaelis-Arbuzov reaction **42**
- Scheme 3.** Panel A: HWE reaction scheme of methyl ester phosphonate with the piperonal to form methyl piperate (**2**). Panel B: HWE reaction mechanism for formation of **2** **43**
- Scheme 4.** Panel A: Reaction scheme for the synthesis of piperic acid (**3**). Panel B: Reaction mechanism for the hydrolysis of methyl piperate into **3**..... **44**
- Scheme 5.** Panel A shows the synthetic scheme for the synthesis of piperine derivatives **4a-m** from piperic acid via nucleophilic acyl substitution. Panel B is the arrow pushing mechanism for the DMF catalyzed chlorination by oxalyl chloride and subsequent acyl substitution reaction with primary or secondary amines to form piperine derivatives **45**
- Scheme 6.** Panel A: Reaction scheme for the triethylamine (TEA) catalyzed synthesis of **4f** and **4g** using Oxone for the oxidation of **4b** into its sulfone (**4f**) and sulfoxide (**4g**) products. Panels B and C: Reaction mechanism for the oxidation of thiomorpholine (B) and sulfone (C) functional groups **46**

List of Tables

Table 1. cLogP and PSA values for all targeted piperine derivatives and known anti-AD agents, calculated using BIOVIA Discovery Studio: Structure-Based-Design Software. CYP inhibition ability was determined with Swiss ADME web tool. PPN = piperine, CCM = curcumin, RVT = resveratrol, DPZ = donepezil, GLM = galantamine	37
Table 2. Percentage inhibition of A β 42 aggregation for all the synthesized piperine derivatives and reference standards at 10 μ M. Results are expressed as average \pm s.d (n = 3) based on three independent experiments. NA = no activity	57
Table 3. Binding energy calculations from the implicit solvent binding energy simulation of top CDOCKER generated poses for piperine derivatives 4a-c and the piperine.....	68
Table 4. Summary of biochemical properties of piperine derivatives 4a-m evaluated during this study	72
Table 5. Concentrations of stocks, working solutions and wells used in the aggregation kinetics assay along with their percentage of DMSO content (v/v).....	86
Table 6. Exact well volumes of stock solution used for each well category in the aggregation kinetics assay	87
Table 7. Reagents required to produce various types of cell culture media to be used for processes including cell proliferation, cell starving and cell storage	91
Table 8. Schematic of a 96-well plate layout for the CCK-8 assay and solution compositions for cell treatments applied for testing during this cytotoxicity assay	94

List of Abbreviations

AChE = Acetylcholinesterase enzyme

APH-1 = anterior pharynx defective 1

^{13}C NMR = Carbon nuclear magnetic resonance spectroscopy

^1H NMR = Proton nuclear magnetic resonance spectroscopy

Å = angstrom

ACh = Acetylcholine

AD = Alzheimer's Disease

ADAM = a disintegrin and metalloproteinase

AICD = Amyloid intracellular domain

AMPA = α -Amino-3-hydroxy-5-methyl-4-isoxazolepropionic acid receptor

APP = Amyloid precursor protein

A β = amyloid- β

BACE-1 = β -site APP cleaving enzyme

BBB = Blood brain barrier

BDNF = brain-derived neurotrophic factor

bs = broad singlet

BuChE = Butyryl cholinesterase

CaN = Ca^{2+} /calmodulin-dependent phosphatase calcineurin

CCM = Curcumin

CDCl_3 = deuterated chloroform

CDOCKER = CHARMM-based DOCKER

cdk = Cyclin dependent kinase

CHARMm = Chemistry at Harvard Molecular Mechanics

cLoP = calculated LogP

CNS = Central nervous system

CSF = cerebrospinal fluid

CTF = C-terminal fragment

CYP = cytochrome P450

d = doublet

Da = Daltons

DCM = Dichloromethane

DMF = Dimethyl formamide

DMSO = Dimethyl sulfoxide

DMSO-*d*₆ = deuterated dimethylsulfoxide

DS = Discovery Studio

EC = Extracellular Space

ER = Endoplasmic Reticulum

FAD = familial early-onset AD

FBS = Fetal Bovine Serum

GBSW = Generalized Born with a simple SWitching

gem-diol = geminal diol

GFP = green fluorescence protein

GPCR = G-protein coupled receptor

HFIP = 1,1,3,3,3-hexafluoro-2-propanol ethanol

HPLC = high performance liquid chromatography

HRMS = High-resolution mass spectra

HWE = Horner-Wadsworth-Emmons

Hz = Hertz

IC = Intracellular Space

IGF = insulin-like growth factor

IgG1 = human immunoglobulin gamma 1

IL-1 = interleukin-1

kbp = kilobasepairs

KPI = Kunitz-type serine protease inhibitor

LC-MS = liquid chromatography-mass spectrometry

LiOH = lithium hydroxide

m = multiplet

mAb = monoclonal antibody

mAChR = Muscarinic acetylcholine receptor

MAO = monoamine oxidase

MAPs = Microtubule-associated proteins

MB = Methylene blue

MDP = methylenedioxyphenyl

MeOH = Methanol

mGluR5 = metabotropic glutamate receptor subtype 5

MTT = 3-(4,5-Dimethylthiazol-2-yl)-2,5-diphenyl tetrazolium bromide

nAChR = Nicotinic acetylcholine receptor

NFT = Neurofibrillary tangle

NGF = nerve growth factor

NMDAR = N-methyl-D-aspartate receptor
NSAID = non-steroidal anti-inflammatory drug
OG = Orange G
p75NTR = p75 neurotrophin receptor
PAS = peripheral anionic site
PBS = phosphate buffered saline
pdb = Protein data bank
PEN-2 = presenilin enhancer 2
PHF = Paired helical filaments
PNS = Parasympathetic nervous system
PPAR = peroxisome proliferator-activated receptor
PPN = piperine
PrP^c = cellular prion proteins
PS = Penicillin Streptomycin
PS1 = presenilin 1
PS2 = presenilin 2
PSA = polar surface area
PTA = Phosphotungstic acid
QCT = Quercetin
RBF = Round-bottom flask
RFU = Relative fluorescence units
ROS = reactive oxygen species
RVT = Resveratrol
s = singlet

SAR = Structure-activity relationship

SBD = *Structure-Based-Design*

ssNMR = Solid-state NMR

t = triplet

TcAChE = torpedo californica AChE

TGN = trans-Golgi network

THF = tetrahydrofuran

ThT = Thioflavin T

TLC = Thin layer chromatography

TEA = Triethylamine

UPW = Ultrapure water

UV = Ultra-violet

UV-Vis = UV-Visible

WHO = World Health Organization

WST = water-soluble tetrazolium salt

$\alpha 7nAChR$ = $\alpha 7$ -nicotinic acetylcholine receptor

α -APPs = APP-alpha fragment

$\beta 2$ -AR = $\beta 2$ -adrenergic receptor

β -APPs = APP- β fragment

Chapter 1: Introduction to Alzheimer's Disease

1.1 Alzheimer's Disease - Background and Statistics

Since first reported in 1905, Alzheimer's Disease (AD), a neurodegenerative disorder discovered by the German physician Alois Alzheimer, has been an increasing burden on the health care systems, economy, patients, and their loved ones year after year.^{1,2} AD mainly affects those over the age of 65 and is a debilitating form of dementia where patients progressively lose their cognitive function and overall independence due to loss of synapses in the brain and neuronal atrophy.^{1, 3, 4} Once neurodegeneration begins in the patient's brain, behavioral symptoms that typically emerge include depression, disturbed sleep, apathy, aggression, agitation, memory loss and psychosis.^{5, 6} In 2022, the World Health Organization (WHO) reported that by 2050, 1 in 4 people in North America and Europe will be over the age of 65. With the rapidly aging population, it's no wonder that over 50% of Canadians are concerned about being affected by this disease.² A recent epidemiology report revealed the global prevalence of AD to have escalated by 148% over the past 30 years (1990-2019).⁷ Costing over 1.3 trillion dollars annually for care, the world-wide totals of dementia patients have skyrocketed to over 55 million since 2021 where 60-70% of those totals are AD cases.^{8, 9} These numbers are only forecasted to rise beyond 78 million in 2030 and to 139 million by 2050.⁹ Within Canada, the trends are no different with 597,000 people living with dementia since 2020, costing the Canadian economy over 10.4 billion dollars annually.² As shown in Figure 1, the Canadian dementia cases are forecasted to rise to almost 1 million by 2033, and projected to cost over 16 billion dollars per annum (Figure 2).¹⁰ It is evident from these statistics that research efforts to find a cure for AD are urgently needed. AD is an extremely complex disease in that there are a multitude of pathological pathways involved in neurodegeneration. There are two hypotheses that are widely accepted amongst those who research

the pathologies of AD. These pathways are the main targets for most of the AD research to date and include the amyloid- β aggregation pathways and the tau phosphorylation and fibrillation pathway, to be discussed in detail in Section 1.2 of this thesis.^{1, 3, 11-15}

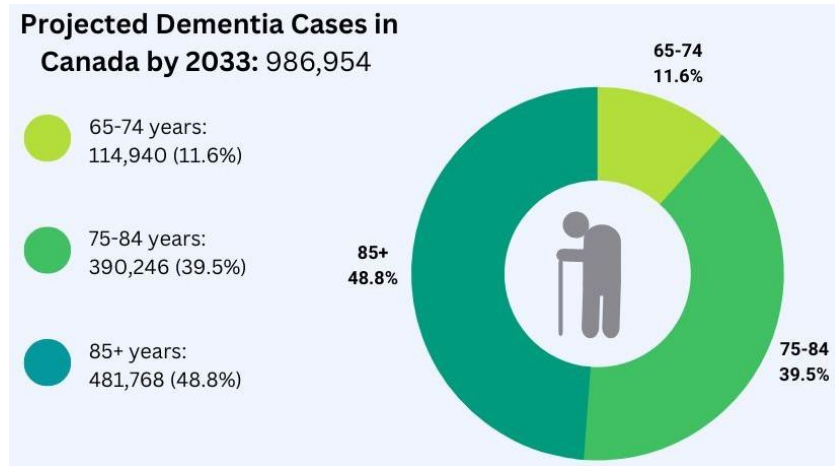


Figure 1. Canada’s forecasted number and ages of people over the age of 65 that will have dementia in 2033. Image adapted from the Alzheimer’s Society of Canada.¹⁰

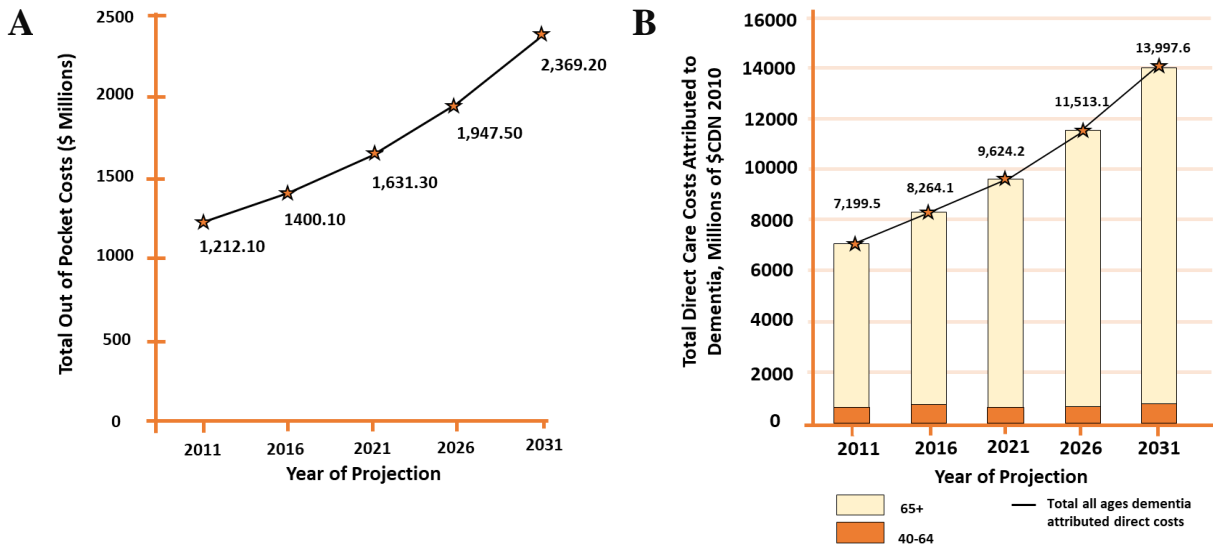


Figure 2. Projected out of pocket (A) and direct care (B) costs associated with dementia care for the Canadian economy. Bars indicate the number of patients accounted for and the proportion of two age brackets (65+ and 40-64 years old). Note that panel B figures do not account for out-of-pocket costs. Figure adapted from Alzheimer Society of Canada.^{10, 16}

1.2 Pathophysiology of Alzheimer's Disease

1.2.1 The Cholinergic Hypothesis

Research conducted on AD reports that there is a much lower concentration of the neurotransmitter acetylcholine (ACh) in the central nervous system (CNS) of AD patients relative to the concentrations observed in the average human brain as shown in Figure 3.¹⁷ This finding is the basis for the cholinergic hypothesis because ACh is associated with learning and memory and it is noted that a decrease in ACh results in cognitive impairments such as memory loss, deficits in attention and awareness, as well as a plethora of additional mnemonic processes.¹⁸

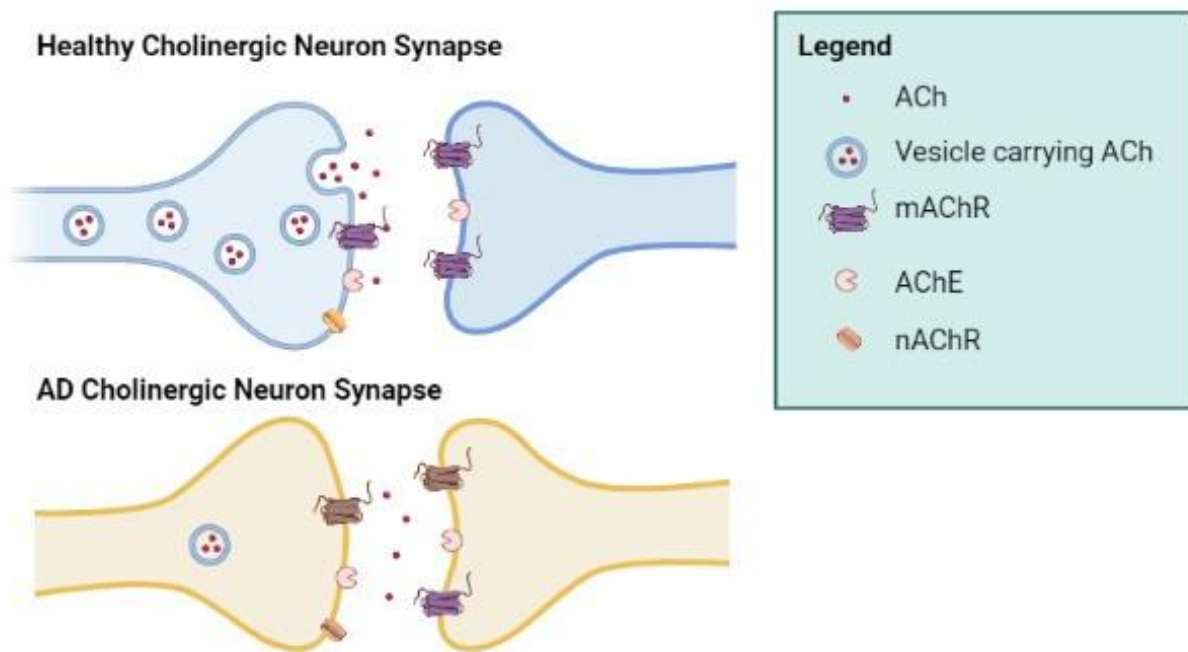


Figure 3. AD patient brains exhibit a significantly lower amount of ACh and cholinergic neurogenesis compared with a healthy brain, shown by a decrease in the number of ACh neurotransmitters present during axonal transport and within the synaptic cleft. Dysfunctional cholinergic neurons result from deficits in receptor expression (nAChR and mAChR), shown in this figure by a decrease in color vibrancy. Figure adapted using Biorender.¹⁸

Current therapeutics that target the cholinesterase pathway aim to inhibit the acetylcholinesterase enzyme (AChE), due to its primary role in degrading ACh into acetate and

choline. Butyryl cholinesterase (BuChE) is another cholinesterase enzyme that may be targeted for inhibiting the cholinesterase pathology, however it is less common since ACh is not its natural substrate.¹⁷ AChE is mainly found within the CNS but can also exist on the surface of erythrocytes or muscle tissue and while BuChE has also been observed in the CNS, it is more spread out in the body in places like the liver and plasma.¹⁷ When these cholinesterases are inhibited, a subsequent spike in the concentration of ACh occurs in the synapses of cholinergic neurons. Two types of receptors can then be bound by ACh molecules including the nicotinic ACh receptors (nAChR) and the muscarinic ACh receptors (mAChR). The nAChRs are a type of ligand gated cation channel receptor primarily located in the axon terminals of the pre-synaptic neurons in the CNS. When bound by ACh, the nAChRs will activate causing the ion channels to open, releasing ACh into the synaptic cleft and thus inducing neurotransmission in downstream neurons.¹⁹ More spreadout throughout the body, mAChRs are a type of G-coupled protein receptor (GPCR), found within the parasympathetic nervous system (PNS). Once ACh is bound, the mAChRs in certain organs and tissues prompt parasympathetic reactions to occur including peristalsis, muscle contraction, micturition and bronchoconstriction.²⁰ Mechanistically, the AChE acts as a serine hydrolase enzyme via its catalytic triad residues, histidine and glutamic acid, which activate the side chain of the third residue in the triad, serine. This active site is located at the bottom of an hour-glass shaped, 20 angstrom (Å) deep gorge, below the enzyme's surface region known as the peripheral anionic site (PAS). Interestingly, many reports have been published indicating that the PAS of AChE plays a large role in AChE-induced A β fibrillogenesis via neurotoxic complex formation.²¹⁻²³ Below the PAS is the bottleneck entry point to the active site, lined with 16 aromatic residues to aid in enzyme specificity. For example, the Phe288 and Phe290 amino acid residues (Torpedo californica AChE numbering) within the acyl pocket help with stabilizing the acetyl

portion of the ACh substrate.^{17, 24} Upon formation of a tetrahedral intermediate between the ACh carbonyl moiety and the activated serine, choline may be released. Lastly, an active site water molecule is recruited to restore the initial active site conformation via the release of acetate from serine. Currently, the most widely used therapeutics for AD treatment are cholinesterase inhibitors, further discussed in Section 1.4.

1.2.2 The Tau Hypothesis

Phosphorylated tau proteins are observed in the brains of many AD patients which have been reported to accelerate neurodegeneration by forming neurotoxic aggregates of insoluble neurofibrillary tangles (NFTs).²⁵ The hydrophilic tau proteins are primarily located in the CNS neural tissue of the neuronal axes, where they and the microtubule-associated proteins (MAPs), are responsible for the stabilization of microtubules. As an essential component of the cytoskeletal makeup of a cell, microtubules aid in performing cytoskeletal rearrangements during the neuronal growth phase while it is undergoing axon elongation and synapse formation.^{14, 25} Under normal conditions, cell regulation of the tau proteins is carried out by tau kinases and tau phosphatases. However, in pathological conditions such as AD, it is hypothesized that there are less tau phosphatases resulting in an aberrant amount of phosphorylated tau proteins.²⁶ Disequilibrium between the two states of tau proteins causes the phosphorylated tau to dissociate from the microtubules leading to de-stabilizing changes in neuronal structure as shown in Figure 4.¹⁷ At this stage, the structural integrity of the neuron's cytoskeleton is lost due to the tau protein dissociation and neurodegeneration occurs. Processes involving the microtubules such as intersynaptic transport of cargo across their tracts by motor proteins will then begin to fail. This results in a loss of signal transmission within the synapses and ultimately presents itself as cognitive impairment.¹⁴ Phosphorylated tau not only has a reduced affinity for microtubules but

is also shown to undergo self-assembly to form aggregates of straight or helical filaments called paired helical filaments (PHFs). PHFs can eventually aggregate into neurotoxic, sticky NFTs that coat the outer neuron and slow down their signal transmission. Neuron-bound NFTs may also act as a barrier, inhibiting them from receiving essential metabolic proteins such as ferritin.²⁵ Once inside the cell, the NFTs may continue to act as a physical barrier within the cytoplasm, disrupting normal cellular function.¹⁴ Moreover, Avila et al. report an inverse relationship between the number of NFTs observed versus the number of surviving neurons, supporting the hypothesis of NFTs inducing neurodegeneration.²⁵ Cumulatively, these are promising reasons for many researchers to target tau phosphatases, kinases and phosphorylated tau proteins as a means of developing novel anti-AD therapeutics to restore the tau protein equilibrium.

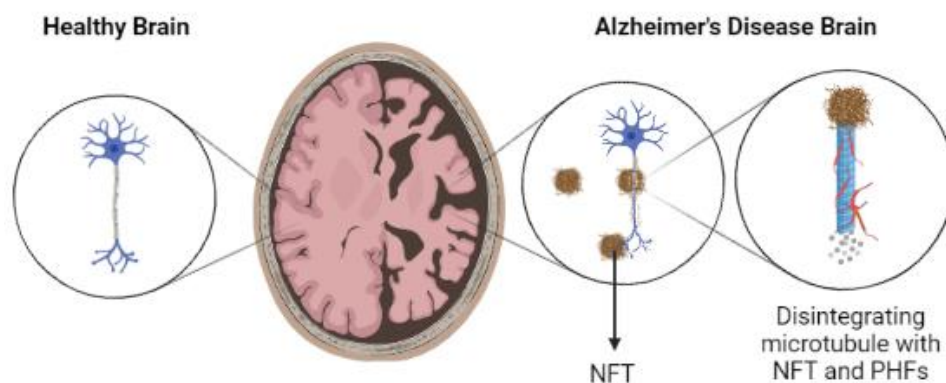


Figure 4. Dissociation of aberrantly phosphorylated tau proteins results in microtubule disintegration and neurodegeneration. NFT formation may also occur, sticking to the outer neuron and reducing signal transmission abilities of affected neurons. Figure adapted using Biorender.²⁷

1.2.3 The Amyloid Beta ($A\beta$) Hypothesis

The main focus of this thesis research project is on targeting the pathological pathways encompassed by the amyloid- β hypothesis, first proposed in 1992.²⁸ At a high level, the amyloid cascade results in neurodegeneration due to rapid increases in toxic $A\beta$ aggregates with various degrees of solubility in the CNS. Amyloid- β aggregates can be located throughout the body but

are primarily found in the hippocampus and cortex of the brain and their accumulation leads to the formation of extracellular senile plaques.^{13, 29, 30} Formation of amyloid- β aggregates starts from a precursor protein known as the amyloid precursor protein (APP). Starting in the nucleus, the APP gene is located on chromosome 21 and is comprised of 18 exons, spanning ~240 kbp.^{13, 31} High concentrations of APP are constitutively produced in the neuronal endoplasmic reticulum (ER) and transported to the Golgi-apparatus through the trans-Golgi network (TGN). Subsequently, the APPs are packaged into secretory vesicles for transport to the neuronal membrane where further processing occurs on this single membrane-spanning protein (Figure 5).^{30, 32} There are a variety of isoforms of the human APP gene ranging from 365 to 770 amino acid residues long, but the main A β encoding isoforms within the neural membrane are APP695, APP751 and APP770.³¹ Structurally, the APP is classified as a type I transmembrane glycoprotein and has a large extracellular N-terminal domain and an intracellular C-terminal domain that lies within cell membrane of the synaptic cleft.³² The N-terminal portion of the APP is divided into subsections starting with the E1 domain that has a metal binding motif and growth factor-like domain which are highly conserved, followed by a Kunitz-type serine protease inhibitor (KPI) domain, the E2 domain, and lastly two glycosylation sites just upstream of the A β fragment. A slight difference can be noted in APP695 when compared to the other isoforms because it lacks the KPI domain and is detected in mainly neural membranes. However, the APP751 and APP770 isoforms are detected in most tissues examined. Reasoning behind this slight splicing variation is poorly understood.³¹ Although there is extensive literature about the pathological roles of APP and its proteolysis, detailed reports of its physiological roles are lacking.³² Current evidence suggests that the APP plays a variety of roles involving the formation of synapses and contributes to neuroplasticity by aiding in processes such as metal ion homeostasis, binding and metabolism of

proteoglycans, neuritogenesis, haemostasis and thrombosis, glucose homeostasis, cell adhesion, and regulation of cell signalling.^{13, 32–35} Furthermore, it is shown that a lack of APP in the brain correlates with neuronal death and a subsequent deficit in motor and cognitive functions.³² It has also been shown that over 50 pathogenic mutations of the APP gene exist, a subset of which may increase the risk for developing AD due to accelerated rates of A β accumulation.³⁶ Some of the most common mutations associated with AD include the Swedish, Flemish, Dutch, Florida, and London mutations which all lead to elevated A β 42 concentrations with the Swedish variant also elevating A β 40 concentrations.³⁷ Moreover, A β elevation has been shown to have a cascading effect of neurotoxicity by leading to downstream changes and aggregate formation in wild-type tau proteins.⁴ Ultimately, normal processing of the APP occurs in two different ways and it is the balance of the two pathways, in-tandem with its metabolite clearance, that will determine its neurotoxicity towards the brain. Enzymes involved in APP processing include α -, β - and γ -secretases which will excise the protein into fragments in an amyloidogenic (Figure 5) or a non-amyloidogenic (Figure 6) manner.

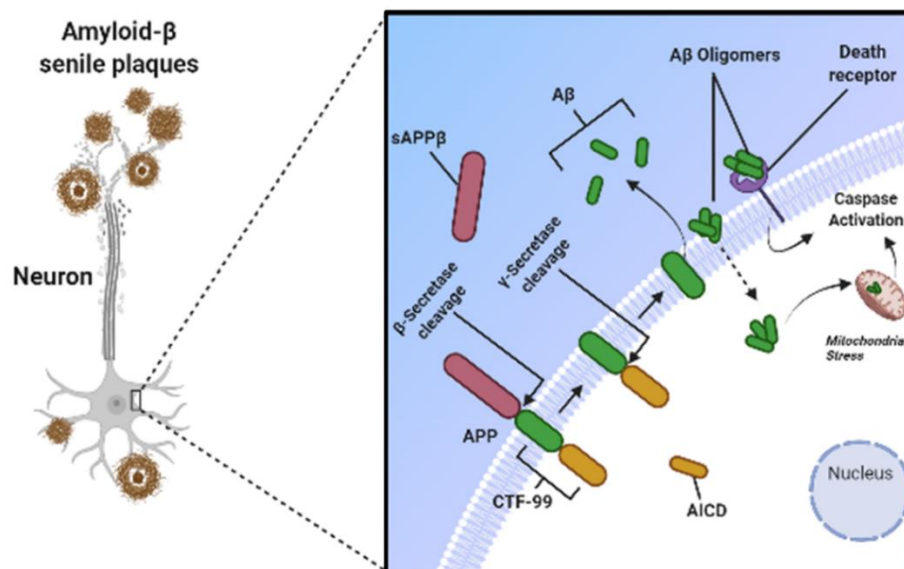


Figure 5. Amyloidogenic cleavage of the APP by β - and γ - secretases within the neuronal membrane releases extracellular A β monomers which may aggregate to form neurotoxic

oligomers. Oligomers of A β may cause cell death by binding various receptors or inducing dyshomeostasis via pore formation. Created with Biorender.³⁸⁻⁴⁰

1.2.3.1 Non-amyloidogenic APP Processing

When the APP is processed in a non-amyloidogenic manner, it means that the resulting peptide fragment is not prone to aggregation and subsequent toxicity. In healthy individuals, the APP gets excised by the α -secretase enzyme, releasing its non-amyloidogenic fragments into the cytoplasm where they are rapidly degraded.⁴¹ Roberts et al. first classified the α -secretase to be a zinc metalloprotease through the use of proteinase inhibitor profiling.^{30, 42} Since then, advances in research have revealed many α -secretase-like enzymes that are grouped within the ADAM (a disintegrin and metalloproteinase) endopeptidase family. In the past, scientists have debated about which of these enzymes (ADAM17, ADAM10 and ADAM9) are primarily responsible for APP cleavage. More recently, Hitschler and Lang conducted a study using super resolution light microscopy and confocal microscopy with a green fluorescence protein (GFP) tag that revealed ADAM10 undergoes physical linkage to the transmembrane domain of the APP, but ADAM17 does not. A knock-down based approach conducted in 2010 also came to this conclusion when knockdown of ADAM10, but not ADAM17 or ADAM9, fully suppressed α -secretase cleavage.⁴³ This provides strong evidence for presenting ADAM10, found on chromosome 15, as the dominant α -secretase enzyme that facilitates α -processing of APP.^{44, 45} ADAM10 is most commonly known to be constitutively active however, it is also reported that a fraction of this enzyme's activity can be regulated by protein kinase C.⁴⁶ Points of excision for α -secretase on the APP are located near the surface of the cell membrane between the amino acid residues Lys16 and Leu17 (in reference to A β peptide numbering). The products produced from enzymatic cleavage at these sites include an extracellularly released large soluble fragment called the APP- α fragment (α -APPs) and a membrane-bound C-terminal fragment known as CTF-83.¹³ Further metabolization of the α -APPs

is not necessary and it is at this point where they will play roles in enhancing neurite outgrowth and promote cortical synaptogenesis.³² Additional metabolites are formed from the CTF-83 fragment as the γ -secretase cleaves it to produce an amyloid intracellular domain (AICD) fragment and a 3 kDa p3 fragment whose function has been unclear until recently.^{13, 32} A study by Nhan et al. postulates that the p3 fragment induces similar, but less potent effects as A β peptides, likely due to the significant overlap in the amino acid residues from A β 's hydrophobic seeding region. Some of the reported neurotoxic effects of p3 include induction of inflammatory responses and cellular apoptosis.⁴⁷ APP cleavage points for the α - and γ -secretases are shown in Figure 6 demonstrating that a portion of the neurotoxic segment amyloid- β (A β) peptide gets excised during the initial α -secretase cleavage.

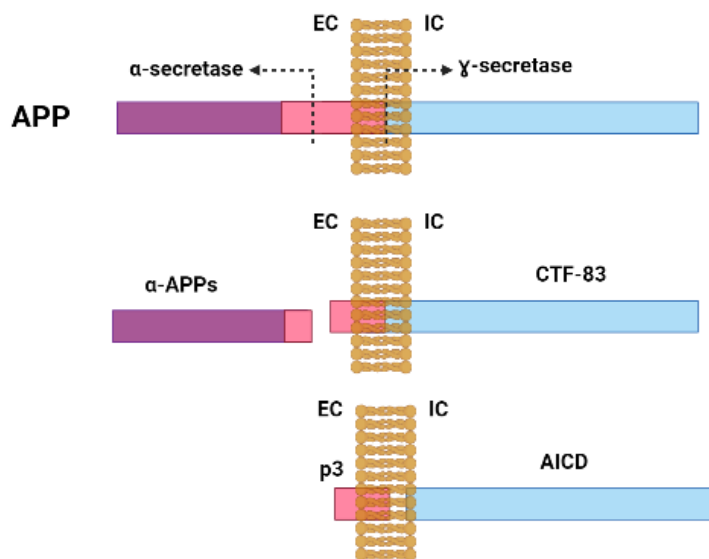


Figure 6. Schematic of non-amyloidogenic APP processing (EC = Extracellular Space, IC = Intracellular Space). The pink segment represents the 40/42 amino acid residue long A β peptide, known for its neurotoxic effects. Once cleaved by α -secretase, it is released.

1.2.3.2 Amyloidogenic APP Processing

During the pathogenesis of AD, metabolism of the APP results in the production of neurotoxic peptides A β 40 (~90%) and A β 42 (~10%).⁴⁸ Normally, the A β 40/42 peptides are both produced

and degraded as a natural part of the brain's physiological function thus, sole production of A β peptides is not a pathogenic trait. However in AD brains, their ability to metabolize these peptides begin to fail leading to inefficient clearing mechanisms of A β peptides and subsequent build-up.⁴¹ As shown in Figure 7, A β 40/42 peptides are formed upon APP cleavage by two transmembrane proteins starting with the β -secretase (BACE-1) and followed by the γ -secretase. BACE-1 (β -site APP cleaving enzyme) has a large N-terminal domain that aids in excision between the Met596 and Asp597 (APP695 numbering) residues within the APP cleavage site, upstream of the α -secretase cleavage site.⁴⁹⁻⁵² Upon cleavage by BACE-1, an APP- β fragment (β -APPs) is released extracellularly while a 99-residue long, membrane-bound C-terminal fragment (CTF-99) still carries the β -amyloid peptide segment.^{49, 53} Once again, the β -APPs are reported to be neuroprotective and are not processed beyond this state. On the other hand, the CTF-99 is processed further by γ -secretase proteolysis between Ala42 and Trp43, or Val40 and Ile41, releasing the neurotoxic A β 42 and A β 40 peptides respectively into the extracellular matrix and releasing the amyloid intracellular domain (AICD) fragment into the cytoplasm.^{13, 32, 38}

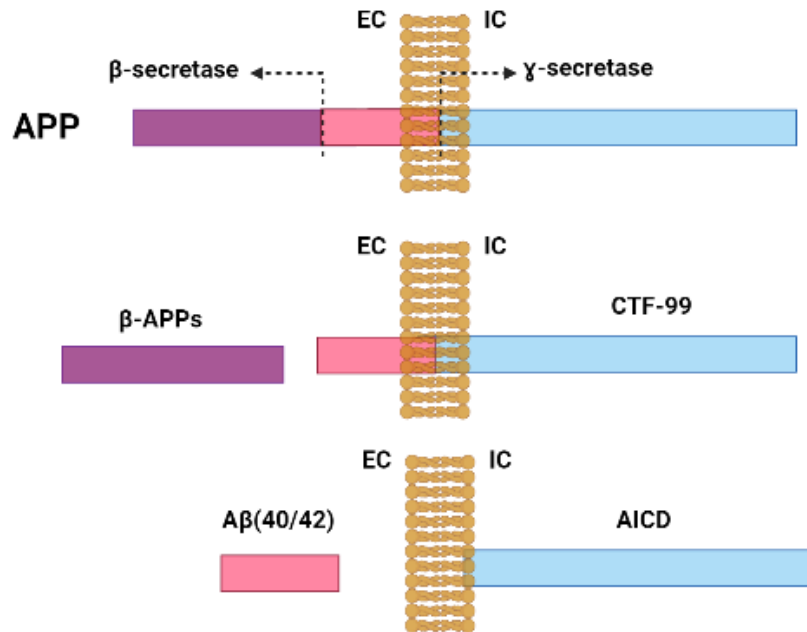


Figure 7. Schematic of amyloidogenic APP processing.¹³ Recreated with Biorender.com.

Understanding the etiology initiated by BACE-1 cleavage of APP is important for developing therapeutics that aim to prevent the formation of neurotoxic A β peptides from the root. β -secretase activity is found in most cells and tissues within the body, but the highest amounts of activity are observed within neuronal cells containing BACE-1. The highest concentrations of BACE-1 are observed in the TGN and endosomes as the enzymes are transported during cellular trafficking.^{51, 53, 54} Proteolytic activity seen in the neurons can either be attributed to BACE-1 (located on chromosome 11) or BACE-2 (located on chromosome 21), a homolog that shares 64% amino acid sequence overlap with BACE-1. Although the two β -secretases share structural similarities including two active site motifs, six conserved cysteine residues, N-linked glycosylation sites, and a C-terminal transmembrane domain, BACE-2 proteolysis is more commonly observed at two sites located within the A β 40/42 fragment. Thus, BACE-2 activity does not liberate A β peptides as frequently as BACE-1, making BACE-1 the most useful β -secretase target for developing anti-amyloid therapies and will be the focus of this section.^{51, 53}

BACE-1 is a constitutively secreted, transmembrane aspartic protease with its two active site motifs extracellularly located at amino acid residues 93 to 96 (D-T-G-S) and 289 to 292 (D-S-G-T).^{50, 51} This amino acid pattern is a key feature observed in aspartic proteases. As the name implies, a key amino acid residue within this sequence is Asp because it is required for catalytic activity. Optimal activity for BACE-1 occurs under acidic conditions (~pH 4.0-5.0) and at higher pH levels, this β -secretase is inactive (~pH 7.0).⁵⁰

The mechanism by which BACE-1 cleaves the APP is shown in Figure 8.^{54, 55} Shimizu et al. reported the X-ray crystal structure of BACE-1 and showed a flexible antiparallel β -hairpin covers the active site, guarding it from unintended access and orienting its substrate appropriately for catalytic activity. An important feature of this reaction is the two conserved water molecules oriented between Asp32 and Asp228 of BACE-1, termed W1 and W2 respectively. This is because the APP cleavage by BACE-1 involves hydrolysis of the peptide bond via an acid-base catalysis mechanism. Upon entry of the substrate, hydrogen bonding between the Asp pair and W1 activates W1 to undergo a nucleophilic attack of the C-terminal carbonyl from Met596 forming a geminal diol (gem-diol) intermediate. The gem-diol is stabilized by hydrogen bonding carboxyl groups of the catalytic Asp residues while the last proton is transferred from the other catalytic Asp to the amino leaving group on Asp597. Subsequent rearrangements release the soluble β -APPs and membrane-bound CTF-99 previously mentioned. Lastly, W2 enters the active site initiating a proton transfer and returning the Asp pair back to their original conformation.^{52, 54, 55}

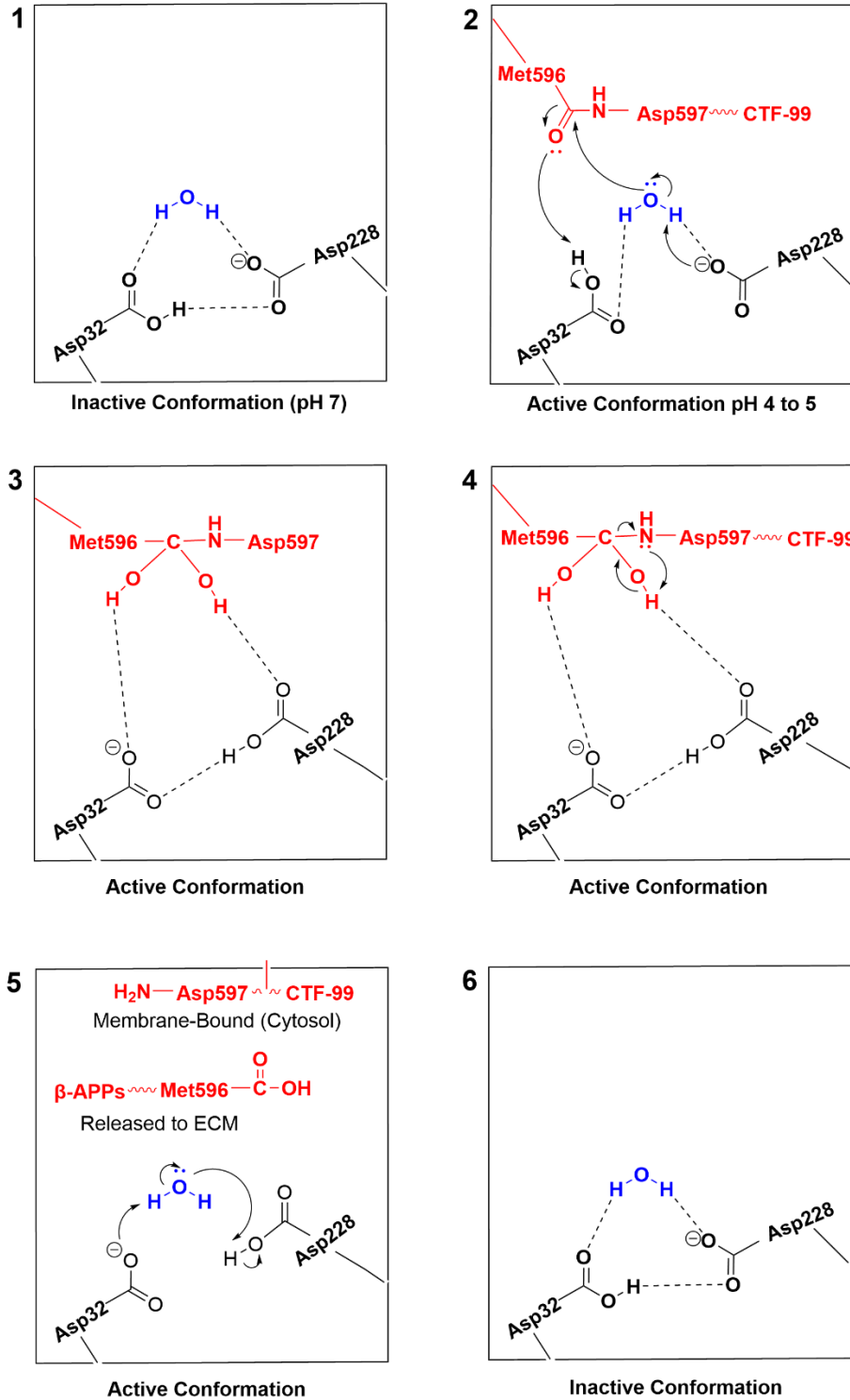


Figure 8. Mechanism of action (panels 1-6) for BACE-1 proteolysis of the APP between amino acid residues Met596 and Asp597. Note that extracellular and intracellular domains are not shown in this schematic. Red colored bonds and text are representative of the substrate (APP), blue

represents water molecule(s) and black text represents the amino acid residues in the BACE-1 active site participating in hydrolysis.⁵⁴

In the final stage of amyloidogenic APP processing, γ -secretase takes the stage as another crucial enzyme needed to liberate A β peptides making it an attractive therapeutic target. Similarly to β -secretase, a small subset of γ -secretase can be found at the cell surface while most of the enzymes are in the ER, Golgi/TGN and endosomal membranes. The type I transmembrane protein γ -secretase is a large ~230 kDa complex consisting of four subunits known as presenilins (PS1 and PS2), nicastrin, anterior pharynx defective 1 (APH-1) and presenilin enhancer 2 (PEN-2).^{56, 57} Since the 1990's, over two decades of research has been put into building our understanding of γ -secretase function, however the exact functions of each subunit are still speculative and to be fully elucidated.^{58, 59} So far, scientists have discovered two homologous genes found at two AD-related loci on chromosomes 1 and 14 which corresponded to PS1 and PS2 respectively.^{60, 61} Over 150 mutations in these genes have been discovered to contribute to familial early-onset AD (FAD), with a majority reported on PS1.^{62, 63} The effects of these mutations are seen to increase the ratio of A β 42 to A β 40 production. This is because the trafficking of APP gets modified such that vesicular transport to the neuronal membrane is halted, and as a result, amyloidogenic processing within the ER and TGN are increased.^{59, 64} Structurally, the PS subunits are known to have 9 transmembrane domains with two highly conserved, cytoplasm-facing, Asp (Asp257 and Asp385) residues on TM6 and TM7) that are necessary for γ -secretase catalysis.^{57, 65} The PSs have some functional overlap with the APPs in that they can aid in Ca²⁺ homeostasis, neurite elongation, autophagy, apoptosis, tumorigenesis, and synaptic function along with their contributions to γ -secretase activity.^{59, 66-68} As for the nicastrin subunit, it is a 130 kDa type I transmembrane protein that was the first cofactor to be discovered for the PS subunits. Nicastrin has been shown to interact with both PSs but preferentially PS1 to form a complex necessary for proteolysis of the substrates

within their transmembrane domains.⁶⁹ Some studies suggest that the PS-nicastrin complex may behave dynamically to load the γ -secretase substrate onto nicastrin in the extracellular matrix using its highly glycosylated N-terminus, specifically Glu333.⁷⁰ However, other studies have reported that Glu333 primarily aids in the maturation of the γ -secretase complex.⁵⁸ The third subunit, PEN-2 has two membrane spanning domains that contain both of their C- and N-terminals facing the ER lumen or extracellular matrix.⁷¹ Functionally, PEN-2 has been reported to aid in the stabilization and maturation of the γ -secretase complex by interacting with TM4 of PS and has been suggested to aid in PS1 endoproteolysis between TM6 and TM7.⁷² Lastly, the APH-1 has certain polar amino acid residues including two highly conserved Histidine residues (His171 and His197) demonstrated to help with the presentation of substrates for catalysis, further contributions have yet to be elucidated.⁵⁸ The overall arrangements of the γ -secretase subunits are still being speculated however the most recent efforts involving cryo-electron microscopy techniques suggest a “horseshoe” shape with the PS-CTF, APH1 and nicastrin located near the tips while the PS-NTF and PEN-2 are located near the middle.⁵⁹

1.2.3.3 Post-processing Fates of A β Peptides

As the human brain goes from a healthy physiological state to a diseased state during the onset of AD, a previously balanced production and clearance of A β shifts towards the former. In this sense, the metabolic routes that normally degrade A β peptides rapidly begin to malfunction leading to ineffective degradation of the amyloidogenic peptides and subsequent accumulation in the CNS. Additionally, the pathology is accelerated when the ratio of amyloidogenic to non-amyloidogenic processing of APP reverses, going from mostly non-amyloidogenic to mostly amyloidogenic processing pathways.¹³ Monomers of A β are soluble in biological matrices and due to their highly disordered nature, tend to undergo self-assembly. Formation of the aggregates is according to a

size-based hierarchy beginning with soluble monomers, dimers, trimers and oligomers followed by insoluble protofilaments that wrap around to form mature fibrils that are the primary components of the dense senile plaques seen to accumulate on neurons during AD pathogenesis (Figure 9).^{13, 73}

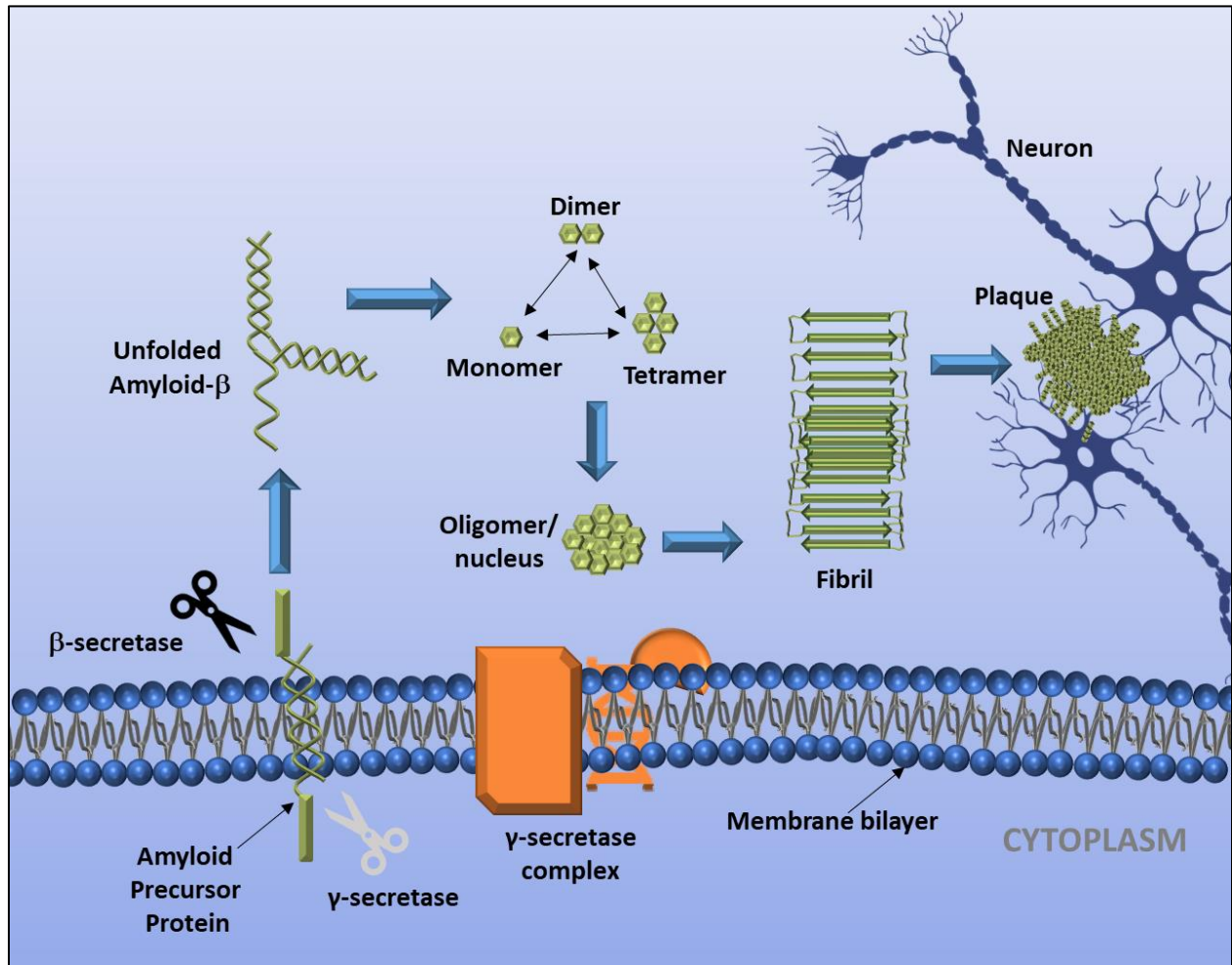


Figure 9. Aβ step-wise aggregation process into senile plaques. After Aβ(42/40) is released via the β-secretase cleavage, it undergoes self-assembly to produce soluble aggregates with varying degrees of toxicity. These soluble aggregates further assemble into insoluble fibrils in a β-pleated sheet conformation, resulting in disruption of the synapses ability to transmit signals ultimately causing neuronal death. Figure adapted from Safura et al.¹

Between the two amyloidogenic peptides, Aβ40 and Aβ42, Aβ42 is more toxic in nature. This is because Aβ42 contains an extra two amino acid residues at its C-terminus, Ile41 and Ala42,

making it more hydrophobic and thereby enhancing its seeding capabilities. Recently, Itoh et al. discovered the mechanism of action behind why the extra two residues make such a large difference in aggregation capabilities. Structurally, the A β aggregates are formed via folding into a β -hairpin loop containing hydrogen-bonding interactions along the fold. For A β 42, the extra two residues add just enough length to allow for another close-proximity interaction at the C-terminus, forming an electrostatic interaction between Ala42 and Arg5, a key residue involved in its enhanced β -hairpin stabilization (Figure 10).⁷⁴

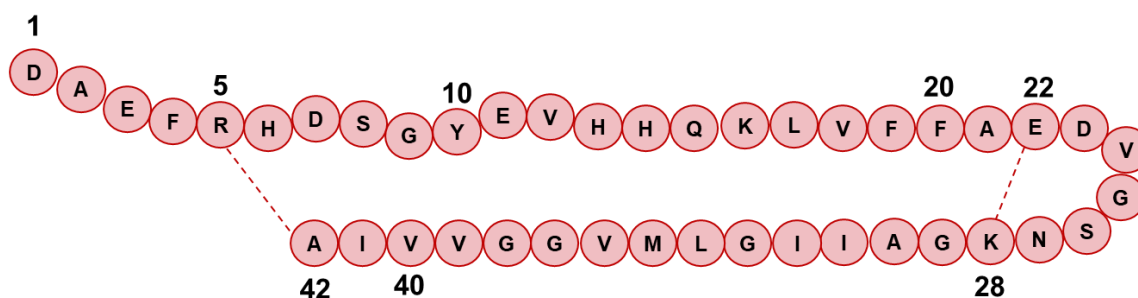


Figure 10. Amino acid sequence of A β 42, folded into a β -sheet conformation. Ala42 and Arg5 are key residues involved in the enhanced stabilization of the β -hairpin structure of A β 42 relative to A β 40 peptides.⁷⁴

Of the aggregates shown in Figure 9, the most toxic form of A β 42 assemblies is generally reported to be the high order, soluble, oligomeric forms while the most stable and abundant oligomer is the pentamer.^{2, 76} This is because the oligomers are soluble in the matrices of the brain, allowing for passive diffusion into neurons and synapses. As oligomers accumulate within both synapses and neurons, cognitive deficits start to emerge and are observed through the patient's gradual loss of memory, behavioral regulation and independence.^{2, 3, 73} Studies have shown that by binding a pre-oligomeric form of A β like the monomer, advances towards higher order aggregates may be halted, thereby significantly reducing neurotoxicity from high order A β oligomers.⁷⁶ For instance, in 2019 this was demonstrated by a research group who applied a known A β monomer binding peptide

(RD2) to transgenic mice with full-blown AD pathologies. What they revealed was that upon exposure to RD2, the traditional AD symptoms such as cognitive decline, behavioral issues, and high concentrations of A β plaque observed in the brain, were reversed in the old-aged mice.⁷³ Thus, studying the site of nucleation within the A β monomers becomes of great importance when developing AD therapeutics that target lower order units of A β .

Formation of the highly ordered fibrils occurs through a nucleation-dependent pathway where a nucleus is formed from the self-association of monomeric A β through pi-stacking interactions between its aromatic amino acids.⁷⁷ Research shows that promotion of nucleation occurs along the hydrophobic seeding region, composed of the hexapeptide ¹⁶KLVFFA²¹, and the pentapeptide ³²IGLMV³⁶, which serves as the “steric zipper” of the A β oligomer and fibril forms.⁷⁷⁻⁷⁹

Oligomers of A β were first detected in 1994 and since then, various hypotheses have been reported regarding their mechanism of neurotoxicity. Moreover, A β oligomers have been found both intracellularly and extracellularly in the cerebrospinal fluid (CSF) and interstitial fluid allowing for an expansive number of toxicological targets. To start off, the bilayer insertion hypothesis reports A β oligomers to have a higher affinity for membranes than monomers do and can directly insert inside of the lipid bilayer of neurons, forming a pore in the membrane, and disrupting its homeostasis. For A β 42 specifically, this dyshomeostasis occurs via ion channel formation in these created pores known as β -barrels. Similarly, as the oligomers cross the cell membrane, they can induce a Ca²⁺ influx which further disturbs the cell’s homeostasis. On the other hand, the receptor hypothesis provides a mode of action that explains cell-specific toxicity stating that A β oligomers may bind a variety of receptors within the membrane and induce intracellular responses associated with neural damage.³ For example, A β oligomers have been

reported to bind cellular prion proteins (PrP^c) within neural membranes and initiate toxicity. This occurs through the post-synaptic GPCR, metabotropic glutamate receptor subtype 5 (mGluR5), activation of Fyn tyrosine kinase and subsequent phosphorylation of the N-methyl-D-aspartate receptor (NMDAR). This cascade induces calcium dyshomeostasis, generation of reactive oxygen species (ROS), intracellular tau hyperphosphorylation, neuritic dystrophy as well as synaptic dysfunction and loss.^{2, 81} The NMDAR is a glutamate receptor responsible for regulating synapse formation and plasticity through modulation of ion channels. Thus, impairment of the NMDAR as a result of oligomeric A β binding causes serious implications such as decreases in spinal density and synapse deterioration.⁸⁰⁻⁸² Meanwhile, oligomeric binding to Na⁺K⁺ ATPase alpha3 subunits leads to a gradual decline in ATPase activity. This leads to Ca²⁺ accumulation via N-type voltage-sensitive Ca²⁺ channels and mitochondrial channels causing mitochondrial dysfunction and ultimately results in apoptosis.³ Another membrane lipid that the oligomers can bind are GM1 ganglioside sphingolipids, which regulate neuronal development and maturation. Oligomeric binding of these membrane sphingolipids also results in neuronal cell death led by nerve growth factor (NGF) receptors.^{84, 85} The lists goes on, currently accounting for 20 receptor types that are known to be bound by A β oligomers resulting in neurodegeneration (more of which are displayed in Figure 11), making this a well-supported hypothesis for A β mechanisms of toxicity.

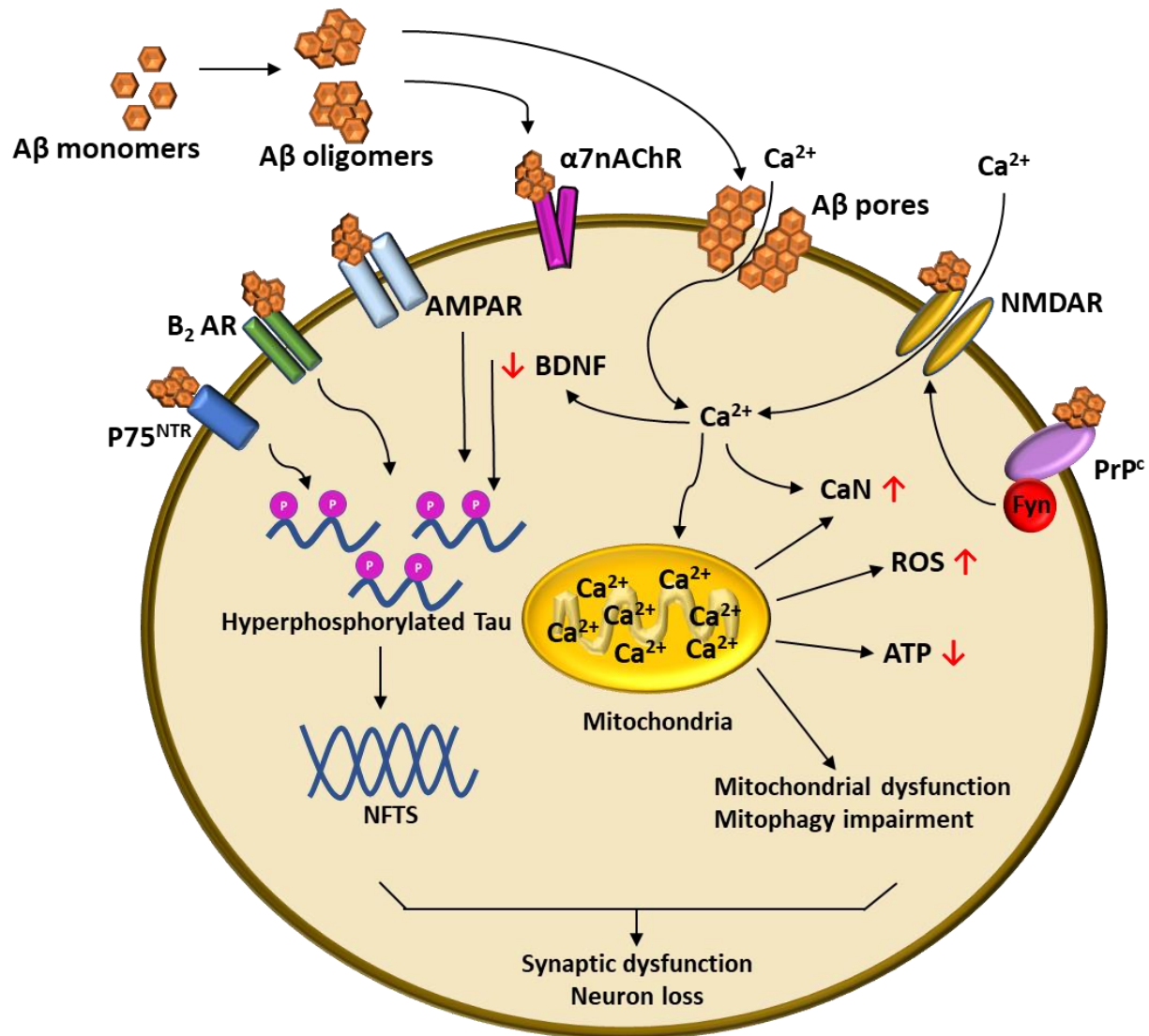


Figure 11. Schematic of the various mechanisms by which Aβ oligomers are hypothesized to induce neurotoxicity. There are two main hypotheses used to describe Aβ oligomer toxicity; i) the bilayer insertion hypothesis, and ii) the receptor hypothesis which both induce a plethora of toxic pathways including Ca²⁺ dyshomeostasis, tau hyperphosphorylation, mitochondrial dysfunction, reactive oxygen species formation, decreases in ATP generation, impaired transport of brain-derived neurotrophic factor (BDNF), hyperactivity of Ca²⁺/calmodulin-dependent phosphatase calcineurin (CaN), and ultimately neuronal apoptosis. Known Aβ oligomer binding receptors shown in this diagram include the previously mentioned PrP^c, NMDAR, causing Ca²⁺ dyshomeostasis and other receptors that cause tau hyperphosphorylation: α-Amino-3-hydroxy-5-methyl-4-isoxazolepropionic acid receptor (AMPA), β₂-adrenergic receptor (β₂-AR), p75 neurotrophin receptor (p75^{NTR}) and α₇-nicotinic acetylcholine receptor (α₇nAChR). Figure adapted from Huang et al.⁸⁰

It is widely accepted that once fibrillogenesis occurs, these larger aggregates of insoluble fibrils are less toxic than the oligomeric species of A β peptides.^{2, 76, 79, 86} However, the fibril forms are not entirely exempt from causing neural damage within the AD brain. Although their modes of toxicity are less expansive than those reported for oligomers, A β fibrils are seen to be capable of physically piercing the neural membranes by 3D constructions of high-resolution confocal microscopy images. This occurs as the intraneuronal A β buildup leads to fibril development and elongation within the dendrites, soma and even the spines of neurons. Physical accumulation and subsequent penetration of A β fibrils can cause disruptions in synaptic and neuritic cytoarchitecture. This disruption has been associated with a decrease in cytoskeletal proteins, which can cause the degeneration of a neuron, known as dystrophy. On a similar note, build-up of the long, needle-like fibrils around the blood vessels of the blood-brain barrier is known as cerebral amyloid angiopathy.⁷⁶ Accumulated fibrils may eventually pierce the neural membrane affecting the structural integrity of the blood brain barrier resulting in leaky membranes and compromised blood vessels.⁸⁶ In the long-run, membrane breakdown means the blood-brain barrier will no longer be able to protect the brain from harmful substances and physical symptoms will emerge as seizures, headaches, decreased consciousness and overall cognitive decline.^{87, 88}

1.2.4 Other Hypotheses for Pathological Routes to AD

So far, three of the most significant hypotheses that define the core pathological pathways of AD development have been discussed. In this section, additional secondary hypotheses will be discussed briefly that have connections to the AD pathology. These hypotheses will focus on i) monoamine oxidase (MAO) inhibitors and anti-depressants, ii) N-methyl-D-aspartate receptors (NMDARs), iii) ROS, antioxidants and metal chelators, and iv) neural inflammation and anti-inflammatory medications, and v) type-III diabetes and obesity.¹⁷ MAO enzymes are affiliated

with the mitochondria and play a role in the degradation of monoamine substrates such as serotonin and dopamine via oxidative processes. These processes lead to the generation of peroxides, known to exacerbate oxidative stresses and neurodegeneration. AD patients are reported to have altered levels of MAO neurotransmitters due to overactivity of MAO enzymes. Additionally, MAO activity has been shown to contribute to A β deposition by inducing the amyloidogenic processing of APP and further exacerbate NFT formation, all leading to neurotoxicity. MAO inhibitors have been historically used as anti-depressants and many of them are now commonly prescribed for treatment of AD depressive symptoms due to their decreased serotonin and dopamine levels.⁸⁸

NMDARs are a subtype of glutamate receptor that demonstrate hyperactivity in AD brains and traditionally play a role in neuronal signaling. Toxicity arises from overactivation of the NMDARs through increased concentrations of glutamate, ultimately leading to neuronal death. This mechanism and current treatment plans for combatting this pathological pathway are further described in Section 1.4.¹⁷ Another phenomenon that is frequently observed in AD patient brains are increased levels of ROS-induced impairments. Examples of detrimental effects from irreversible ROS-induced oxidative activity are disrupted cell membrane integrity, protein malfunction, and DNA damage leading to neuronal impairment. Because unquenched ROS pose great consequences for neuronal function, antioxidant therapy has been proposed as a therapeutic solution due to their ability to reduce ROS formation, scavenge free radicals, and chelate redox metals.⁸⁹ On another note, preclinical and clinical studies have shown that certain biometals such as Fe²⁺, Cu²⁺ and Zn²⁺ will accumulate near A β aggregates in the brain causing neurotoxicity by generating ROS, and exacerbating A β aggregation as well as tau phosphorylation. Thus, metal ion chelators have also been studied as potential AD therapies.^{17, 90} Additionally, chronic neural inflammation has been observed in many AD brains and is currently attributed to A β senile plaque

accumulation and NFT formation. Kinney et al. show that the sustained inflammatory response observed in AD is associated with activated microglia cells and chronic release of proinflammatory cytokines, ROS and other toxic species. For instance, increased release of interleukin-1 (IL-1) is shown to exacerbate A β production through increased APP production. Moreover, IL-1 β can induce a cascade effect activating cytokines that signal activation of CDK5, a kinase notorious for hyper-phosphorylating tau proteins. That being said, long term non-steroidal anti-inflammatory drug (NSAID) use has proven to have neuroprotective effects and may substantially reduce the risk of AD onset.⁹⁰ Lastly, the term “type III diabetes’ has been coined for AD recently due to certain hallmark symptoms including insulin signaling malfunctions and disruptions in glucose signaling contributing to AD pathology.⁹¹ Resistance to insulin and insulin-like growth factor (IGF) are additionally exacerbated by the previously mentioned AD pathologies including oxidative stressors, DNA damage, mitochondrial dysfunction, and inflammation. Further evidence for this pathological route is provided by clinical studies which have concluded that cognitive improvements were observed in AD patients undergoing intranasal insulin treatment and PPAR (peroxisome proliferator-activated receptor) treatment, an insulin sensitizer, anti-diabetes agent.⁹²

1.3 AD Risk Factors

The main risk factors associated with development of the AD pathology include uncontrollable factors such as genetic variables, age, and gender while others involve variables that can be controlled by lifestyle changes. Some of the main risk factors for AD include old age (>65), gender (female dominated disease), genetic inheritance (APOE4 genotype), poor cardiovascular health, poor diet, smoking, mid-life hypertension, diabetes mellitus, mid-life obesity, alcohol misuse, low education, loneliness, and mid-life hypercholesterolaemia.^{92, 94} Interestingly, research shows that in the later stages of life, certain risk factors will reverse. For instance, it is shown that after 75

years of age, hypotension and hypocholesterolaemia are risk factors for subsequent developments of AD and dementia.⁹³ Due to the significant challenges that come with controlling single and multi-intervention trials related to studying lifestyle factors affecting AD, mechanisms behind how certain lifestyle factors affect AD progression remain uncertain. The current hypotheses are vast and suggest that vascular, oxidative and inflammatory stresses in addition to neurotoxic and psychosocial factors are involved. For example, physical activity may reduce stress as well as cardiovascular diseases involving hypertension and additionally, increase the efficiency of A β clearance.⁹³ Moreover, smoking induces oxidative stress that has been associated with negative impacts on vascular, inflammatory and degenerative processes, however, the mode of action is unknown. Overall, a systematic review conducted by Decker et al. ranked depression, diabetes, cognitive/physical activity and hypertension to be the most prominent modifiable risk factors for the development of AD respectively.⁹⁴

Currently, monitoring genetic markers for advising AD treatments are not used clinically due to the contributions from genetic factors being limited. However, there are three classes of AD that may be at least partially explained by certain genetic background variances, these include autosomal dominant AD (also known as FAD), sporadic early onset AD, and late onset AD.⁹¹ The rarest form of AD (estimated to be less than 1% of all AD cases) is autosomal dominant AD, where 5-10% of the cases can be explained by high-penetrant mutations found in the APP, PSEN1 or PSEN2 genes. Mutations in PSEN1 and PSEN2 lead to a shift in the ratio of A β 40 to A β 42 peptides, enhancing production of the more neurotoxic A β 42 or decreasing A β 40 production which increases neurotoxicity.⁴⁸ Sporadic cases of early onset AD account for most early onset cases and is another class of AD that only makes up about 2-10% of the AD patient population.⁴⁸ Most factors leading to sporadic early-onset AD are not genetic however some early onset cases

have been attributed to APOE4 presence. Those with this allele have an AD trajectory that present as a typical amnesic syndrome affecting memory however, those cases that are negative for APOE4 display an atypical non-amnesic syndrome and leads to a more aggressive course of the disease.⁹⁵ As for the most common of the three, late-onset AD, we now know that there are a multitude of genetic risk loci (at least 21 loci) that are associated with contracting the disease.⁹¹ Initially, ApoE was the only major gene that was discovered to be associated with both early and late onset AD. Over time, scientists have found that this gene plays a role in cholesterol and lipid metabolism, and it has been long standing knowledge that inheritance of the ApoE4 allele is the most prominent genetic risk factor for sporadic cases of late onset AD. This is a glycoprotein that usually aids in lipid transportation, neuron growth, repair, rearrangement and overall maintenance.^{92, 97} Research shows that individuals with the ApoE4 allele are not only predisposed to an earlier age of AD onset but seem to also have more pronounced accumulation of NFTs and senile plaques relative to other AD cases.⁹⁶ Interestingly, the other ApoE2 allele is associated with a reduced likelihood of contracting AD as individuals with this allele are shown to have much less NFTs and senile plaques present in the brain.^{22, 23} Although ApoE4 is the most prominent genetic risk factor, it only accounts for ~50% of AD cases and additionally, 75% of people who carry this allele never end up developing AD. Thus, there is much to be explained when it comes to heritability of AD and detection of genetic risk factors during genome sequencing cannot be considered as an effective tool for diagnosis of AD.⁴⁸

1.4 Advances in AD Therapeutics: Present and Past

Over the years, a variety of strategies have been attempted by researchers in search of developing a disease modifying, anti-AD therapeutic. One of the most targeted pathological routes in the field of AD drug development is the amyloid- β aggregation pathway. In this sense, the core mechanisms

of A β -induced neurodegeneration are hypothesized to be reversible by: i) promoting the clearance of neuritic plaques, ii) enhancement of A β metabolism, iii) promotion of A β aggregation towards less toxic fibrils, and iv) preventing A β aggregation into soluble toxic oligomers.^{49, 77, 98, 99} The first of these strategies has had a large amount of recent success after over two decades with no new AD therapeutics coming to market. Biogen's Aducanumab (Aduhelm™) was the first anti-amyloid therapy to show moderate to high amounts of efficacy for reduction of cognitive decline in early-stage AD patients with mild cognitive decline during phase III trials. Aducanumab is a human immunoglobulin gamma 1 (IgG1) monoclonal antibody (mAb) whose mechanism of action involves targeting a specific sequence of amino acid residues on both soluble and insoluble A β aggregates for degradation by macrophages. After two independent randomized, double-blind, placebo-controlled, multicenter studies (EMERGE and ENGAGE) were conducted, aducanumab was demonstrated to significantly reduce A β -induced pathologies when compared to placebo ($P < 0.0001$) in the EMERGE study but not the ENGAGE study.⁹⁸ This discrepancy in results could be attributed to a variety of factors including the inherent stage of mild AD being skewed in one study versus the other, or lifestyle factor variations that could negatively impact AD progression in the ENGAGE study. It is important to note that a dose- and time- dependent decrease in pathophysiological biomarkers of AD including amyloid plaques were seen in both trials. To further validate this therapy, additional Phase 3b trials (EMBARC, NCT04241068) are on-going, however no results have been posted.^{98, 99} This was a major breakthrough in the field of AD drug development and received accelerated US FDA approval in June of 2021.^{99, 101} Not surprisingly, within one year of its reported success, another mAb called lecanemab (Leqembi™) received FDA approval, demonstrating great success at targeting soluble A β protofibrils and reducing cognitive decline in a similar study (NCT01767311).^{98, 102} Overall, both aducanumab and lecanemab are

huge steps forward in the progression of AD therapeutics and reinforce the necessity to continue targeting products of the amyloid- β aggregation pathway as a means of treating AD.

Other anti-AD drugs currently on the market are only able to provide symptomatic relief, however the disease state remains unchanged. The main therapies that have been prescribed for AD management prior to the inception of aducanumab and lecanemab include the cholinesterase inhibitors; donepezil (Aricept®), galantamine (Razadyne®), rivastigmine (Exelon®), and the NMDAR antagonist, memantine.⁷⁶ Donepezil aids in treating AD symptoms including memory loss, cognitive deficits, and general loss of function by inhibiting AChE. As a result of this, an increase in the levels of ACh available for cholinergic neurotransmission is observed. This increase in ACh will help to compensate for cholinergic neurons that have undergone neurodegeneration and no longer function.¹⁰² The binding mode of donepezil in the torpedo californica AChE (TcAChE) was shown by Mohamed et al. revealing that the benzylpiperidine moiety is oriented towards the AChE's catalytic triad, and also aids in blocking the PAS through positioning the indanone moiety towards the PAS residues. Additionally, donepezil can target the BuChE enzyme ($IC_{50} = >1000$ nM), but with a highly reduced affinity compared to AChE ($IC_{50} = \sim 6.7-11.6$ nM).^{104, 105} Targeting both cholinesterases is important because the ratio of AChE (primarily located in the CNS) to BuChE (primarily distributed throughout the body) decreases during the course of AD progression and subsequently, BuChE's metabolic activities towards ACh are elevated. AChE has also been reported to exacerbate amyloid aggregation, thus inhibiting this enzyme may serve as a multi-targeted therapy.¹⁷

Galantamine is another cholinesterase inhibitor that is an alkaloid found in a variety of plants such as daffodil bulbs. In 2001, this drug was approved to treat the cognitive deficits associated with AD through inhibiting AChE.^{105, 106} Other uses of this drug include treatment of

sensory and motor issues within the CNS in addition to myasthenia and myopathy. Galantamine is considered to be a mild cholinesterase inhibitor compared to donepezil because it is less potent ($IC_{50} = \sim 2 \mu M$) and also has a shorter half-life of 6 hours compared to 70 hours for donepezil.¹⁰⁴ Unfortunately, galantamine treatments are not well tolerated amongst patients as many side effects can emerge including severe nausea, convulsions, vomiting, stomach cramping, breathing abnormalities, confusion, weak muscles and watering eyes.¹⁰⁵ An alternative option for increasing cholinergic function is rivastigmine, which was approved to treat AD symptoms and Parkinson's disease-associated dementia in 2000. Unlike the previous drugs, rivastigmine can reversibly inhibit both AChE ($IC_{50} = 4.3 \text{ nM}$) and BuChE. This occurs due to a stronger binding interaction between the active site residues in the catalytic triad and the carbamate moiety than the acetate group of the ACh, thus preventing its hydrolysis and rendering AChE inactive. Upon binding, rivastigmine gets metabolized by AChE into a plethora of phenolic derivatives which are eliminated quickly through excretion pathways.¹⁰⁵ Like galantamine, rivastigmine also has poor side effects such as stomach aches, diarrhea, weight loss, vomiting and nausea, and appetite loss.

Another class of drugs used to treat AD are NMDAR antagonists, previously mentioned in Section 1.2.3. NMDARs are voltage-gated cation channels which are naturally guarded by Mg^{2+} ions in the inactive state and allow for Ca^{2+} influx during activation.¹⁰⁶ An example of an NMDAR antagonist is memantine, currently used to treat AD through regulating the activity of this glutamate receptor subtype. By binding to the NMDAR, memantine prevents hyperactivation that would result in an overactive glutaminergic system leading to neurodegeneration in the CNS, thus allowing for normal function. It is important to note that glutamate is a crucial neurotransmitter in the brain and NMDAR activity is necessary for neuronal function. Thus, complete blocking of its binding interactions would be unfeasible and elicit undesirable side effects. To combat this issue,

the antagonistic mechanism of memantine is uncompetitive and low-affinity in nature, only entering the receptor-associated ion channel during periods of hyperactivation. This allows for normal function of synaptic transmission.^{107, 108} Since its inception in 2003, memantine has been the only drug prescribed to treat moderate to severe forms of AD, while the previously discussed cholinesterase inhibitors are used to treat more mild or moderate forms of the disease.¹⁰² Typically, the therapeutic recommendations for AD patients include prescription of both memantine and a cholinesterase inhibitor to provide a dual action course of medical treatment for symptom management.¹⁰⁷ However, the risk-benefit ratio for memantine, has been questioned by researchers again, due to the numerous side effects associated with the use of this drug such as dizziness, headaches, drowsiness, hypertension, constipation and agitation.¹⁰⁸

Over the years, there have been a variety of other approaches that researchers have taken to try and solve the problem of AD. These approaches include peptide and biomolecule synthesis, development of metal chelating agents, and synthesis of small molecules for modulating A β aggregation. Even though many of these drug candidates have shown promise in vitro, none of these developments have made it to market as AD therapies due to various downfalls. For the peptides, this is because once they are in vivo, they are prone to rapid degradation by enzymes thus limiting their therapeutic abilities.¹ The metal-ion chelators showed promise based on the premise that they could prevent A β and tau fibrillogenesis as well as correct for dyshomeostasis of trace metals in the AD brain. Although this proves to be effective in vitro, once in vivo, this drug class cannot cross the BBB due to their hydrophilicity and furthermore, induces neurotoxicity at higher concentrations.^{1, 74, 109} Lastly, a plethora of small molecules have been designed and investigated for A β modulation capabilities including scaffolds based on polyphenols, organofluorines, inositols and quinones.²⁰ Many small molecules are designed to stabilize lower

order aggregates of A β because it has been reported that neurotransmission is negatively affected in the presence of large oligomers due to increased tau-phosphorylation, but this effect is not observed in the presence of dimers or trimers.^{1,27} Curcumin is a prime example of a multifaceted anti-AD small molecule in that it possesses anti-aggregation, antioxidant and anti-inflammatory activity. However, this molecule and many others are not suitable for AD therapy due to their poor pharmacokinetic properties and poor bioavailability in humans.^{74, 113}

Overall, the therapeutic landscape for AD patients has not looked good until recent years as patients have had to choose between continuous cognitive decline or living with other debilitating symptoms induced by medications that only offer symptomatic management. In terms of efficacy and disease-state alteration, aducanumab and lecanemab have set a new precedent for future AD therapies. However, there is more work to be done as these mAbs can only be administered intravenously, are extremely costly for the patients (\$56,000 USD annually for aducanumab), and medications are currently limited.^{114, 115} Therefore, these recent advances continue to pave the way for continued research and development of small molecule therapeutics that target the amyloid aggregation pathway.

1.5 Piperine Background

In a vast world of spices, black pepper stands out as one of the most used spices with its characteristic pungent flavor which can be attributed to the molecule piperine, formally known as (2*E*,4*E*)-5-(1,3-benzodioxol-5-yl)-1-(1-piperidinyl)-2,4-pentadien-1-one.¹¹⁴ The amount of piperine in black pepper kernels falls between 1-5% and can be extracted using maceration and polar organic solvents followed by purification techniques such as column chromatography and recrystallization.¹¹⁵ Piperine belongs to the class of molecules known as alkaloids and is derived from the black pepper plant known as *Piper nigrum*, in the Piperaceae family.^{116, 117} Alkaloids are

naturally occurring compounds that are typically weakly basic in nature and contain at least one nitrogen atom. In fact, the previously mentioned FDA approved cholinesterase inhibitor, galantamine is an alkaloid.¹¹⁶ A variety of other alkaloids have been known to elicit medicinal benefits for treatment of diseases including malaria, cancer, diabetes and cardiac dysfunction.¹¹⁷ Piperine is no different and has been extensively studied for its beneficial roles in chronic diseases, preservatives, and perfumes.¹¹⁴ For instance, piperine has been demonstrated to enhance the bioavailability of other therapeutic compounds such as curcumin through its ability to alter drug metabolism by inhibiting certain major cytochrome P450 (CYP) isoforms such as CYP3A4 and CYP3A5.^{120, 121} On its own, piperine possesses a vast portfolio of biological activities including anti-inflammatory, anti-cancer, anti-larvicidal, anti-viral, antidepressant, pesticide, and anti-AD activity.¹¹⁵ Structurally, piperine contains a piperidine ring attached via an amide bond to a conjugated pi-bond system composed of a *trans* alkene and a methylenedioxyphenyl (MDP) bicyclic ring system. There are several isomers of piperine known as isopiperine, (*Z, E*), chavicine (*Z, Z*), and isochavicine (*E, Z*) shown in Figure 12. However, the bioactive form of piperine is the (*E, E*) isomer and its geometric isoforms do not exhibit any pungency.^{122, 123} In terms of stability, piperine may undergo isomerization upon exposure to light over extended periods of time and this process is directly dependent on light intensity and time exposed. Major metabolites of piperine are processed by CYP1A2 and include the hydrolyzed products; piperic acid and piperidine, as well as others such as piperonal, vanillic acid, piperonyl alcohol and piperonylic acid.^{115, 118} Nevertheless, piperine has been reported to undergo minimal phase I hepatic metabolism. This is likely because of its CYP3A enzyme inhibition abilities and because CYP1A2 is not as abundant within the body as some of the other CYP isoforms.^{122, 123} For example, when administered orally in rats, Ren et al. demonstrated that piperine crosses the BBB into the brain effectively at the

clinically relevant dose of 35 mg/kg.¹²³ Although piperine has proven itself as an effective bioenhancer, improving the bioavailability of at least 16 drugs by amounts ranging from 0.54-fold to 20-fold, its own bioavailability has only been reported to be 25.4% and 23.2% in rats and mice respectively.^{117, 124} Even so, the pre-clinical reported levels of brain penetration and distribution in combination with its known neuroprotective effects against AD and other CNS diseases makes it a promising molecular template for further development and optimization.¹²³⁻¹²⁵

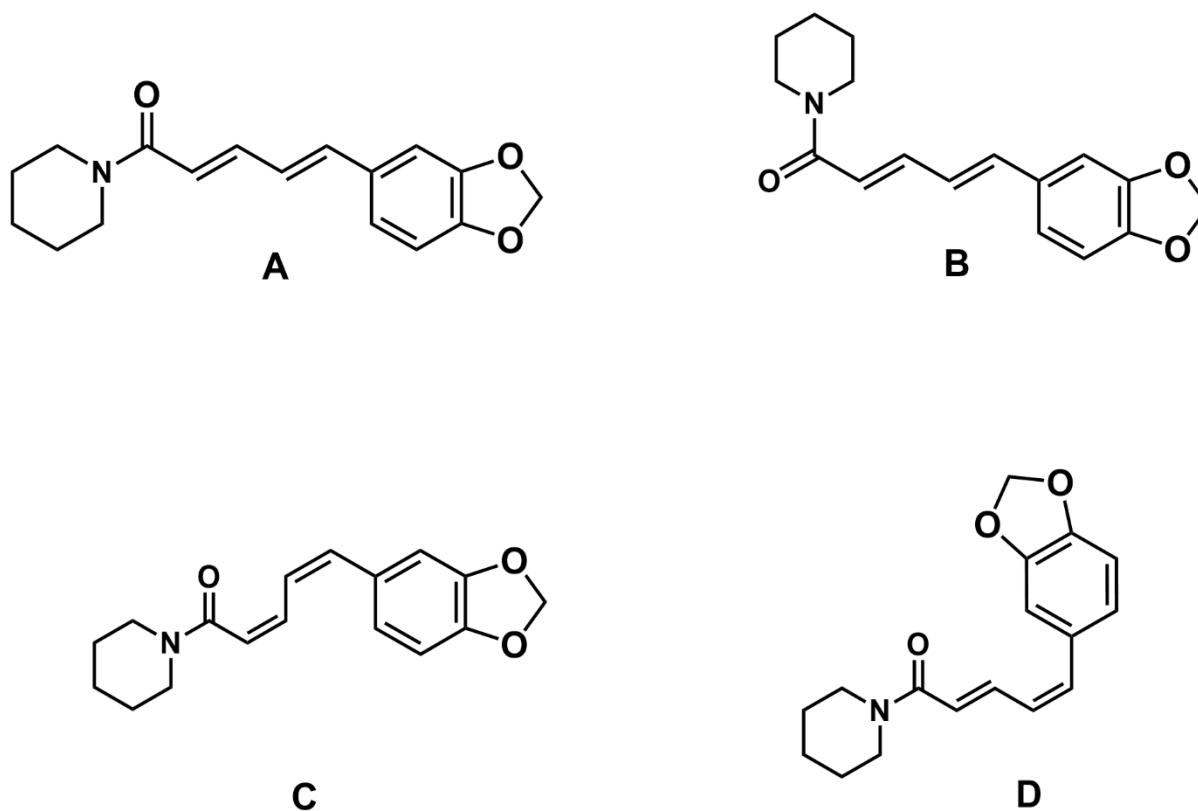


Figure 12. Piperine and its structural isomers. **A** = piperine, **B** = isopiperine, **C** = chavicine, **D** = isochavicine.¹¹⁵

Chapter 2: Objectives and Hypothesis

Natural products are a great source of inspiration in drug discovery. In the AD space, several natural products are known to prevent the aggregation of A β into toxic aggregates. For example, both curcumin and resveratrol are known to exhibit anti-A β activity.²⁹ Both curcumin and piperine have structural similarities as they possess common features such as the α,β -unsaturated system and aromatic moiety, highlighted in Figure 13 in red. Similar to curcumin, the planarity seen in piperine provides an extended linear conformation that should allow it to bind to A β aggregates and prevent their self-assembly into higher order structures. The current proposal aims to study the ability of piperine and its derivatives to bind and prevent A β 42 aggregation. Interestingly, previous reports show that piperine can enhance cognition in animal models of AD. Suggested mechanisms include inhibition of acetylcholinesterase enzyme in the CNS, reduction in oxidative stress and reducing the aggregation of A β 42 into toxic forms.^{124, 126, 127} These studies indicate that piperine itself has anti-AD properties although the exact mechanisms of its anti-A β activity is not clear. Therefore, the major objectives of the current proposal are to i) design and synthesize a novel library of piperine derivatives (Figure 14), and ii) evaluate them as A β 42 aggregation inhibitors to determine their interactions with A β 42.

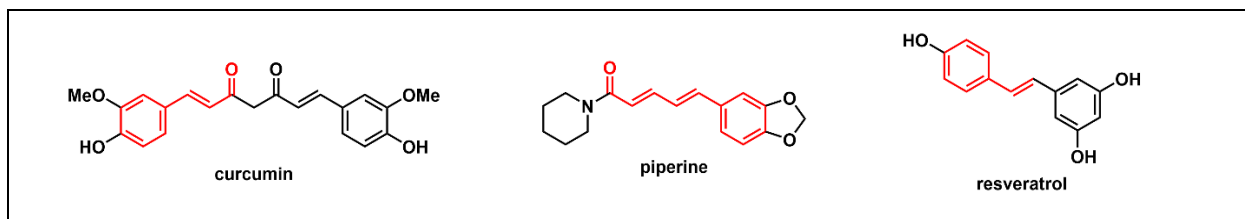


Figure 13. Key pharmacophores in curcumin, and resveratrol. These planar molecules have similar functional groups (aromatic and alkene moieties) to piperine and this planarity is a key feature that we hypothesize to play a role in its bioactivity against A β aggregation.

SAR studies presented on curcumin reveal that the minimum structural features needed to exhibit anti-A β aggregation properties includes the following molecular features; i) two hydrophobic and

aromatic moieties, ii) two hydrogen bond donors, and iii) one hydrogen acceptor. For piperine, SAR studies have not been reported and thus, this project aims to evaluate the anti-aggregation properties of piperine derivatives **4a-m**, shown in Figure 14, to uncover its SAR by modifying the electronic and steric properties at the terminal amide end of piperine. There are three chemically relevant features of piperine that are hypothesized to be primarily responsible for its anti-A β activity. These include the methylenedioxyphenyl (MDP) ring, the *2E*, *4E*-diene linker, and the piperidine functional group that is attached to the *trans* alkene system through an amide bond. To reveal the SAR of piperine, this project focusses on modifications of the piperidine group, replacing it with a variety of alternative moieties to study the effects of a diverse set of bioisosteres, steric groups, as well as polarities on piperine's pharmacological activity. Examples of such bioisosteres include comparisons between piperidine and piperazine or thiomorpholine and morpholine. Additionally, steric effects can be investigated through comparing larger moieties to smaller moieties such as piperidine ethanol, piperidine methanol, piperidine and pyrrolidine. Effects related to polarity can be studied through many of the chosen functional groups which range from relatively hydrophobic species such as benzylamine to relatively hydrophilic species like thiomorpholine dioxide.

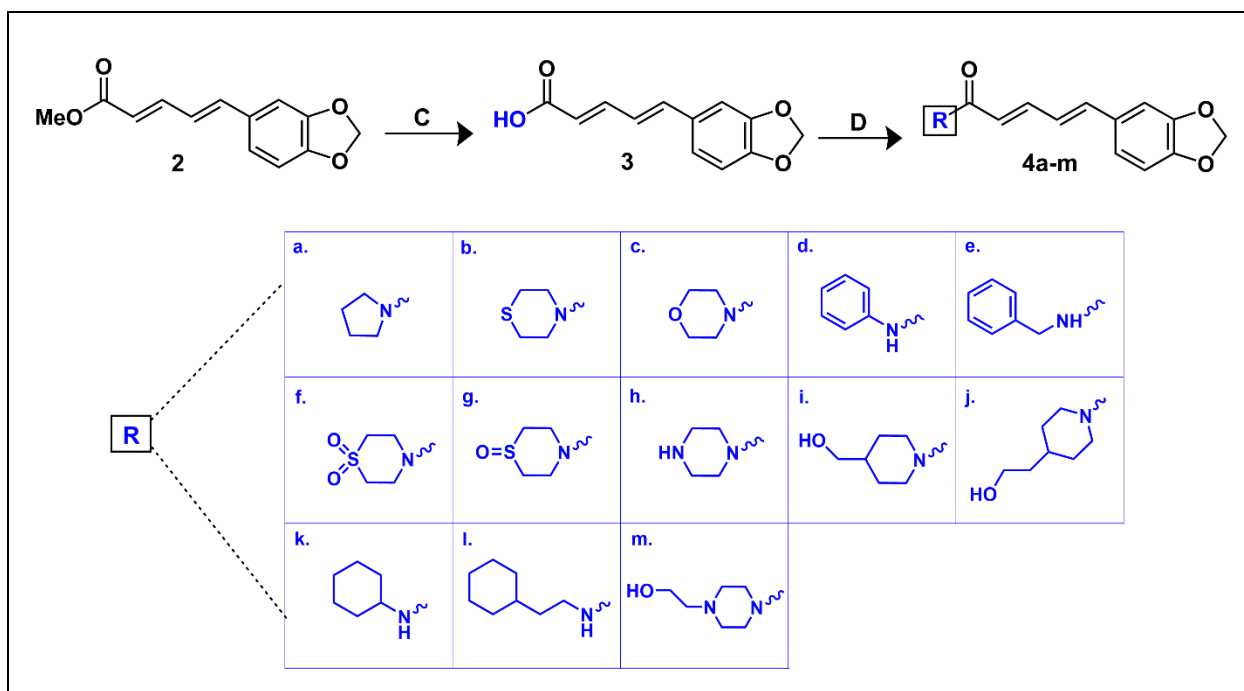


Figure 14. Proposed piperine derivatives **4a-m**. Precursor molecule, piperic acid (**3**) will also be included in the scaffold for comparison of activity. Reaction conditions: **(C)** Methyl Piperate, 1:1 ratio of 2 M NaOH to methanol (MeOH), 70 °C, 3 h. **(D)** Oxalyl chloride, piperic acid, dry dichloromethane (DCM), dimethyl formamide DMF (cat.), Ar (g), 0 °C to rt. over 3 h, then dropwise addition of amine to reconstituted reaction mixture in dry DCM, stir overnight at rt. (18 h).

Another promising feature that the piperine derivatives have is that they fulfill Lipinski's rule of 5 standards, created to aid in the process of designing a successful drug. The rule of 5 was first developed in 1997 using computational chemistry methods and has now been used for several decades for designing novel drugs with little modification. Lipinski's rule of 5, outlines the ideal physicochemical requirements for a potential small molecule drug candidate. These molecular requirements are as follows; i) the compound molecular weight should not exceed 500 Daltons (Da), ii) the compound should have less than five hydrogen bond donors, iii) the compound should have less than ten hydrogen bond acceptors, and iv) the compound should have a calculated LogP (cLogP) that is below 5.¹²⁸ By fulfilling Lipinski's recommendations, the proposed piperine derivatives (**4a-m**), are likely to exhibit favorable biological activity, pharmacokinetic properties

and reduced side effects in a biological system. However, these conditions were developed for drug candidates that do not necessarily need to cross the BBB. Thus, these guidelines must be further modified for a more useful evaluation of their BBB permeating abilities, a necessary feature when designing drug candidates for treatment of AD. Pardridge and coworkers reported revised guidelines for the evaluation of BBB penetrating small molecule drug candidates and state that drugs may permeate the BBB if; i) they have a molecular weight of less than 400 Da, and ii) form less than 8 hydrogen bonds.¹²⁹ In terms of cLogP, values between 1.5 and 2.7 have been reported to be acceptable where a cLogP of 2.1 is optimal. For making comparisons to all CNS marketed drugs, they had an average cLogP of 2.5, while the top 25 CNS marketed drugs have an average cLogP of 2.8.¹³⁰⁻¹³² Other studies have reported that the cLogP range required for BBB crossing is larger, lying between 2 and 5, which would account for certain known BBB crossing drugs such as donepezil.¹³² The cLogP values for the derivatives and known anti-AD agents are shown in Table 1 and reveal that all but three of the derivatives have cLogP values falling within one of the aforementioned ideal ranges. Additionally, the molecular weight range lies between 271.12 Da and 335.08 Da for these derivatives, making them an ideal size for BBB penetration. Another parameter that should be considered when designing CNS acting drugs is called polar surface area (PSA). The ideal PSA for BBB permeating drugs is estimated to be between 60–70 Å, with an upper limit of 90 Å.¹³⁰ However, Hitchcock and Pennington calculated the average PSA for the top 25 CNS marketed drugs to be 47 Å indicating that the previously reported range is likely flexible.¹³² Table 1 also shows the computed values of PSA for the piperine derivatives, demonstrating that they also have PSA values that fall near the ideal ranges for CNS acting drug candidates.

Table 1. cLogP and PSA values for all targeted piperine derivatives and known anti-AD agents, calculated using BIOVIA Discovery Studio: Structure-Based-Design Software. CYP inhibition

ability was determined with Swiss ADME web tool. PPN = piperine, CCM = curcumin, RVT = resveratrol, DPZ = donepezil, GLM = galantamine.

<i>Compound Name</i>	<i>cLogP</i>	<i>PSA (Å²)</i>	<i>Predicted CYP Inhibition Property</i>				
			<i>CYP1A2</i>	<i>CYP2C9</i>	<i>CYP3A4</i>	<i>CYP2C19</i>	<i>CYP2D6</i>
<i>4a</i>	2.41	38.5	Yes	No	No	Yes	No
<i>4b</i>	2.38	38.5	Yes	No	No	Yes	No
<i>4c</i>	1.64	47.4	Yes	Yes	No	Yes	No
<i>4d</i>	3.32	48	Yes	Yes	No	Yes	No
<i>4e</i>	3.32	48	Yes	Yes	No	Yes	Yes
<i>4f</i>	1.36	73.1	Yes	No	No	No	No
<i>4g</i>	1.27	55.8	No	No	No	Yes	No
<i>4h</i>	1.37	51.3	Yes	No	No	Yes	No
<i>4i</i>	1.96	59.3	No	Yes	No	Yes	No
<i>4j</i>	2.35	59.3	No	Yes	No	No	No
<i>4k</i>	3.6	48	Yes	Yes	Yes	Yes	No
<i>4l</i>	4.32	48	No	Yes	Yes	Yes	No
<i>4m</i>	1.37	62.7	No	No	No	No	No
<i>PPN</i>	2.86	38.5	Yes	Yes	No	Yes	No
<i>CCM</i>	3.2	93.1	No	Yes	Yes	No	No
<i>RVT</i>	3.09	60.7	Yes	Yes	Yes	No	Yes
<i>DPZ</i>	4.21	38.8	No	No	Yes	No	Yes
<i>GLM</i>	1.16	41.9	No	No	No	No	Yes

Table 1 also lists the Swiss ADME predicted parameters for CYP inhibition for five isoforms of the enzyme with CYP1A4, CYP2C9 and CYP3A4 being the most abundant isoforms in the body while CYP3A4, CYP2D6 and CYP2C9 are the top drug-metabolizing isoforms.¹³² Overall, the calculated PSA, cLogP values and predicted CYP inhibiting properties show that the proposed piperine derivatives possess desirable physicochemical properties for designing and developing novel, CNS acting, small molecule agents.

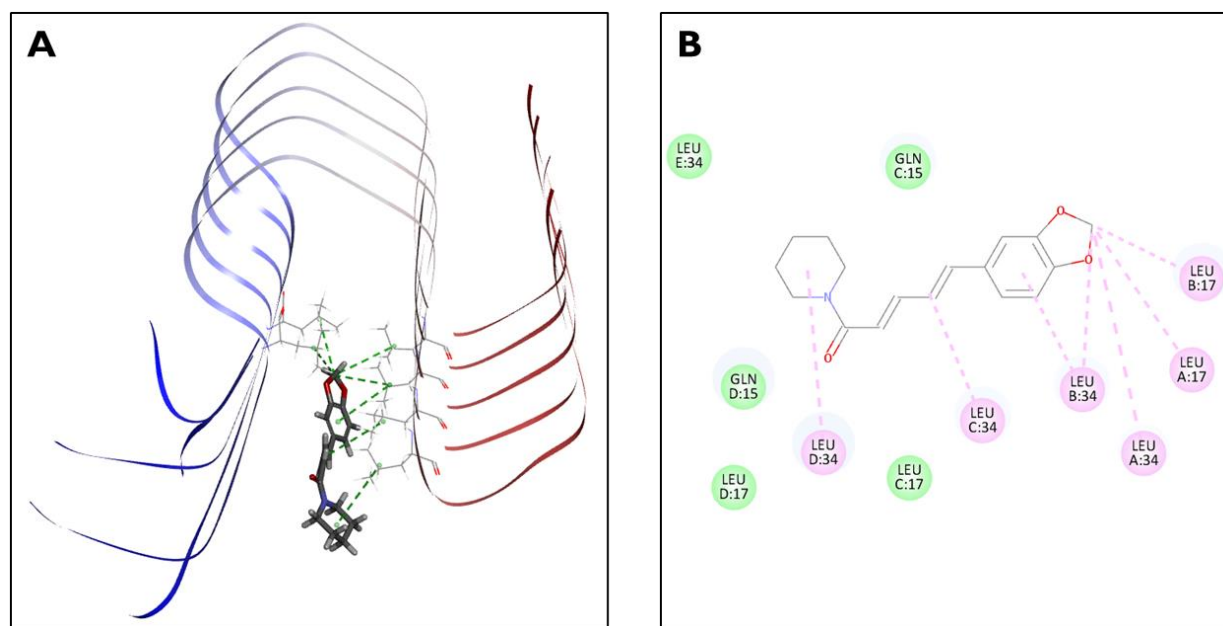


Figure 15. Panel A: 3D diagram of A β 42 pentamer model (pdb id: 5KK3) with piperine nested within the KLVFFA seeding region. All simulated interactions with residues are shown via green dotted lines.¹³³ **Panel B:** 2D interaction map of piperine docked in A β 42 pentamer model. Hydrophobic interactions such as pi-alkyl and alkyl-alkyl interactions are displayed in pink dotted lines whereas van der Waals interactions are displayed by green spheres representing the interacting amino acid residues.

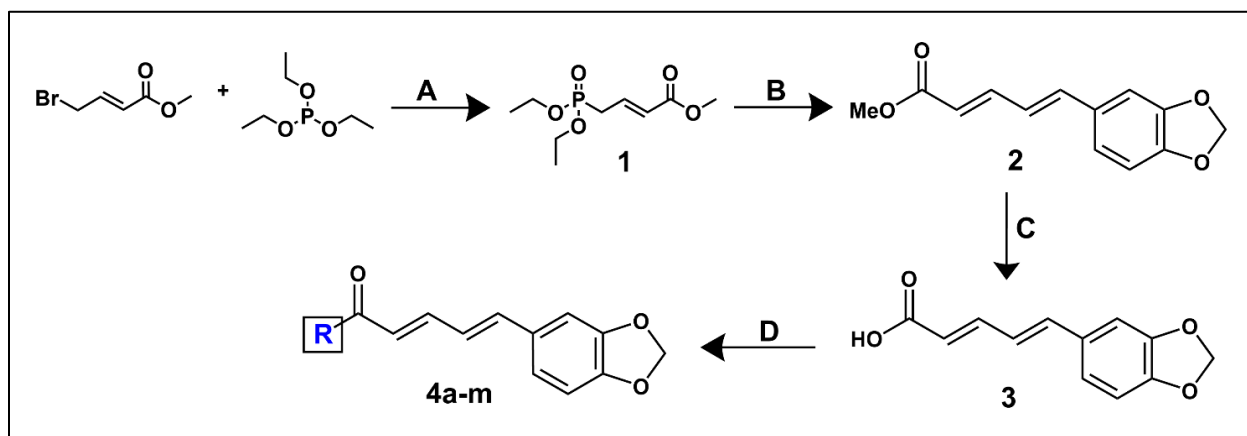
Preliminary computational modelling studies were conducted to examine the binding interactions of piperine and the A β 42 pentamer (pdb id: 5KK3, Figure 15). These docking studies show that a number of nonpolar contacts (eg: alkyl and pi-alkyl interactions) were seen between piperine and the KLVFFA seeding region of the A β 42 peptide. In particular, the MDP ring was in contact with the KLVFFA region and underwent multiple van der Waal's interactions with amino acids Leu34 and Leu17 from chains A and B of A β 42. These interactions ranged from 4.2 to 5.2 Å in distance.¹³⁴ This study also showed that the piperidine moiety exhibited weaker binding in the A β 42 pentamer model compared to the MDP ring suggesting that the piperidine moiety would be amenable for SAR modification to increase its binding to A β 42 and prevent its aggregation. Based on modeling studies, we hypothesize that modifying the piperidine substituent of piperine with the listed cyclic and aliphatic substituents (Figure 14), will lead to favorable interactions of

the proposed derivatives in the amyloidogenic region (KLVFFA) of A β 42, thereby enhancing their anti-aggregation properties compared to piperine. Furthermore, the proposed piperine derivatives possess desirable cLogP and PSA values (Table 1) making them suitable small molecule candidates to design novel anti-AD agents. The thesis objectives and hypothesis will be addressed by carrying out i) piperine derivative synthesis and their characterization by NMR and LC-MS analysis, ii) biophysical studies to determine their binding interactions with A β 42 via thioflavin T (ThT) based fluorescence aggregation kinetics assays and transmission electron microscopy (TEM) studies, iii) computational modeling studies using the 3D structure of A β 42, and iv) cell culture studies using mouse hippocampal neuronal HT22 cells to determine their cytotoxicity.

Chapter 3: Methodology

3.1 Synthetic Chemistry

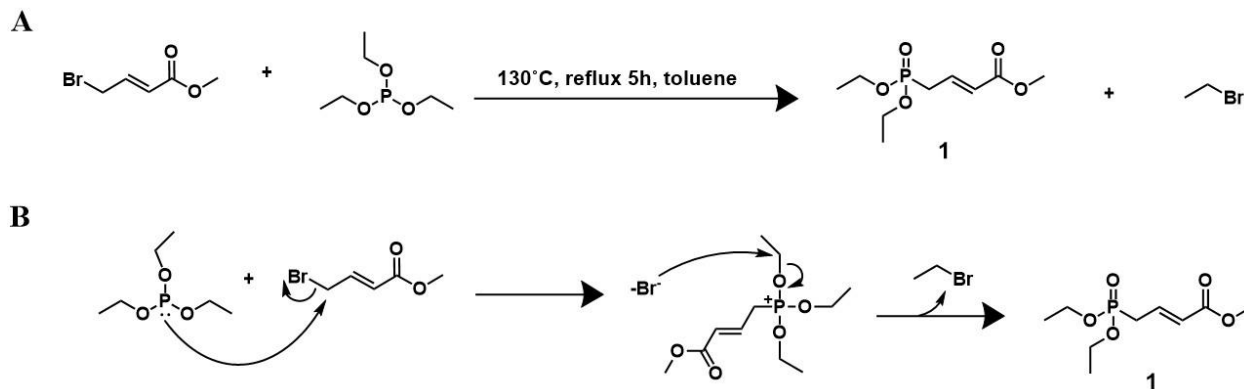
To synthesize the target piperine derivatives **4a-m**, a variety of methods have been reported. In this project, a four-step synthetic reaction scheme was utilised, based on previous literature reports.¹³⁵⁻¹⁴¹ These reactions consist of well-known name reactions including i) the Michaelis-Arbuzov rearrangement reaction, ii) the Horner-Wasworth Emmons reaction, followed by iii) hydrolysis, and iv) nucleophilic acyl substitution reactions. A summary of the four-step reaction scheme is shown in Scheme 1.



Scheme 1. Summary of reaction schemes used to synthesize piperine derivatives (**4a-m**) and precursor molecules (**2** and **3**). **(A)** Toluene, 130 °C reflux, 5 h. **(B)** Piperonal, lithium hydroxide (LiOH), dry tetrahydrofuran (THF), 70 °C reflux, 8 h, Ar (g). **(C)** Methyl Piperate, 1:1 ratio of 2 M NaOH to MeOH, 70 °C, 3 h. **(D)** (COCl)₂, piperic acid, dry dichloromethane (DCM), dimethyl formamide DMF (cat.), Ar (g), 0 °C to rt. over 3 h, then dropwise addition of amine to reconstituted reaction mixture in dry DCM, stir overnight at rt. (18 h). R groups for final piperine derivatives are displayed in Figure 14.

The first reaction is known as the Michaelis-Arbuzov rearrangement or Arbuzov reaction for short. This transformation is a versatile route for carbon-phosphorous (C-P) bond formation where a trivalent phosphorous is coupled with an alkyl halide.¹⁴² The nucleophilic phosphorous of trialkylphosphite attacks the electrophilic methylene group of the alkyl halide with bromine as a

leaving group. A tetrahedral intermediate forms and soon after, the nucleophilic bromide ion reacts with the phosphonium salt to form the phosphonate ester **1**, and the volatile ethyl bromide as seen in Scheme 2.^{137, 142}



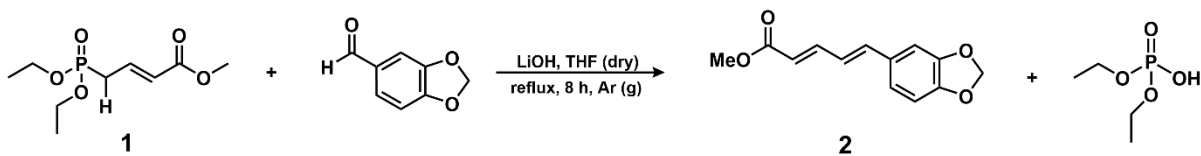
Scheme 2. Panel A is the overall Michaelis-Arbuzov reaction scheme where triethyl phosphite is coupled to 4-bromo-butenoate. Panel B shows the mechanism of the Michaelis-Arbuzov reaction.

To conduct the Michaelis-Arbuzov rearrangement, triethylphosphite was added to 4-bromo-butenoate at room temperature and then refluxed in toluene. The crude product was then rotary evaporated to remove toluene and then purified using flash chromatography (silica gel, *n*-Hexane:EtOAc 10:1 or DCM:MeOH, 9:1) to obtain the methyl ester phosphonate (**1**).

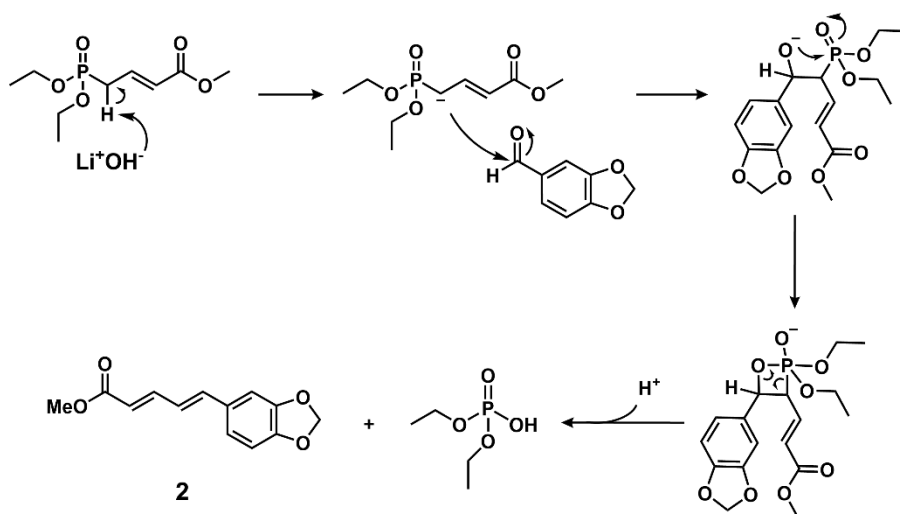
The second step in the synthesis of piperine is a variant of the Wittig reaction known as the Horner-Wadsworth-Emmons (HWE) reaction, shown in Scheme 3.¹³⁶ The HWE reaction is a reliable method used broadly for the stereoselective synthesis of alkenes by reacting aldehydes and ketones with dialkylphosphine oxide carbanions. This robust technique is known for its (*E*), (*E*) selectivity, efficient reactivity and easy preparation of the phosphonate precursors.¹⁴³ In the HWE reaction mechanism (Scheme 3), compound (**1**) was deprotonated with a base (LiOH) to generate the carbanion of the phosphonate ester. The carbanion then reacts with the aldehyde (piperonal) to form a four-membered ring intermediate which undergoes a rearrangement to release methyl

piperate (**2**), and the diethyl hydrogen phosphate side product, easily removable by liquid-liquid extraction.^{136, 143}

A



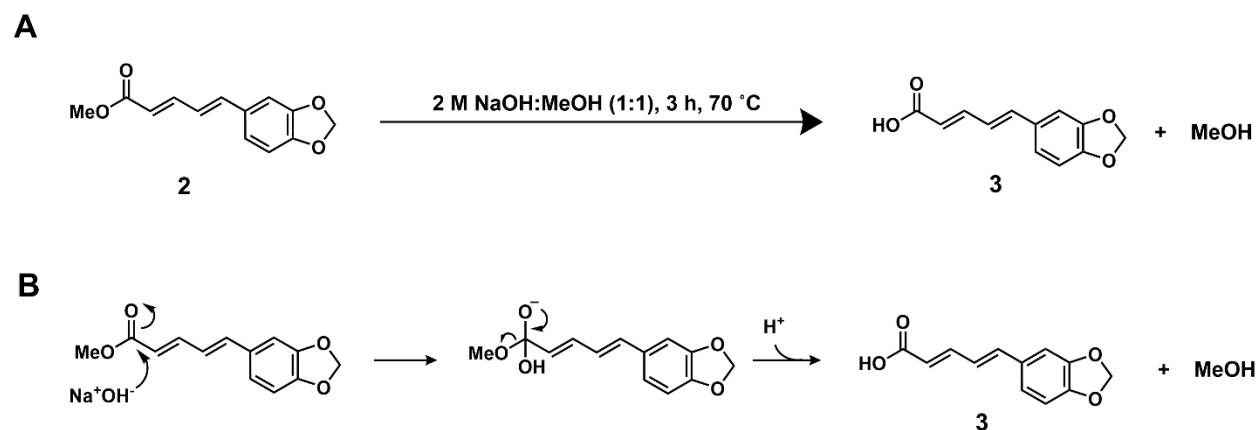
B



Scheme 3. Panel A: HWE reaction scheme of methyl ester phosphonate with the piperonal to form methyl piperate (**2**). Panel B: HWE reaction mechanism for formation of **2**.¹³⁶

In this reaction, **1** was converted to its carbanion form by treating it with LiOH in THF, next the mixture was reacted with piperonal and was refluxed under argon. The final product was purified by silica gel column chromatography using DCM as the eluent to afford **2**.

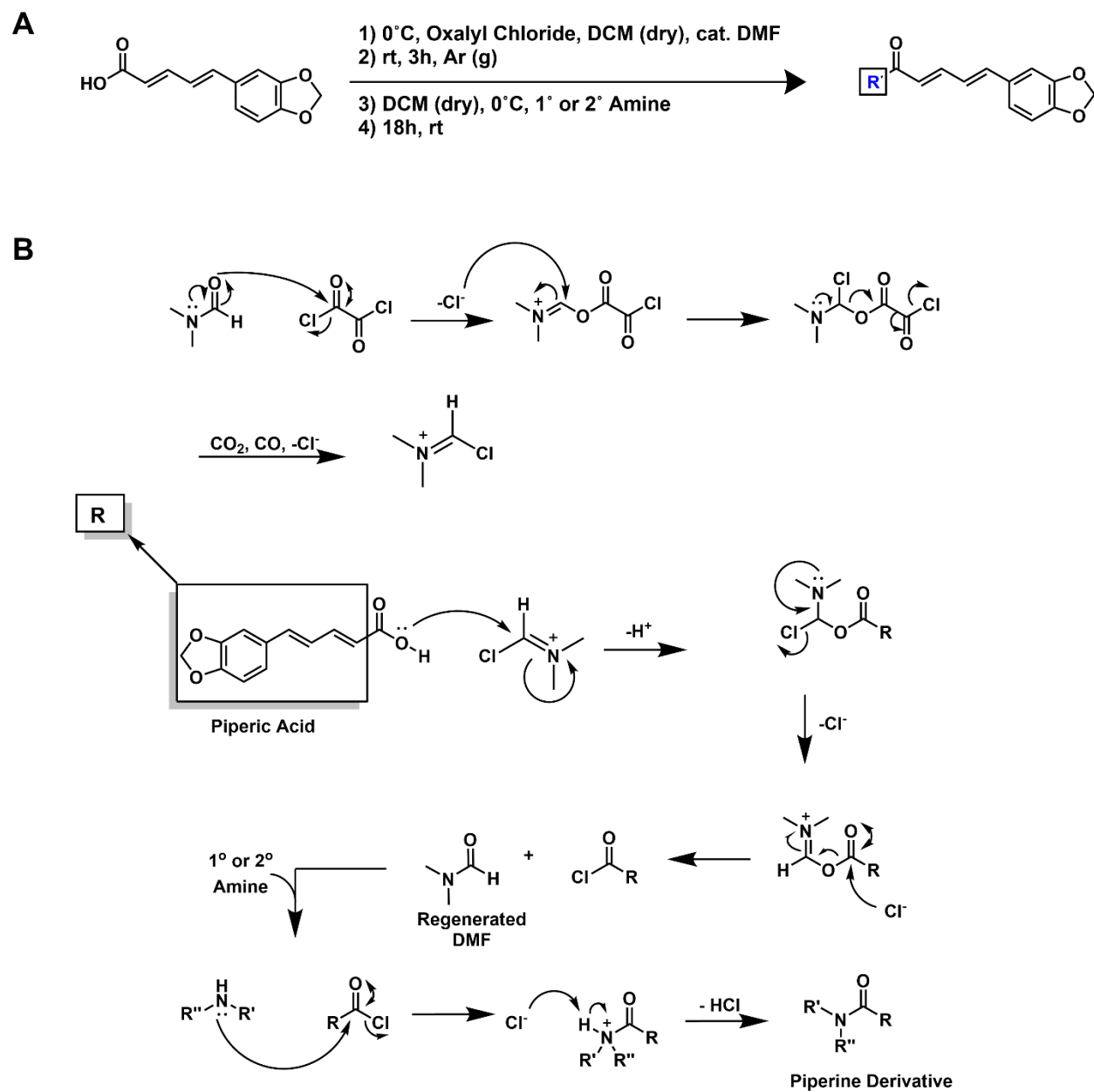
The third step involves a simple hydrolysis mechanism by which methyl piperate (**2**) was hydrolyzed by sodium hydroxide to form piperic acid (**3**) as shown in Scheme 4.¹³⁶



Scheme 4. Panel A: Reaction scheme for the synthesis of piperic acid (**3**). Panel B: Reaction mechanism for the hydrolysis of methyl piperate into **3**.¹³⁶

Methyl piperate (**2**) was refluxed in a solution of sodium hydroxide (2 M NaOH) and methanol (1:1) to afford **3** by hydrolysis.

For the last step, a variety of conditions were investigated to successfully convert the ester to amide. At a high-level, the most optimal route begins with generating the acid chloride of piperic acid in situ by reacting it with oxalyl chloride and using DMF as a catalyst which forms the Vilsmeier reagent.¹⁴⁴ The reaction scheme and mechanisms are shown in Scheme 5 and step-wise details follow. This quick and efficient conversion of the carboxylic acid into acid chloride was followed by the dropwise addition of this reaction mixture into the appropriate primary or secondary amine substrates.^{135, 141} Anhydrous conditions are required for this reaction to proceed well since oxalyl chloride is sensitive to moisture, reacting to form gaseous products including CO₂, HCl, and CO. Additionally, the excess oxalyl chloride was removed by rotary evaporation prior to its dropwise addition into the amine containing vessel to avoid the reaction of excess oxalyl chloride with the amines which can form diamine side products that may be difficult to remove.¹³⁵

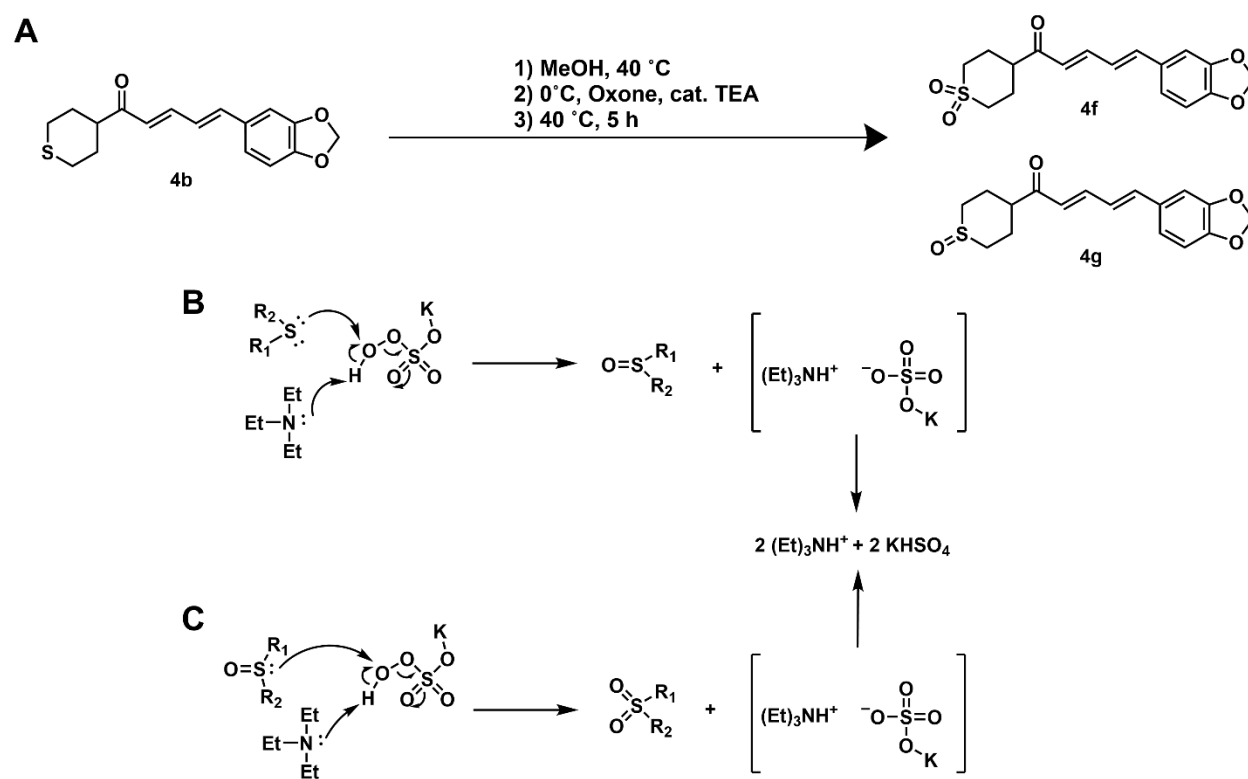


Scheme 5. Panel A shows the synthetic scheme for the synthesis of piperine derivatives **4a-m** from piperic acid via nucleophilic acyl substitution. Panel B is the arrow pushing mechanism for the DMF catalyzed chlorination by oxalyl chloride and subsequent acyl substitution reaction with primary or secondary amines to form piperine derivatives.¹⁴⁵

Amidation reactions were carried out by using oven-dried (80 °C) glassware and stir bars. The acid chloride was first generated by treating **3** in dry DCM with, a catalytic amount of DMF (2 drops) and oxalyl chloride under argon gas. The acid chloride was then treated with the appropriate amines with overnight stirring to obtain the crude product which was purified via flash

chromatography (*n*-hexanes:EtOAc 10:1 or DCM:MeOH 95:5) to obtain the corresponding piperine derivatives **4a-e** and **4h-m** (Scheme 5).

The preparation of thiomorpholine dioxide (**4f**) and thiomorpholine oxide (**4g**) was unique in that it relied on using the previously synthesized thiomorpholine derivative (**4b**) and subjecting it to oxidation (Scheme 6).



Scheme 6. Panel A: Reaction scheme for the triethylamine (TEA) catalyzed synthesis of **4f** and **4g** using Oxone for the oxidation of **4b** into its sulfone (**4f**) and sulfoxide (**4g**) products. Panels B and C: Reaction mechanism for the oxidation of thiomorpholine (B) and sulfone (C) functional groups.

The oxidized derivatives of piperine derivatives **4f** and **4g** were prepared by treating **4b** with the oxidizing agent Oxone (potassium peroxymonosulfate) in a methanol:water mixture in the presence of a catalytic amount of TEA. The reaction mixture was allowed to stir for 5 hours at 40

°C to obtain **4f** and **4g** respectively. The crude product was subject to flash chromatography using a solvent system of 95:5 DCM:MeOH to separate the two target compounds to obtain **4f** and **4g**.

In preparing the various piperine derivatives, the novel compounds discovered include **4g**, **4i**, **4j**, **4l** and **4m** while the other compounds have been previously reported.^{135, 136, 146, 147} Analytical data (NMR and LCMS) for compounds **4a-m** are reported in section 6.1.1 (Chapter 6).

3.2 Aggregation Kinetics Fluorescence Assay

The ability of piperine derivatives to modulate and prevent A β 42 aggregation was evaluated using the thioflavin T (ThT) based fluorescence assays.^{49, 148} ThT is a benzothiazole fluorophore that binds along the β -sheets formed in amyloid fibrils, and thus aids in detecting the formation of A β aggregates by fluorescence spectroscopy. The conformational changes of ThT that occur upon binding to the β -sheets enhances the ThT-fluorescence, characterized by a shift in the wavelength maxima from excitation and emission from 385 nm and 445 nm, to excitation and emission at 450 nm and 482 nm respectively, as shown in Figure 16.^{149, 150}

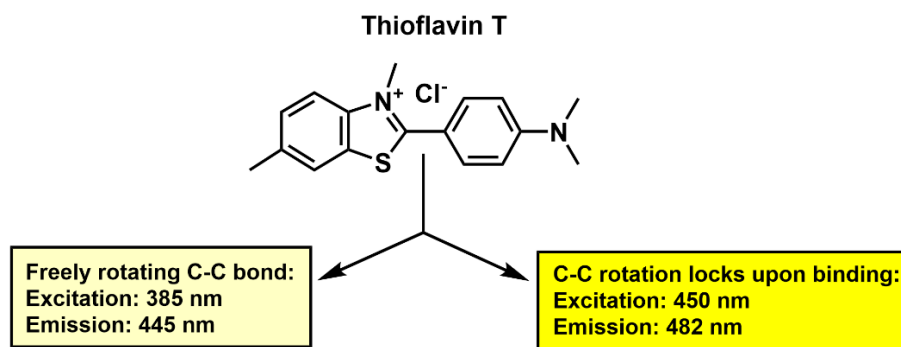


Figure 16. Conformational change of ThT upon binding to β -sheets of A β fibrils causes the C-C bond to lock, resulting in a fluorescence maxima shift.^{149, 150}

A schematic of the ThT fluorescence assay is depicted in Figure 17. As previously reported by the Nekkar lab, the assay involves the addition of buffer, ThT, and test compounds followed by adding the A β peptide and incubating the solution at pH 7.4 and 37 °C to monitor A β

fibrillogenesis over a 24 h time period. The relative fluorescence intensity (RFU) is monitored to determine the anti-aggregation activity of test compounds.¹⁴⁷ Untreated A β containing samples show a sigmoidal curve, with an initial lag phase, followed by a rapid growth phase and lastly a saturated plateau phase (Figure 17). The lag phase is the rate-limiting step and has slow fibril formation as the A β monomers are just beginning to aggregate into dimers, trimers, and oligomers prior to forming protofibrils and subsequent fibrils. Once the maturation of a single A β fibril is achieved, rapid growth of other fibrils will occur due to the ability of one fibril to act as the nucleus for seeding the formation of another. The last stage of growth is the plateau phase in which an equilibrium is formed between fibril formation and disaggregation.³⁸ These three stages were evaluated during data analysis to interpret the aggregation kinetics results that were obtained for each test compound in determining their A β 42 aggregation inhibition properties. For instance, an extended lag phase indicates the test compound's ability to slow down the rate of fibril formation which may potentially correlate to a delay in symptomatic onset of AD. Moreover, a reduced slope during the growth phase could also indicate a reduction in rates of fibril formation and potentially delayed AD onset. Lastly, a reduced endpoint RFU observed during the plateau phase would demonstrate the test compound's ability to reduce overall fibrillogenesis at the endpoint which is associated with reduced neurotoxicity.^{39, 49, 148} The anti-aggregation properties were compared with known inhibitors methylene blue (MB) and resveratrol (RVT). In addition, the activity of piperine was also evaluated. Details of the experimental procedure for performing the ThT based aggregation kinetics assay is reported in Chapter 6, section 6.2.

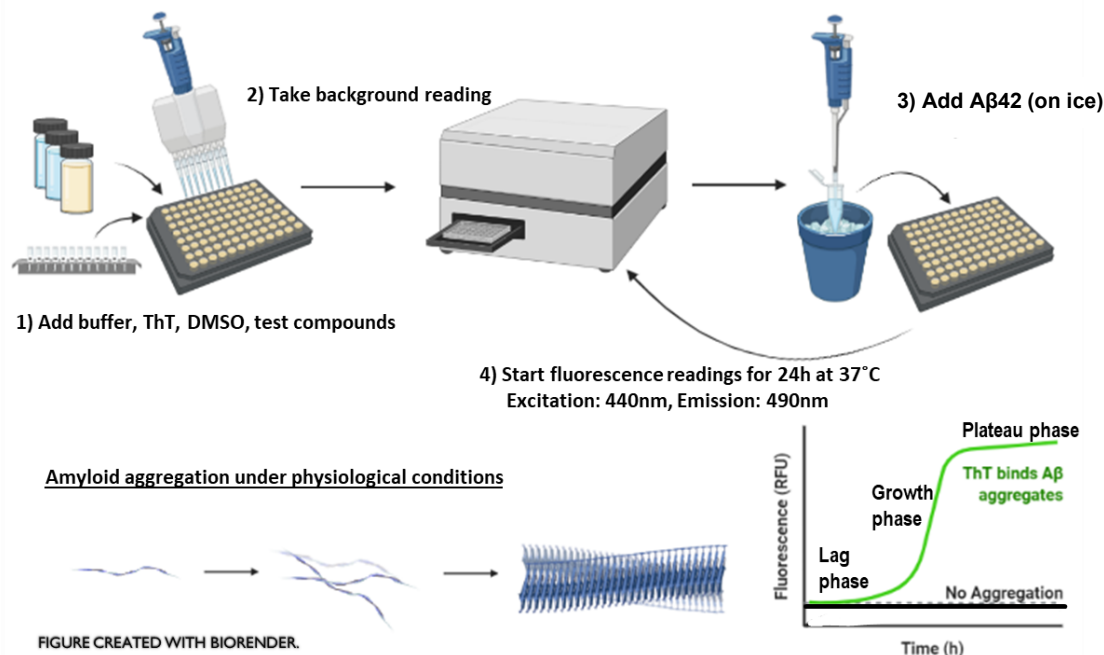


Figure 17. Flow diagram demonstrating the order of operations for the A β 42 aggregation kinetics assay. Under physiological conditions at pH 7.4 and 37 °C, the A β 42 aggregates form mature fibrils which are bound by ThT fluorophores and produce an increase in fluorescence, indicative of relative amounts of fibril formation per well. Note that the experimental lag phase may be shorter than displayed due to rapid aggregate formation of A β 42.¹⁴⁸

3.3 Transmission Electron Microscopy (TEM) Studies Methodology

To visualize and qualitatively assess the morphology of A β 42 aggregates, both in the presence and absence of test compounds, TEM analysis was conducted. TEM samples were drawn directly from the appropriate compound wells and control wells of the aggregation kinetics assay plate, immediately after the 24 h incubation period. This data acts as a supporting piece of information that can confirm the results of the aggregation kinetics assay. The principle behind TEM technology relies on an electron beam emitted from a tungsten filament that bombards the copper coated grid containing stained A β aggregates on top. Through this bombardment, some electrons may pass through the sample while others are scattered by the stained A β aggregates. Due to this electron scattering, an image is produced where the specimen appears as darker shades of grey-scale relative to the light background. This method of viewing and deciphering the morphology of

micro-sized specimens has been in use since the 1930's and was first pioneered by Ernst Ruska and Manfred von Ardenne.^{151, 152} The images are typically captured using a high-resolution digital camera that is embedded within the software, capable of resolutions down to 0.10 nm.¹⁵³ To view A β 42 fibrils, they must be stained with an electron dense stain such as phosphotungstic acid (PTA), which is able to bind the fibrils and allow for high contrast between the sample and the background due to electron deflection.^{49, 152} Details of the experimental procedure for preparing the TEM samples is reported in Chapter 6, section 6.3.

3.4 Molecular Docking Studies Methodology

In silico studies of the molecular docking interactions between the pentamers of A β 42 and piperine derivatives were conducted using the software Discovery Studio (DS) *Structure-Based-Design (SBD)* from Dassault Systemes Biovia Corp. USA (v20.1.0.19295). The aim of this study was to understand the binding interactions of piperine derivatives with the A β 42 peptide and to build a SAR to uncover the mechanism of action behind its anti-aggregation abilities. For the molecular docking study, the CHARMM (Chemistry at Harvard Molecular Mechanics)-based DOCKER (CDOCKER) algorithm was used where CHARMM is a computational software package that provides an array of tools and algorithms used for molecular dynamics and modelling simulations. The CDOCKER algorithm has been shown to predict, with high accuracy, the binding modes of small molecules and their affinity for a specific binding site. This algorithm is based on a technique known as molecular dynamics simulations which can be used to calculate the free energy of a ligand-receptor complex upon binding. Molecular dynamics is a grid-based docking algorithm that accounts for the full flexibility of the ligand while keeping the protein rigid during the docking simulation. Accounting for variables such as flexibility is important for making accurate binding affinity predictions as well as generating accurate molecular poses within the binding domain.

Additionally, CDOCKER utilizes a scoring function to examine the ligand's affinity for binding to the receptor factoring in van der Waals interactions, electrostatic interactions and hydrogen bonding.¹⁵⁴

In preparation for the docking simulation, the chemistry of compounds and peptides were assigned using the CHARMM force field to add hydrogens and fix bond angles. Moreover, partial charges were assigned by the Momany-Rone partial charge method. The solid-state NMR (ssNMR) structure of A β 42 (pdb id: 5KK3) was obtained from RCSB protein data bank (pdb) and subsequently used for the construction of A β 42 pentamer models.^{133, 155} For the molecular docking studies, a 20 Å binding sphere was constructed that encompasses the amyloidogenic core residues, ¹⁶KLVFFA²¹ and ³²IGLMV³⁶ within A β 42 for docking.¹³ The top ten binding poses generated from the CDOCKER algorithm were then ranked based on CDOCKER energy and CDOCKER interaction energy in kcal/mol. CDOCKER energy represents the energy of the entire complex, a more negative value indicates higher stability of docking in the binding site, whereas the CDOCKER interaction energy represents the localized interaction within the binding site between the ligand and its local amino acid residues.¹⁵⁶ Top poses of the piperine derivatives obtained from the CDOCKER algorithm were then used to calculate their binding energy (in kcal/mol) toward the A β 42 pentamer. Binding energy simulations provide a more accurate prediction of binding affinity between the protein-ligand complex due to accounting for additional parameters such as solvent effects.^{156, 157} The Generalized Born with a simple SWitching (GBSW) implicit solvent model was used to obtain the binding energies in kcal/mol. Similar to the CDOCKER energies, higher, and positive values are associated with less stable complexes while lower, and negative values are associated with more stable ones. In the end, the docked poses were compared and

analyzed by ranking their binding energies, and evaluating the polar and nonpolar contacts seen between the piperine derivatives and the amino acids in the amyloidogenic core of A β 42.¹⁵⁶

3.5 Cytotoxicity of Piperine Derivatives to HT22 Neuronal Cells

The toxicity of synthesized piperine derivatives were evaluated in the mouse hippocampal neuronal HT22 cell line.^{1, 158-160} This data provides valuable information about potential toxicity of novel test compounds. If the piperine derivatives show low toxicity (> 95% cell viability) towards the HT22 cells, it would suggest that those molecules exhibit low risk of toxicity in vivo. Historically, the dye MTT (3-(4,5-dimethylthiazol-2-yl)-2,5-diphenyl tetrazolium bromide) is used for monitoring cell viability.^{15, 49, 161} However, with recent technological advances in the field, there are better reagents to measure cell viability that follow the same assay principle as the MTT based methods. We used the CCK-8 assay to monitor the mitochondrial dehydrogenase catalyzed metabolism of a water-soluble tetrazolium salt (WST-8) into its formazan intermediate in viable cells (Figure 18). WST-8 formazan production can then be monitored using a multi-well UV-Vis spectrophotometer (Varioskan LUX Multimode Microplate Reader, Thermo Fisher Scientific, MA, USA) at a wavelength of 450 nm due to a colorimetric change observed in living cells from colorless to orange (formazan intermediate), as shown in Figure 18.^{162, 163}

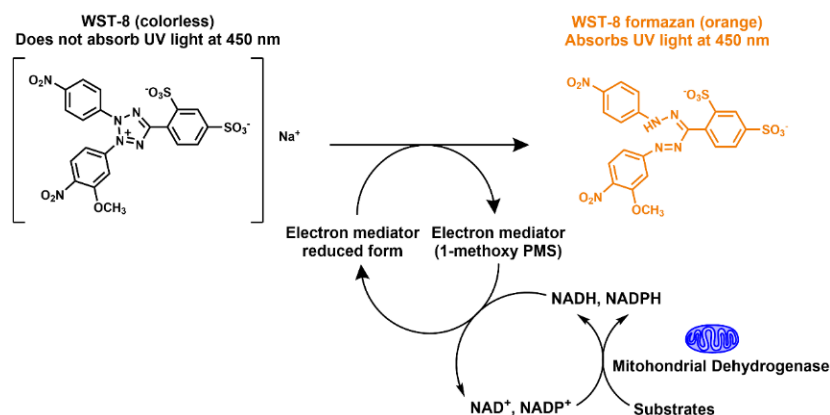


Figure 18. Schematic of colorimetric changes that occur upon WST-8 entry into the mitochondria of a cell due to metabolism by mitochondrial dehydrogenases into the orange WST-8 formazan intermediate. This change is detected using a UV-Vis spectrophotometer at 450 nm.¹⁶²

The top three piperine derivatives **4a-c** (based on the aggregation kinetics assay and TEM studies), were tested for cytotoxicity toward HT22 mouse hippocampal cells. To do so, the cells were treated with each derivate at 10 μ M and 25 μ M for 24 hours before conducting the CCK-8 assay to determine if the compounds incurred any toxic effects on the cells. If the cells were alive, they would have an active metabolism which resulted in transformation of the WST-8 into the formazan intermediate upon entry. If cells were dead due to toxic effects of A β , metabolism would halt, and a color change would not be observed.^{162, 163} To quantify percent viability, the relative absorption was calculated between the treated and untreated cells where 100% viability corresponds to an absorption value equal to that of the untreated cells calculated by the following equation:

$$\% \text{ Viability} = [\bar{X} \text{ Absorption of compound treated cells} \div \bar{X} \text{ Absorption of untreated cells}] \times 100 \% \text{ (Equation 1)}$$

The cytotoxicity of piperine and RVT were also evaluated. Details of the experimental procedure for the cell culture studies are reported in Chapter 6, section 6.5.

Chapter 4: Results and Discussion

Overall, the objectives of this thesis project were to use medicinal chemistry principles to synthesize a library of piperine derivatives based on the natural product/spice piperine. A group of 13 piperine derivatives were synthesized, characterized, and evaluated to assess their anti-A β 42 activity and cytotoxicity. ThT-based fluorescence aggregation kinetics, TEM, computational modeling, and cell culture studies were carried out. Results from these SAR studies are reported in this Chapter.

4.1 Synthesis of Piperine Derivatives 4a-m

A library of 13 piperine derivatives (**4a-m**) and piperic acid were synthesized using a series of reactions (Scheme 1 and 6, Section 3.1, Chapter 3). In the first step, the phosphonate ester (**1**) was synthesized using the Michaelis-Arbuzov rearrangement reaction. The phosphonate ester was obtained as a colorless oil in excellent yield (90%). In the next step, the phosphonate ester was reacted with the aldehyde (piperonal) using the HWE reaction conditions to give the corresponding ester, methyl piperate (**2**) as yellow crystals in good yield (86%). In the next step, methyl piperate (**2**) was hydrolyzed under basic conditions to obtain piperic acid (**3**) as a yellow solid in excellent yield (94%). This intermediate is the crucial precursor required to synthesize the target piperine derivatives **4a-m** (Scheme 1).

An alternative route of synthesis that directly converts the methyl piperate (**1**) into its amide derivative in situ without isolating the piperic acid (**3**) was tested prior to arriving at the optimal reaction process. This was achieved by using a non-nucleophilic base such as sodium hydride to deprotonate the amine which subsequently reacts with methyl piperate (**2**) to form the final amide products. However, this synthesis was not very efficient due to low reactivity and poor yields. Therefore, the piperine derivatives **4a-e** and **4h-m** were prepared by first acylating piperic acid (**3**)

in situ using oxalyl chloride and DMF as a catalyst, before subjecting it to nucleophilic acyl substitution reactions with various amines to obtain the target derivatives **4a-e** and **4h-m**. These target compounds were obtained in moderate-to-good yields (16-84%). The thiomorpholine derivatives **4f** and **4g** were synthesized starting from **4b**, which was oxidized using Oxone to obtain **4f** and **4g** in low-to-moderate yields (12% and 27% respectively, Scheme 6, Section 3.1, Chapter 3). All the synthesized intermediates and final compounds were characterized by $^1\text{H}/^{13}\text{C}$ NMR, and LC-MS to confirm their chemical structure and purity (>95%). Novel compounds were also characterized by high-resolution mass spectrometry (HRMS). The analytical data for final compounds **4a-m** are reported in Chapter 6 (Section 6.1.1).

4.2 Aggregation Kinetics Assay

All synthesized piperine derivatives (**4a-m**) were evaluated using the ThT-based fluorescence aggregation kinetics assay in the presence of A β 42 at 10 μM to assess their A β 42 aggregation inhibition activity. The anti-aggregation activity of piperine derivatives were reported as percentage inhibition, at the 24 h time point. Table 2 gives a summary data for all the compounds tested (**4a-m**), piperine and known inhibitors resveratrol (RVT) and methylene blue (MB). The SAR studies show that replacing the 6-member piperidine ring (piperine, R = piperidine, Table 2), with a 5-membered pyrrolidine ring in compound **4a** (R= pyrrolidine, Table 2), led to a 3.0-fold increase in anti-A β 42 activity (16% inhibition for piperine at 10 μM vs 48% inhibition for **4a** at 10 μM , Table 2). Similarly replacing the 6-member piperidine in piperine with a corresponding bioisostere in compound **4b** (R = thiomorpholine, Table 2) led to a 2.9-fold increase in anti-A β 42 activity (46% inhibition for compound **4b** at 10 μM , Table 2). Furthermore, incorporating another 6-member morpholine substituent also led to increased inhibition activity in compound **4c** (35% inhibition for compound **4c** at 10 μM , Table 2) compared to piperine. Encouraged by these studies

the thiomorpholine compound **4b** was oxidized to the corresponding sulfone and sulfoxide derivatives (compounds **4f** and **4g**, Table 2). Strikingly, addition of these polar substituents did not improve upon the initial promising activity seen in thiomorpholine but led to a dramatic decline in their anti-aggregation properties with weak inhibition profile (7-9% inhibition at 10 μ M, Table 2). A similar trend was seen for the piperazine derivative **4h** (6% inhibition, at 10 μ M, Table 2). Addition of an aromatic ring to the acyl nitrogen of piperine led to reduced inhibition with compound **4d** exhibiting weak inhibition (10% inhibition at 10 μ M, Table 2), whereas linking the acyl nitrogen with a benzylamine substituent led to a complete loss in activity (**4e**, not active at 10 μ M, Table 2). Other SAR modifications including linking the acyl carbon with polar substituents including piperidine methanol (**4i**), piperidine ethanol (**4j**) and piperazine ethanol (**4m**) also led to a complete loss in their anti-A β 42 activity (Table 2). Furthermore, incorporating a cyclohexylamine (**4k**) or a cyclohexylethanamine (**4l**) to the acyl carbon also gave inactive compounds (Table 2). Similarly, evaluating the free acid (piperic acid **3**) shows that it has weak activity (10% inhibition at 10 μ M, Table 2) which further indicates that the terminal substituents play a major role in the anti-aggregation properties of piperine derivatives. This study identified three top performing piperine derivatives **4a** (R = pyrrolidine, 48% inhibition), **4b** (R = thiomorpholine, 46% inhibition) and **4c** (R = morpholine, 35% inhibition). These compounds were not as potent as the reference agents, RVT and MB (63% and 86% inhibition at 10 μ M, Table 2). However, this study shows that **4a**, **4b** and **4c** exhibit superior inhibition compared to the parent compound piperine and hold promise as novel agents to target the amyloid cascade in AD.

Table 2. Percentage inhibition of A β 42 aggregation for all the synthesized piperine derivatives and reference standards at 10 μ M. Results are expressed as average \pm s.d (n = 3) based on three independent experiments. NA = no activity.

<i>Compound</i>	<i>R</i>	<i>Inhibition (%)</i>
4a	Pyrrolidine	48 \pm 0.7
4b	Thiomorpholine	46 \pm 3.5
4c	Morpholine	35 \pm 2.1
4d	Aniline	10 \pm 1.4
4e	Benzylamine	NA
4f	Thiomorpholine Dioxide	9 \pm 1.4
4g	Thiomorpholine Monoxide	7 \pm 3.5
4h	Piperazine	6 \pm 0.7
4i	4-Piperidine Methanol	NA
4j	4-Piperidine Ethanol	NA
4k	Cyclohexylamine	NA
4l	Cyclohexylethanamine	NA
4m	Piperazine Ethanol	NA
Piperine	–	16 \pm 3.5
RVT	–	63 \pm 1.4
MB	–	86 \pm 2.1
Piperic Acid (3)	–	12 \pm 0.7

In order to understand the effect of top compounds **4a**, **4b** and **4c** on A β 42 aggregation kinetics, the ThT based fluorescence assay was carried out using a range of compound concentrations (1, 5, 10 and 25 μ M) over a 24 h time period. The aggregation kinetics plots are given in Figures 19-22.

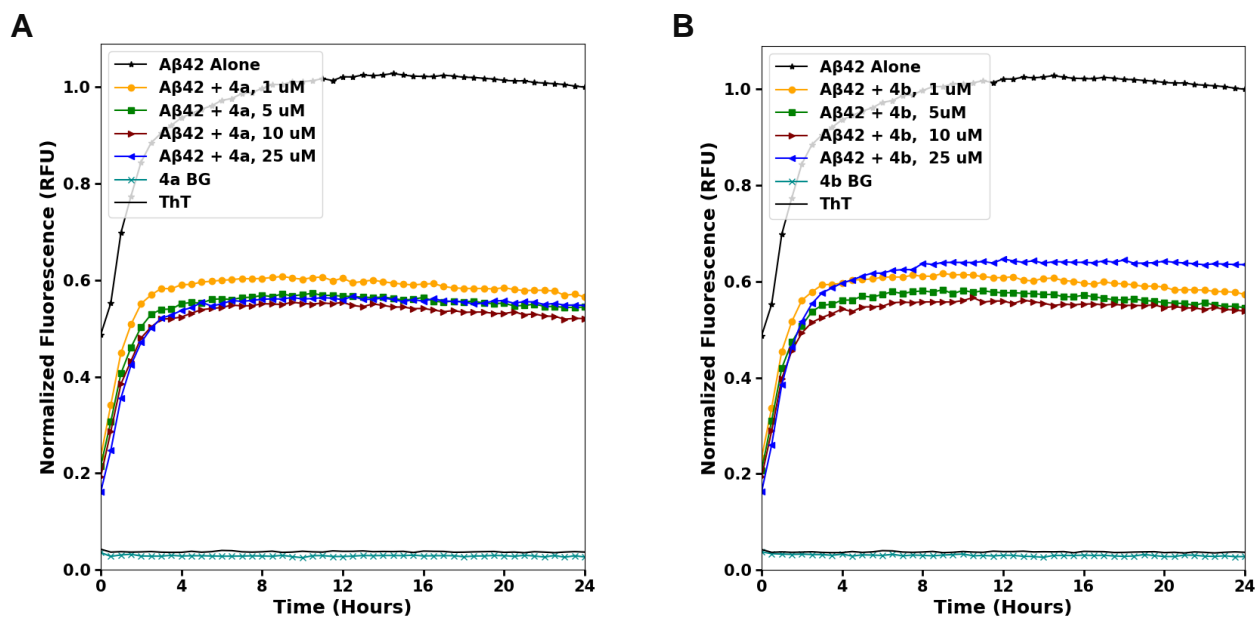


Figure 19. Panels A and B display the aggregation kinetics experimental results when 10 μM of A β 42 was incubated with **4a** and **4b** respectively. Compounds were tested at 1, 5, 10, and 25 μM , pH 7.4 phosphate buffer and monitored over 24 hours at 37 $^{\circ}\text{C}$. ThT fluorescence was determined using an excitation and emission λ of 440 and 490 nm respectively. The data presented are an average of three independent experiments ($n = 3$). ThT = Thioflavin T control fluorescence, BG = Background compound fluorescence.

Following the 24 h treatment, the untreated A β 42 control curve exhibited the highest fluorescence intensity (RFU) indicating the formation of A β 42 aggregates (Figure 19). In the absence of test compounds, the A β 42 curve lacks a clear lag phase as A β 42 tends to undergo rapid fibrillogenesis. However, the growth and plateau phases were visible. In the presence of compound **4a**, there was a significant decline in the ThT fluorescence intensity (~ 1.9 -fold decline) compared to the A β 42 control curve during the 24 h incubation period (Figure 19). The decline in the ThT fluorescence intensity demonstrates a decrease in the formation of A β 42 aggregates and A β 42 load. The aggregation kinetics curve also shows that **4a** was able to reduce the duration of the growth phase to a significant extent (~ 4 h), compared to A β 42 control curve which lasted for ~ 12 h (Figure 19). The aggregation kinetics curve in the presence of **4a** also shows that the compound can interact with both the lower and higher order structures of A β 42 aggregates to reduce the self-assembly process. Interestingly, **4a** (R = pyrrolidine) exhibited a similar activity profile at all the tested concentrations with 43-48% inhibition of A β 42 fibrillogenesis at the 24 h time point. A β 42 aggregation kinetics data for **4b** (R = thiomorpholine) exhibited a similar trend as compound **4a** (Figure 19). It was able to inhibit A β 42 aggregation at all the tested concentrations and its activity ranged from 36-46% at the 24 h time point, which was very similar to **4a**. The aggregation kinetics data also shows that compound **4b** has the ability to bind to various forms of A β 42 aggregates due to a major reduction in overall fluorescence at both the end point (where mainly fibrils are observed) and the growth phase (where aggregates of all sizes are present) in the kinetics curve. In contrast, compound **4c** (R = morpholine) was a weaker inhibitor of A β 42 aggregation (25-35%

inhibition at 24 h, Figure 20). Furthermore, the presence of a piperidine ring in piperine reduced the anti-aggregation properties even further (5-26% inhibition at 24 h) (Figure 21).

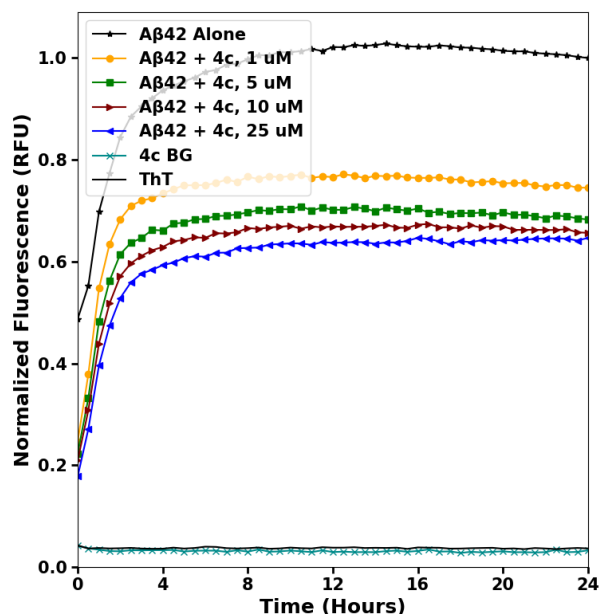


Figure 20. The aggregation kinetics experimental results when 10 μM of A β 42 was incubated with **4c**. **4c** was tested at 1, 5, 10, and 25 μM , pH 7.4 phosphate buffer and monitored over 24 hours at 37 $^{\circ}\text{C}$. ThT fluorescence was determined using an excitation and emission λ of 440 and 490 nm respectively. The data presented are an average of three independent experiments ($n = 3$). ThT = Thioflavin T control fluorescence, BG = Background compound fluorescence.

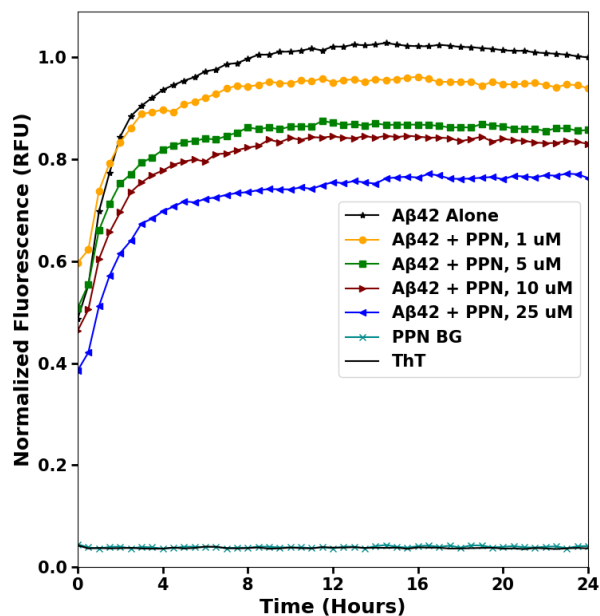


Figure 21. The aggregation kinetics experimental results when 10 μM of A β 42 was incubated with piperine. Piperine was tested at 1, 5, 10, and 25 μM , pH 7.4 phosphate buffer and monitored over 24 hours at 37 $^{\circ}\text{C}$. ThT fluorescence was determined using an excitation and emission λ of

440 and 490 nm respectively. The data presented are an average of three independent experiments (n = 3). ThT = Thioflavin T control fluorescence, BG = Background compound fluorescence.

These studies demonstrate that the R substituents play an important role in their anti-aggregation activity, showing the order of activity being **4a** (R = pyrrolidine) \approx **4b** (R = thiomorpholine) > **4c** (R = morpholine) > Piperine (R = piperidine). The reference agents RVT and MB showed a concentration dependent decline in the ThT fluorescence intensity and superior activity in preventing A β 42 aggregation compared to piperine and piperine derivatives **4a**, **4b** and **4c** (Figures 19-22). Both RVT and MB were able to reduce the duration of the growth phase to a significant extent (\sim 5 h and \sim 4 h respectively for RVT and MB at 25 μ M). At the tested concentrations, RVT exhibited an inhibition range of 36-76% whereas MB was far superior and its anti-A β 42 activity ranged from 66-94% (Figure 22). The aggregation kinetics data for other piperine derivatives (**4d**, **4e**, **4f**, **4g**, **4h**, **4i**, **4j**, **4k**, **4l**, **4m**) and **3**, that were either not active or weak inhibitors is given in Appendix A (Figure S1).

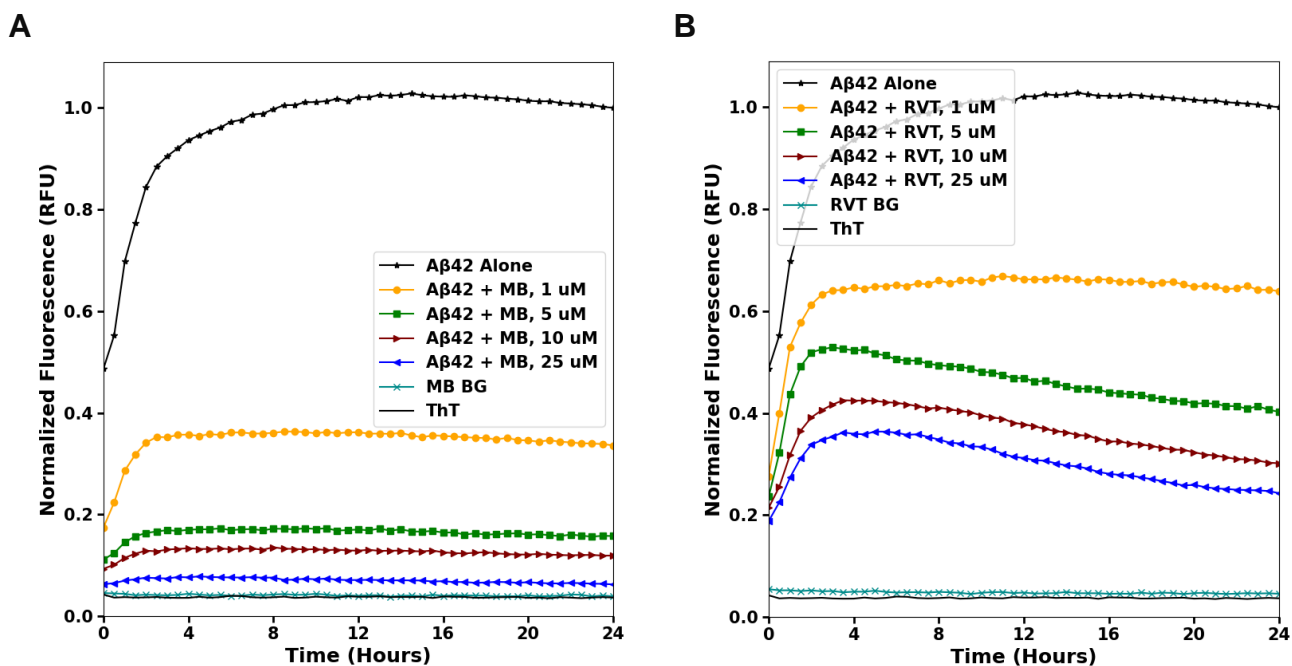


Figure 22. Panels A and B display the aggregation kinetics experimental results when 10 μ M of A β 42 was incubated with MB and RVT respectively. Compounds were tested at 1, 5, 10, and 25

μM , pH 7.4 phosphate buffer and monitored over 24 hours at 37 °C. ThT fluorescence was determined using an excitation and emission λ of 440 and 490 nm respectively. The data presented are an average of three independent experiments ($n = 3$). ThT = Thioflavin T control fluorescence, BG = Background compound fluorescence.

Comparing the CLogP values of top compounds **4a** (2.41), **4b** (2.38) and **4c** (1.64) shows that **4a** is most lipophilic followed by **4b** and **4c** (Table 1, Chapter 2). Interestingly this parameter directly correlates with their anti-aggregation properties suggesting that the presence of more lipophilic pyrrolidine and thiomorpholine moieties assist in binding to A β 42 to prevent their self-assembly. Increasing the polarity of the amide linker leads to a reduction in their anti-aggregation properties (compounds **4f**, **4g**, and **4h**). Section 4.4 in this Chapter describes a detailed computational modeling study of **4a**, **4b** and **4c** to further aid in understanding their binding interactions with A β 42.

4.3 TEM Analysis of A β 42 co-incubated with Piperine Derivatives **4a**, **4b** and **4c**

To validate the aggregation kinetics results presented in section 4.2, qualitative TEM experiments were conducted to note morphological changes in the A β 42 aggregate appearance upon exposure to the piperine derivatives **4a-c** which were identified as the compounds with superior anti-aggregation properties. The micrographs presented in Figure 23 show that the A β 42 alone formed coarse, fibrils with a high density (Figure 23A). The reference agents resveratrol and piperine were able to reduce the formation of A β 42 fibrils at 10 μM (Figure 23C and 23D). Similarly significant reduction in fibrillogenesis was noted for compounds **4a-c** (Figure 23 panels E, F, G). The TEM images show that both **4a** and **4b** exhibited superior inhibition compared to **4c**. It is evident that the piperine derivatives **4a-c** were able to reduce the formation of thick and dense A β 42 fibrils at 10 μM . These electron microscopy studies further support the anti-A β 42 activity demonstrated by piperine derivatives **4a-c** in the ThT fluorescence-based aggregation kinetics experiments.

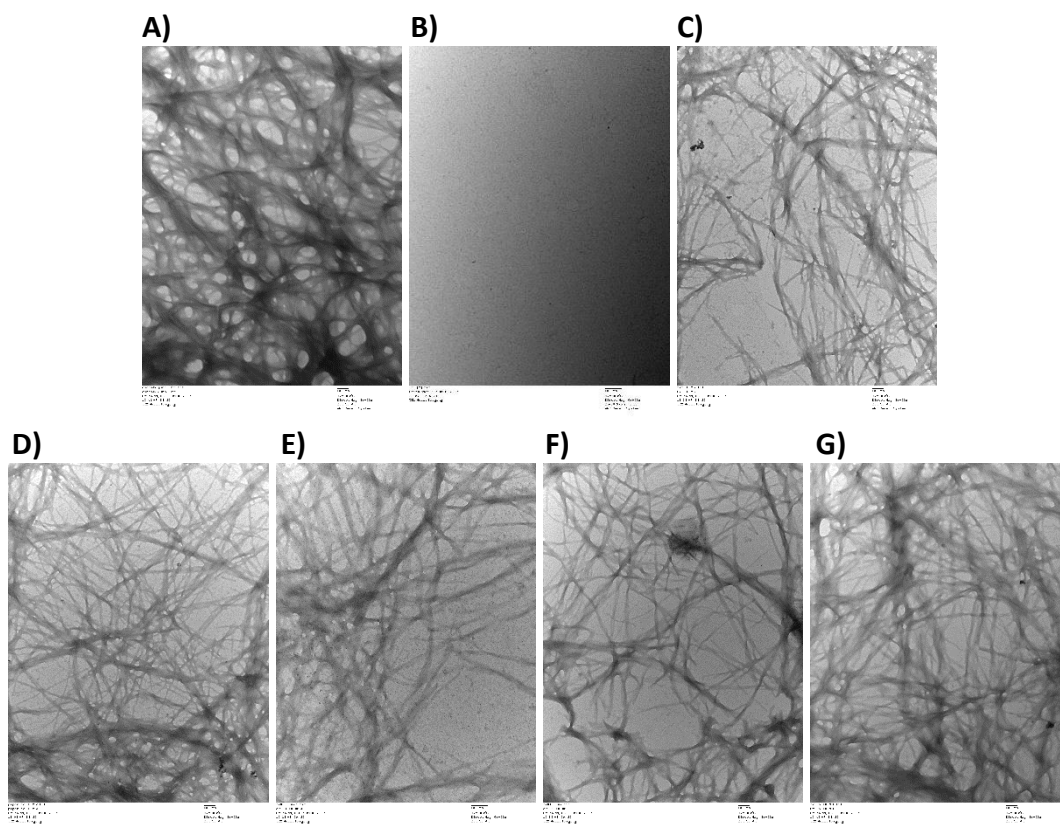


Figure 23. The micrograph presented in panel A represents the morphology of the 10 μM A β 42 fibril control and panel B shows the ThT control well after 24 hours of incubation at 37 $^{\circ}\text{C}$. Panels C-G represent A β 42 aggregate morphology in the presence of resveratrol, piperine, and **4a-c** respectively (10 μM each).

4.4 In Silico Studies of **4a-c** Docked into the A β 42 Pentamer Model

The binding interactions of top piperine derivatives **4a-c** that exhibited 35-48% inhibition of A β 42 aggregation in the ThT assay, were studied by computational modeling to investigate their binding modes using the solved 3D structure of A β 42. Molecular docking studies were performed, by docking **4a**, **4b** and **4c** using the A β 42 pentamer model (pdb id: 5KK3) (Figures 24-27).¹³³ The solid-state NMR structure of A β 42 fibrils reported by Colvin and coworkers was used to build the pentamer model in which each monomer has a characteristic “S” shaped conformation.¹³³ Docking of the lead compounds, **4a-c**, into the amyloidogenic region of A β 42 was carried out using the

CDOCKER algorithm in the software Discovery Studio: *Structure-Based-Design* (BIOVIA, Inc. San Diego, USA). Details of the docking protocol is described in Chapter 6, section 6.4.

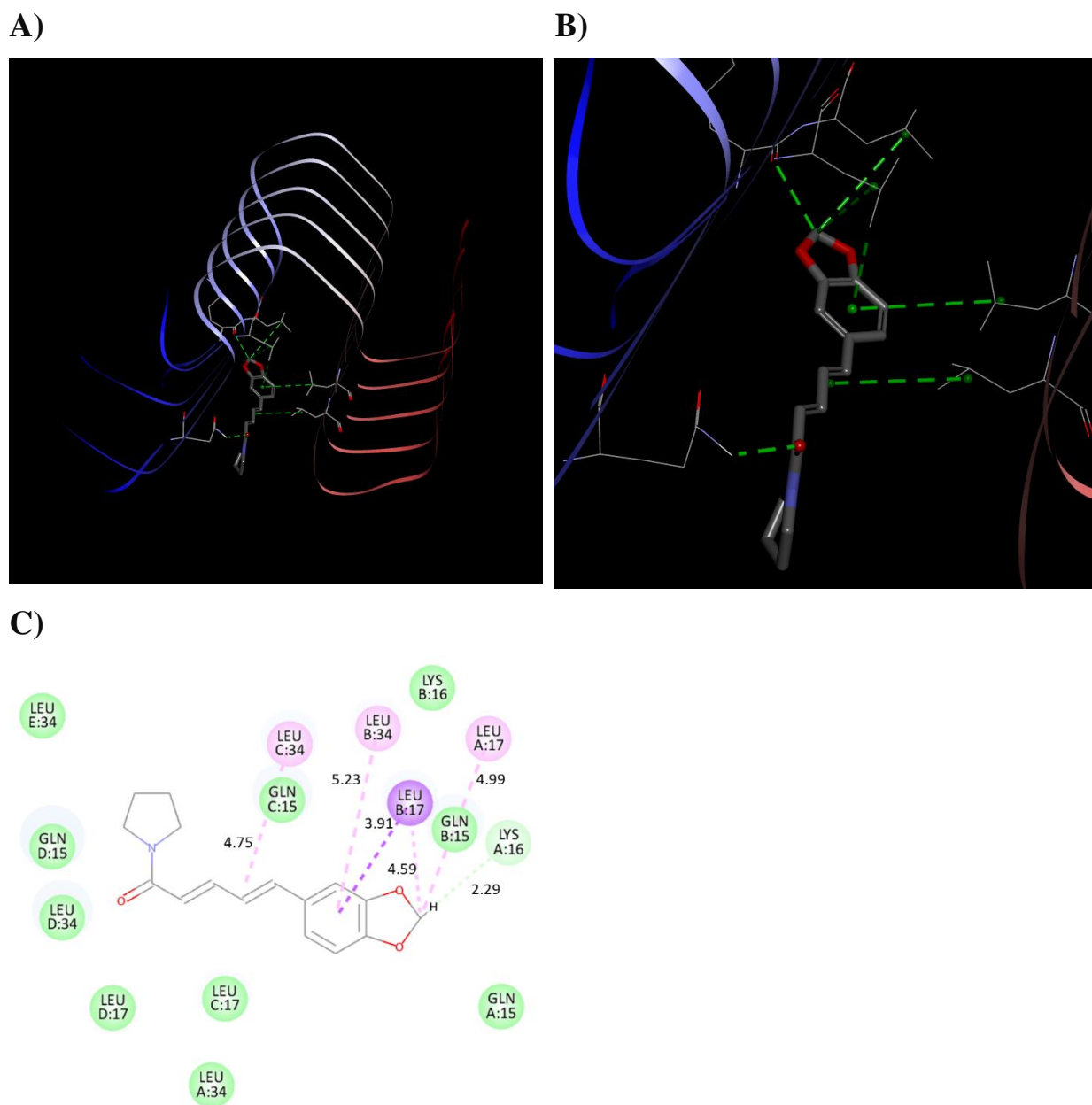


Figure 24. Panels A and B: Compound **4a** docked into A β 42 pentamer model (pdb id: 5KK3) full view (A) and zoomed into binding site (B) with green dotted lines representing intermolecular interactions. Panel C: 2D schematic of intermolecular interactions colored by interaction type. Pink = alkyl interactions, green = van der Waals interactions, purple = pi-sigma interaction. Hydrogen atoms were removed for clarity.

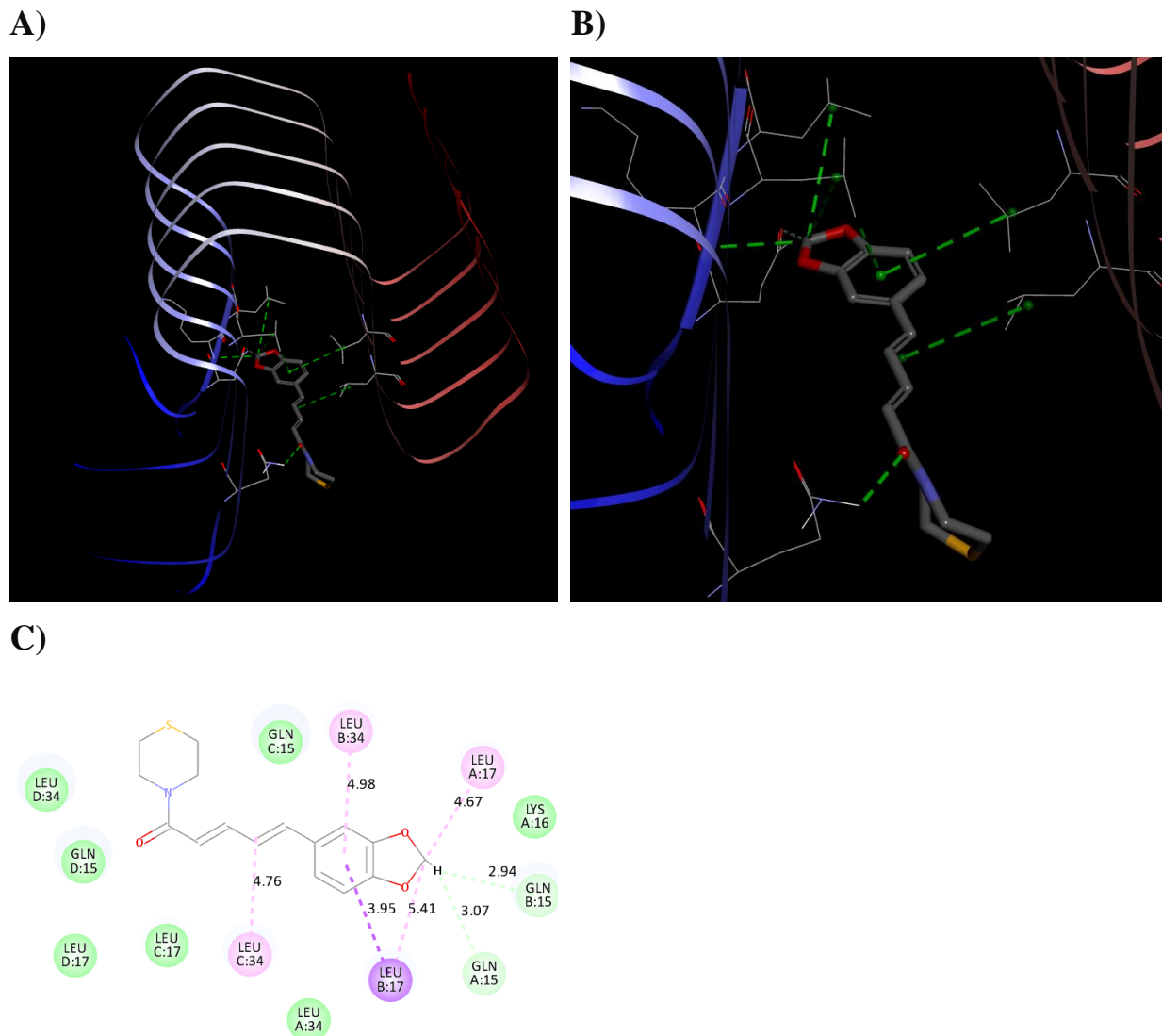


Figure 25. Panels A and B: Compound **4b** docked into A β 42 pentamer model (pdb id: 5KK3) full view (A) and zoomed into binding site (B) with green dotted lines representing intermolecular interactions. Panel C: 2D schematic of intermolecular interactions colored by interaction type. Pink = alkyl interactions, green = van der Waals interactions, purple = pi-sigma interaction. Hydrogen atoms were removed for clarity.

While analyzing the common binding interactions it was noted that **4a** (Figure 24), **4b** (Figure 25), and piperine (Figure 27) interacted with A β 42's Leu34 (chain C) via their *trans*-alkene functional group through pi-alkyl interactions, whereas compound **4c** (Figure 26) was in hydrophobic contact with Leu34 via its benzene and MDP group. This indicates that the nonpolar contact with Leu34 at the C-terminus of A β 42 is likely a strong contributor towards stabilizing the

A β 42 pentamer species from undergoing further aggregation and self-assembly. Taking a closer look, the bond distance between Leu34 and piperine was 5.1 Å whereas for **4a** and **4b**, the distance 4.8 Å for both, demonstrating more favorable interactions compared to piperine.

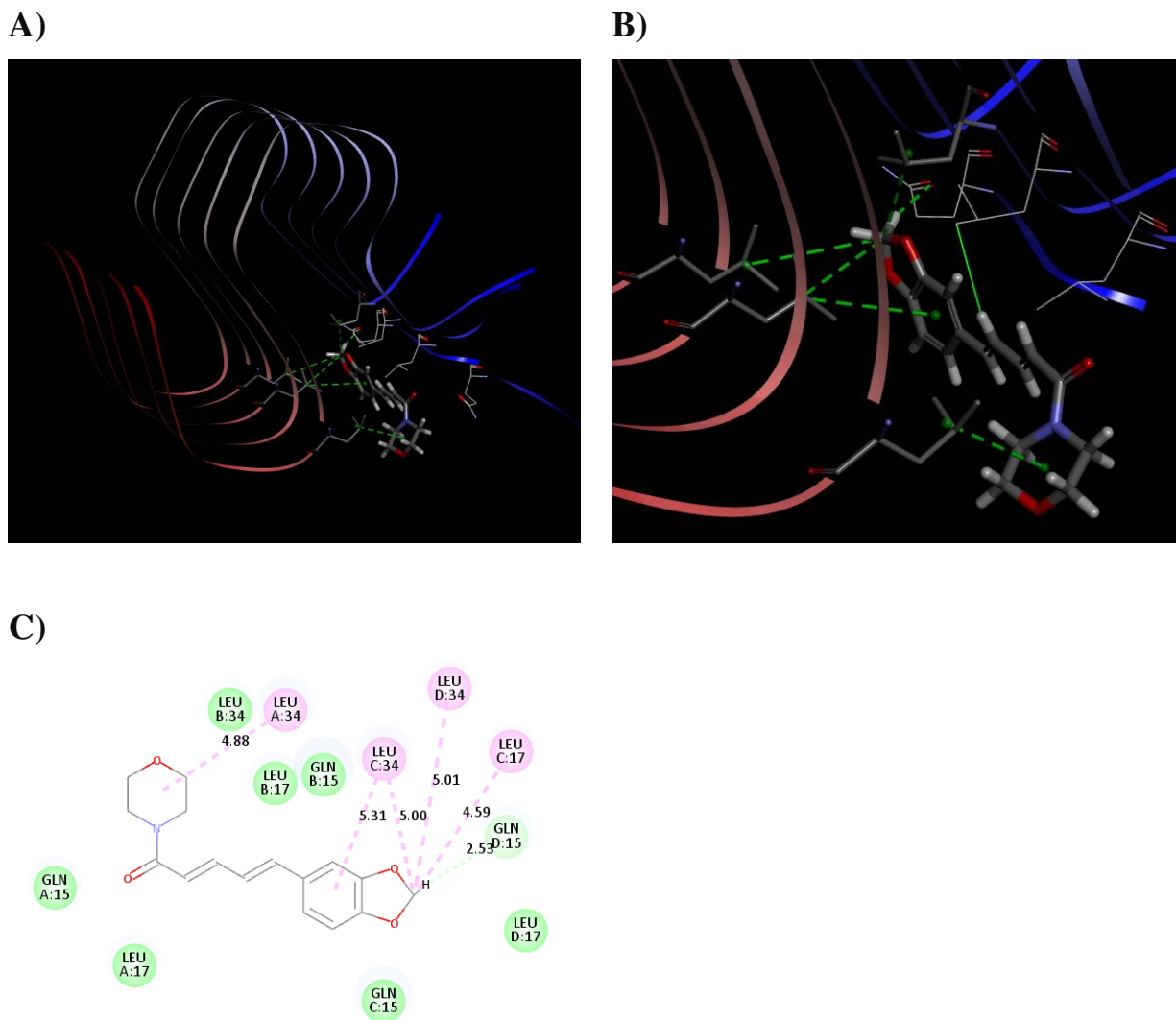
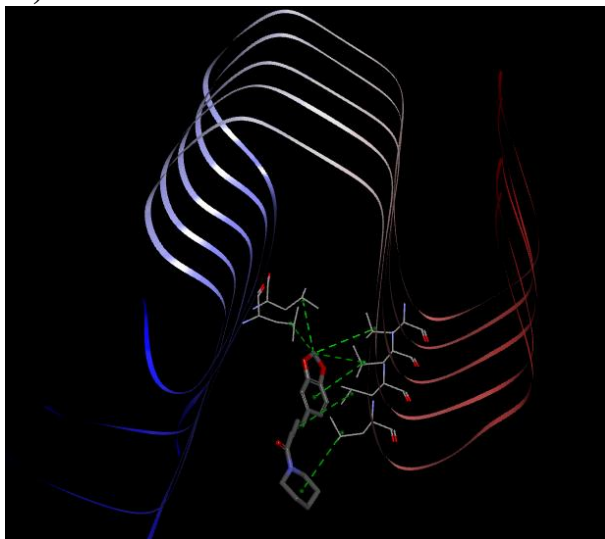


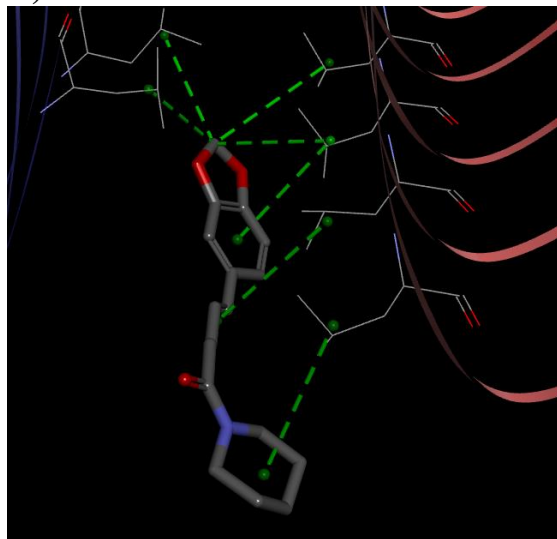
Figure 26. Panels A and B: Compound **4c** docked into A β 42 pentamer model (pdb id: 5KK3) full view (A) and zoomed into binding site (B) with green dotted and solid lines representing intermolecular interactions. Panel C: 2D schematic of intermolecular interactions colored by interaction type. Pink = alkyl interactions, green = van der Waals interactions. Hydrogen atoms were removed for clarity.

For **4c**, the bond distance between its benzene ring and Leu34 was 5.3 Å, while the distance to the MDP methylene group was 5.0 Å, indicating the formation of a slightly weaker interaction than **4a** and **4b**. Although the *trans* alkene of **4c** did not interact with Leu34 like the others, it did undergo an additional hydrophobic interaction with Leu17 (chain B, distance = 3.4 Å), which had a stabilizing effect. On another note, the isobutyl moiety of Leu17 (chains A and B) underwent van der Waals interactions with **4a** (5.0 and 4.6 Å respectively) and **4b** (4.7 and 5.4 Å respectively) at the MDP ring's methylene segment. In piperine, the MDP ring participates in additional alkyl and pi-alkyl interactions with the isobutyl group of Leu34 (distance = 5.2 Å) with chain A and with chain B's Leu34 residue (distance = 4.5 Å).

A)



B)



C)

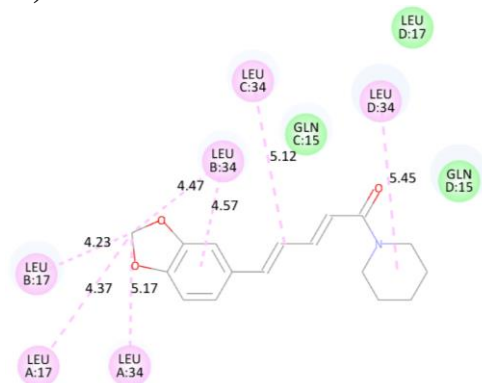


Figure 27. Panels A and B: Piperine docked into A β 42 pentamer model (pdb id: 5KK3) full view (A) and zoomed into binding site (B) with green dotted lines representing intermolecular interactions. Panel C: 2D schematic of intermolecular interactions colored by interaction type. Pink = alkyl interactions, green = van der Waals interactions. Hydrogen atoms were removed for clarity.

In the MDP methylene segment of **4c**, two interactions were observed, one with Leu34 (chain D, distance = 5.0 Å) and another with Leu17 (chain C, distance = 4.6 Å) respectively. These bond distances are comparable to those observed with piperine and are much longer than those seen in the other lead compounds **4a** and **4b**. Furthermore, the bond distances observed in **4a**, **4b** and **4c** are shorter than the bond distances between piperine and A β 42 at the *trans*-alkene moiety and MDP ring methylene group. This suggests that the binding orientation of **4a**, **4b** and **4c** is more favorable compared to piperine. It was also noted that in piperine, the benzene ring only interacts with Leu34 of chain B via one pi-alkyl (distance = 4.6 Å). However, in **4b**, the benzene ring forms two pi-alkyl bonds; one with chain B's Leu17 measuring 4.0 Å and another with its Leu34 measuring 5.0 Å. This exact interaction was also seen between **4a** and **4c** and Leu34 (5.2 and 5.3 Å respectively). However, a distinct pi-sigma interaction between **4a**'s benzene ring and Leu17 of chain B (3.9 Å) puts **4a** at the top in terms of having the greatest number of interactions with A β 42 at this binding domain.

On careful examination of binding modes of **4a**, **4b** and **4c**, it was observed that the type of substituents present at the acyl group of piperine derivatives plays a major role in the orientation of these derivatives in the A β 42 pentamer model. Additionally, derivatives **4a** and **4b** formed a key hydrogen bonding interaction with the N-terminus Gln15 at the carboxy terminus of A β 42 (distance = 2.3-2.9 Å, Figure 24-25). This interaction was not seen with piperine or derivative **4c** however, **4c** displayed a prominent dipole-dipole interaction with Gln15 at the N-terminus (2.5 Å). This suggests that the size and type of rings present play a major role in their binding affinity

toward A β 42. Furthermore, compound **4a** with a smaller 5-member pyrrolidine substituent was able to orient much closer to Leu17 and Leu34. Similarly, both **4b** and **4c** possessing either thiomorpholine or morpholine substituents were able to interact with Leu34 as well as Gln15 which led to their stabilizing effect and more favorable binding with A β 42 compared to piperine. Modeling studies also show that the presence of either a pyrrolidine or thiomorpholine or morpholine substituents promote a linear conformation of these derivatives that undergoes superior interaction in the narrow binding pocket at the interface between the C- and N-terminals in the A β 42 pentamer model. These modeling studies further validate the superior anti-aggregation activity seen for **4a** (48% inhibition), **4b** (46% inhibition) and **4c** (35% inhibition) compared to piperine (16% inhibition) at 10 μ M.

Table 3. Binding energy calculations from the implicit solvent binding energy simulation of top CDOCKER generated poses for piperine derivatives **4a-c** and the piperine.

<i>Compound</i>	<i>Binding Energy (kcal/mol)</i>
4a	-15.29
4b	-14.25
4c	-13.26
Piperine	-10.92

As a next step, the binding affinities of top piperine derivatives **4a**, **4b** and **4c** were calculated and compared to piperine using the computational software Discovery Studio (Table 3). The top ligand binding poses obtained from the CDOCKER docking algorithm was used to predict their affinity for the A β 42 amyloidogenic region. Binding energy calculations are more computationally intensive and predicts the binding affinities more accurately than CDOCKER energies alone as the algorithm used relies on quantum mechanics and more significantly, considers the effect of solvent during ligand binding.^{156, 157} The binding energy calculations were

carried out using the GBSW implicit solvent functionality applying the following equation: $E_{\text{binding}} = \text{Energy of complex } (E_{\text{ligand-receptor}}) - \text{Energy of ligand } (E_{\text{ligand}}) - \text{Energy of receptor } (E_{\text{receptor}})$. Table 3 shows the calculated binding energy values for **4a**, **4b**, **4c** and piperine. These studies show that compound **4a** exhibited superior binding affinity (−15.29 kcal/mol), compared to **4b** (−14.25 kcal/mol) and **4c** (−13.26 kcal/mol). It was also observed that piperine exhibited weaker binding toward Aβ42 (−10.9 kcal/mol) compared to piperine derivatives **4a**, **4b** and **4c**. This study again shows the key role of Gln15 in enhancing the binding affinity of piperine derivatives toward Aβ42 through their hydrogen bonding and dipole-dipole interactions. It was also pleasing to see that the binding affinity data correlated with the in vitro anti-aggregation activity profile of **4a**, **4b** and **4c**, further validating the results.

In summary, the findings of this in silico study show the binding modes of piperine and its derivatives demonstrating that derivatives **4a**, **4b** and **4c** can stabilize Aβ42 pentamers through a range of non-covalent intermolecular interactions. These include hydrogen bonds, dipole-dipole interactions, alkyl, and pi-alkyl interactions that were greater in number between the piperine derivatives and the Aβ42 peptide relative to piperine itself. Overall, the computational modelling studies further validate the in vitro assay results presented in section 4.1 (aggregation kinetics assays) and 4.2 (TEM experiments) demonstrating why compounds **4a**, **4b** and **4c** exhibit superior anti-Aβ42 activity compared to piperine.

4.5 Cytotoxicity Studies of HT22 Mouse Hippocampal Cells

The cytotoxic effects of lead piperine derivatives **4a**, **4b**, **4c** and piperine were investigated in the HT22 mouse hippocampal cell line using the CCK-8 cell viability assay. This cell was chosen as there is an accumulation of Aβ42 aggregates in hippocampal cells in the AD brain leading to neurodegeneration.¹⁶⁴ The cell viability was assessed upon 24 hours of incubation with either 10

or 25 μM treatments of each piperine derivative or 25 μM treatments of the reference standards (piperine and resveratrol). The results obtained show that the piperine derivatives were not toxic (91-97% viability range) when tested at either 10 μM or 25 μM (Figure 28). These studies demonstrate that the piperine derivatives evaluated had negligible amounts of toxicity towards the HT22 hippocampal neuronal cell line and exhibited similar viability profile compared to piperine (94% viability at 25 μM , Figure 28). These findings suggest that the piperine derivatives are feasible candidates for future pre-clinical animal studies.

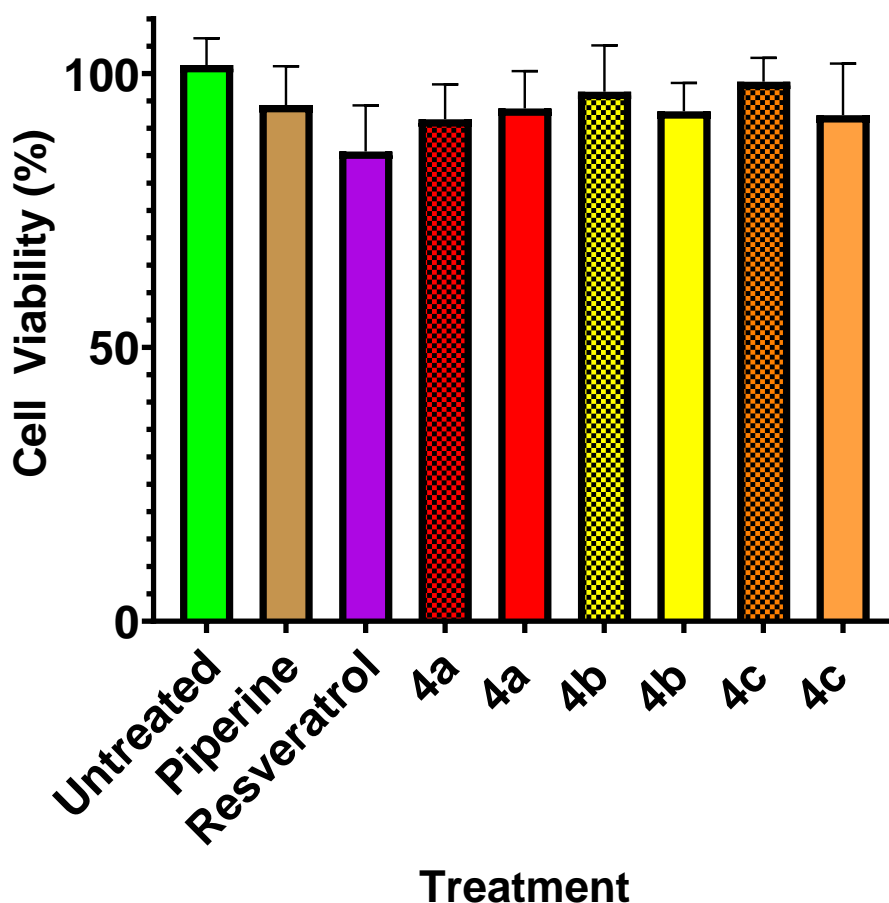


Figure 28. Cell viability data from the CCK-8 cytotoxicity assay. The lead compounds **4a-c** were evaluated at 10 μM (dotted coloured bars) and 25 μM (solid-coloured bars) while the controls RVT and PPN were tested at 25 μM . Data reported represents the average \pm s.d (n = 3) based on three independent experiments.

Chapter 5: Conclusion and Future Directions

The objective of this thesis was to design, synthesize and evaluate a series of piperine derivatives as inhibitors of A β 42 aggregation, and their potential application as novel pharmacological agents to study and treat AD. A library of 13 piperine derivatives (**4a-m**) possessing various steric and electronic features at the acyl end of piperine were synthesized. The synthetic methodology included a series of steps starting from the Arbuzov reaction, followed by the Horner-Wadsworth Emmons reaction, hydrolysis, nucleophilic acyl substitution and oxidation, to obtain the target compounds in 12-94% yields. The final piperine derivatives were fully characterized by ¹H and ¹³C NMR, LCMS and high-resolution mass spectrometry studies. The biochemical studies performed included the ThT-based fluorescence aggregation kinetics assay to screen for each compound's anti-A β 42 activity and to understand the SAR of piperine derivatives. The anti-aggregation assay results were further investigated by conducting TEM experiments to study A β 42 aggregate morphology in the presence of piperine derivatives. Further assay validation was done by conducting in silico studies where piperine derivatives were docked in the A β 42 pentamer model to understand their binding modes, interactions, and binding affinity toward A β 42. In addition, the toxicity profiles of top ranked piperine derivatives were studied in mouse hippocampal neuronal HT22 cells. These studies led to the identification of three piperine derivatives (**4a**, **4b** and **4c**) as the top performing compounds that exhibited 35-48% inhibition of A β 42 aggregation at 10 μ M. These compounds exhibited superior inhibition of A β 42 aggregation compared to piperine (16% inhibition at 10 μ M). These SAR studies show that the presence of a 5-membered pyrrolidine (**4a**, R = pyrrolidine), a 6-membered thiomorpholine (**4b**, R = thiomorpholine) and the corresponding bioisostere, morpholine (**4c**, R = morpholine), played a crucial role in enhancing their anti-aggregation properties. Computational modeling studies also

demonstrate that these acyl amide substituents were involved in maintaining a linear conformation of these piperine derivatives in the A β 42 amyloidogenic region and promotes favorable interactions with both C- and N-terminal amino acids such as Leu17, and Leu34 that line the narrow binding pocket of A β 42. More significantly, the terminal cyclic amine rings in **4a** and **4b** underwent hydrogen bonding interactions with the N-terminal Gln15 which was able to orient the MDP ring much closer to Leu17 and Leu34, further stabilizing the pentamer assembly and reducing their self-assembly into higher order structures. In contrast, piperine which contains a 6-membered piperidine substituent was unable to interact with Gln15 and consequently exhibited weaker inhibition. Lastly, cell viability studies of piperine derivatives show that they were not toxic to HT22 hippocampal cells (91-97% viability). Table 4 gives a summary profile of the physicochemical properties and biochemical activity data for piperine derivatives (**4a-m**). These studies demonstrate that piperine and its derivatives possess anti-A β 42 activity and that this class of compounds exhibit direct binding to A β 42 and reduces its aggregation. These investigations show that the spice piperine is a suitable template to use for the design and development of a novel class of compounds as anti-AD agents.

Table 4. Summary of biochemical properties of piperine derivatives **4a-m** evaluated during this study.

<i>Biochemical Property</i>	<i>Ranges Observed for 4a-m</i>
<i>Molecular Weight</i>	271.12 to 335.08 g/mol
<i>Partition Coefficient, cLogP</i>	1.27 to 4.32
<i>Topological Polar Surface Area</i>	38.5 to 73.1 Å ²
<i>Aβ42 Inhibition</i>	6 to 48 %
<i>Cell Viability</i>	91 to 97 %

Future studies proposed includes modification of the lead compounds **4a** and **4b** at various positions including SAR studies at the acyl end, the *trans*-alkene positions and the MDP ring (Figure 29). For instance, replacing the current alkyl amine rings with aromatic moieties and

incorporating polar substituents could help maintain the polarity, potentially allow for additional hydrogen bonding interactions with Gln15, and increase the planarity of the molecule. As described in the literature, molecules with high degrees of planarity have been reported to have excellent A β binding properties with curcumin and chalcones being prime examples of this.^{29, 110, 165} At the *trans*-alkene position, bioisosteric replacement of the α , β -unsaturated Michael acceptor fragment could be useful for preventing potential conjugate additions via Michael addition reactions in vivo. Such bioisosteric replacements could include an alkyne or aromatic ring that would harbour similar planar, steric and electronic properties, continuing to provide the favorable pi-electron delocalization, but without the reactive Michael acceptor functionality. Furthermore, the MDP ring can be changed to other bicyclic rings in order to promote stronger intermolecular interactions within the seeding regions of A β 42 as opposed to only alkyl interactions (Figure 29).

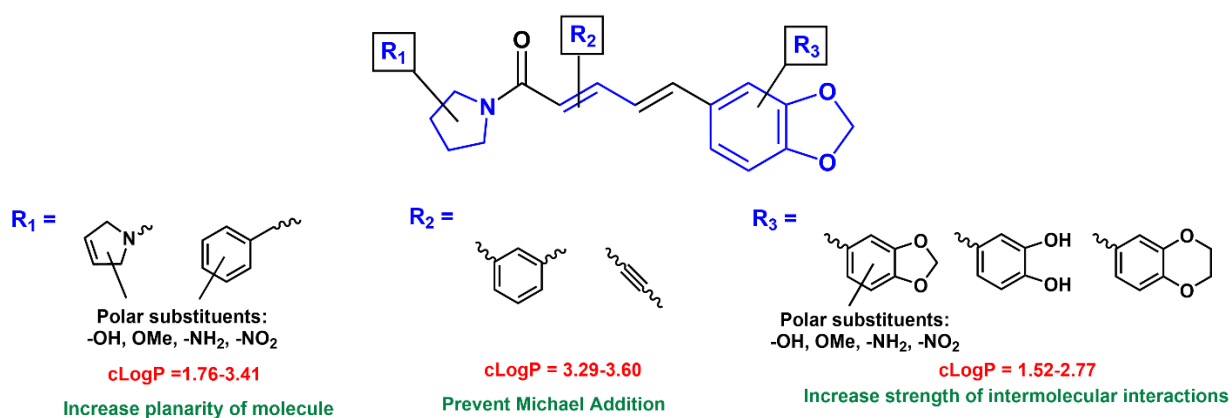


Figure 29. Potential modifications to the current lead template of this thesis (**4a**) that are hypothesized to improve A β 42 binding potential.

Other future investigations include the evaluation of piperine derivatives against A β 40 aggregation. As previously mentioned, A β 40 peptides are less toxic than A β 42 peptides, however the ideal anti-amyloid candidate should also be able to prevent the aggregation of both amyloid species for maximum therapeutic potential. Additionally, cell rescue studies on the ability of these

derivatives to protect HT22 mouse hippocampal cells from A β -induced toxicity and cell death would be of great interest to identify molecules for advancement in animal models of AD. Another favorable anti-AD property to screen for is the compound's ability to inhibit cholinesterase enzymes for maintaining the concentrations of ACh in the brain, thus promoting neurotransmission. The cholinesterase inhibition assay has been previously reported by Nekkar lab and will provide valuable insights regarding the dual-inhibition abilities of the piperine derivatives to target both the amyloid and cholinergic cascades of AD pathophysiology.

To conclude, the results from this thesis reveal that piperine's structure provides a novel template to design anti-A β compounds. Additionally, SAR modification of piperine provides novel molecules that are able to bind and inhibit A β 42 aggregation and prevent their self-assembly into higher-order neurotoxic oligomers. Moreover, the lead candidates from this research were successful in outperforming their parent molecule piperine in preventing A β 42 aggregation. In the short-term, this discovery provides valuable insights toward current and future research efforts on novel AD therapeutics with anti-A β activity. The molecules discovered from this study will have application as novel pharmacological tools to understand the mechanisms of A β 42 aggregation which will be useful to design novel anti-AD therapeutics. With the launch of the new anti-AD biological drugs (Aducanumab and Lecanemab) in the past couple of years, research toward novel AD therapies focused on the amyloid cascade is gathering momentum. Discovery of small molecule anti-AD therapies are a crucial next step as they are more economical, easier to scale during manufacturing, store, and are less demanding of the health care system due to their non-invasive nature of administration. Future research in this space will benefit the ever-increasing global AD patient population.

Chapter 6: Experimental

6.1 Chemistry

All reagents used in synthetic procedures were purchased from commercial sources such as Sigma-Aldrich, AA Blocks, Alfa Aesar, TCI Chemicals, and Acros Organics. High resolution nuclear magnetic resonance spectroscopy (^1H NMR and ^{13}C NMR) were obtained at the University of Waterloo Chemistry 2 building using a Bruker Avance spectrometer with deuterated chloroform (CDCl_3) or deuterated dimethylsulfoxide ($\text{DMSO-}d_6$) as reference solvents. All coupling constants (J values) are expressed in hertz (Hz) with multiplets assigned to NMR signals according to the following abbreviations: singlet (s), doublet (d), triplet (t), multiplet (m), broad singlet (br s). Flash column chromatography was used to purify all compounds with Merck 230-400 mesh sized silica gel 60. Thin layer chromatography (TLC) techniques were used for the preliminary purity analysis and product identification, TLC plates are Merck 60 F254 silica gel plates (0.2 mm) and a 254 nm ultra-violet (UV) lamp were used for all TLC analyses. Solvent systems used for TLC include DCM to MeOH in a 90:10, 95:5, and 98:2 ratio or hexanes to ethyl acetate at 10:1, 7:3 and 1:1 ratios. Purity analysis of all compounds exhibiting a single spot on TLC were obtained via LC-MS (liquid chromatography-mass spectrometry) assays. HPLC (high performance liquid chromatography) grade solvents from Sigma Aldrich including ultrapure water with 0.1% formic acid, and acetonitrile with 0.1% formic acid were used to generate the mobile phases. An isocratic mobile phase was used at a solvent ratio of either 60:40 or 50:50 ultrapure water to acetonitrile with each containing 0.1% formic acid and a flow rate of 0.5 ml/min. The Agilent 6100 single quad LC-MS system was equipped with an Agilent 1.8 μm Zorbax Eclipse Plus C18 column (2.1 mm i.d. x 50 mm) and coupled to a UV-Visible (UV-Vis) detector set to measure absorbance at

254 nm. All the final compounds were obtained in $\geq 95\%$ purity as determined by LC-MS analysis. Melting point determination was conducted on a Fisher-Johns melting point apparatus. High-resolution mass spectra (HR-MS) were collected from a Thermo Scientific Q ExactiveTM mass spectrometer with an ESI source, Department of Chemistry, University of Waterloo.

6.1.1 Synthesis and Characterization (NMR and LC-MS)

The piperine derivatives were synthesized using a four-step process to obtain their (*E*), (*E*)-stereoisomers, as reported in section 3.1 (Chapter 3).

General procedure for synthesis of methyl (*E*)-4-(diethoxyphosphoryl)but-2-enoate (**1**)

Starting off with a Michaelis-Arbuzov rearrangement, triethylphosphite (1.16 mL, 6.71 mmol) was added to 4-bromo-butenoate (0.68 mL, 5.59 mmol) at room temperature in a 50 mL RBF, then refluxed in 4 mL of toluene at 130 °C for 6 hours. The crude product was then rotary evaporated to remove toluene and then purified using flash chromatography (silica gel, *n*-Hexane:EtOAc 10:1 or DCM:MeOH, 9:1) to obtain the methyl ester phosphonate (**1**) in excellent yield (1.19 g, 5.03 mmol, 90%) as a clear, colorless oil. ¹H NMR (300 MHz, CDCl₃) δ 6.85 (td, *J* = 15.4, 7.8 Hz, 1H), 5.93 (dd, *J* = 15.6, 5.0 Hz, 1H), 4.17–4.01 (m, 4H), 3.70 (s, 3H), 2.71 (dd, *J* = 23.0, 7.8, 1.5 Hz, 2H), 1.29 (t, *J* = 7.1 Hz, 6H).

General procedure for synthesis of methyl piperate (**2**)

Methyl piperate (**2**) was synthesized via the HWE reaction. In a 100 mL RBF, **1** (1.09 g, 4.61 mmol) was converted into its carbanion form by dissolving in 30 mL of anhydrous THF and stirring with lithium hydroxide (0.184 g, 7.68 mmol) for 5 minutes. Meanwhile, piperonal (0.462 g, 3.07 mmol) was dissolved in 5 mL of anhydrous THF then added to the reaction mixture and refluxed under argon gas. After 8 hours of reflux, the reaction was cooled to room temperature and filtered through a thin pad of celite before removing residual THF under reduced pressure.

Subsequent purification was done using silica gel column chromatography with 100% DCM as the eluent to afford **2** (610 mg, 2.63 mmol, 86%) as yellow crystals. ¹H NMR (300 MHz, CDCl₃) δ 7.45–7.29 (m, 1H), 6.92–6.84 (m, 1H), 6.83–6.60 (m, 4H), 6.04–5.89 (m, 1H), 5.94 (s, 2H), 3.74 (s, 3H).

General procedure for synthesis of piperic acid (3**)**

Piperic acid was synthesized by a hydrolysis mechanism by first dissolving methyl piperate (0.70 g, 3.01 mmol) in 30 mL of 1:1 2 M sodium hydroxide to methanol and stirred at 70 °C in a 100 mL RBF equipped with a reflux condenser for 3 hours. The reaction mixture was then cooled to room temperature and residual methanol was evaporated under reduced pressure. Afterwards, the aqueous mixture was acidified using 1 M hydrochloric acid to pH 3 and the resulting precipitate was collected via vacuum filtration through a Buchner funnel equipped with Whatman filter paper. After washing the precipitate with water, it was allowed to dry using air flow to yield **3** (94%, 0.62 g, 2.83 mmol) as a yellow solid. ¹H NMR (300 MHz, DMSO-*d*₆) δ 7.32–7.20 (m, 2H), 7.02–6.84 (m, 4H), 6.02 (s, 2H), 5.89 (d, *J* = 15.2 Hz, 1H). LR-MS *m/z* calculated for C₁₂H₁₀O₄ [M+H]⁺ 219.1 *m/z*, found 219.1 *m/z*. Purity: 94% (LC-MS).

General procedure for synthesis of piperine derivatives (4a-e**, **4h-m**)**

A variety of conditions were investigated to successfully convert the ester to amide. The optimal route was identified and starts with dissolving **3** (218 mg, 1.0 mmol) in anhydrous DCM. The crude acid chloride was then generated by an in-situ acylation where a DMF catalyst (2 drops) and oxalyl chloride (0.214 mL, 2.5 mmol) were added to the reaction mixture on ice, under argon, then stirred at room temperature for 3 hours. Subsequently, the reaction mixture was rotary evaporated to dryness to remove excess oxalyl chloride. The crude acid chloride was then re-dissolved in anhydrous DCM before adding it drop-wise to a solution of the appropriate amine dissolved in anhydrous DCM at 0 °C. At room temperature, overnight (~18 h), the reaction mixture was allowed

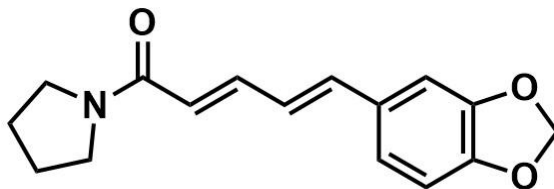
to stir to completion before adding ice water and extracting the product with DCM three times (50 mL x 3). The organic layer was then washed with 50 mL aliquots of 2 M HCl, saturated sodium bicarbonate (NaHCO₃), water, and finally, brine before it was dried over sodium sulfate (Na₂SO₄). Residual DCM was evaporated under reduced pressure to yield the crude product and it was further purified via flash chromatography (*n*-hexanes:EtOAc 10:1 or 95:5 DCM:MeOH) to obtain the corresponding piperine derivatives **4a-e** and **4h-m** as yellow, beige or white solids (16-84% yield).

General procedure for synthesis of thiomorpholine dioxide and thiomorpholine monoxide piperine derivatives (4f, 4g)

The synthetic procedure for thiomorpholine dioxide (**4f**) and thiomorpholine oxide (**4g**) relied on using the previously synthesized thiomorpholine derivative (**4b**) and subjecting it to oxidation. Initially, **4b** (48 mg, 0.157 mmol) was stirred in 20 mL of methanol at 40 °C for 5 minutes until fully dissolved. Then the reaction mixture was cooled on ice while two equivalents of Oxone (97 mg, 0.314 mmol) was dissolved in 10 mL of water. The Oxone in water mixture was added dropwise to the reaction along with a catalytic amount of triethylamine (3 drops) before the mixture was allowed to stir for 5 hours at 40 °C. After 5 hours, the crude reaction was tested via TLC to observe two well-resolved spots representing **4f** and **4g**. The reaction was then cooled, and the solvent was removed via rotary evaporation at reduced pressure before being reconstituted in 1 mL of DCM. To purify the reaction mixture and separate the two compounds from the mixture, flash chromatography principles were applied with a solvent system of 95:5 DCM:MeOH. The products fractions were collected and evaporated under reduced pressure to obtain **4f** and **4g** as white solids at yields of 12% and 27% respectively.

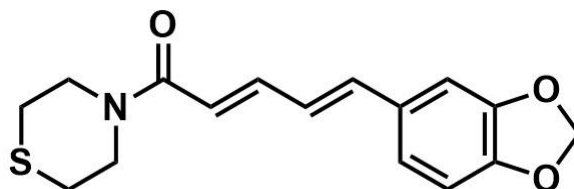
Novel compounds include **4g**, **4i**, **4j**, **4l** and **4m** while other compounds have been previously reported.^{135, 136, 146, 147} Analytical data for compounds **4a-m** are reported below:

Piperyline (4a)¹⁴⁰:



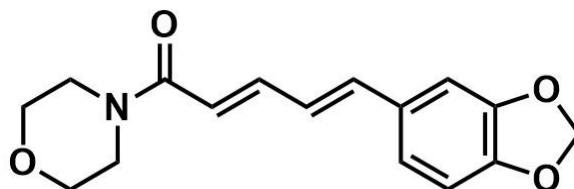
Yield: 150.7 mg, 40%. Appearance: White powder. Mp: 143-145 °C. ¹H NMR (300 MHz, CDCl₃) δ 7.55–7.33 (m, 1H), 6.96-6.88 (m, 2H), 6.83–6.60 (m, 3H), 6.23 (d, *J* = 14.7 Hz, 1H), 5.95 (s, 2H), 3.52-3.39 (m, 4H), 2.14-1.92 (m, 4H). LR-MS *m/z* calculated for C₁₆H₁₇NO₃ [M+H]⁺ 272.1 *m/z*, found 272.2 *m/z*. Purity: 98% (LC-MS).

(2*E*,4*E*)-5-(Benzo[*d*][1,3]dioxol-5-yl)-1-thiomorpholinopenta-2,4-dien-1-one (4b)¹⁶⁶:



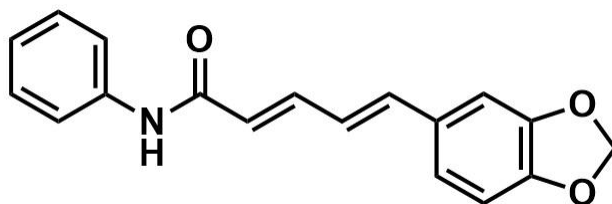
Yield: 191 mg, 84.3%. Appearance: Beige crystals. Mp: 125–28 °C. ¹H NMR (300 MHz, CDCl₃) δ 7.41 (dd, *J* = 14.5, 9.7 Hz, 1H), 6.96–6.88 (m, 2H), 6.81–6.66 (m, 3H), 6.35 (d, *J* = 14.6 Hz, 1H), 5.96 (s, 2H), 3.91-3.87. (m, 4H), 2.65-2.62 (m, 4H). LR-MS *m/z* calculated for C₁₆H₁₇NO₃S [M+H]⁺ 304.1 *m/z*, found 304.1 *m/z*. Purity: 98% (LC-MS).

(2*E*,4*E*)-5-(Benzo[*d*][1,3]dioxol-5-yl)-1-morpholinopenta-2,4-dien-1-one (4c)¹⁶⁷:



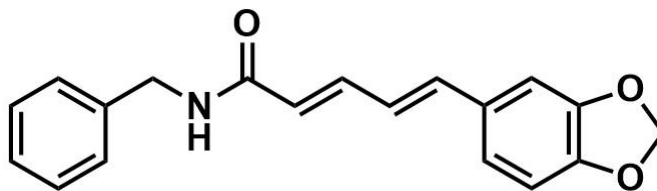
Yield: 105 mg, 73%. Appearance: Off-white powder. Mp: 156-159 °C. ¹H NMR (300 MHz, CDCl₃) δ 7.44 (dd, *J* = 14.6, 9.8 Hz, 1H), 6.96-6.88 (m, 2H), 6.83–6.63 (m, 3H), 6.35 (d, *J* = 14.9 Hz, 1H), 5.97 (s, 2H), 3.70–3.66 (m, 8H). LR-MS *m/z* calculated for C₁₆H₁₇NO₄ [M+H]⁺ 288.1 *m/z*, found 288.2 *m/z*. Purity: 95% (LC-MS).

(2*E*,4*E*)-5-(Benzo[*d*][1,3]dioxol-5-yl)-*N*-phenylpenta-2,4-dienamide (4d)¹⁶⁸:



Yield: 59 mg, 35%. Appearance: Off-white solid. Mp: 173-175 °C. ¹H NMR (300 MHz, CDCl₃) δ 7.64–7.41 (m, 3H), 7.35-7.30 (m, 2H), 7.13-7.08 (m, 1H), 7.01–6.63 (m, 5H), 6.04 (d, *J* = 14.7 Hz, 1H), 5.97 (s, 2H). LR-MS *m/z* calculated for C₁₈H₁₅NO₃ [M+H]⁺ 294.1 *m/z*, found 294.1 *m/z*. Purity: 97% (LC-MS).

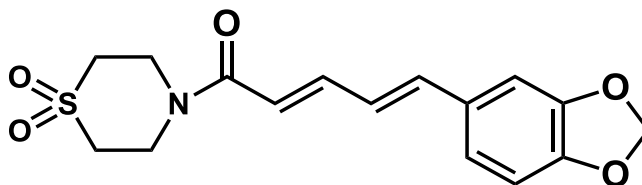
(2*E*,4*E*)-5-(Benzo[*d*][1,3]dioxol-5-yl)-*N*-benzylpenta-2,4-dienamide (4e)¹⁶⁷:



Yield: 100 mg, 53%. Appearance: White solid. Mp: 170-173 °C. ¹H NMR (300 MHz, CDCl₃) δ 7.45–7.37 (m, 1H), 7.37–7.25 (m, 5H), 6.96–6.88 (m, 2H), 6.83–6.58 (m, 3H), 5.96 (s, 2H), 5.91 (d, *J* = 14.9 Hz, 1H), 5.74 (br s, 1H), 4.53 (d, *J* = 5.7 Hz, 2H). LR-MS *m/z* calculated for C₁₉H₁₇NO₃ [M+H]⁺ 308.1 *m/z*, found 308.0 *m/z*. Purity: > 99% (LC-MS).

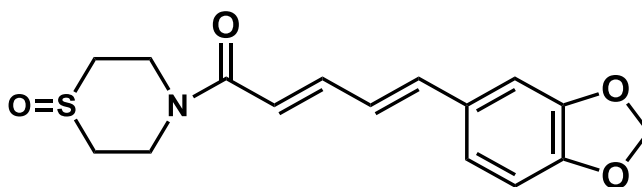
(2E,4E)-5-(benzo[d][1,3]dioxol-5-yl)-1-(1,1-dioxidothiomorpholino)penta-2,4-dien-1-one

(4f)¹³⁶:



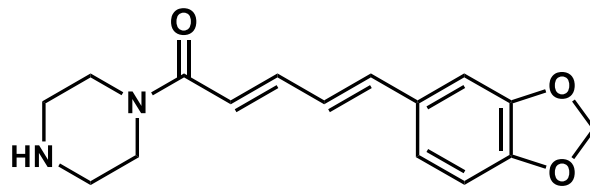
Yield: 6.2 mg, 12%. Appearance: Yellow solid. Mp: 239-241 °C. ¹H NMR (300 MHz, CDCl₃) δ 7.54-7.45 (m, 1H), 6.99 (s, 1H), 6.93-6.88 (t, *J* = 8.1, 8.4 Hz, 1H), 6.82-6.67 (m, 3H), 6.45-6.24 (m, 1H), 5.99 (s, 2H), 4.12 (br s, 4H), 3.07 (br s, 4H). LR-MS *m/z* calculated for C₁₆H₁₇NO₅S [M+H]⁺ 336.1 *m/z*, found 335.9 *m/z*. Purity: 99% (LC-MS).

(2E,4E)-5-(benzo[d][1,3]dioxol-5-yl)-1-(1-oxidothiomorpholino)penta-2,4-dien-1-one (4g):



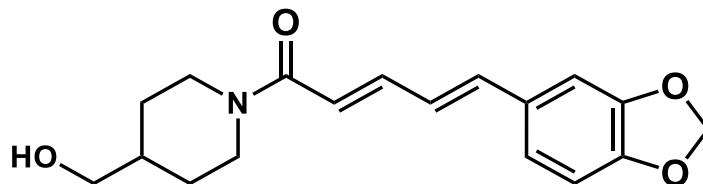
Yield: 13.7 mg, 27%. Appearance: Yellow solid. Mp: 207-209 °C. ¹H NMR (300 MHz, CDCl₃) δ 7.51-7.43 (dd, *J* = 10.5, 10.2 Hz, 1H), 6.99 (s, 1H), 6.92-6.98 (d, *J* = 17.1 Hz, 1H), 6.84-6.68 (m, 3H), 6.43-6.38 (d, *J* = 14.7 Hz, 1H), 5.98 (s, 2H), 2.89-2.84 (d, *J* = 12.6 Hz, 2H), 2.76-2.68 (t, *J* = 13.8, 10.5 Hz, 2H), 1.55 (br s, 4H). ¹³C NMR (300 MHz, CDCl₃) δ 165.89, 148.29, 144.59, 139.89, 130.62, 124.66, 122.93, 117.90, 105.57, 105.72, 101.39, 45.78, 33.46. DEPT135 ¹³C NMR (300 MHz, CDCl₃) δ 144.60 (-CH), 139.90 (-CH), 124.65 (-CH), 122.94 (-CH), 117.88 (-CH), 108.58 (-CH), 105.71 (-CH), 101.40 (-CH₂), 45.86 (-CH₂). HR-MS *m/z* calculated for C₁₆H₁₇NO₄S [M+H]⁺ 320.09564, found 320.09519. Purity: 99% (LC-MS).

(2E,4E)-5-(benzo[d][1,3]dioxol-5-yl)-1-(piperazin-1-yl)penta-2,4-dien-1-one (4h)¹³⁹:



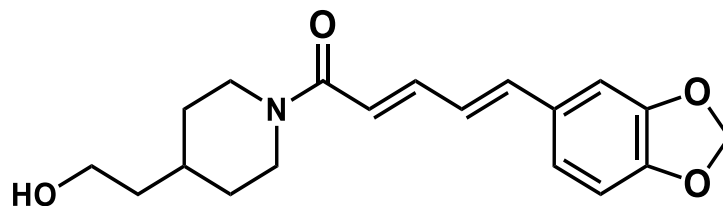
Yield: 16%. Appearance: Yellow solid. Mp: 130-137.5 °C. ^1H NMR (300 MHz, CDCl_3) δ 7.48-7.40 (m, 1H), 7.03-6.74 (m, 4H), 6.66-6.21 (m, 2H), 3.68 (m, 4H), 2.93 (br s, 1H), 2.28 (m, 4H). LR-MS m/z calculated for $\text{C}_{16}\text{H}_{18}\text{N}_2\text{O}_3$ $[\text{M}+\text{H}]^+$ 287.1 m/z , found 287.0 m/z . Purity: 99% (LC-MS).

(2E,4E)-5-(benzo[d][1,3]dioxol-5-yl)-1-(4-(hydroxymethyl)piperidin-1-yl)penta-2,4-dien-1-one (4i):



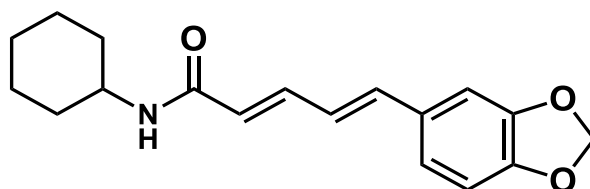
Yield: 34%. Appearance: Yellow solid. Mp: 106-108 °C. ^1H NMR (300 MHz, CDCl_3) δ 7.41-7.33 (m, 1H), 6.95 (s, 1H), 6.88-6.53 (m, 1H), 6.76-6.65 (m, 3H), 6.43-6.38 (d, $J = 15$ Hz, 1H), 5.95 (s, 2H), 4.70-4.67 (m, 1H), 4.08-4.03 (m, 1H), 3.49 (br s, 1H), 3.09-3.01 (m, 1H), 2.67-2.59 (m, 1H), 1.87-1.76 (m, 5H), 1.24-1.12 (m, 2H). ^{13}C NMR (300 MHz, CDCl_3) δ 165.57, 148.20, 148.18, 142.81, 138.50, 130.95, 125.24, 122.59, 119.81, 108.51, 105.68, 101.30, 67.28, 45.86, 42.24, 38.93, 29.55, 28.41. DEPT135 ^{13}C NMR (300 MHz, CDCl_3) δ 142.81 (-CH), 138.51 (-CH), 125.24 (-CH), 122.59 (-CH), 119.81 (-CH), 108.51 (-CH), 105.68 (-CH), 101.30 (-CH), 67.26 (-CH₂), 45.85 (-CH₂), 42.25 (-CH₂), 38.93 (-CH), 29.58 (-CH₂), 28.38 (-CH₂). HR-MS m/z calculated for $\text{C}_{18}\text{H}_{21}\text{NO}_4$ $[\text{M}+\text{H}]^+$ 316.15494, found 316.15492. Purity: 98% (LC-MS).

(2E,4E)-5-(benzo[d][1,3]dioxol-5-yl)-1-(4-(2-hydroxyethyl)piperidin-1-yl)penta-2,4-dien-1-one (4j):



Yield: 43%. Appearance: Orange-yellow solid. Mp: 128-131 °C. ^1H NMR (300 MHz, CDCl_3) δ 7.43-7.36 (m, 1H), 6.97 (s, 1H), 6.90-6.87 (d, $J = 9.0$ Hz, 1H), 6.79-6.67 (m, 3H), 6.45-6.40 (d, $J = 15$ Hz, 1H), 5.97 (s, 2H), 3.73-3.69 (t, $J = 6.3$ Hz, 6.6 Hz, 2H), 1.80-1.59 (m, 3H), 1.59-1.50 (m, 4H), 1.25-1.15 (3H). ^{13}C NMR (300MHz, CDCl_3) δ 165.48, 148.20, 148.16, 142.69, 138.41, 130.96, 125.28, 122.56, 119.88, 108.51, 105.67, 101.29, 60.09, 46.15, 42.57, 39.07, 33.03, 32.76, 31.92, 29.69. DEPT135 ^{13}C NMR (300MHz, CDCl_3) δ 142.70 (-CH), 138.41 (-CH), 125.27 (-CH), 122.57 (-CH), 119.88 (-CH), 108.51 (-CH), 105.66 (-CH), 101.30 (-CH₂), 60.09 (-CH₂), 46.14 (-CH₂), 42.57 (-CH₂), 39.07 (-CH₂), 33.01 (-CH₂), 32.75 (-CH), 31.93 (-CH₂), 29.70 (-CH₂). HR-MS m/z calculated for $\text{C}_{19}\text{H}_{23}\text{NO}_4$ $[\text{M}+\text{H}]^+$ 330.17054, found 330.17038. Purity: 97% (LC-MS).

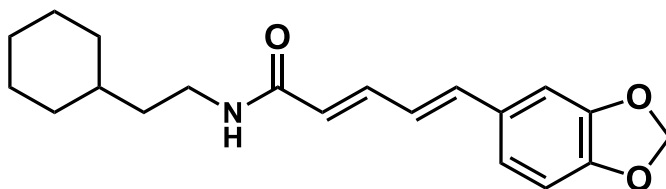
(2E,4E)-5-(benzo[d][1,3]dioxol-5-yl)-1-(piperidin-1-yl)penta-2,4-dien-1-one (4k)¹⁴⁰:



Yield: 27%. Appearance: White fluffy light crystal. Mp: 205-206 °C. ^1H NMR (300 MHz, CDCl_3) δ 7.36-7.29 (m, 1H), 6.96 (s, 1H), 6.89-6.87 (d, $J = 6.0$ Hz, 1H), 6.78-6.60 (m, 3H), 5.96 (s, 2H), 5.88-5.83 (d, $J = 15$ Hz, 1H), 5.31-5.29 (d, $J = 6.0$ Hz, 1H), 3.88-3.85 (d, $J = 9.0$ Hz, 1H), 1.98-

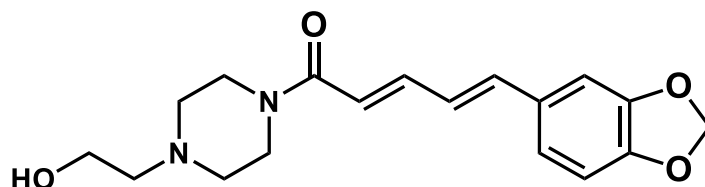
1.94 (d, $J = 12$ Hz, 2H), 1.73-1.60 (m, 3H), 1.41-1.32 (m, 2H), 1.16-1.13 (m, 3H). LR-MS m/z calculated for $C_{18}H_{21}NO_3$ $[M+H]^+$ 300.2 m/z , found 300.2 m/z . Purity: 98 % (LC-MS).

(2*E*,4*E*)-5-(benzo[*d*][1,3]dioxol-5-yl)-N-(2-cyclohexylethyl)penta-2,4-dienamide (4l):



Yield: 55%. Appearance: White fluffy light crystals. Mp: 151-152 °C. 1H NMR (300 MHz, $CDCl_3$) δ 7.39-7.31 (m, 1H), 6.90 (s, 1H), 6.90-6.88 (d, $J = 6.0$ Hz, 1H), 6.79-6.62 (m, 3H), 5.98 (s, 2H), 5.91-5.86 (d, $J = 15$ Hz, 1H), 5.40 (br s, 1H), 3.41-3.34 (m, 2H), 1.75-1.67 (m, 5H), 1.47-1.40 (m, 2H), 1.33-1.18 (m, 4H), 0.98-0.88 (m, 2H). ^{13}C NMR (300 MHz, $CDCl_3$) δ 166.10, 148.17, 140.78, 138.71, 130.88, 124.72, 123.27, 122.56, 108.47, 105.69, 101.29, 37.53, 37.14, 35.41, 33.18, 26.51, 26.22. DEPT135 ^{13}C NMR (300MHz, $CDCl_3$) δ 140.79 (-CH), 138.72 (-CH), 124.71 (-CH), 123.36 (-CH), 122.58 (-CH), 108.47 (-CH), 105.69 (-CH), 101.30 (-CH₂), 37.53 (-CH₂), 37.14 (-CH₂), 35.40 (-CH), 33.18 (-CH₂), 26.51 (-CH₂), 26.22 (-CH₂). HR-MS m/z calculated for $C_{16}H_{17}NO_4S$ $[M+H]^+$ 328.19124, found 328.19104. Purity: 98% (LC-MS).

(2*E*,4*E*)-5-(benzo[*d*][1,3]dioxol-5-yl)-1-(4-(2-hydroxyethyl)piperazin-1-yl)penta-2,4-dien-1-one (4m):



Yield: 67%. Appearance: Yellow-orange solid. Mp: 112-114 °C. 1H NMR (300 MHz, $CDCl_3$) δ 7.46-7.38 (m, 1H), 6.97 (s, 1H), 6.90-6.87 (d, $J = 9.0$ Hz, 1H), 6.78-6.71 (m, 3H), 6.40-6.36 (d, J

= 12 Hz, 1H), 5.96 (s, 2H), 3.64-3.70 (m, 4H), 2.51-2.58 (m, 8H). ¹³C NMR (300 MHz, CDCl₃) δ 165.54, 148.26, 148.22, 143.22, 138.88, 130.84, 125.07, 122.67, 119.16, 108.51, 105.67, 101.32, 59.37, 57.86, 53.25, 52.66, 45.72, 42.04. DEPT135 ¹³C NMR (300 MHz, CDCl₃) δ 143.22 (CH), 138.88 (CH), 125.06 (CH), 122.67 (CH), 119.16 (CH), 108.51 (CH), 105.67 (CH), 101.32 (CH₂), 59.37 (CH₂), 57.85 (CH₂), 53.26 (CH₂), 52.26 (CH₂), 45.74 (CH₂), 42.03 (CH₂). HR-MS m/z calculated for C₁₆H₁₇NO₄S [M+H]⁺ 331.16584, found 331.16558. Purity: 96% (LC-MS).

6.2 Aggregation Kinetics Assay

The anti-aggregation assay reference standards methylene blue (MB), and resveratrol (RVT) were purchased from Sigma Aldrich, St. Louis, MO, USA or Cayman Chemical Company, Ann Harbor, MI, USA. Thioflavin T was purchased from Sigma Aldrich, St. Louis, MO, USA. Ultrapure water (UPW) was purchased from Cayman Chemical Company, Ann Harbor, MI, USA. The human Aβ₄₂ 1,1,3,3,3-hexafluoro-2-propanol ethanol (HFIP) peptide was purchased with a purity of at least 95% from rPeptide, Georgia, USA. Thermo Scientific™ Nunc™ MicroWell™ 384-well optical-bottom black plates and adhesive sealing tape for microplates were purchased from Thermo Scientific™. The plate reader used for the fluorescence assay is a BioTek Synergy H1 microplate reader.

An in vitro aggregation kinetics study was conducted as described in Figure 17 (Section 3.2, Chapter 3), by first weighing the appropriate amounts of test compounds (**3**, **4a–m**) and reference agents; PPN, RVT, and MB, then diluting these solutions to 10,000 μM with DMSO to obtain stock A for each compound. Stock A is then diluted with DMSO to 1250 μM to produce stock A1. Next, the A1 stocks for each compound are diluted with phosphate buffer as per the volumes reported in Tables 5 and 6 to prepare the final working stock solutions; A2, A3, A4, and A5 that were subjected to a 10-fold dilution into the wells containing a final volume of 40 μL and

a maximal concentration of DMSO of 2 % (v/v) per well. Preparation of the A β 42 peptide stock solution is time sensitive as it is prone to undergo aggregation and so it was plated immediately once in solution. To prepare the A β 42 peptide stock solution, the thin film of peptide was dissolved in 10 % ammonium hydroxide to a final concentration of 1 mg/mL. Next, the A β 42 peptide stock was diluted to a final concentration of 250 μ M with sodium phosphate buffer prior to adding it to the wells. Lastly, a 2 % concentration of DMSO was added to each A β control well to mimic the maximum DMSO content contained in the test compound wells.

Table 5. Concentrations of stocks, working solutions and wells used in the aggregation kinetics assay along with their percentage of DMSO content (v/v).

Stock Label	Stock Concentration (μM)	Well Concentration of Compound (μM)	Final Well Concentration of DMSO (%)
A	10,000	-	-
A1	1,250	-	-
A2	250	25	2
A3	100	10	0.8
A4	50	5	0.4
A5	10	1	0.08
Aβ42	250	10	2

For preparation of the sodium phosphate buffer, 300 mL of UPW was used to dissolve 28.81 g of the solid sodium phosphate dibasic heptahydrate crystals, with stirring, to a final concentration of 215 mM. Following dissolution of the salt, 50 mM HCl was used to adjust the pH to 7.4, with stirring, prior to volumetric adjustments with UPW to a final volume of 500 mL. To prepare the ThT stock solution (15 μ M ThT in 50 mM glycine buffer), 0.94 g of glycine and 1.20 mg of ThT was weighed into a breaker with 150 mL of UPW, then the pH was adjusted to 7.4 with 50 mM sodium hydroxide, quantitatively transferred to a 250 mL volumetric flask, and diluted to volume

with the previously prepared 215 mM sodium phosphate buffer. The volumes of each stock solution used in the wells are specified in Table 6.^{49, 148}

Table 6. Exact well volumes of stock solution used for each well category in the aggregation kinetics assay.

Solution Well Label	15 μM ThT (μL)	215 mM Na₂HPO₄ Buffer (μL)	DMSO (μL)	25 μM Aβ42 (μL)	Compound (μL)
ThT Background	11	28	1	0	0
Compound Background	11	25	0	0	4 (25 μ M only)
Compound	11	9	0	16	4
Aβ42 Control	11	12	1	16	0

The ThT background wells provide the baseline fluorescence for the wells, while the compound background wells give us information regarding any interference in the ThT fluorescence due to the test compounds that might produce misleading results (ie. elevated fluorescence). Any observed baseline fluorescence changes in the compound background wells due to compound-ThT interactions were subtracted from the endpoint readings prior to data analysis. Aggregation kinetics experiments for each test compound concentration, and compound backgrounds were carried out in triplicates, while the A β 42 peptide controls were carried out in multiples of 12 or more wells. Piperine derivatives **4a–m** and **3** were tested at 1, 5, 10 and 25 μ M concentrations. Post-plating, the 384-well plate was covered with sealing tape (Thermo ScientificTM) to prevent evaporation of the assay solution and contamination, then incubated for 24 hours at 37 °C with shake cycles occurring every 10 minutes. Fluorescence readings were then monitored on the BioTek Synergy H1 multimode plate reader every 10 minutes at the excitation and emission wavelengths of 440 nm and 490 nm respectively for 24 hours. After completion of the assay, the end point fluorescence reading for each compound concentration was used to calculate the overall percent inhibition of

A β 42 aggregation relative to the A β 42 control wells at the 24 h time point. The following equation was used to determine the percent inhibition of A β 42 aggregation:

$$\% \text{ A}\beta\text{42 inhibition} = [1 - (\bar{X}_{\text{RFU of compound}} \div \bar{X}_{\text{RFU of A}\beta\text{42 control}})] \times 100 \% \text{ (Equation 2)}$$

During data analysis, results were expressed as the average percent inhibition of A β 42 aggregation from triplicate measurements per assay and based on three independent experiments (n = 3).¹⁴⁸

6.3 TEM Studies

TEM formvar-carbon copper grids with a mesh size of 400 was purchased from Canemco-Marivac, Gore, QC, Canada. PTA stain was purchased from Sigma Aldrich, St. Louis, MO, USA. TEM experiments were conducted using a Philips CM 10 transmission electron microscope at 60 kV (Department of Biology, University of Waterloo).

All TEM samples were directly drawn from the appropriate wells immediately after the 24-hour aggregation kinetics assay was completed. To prepare the TEM samples, 20 μ L of the appropriate well were pipette-mixed, drawn up, then dispensed slowly onto copper-coated formvar-carbon grids with a mesh size of 400 and allowed to air dry overnight. Once dry, the remaining buffer salts were washed away with two 20 μ L aliquots of UPW and removed by capillary action onto clean filter paper. Next, the TEM grids were air dried for at least 60 minutes prior to adding 20 μ L of the 2% PTA, removing excess stain with clean filter paper after approximately 10 seconds to avoid over staining and saturation of the sample during imaging. Lastly, excess amounts of PTA were washed away with a single aliquot of UPW and dried with filter paper before air drying for 24 hours. Finally, the TEM samples were analyzed on a Philips CM 10 transmission electron microscope at 60 kV (Department of Biology, University of Waterloo), and the micrographs were obtained with a 14-megapixel AMT camera.¹⁴⁸

6.4 Computational Modelling Studies

The molecular docking studies and binding energy simulations between the pentamer of A β 42 and piperine derivatives were conducted using the software Discovery Studio (DS) *Structure-Based-Design (SBD)* from Dassault Systemes Biovia Corp. (San Diego, USA) (v20.1.0.19295). All simulations were ran on a Dell Optiplex 3040 PC with Windows 10 software, version 21H1 for x64 based systems (KB5007289). The ssNMR structure of the A β 42 fibril (pdb id: 5KK3) was used (retrieved from RCSB protein data bank) to create the pentamer β -sheet assembly by modifying the fibril in the *macromolecules* module to end up with five chains, A-E, of the A β 42 pentamer. In the *simulations* module, the CHARMM forcefield was then applied to the pentamer, while partial charges were assigned using the Momany-Rone partial charge method. The pentamer assembly was given its proper ionization state at pH 7.4 using the *Prepare Protein* tool in the *Macromolecules* module. Afterwards, the 20 Å binding sphere was created by individually selecting the A β 42 amyloidogenic region's amino acid residues (¹⁶KLVFFA²¹ and ³¹IGLMV³⁶) within the middle strand (chain C) of the oligomer and saving the file as a .dsv file for docking. Preparation of the ligands (piperine derivatives **4a-m**) began with drawing the molecular structures in ChemDraw (Perkin Elmer, Massachusetts, USA), and subsequently importing them into DS. After importing, the CHARMM forcefield was applied to each molecule to fix bond angles and add hydrogens. Additionally, the molecules were subjected to minimization using 500 steps each of steepest descent and conjugate gradient minimization (RMS gradient 0.1 kcal/mol). For the minimization process, a distance dependant dielectric constant was incorporated with the implicit solvent model. This considers solvation effects that has been shown to provide an improved initial configuration of the molecules for docking studies as opposed to being in a vacuum. After the molecules were prepared, they were saved as individual .dsv files and subsequently copied into

the prepared A β 42 pentamer model for docking. Molecular docking was then carried out using the CDOCKER algorithm in the *Receptor-Ligand Interactions* module in the SBD suite where the receptor was set to be the A β 42 pentamer and the ligand was set to be the respective piperine derivative. Parameters utilised for the CDOCKER docking study include a 700 K target temperature with 2000 heating steps, followed by a 300 K target temperature with 5000 cooling steps, and the CHARMM forcefield. Results of the docking study were presented in a data file containing the top ten binding configurations for the lead compounds (**4a**, **4b** and **4c**) and piperine as a reference standard. Rankings of the poses included the CDOCKER Energy and CDOCKER Interaction Energy which aided in determining the most stable binding mode while considering the stability of intermolecular interactions. To estimate the binding affinity of the ligands (in kcal/mol), binding energy simulations were run using localized molecular dynamics to simulate water molecules in the binding domain, replicating biological conditions more closely to improve prediction accuracy. The binding energies were calculated using the GBSW implicit solvent function which employed the following equation: $E_{\text{binding}} = \text{Energy of complex } (E_{\text{ligand-receptor}}) - \text{Energy of ligand } (E_{\text{ligand}}) - \text{Energy of receptor } (E_{\text{receptor}})$. Overall, the docking study results were analyzed by ranking the binding energies calculated in kcal/mol, along with evaluating the intermolecular interactions observed and distance parameters.^{154, 156}

6.5 Cell Culture Assays

The reagents used for the cell culture process include DMEM/F-12 50/50 mixture with and without phenol red, pH 7.2 phosphate buffered saline (1X), fetal bovine serum, penicillin streptomycin (10,000 U/mL) and 0.25 % trypsin-EDTA (1x) which were purchased from Gibco, Billings, MT, USA. Mr. Frosty™ freezing chamber was purchased from Thermo Fisher Scientific, MA, USA.

The procedure for the cell culture studies starts with thawing and plating 1 mL of HT22 cells (~1,000,000 cells/mL) in 9 mL of growth medium to a density of ~100,000 cells/mL. Following this, the cells were allowed to incubate (37 °C, 5% CO₂) and grow until ~80 % confluency was attained. Table 7 lists the reagents and their respective amounts that were used to create the media for various steps in the cell culture process that will be discussed in detail below.

Table 7. Reagents required to produce various types of cell culture media to be used for processes including cell proliferation, cell starving and cell storage.

Cell Culture Media Type	Reagent Composition
Growth Medium	1 mL (~10 %) Fetal Bovine Serum (FBS) 0.110 mL (~1 %) Penicillin Streptomycin (PS) 10 mL (~90 %) Dulbecco's Modified Eagle Medium/Ham's F-12 50/50 mix containing 2.5 mM L-glutamine, 15 mM HEPES, 17.5 mmol/L glucose, and 0.999 mmol/L sodium pyruvate (DMEM)
Starving Medium	10 mL (100 %) DMEM
Freeze Medium	5 mL (~80 %) DMEM 0.5 mL (~10 %) FBS 0.55 mL (~10 %) Filtered (0.2 µm) DMSO

The cells grew for two days before reaching 80% confluency where day one involved thawing the frozen cells and incubating (37 °C, 5 % CO₂) them for 24 hours in the growth medium. The next day, the initial growth medium was replaced with 10 mL of fresh growth medium, and the cells were allowed to incubate for another 24 hours. This step aids in removing any remaining DMSO from the freeze medium that may interfere with cell proliferation. On day three, the confluency of the cells was confirmed by viewing through a light microscope, the growth medium was aspirated, and the cells were washed once with 10 mL of PBS before being trypsinized. This step detaches cells from the plate for splitting purposes to avoid over-grown cells.^{169, 170} This process was done by adding 1 mL of trypsin to the plate, swirling to ensure even coverage, and then incubating for

~2 minutes until the cells were visibly detached and floating when viewed under a light microscope. Immediately after, the trypsin was inactivated by adding 9 mL of growth medium to the cells and transferring the solution of cells into a 15 mL falcon tube.¹⁷⁰ Avoiding over-confluent cell growth is necessary during the cell culture process due to a phenomenon known as contact inhibition occurring upon cells touching each other. Briefly, contact inhibition causes cells to behave abnormally due to stress and may cause misleading results during experimentation.^{171, 172} The suspension of cells was then centrifuged for 5 minutes at 120 x g at room temperature before the growth medium-trypsin mixture was discarded and the cells were resuspended in 1 mL of growth medium through gentle, repeated, pipette aspiration. In preparation for the CCK-8 assay, the cells were then counted by applying 10 μ L of the suspension into a hemocytometer. Determination of cell concentration was then calculated using the cell counting workflow displayed in Figure 30.^{173, 174}

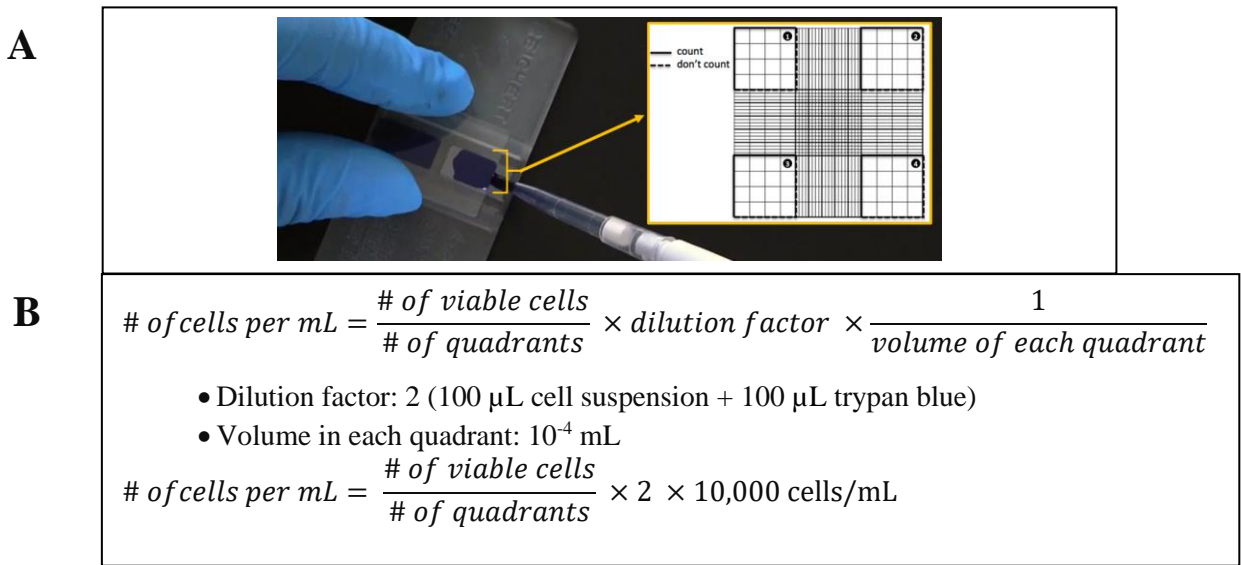


Figure 30. Cell counting workflow for determination of cell concentration. Panel A: Hemocytometer and zoomed view of grid for counting cells manually. Cells within all four white quadrants are counted and boundary touching cells are only counted on the left and topmost borders to avoid over counting. Panel B: Stepwise description of concentration calculation after cells are counted.

After the concentration was determined, the equation $C_1V_1 = C_2V_2$ was used to calculate the volume of cells required for producing 7 mL of cells with a concentration of 5000 cells per 0.1 mL. This was the ideal number of cells per well for the CCK-8 assay to avoid over confluency and achieve high sensitivity during the assay, as reported by the manufacturer (Targetmol, Wellesley Hills, MA, USA). After pipette mixing the growth medium and appropriate volume of cells, they were plated into the 96-well plate in the inner wells (100 μ L each), while the outer wells were filled with 100 μ L of phosphate buffered saline (PBS). Filling the outer wells with PBS is done to avoid the “edge effect”, a phenomenon in which the solutions contained within the wells at the edge of a plate evaporate more rapidly than the centermost wells.¹⁷⁵ A schematic in Figure 31 shows the plate layout of a CCK-8 assay and Table 8 shows the respective list of solutions that are added to the variable and control wells. To conduct the cytotoxicity assay, the mouse hippocampal cells were incubated for 24 hours with the test compounds at 10 and 25 μ M both in the absence (untreated cell controls) and presence of A β 42 at 10 μ M. After 24 hours, the media was exchanged with CCK-8 solution and incubated again (37 °C, 5% CO₂) for 3 hours prior to measuring the fluorescence at 450 nm to allow for WST-8 reduction. Results are reported as an average percent cell viability with six replicates per concentration tested (n = 6) and three independent experiments.

	1	2	3	4	5	6	7	8	9	10	11	12
A	PBS	PBS	PBS	PBS	PBS	PBS	PBS	PBS	PBS	PBS	PBS	PBS
B	PBS	UT	A β	A10	A25	B10	B25	C10	C25	P25	R25	PBS
C	PBS	UT	A β	A10	A25	B10	B25	C10	C25	P25	R25	PBS
D	PBS	UT	A β	A10	A25	B10	B25	C10	C25	P25	R25	PBS
E	PBS	UT	A β	A10	A25	B10	B25	C10	C25	P25	R25	PBS
F	PBS	UT	A β	A10	A25	B10	B25	C10	C25	P25	R25	PBS
G	PBS	UT	A β	A10	A25	B10	B25	C10	C25	P25	R25	PBS
H	PBS	PBS	PBS	PBS	PBS	PBS	PBS	PBS	PBS	PBS	PBS	PBS

Figure 31. A schematic of the 96-well plate layout for the cell culture studies. Legend: UT = Untreated control, A β = A β 42 control (10 μ M), A10 = Compound **4a** (10 μ M), A25 = Compound **4a** (25 μ M), B10 = Compound **4b** (10 μ M), B25 = Compound **4b** (25 μ M), C10 = Compound **4c** (10 μ M), C25 = Compound **4c** (25 μ M), P25 = Piperine (25 μ M), R25 = Resveratrol (25 μ M).

Table 8. Schematic of a 96-well plate layout for the CCK-8 assay and solution compositions for cell treatments applied for testing during this cytotoxicity assay.

Cell Treatment	Well Composition
Untreated (control)	<ul style="list-style-type: none"> • 100 μL DMEM
A β 42 Control (10 μ M)	<ul style="list-style-type: none"> • 90 μL DMEM • 10 μL Aβ42 Stock (100 μM)
Test Compound (25 μ M)	<ul style="list-style-type: none"> • 80 μL DMEM • 10 μL Aβ42 Stock (100 μM) • 10 μL Compound Stock (250 μM)
Test Compound (10 μ M)	<ul style="list-style-type: none"> • 80 μL DMEM • 10 μL Aβ42 Stock (100 μM) • 10 μL Compound Stock (100 μM)

Remaining cells that were not used for the assay on the day of seeding were split using a passage ratio of 1:50 (ie. 0.2 mL of cells to 10 mL of growth medium per petri dish) and ensuring even distribution prior to incubation at 37 °C. After two days of growth, the cells were either passaged once again or harvested for a cytotoxicity assay, as previously described.

After the completion of experiments, the cells were prepared for freezing and storage by first removing the growth medium upon reaching 80% confluency, then adding 10 mL of DMEM and incubating for 24 hours. The next day, the starving medium was removed, and the cells were washed with 10 mL of PBS before being trypsinized and resuspended in 5 mL of freeze medium. Lastly, the cells were thoroughly mixed before distributing 1 mL aliquots into labelled cryovials and slowly freezing them (~1°C per minute) to –80°C in a Mr. Frosty™ freezing container for 24 hours. Slow freezing methods enhance cell preservation while final, long-term storage of the cell vials were kept in liquid nitrogen for optimal preservation and cell recovery upon thawing.

References

- (1) Safura, J.; Saeedeh, K.; Xaniar, E. G.; Mona, K.; Behnam, Y.; Mohammad, S.; Davood, B.; Omid, B. Amyloid β -Targeted Inhibitory Peptides for Alzheimer's Disease: Current State and Future Perspectives. In *Alzheimer's Disease: Drug Discovery*; Huang, X., Ed.; Brisbane (AU): Exon Publications: Brisbane, 2020; pp 51–68.
<https://doi.org/10.36255/exonpublications.alzheimersdisease.2020>.
- (2) Goldman, B. Navigating the Path Forward for Dementia in Canada: The Landmark Study Report #1. Toronto. September 2022, pp 1–54.
- (3) Cline, E. N.; Bicca, M. A.; Viola, K. L.; Klein, W. L. The Amyloid- β Oligomer Hypothesis: Beginning of the Third Decade. *J. Alzheimer's Dis.* **2018**, *64* (s1), S567–S610. <https://doi.org/10.3233/JAD-179941>.
- (4) Selkoe, D. J.; Hardy, J. The Amyloid Hypothesis of Alzheimer's Disease at 25 Years. *EMBO Mol. Med.* **2016**, *8* (6), 595–608. <https://doi.org/10.15252/emmm.201606210>.
- (5) Josephs, K. A.; Murray, M. E.; Whitwell, J. L.; Parisi, J. E.; Petrucelli, L.; Jack, C. R.; Petersen, R. C.; Dickson, D. W. Staging TDP-43 Pathology in Alzheimer's Disease. *Acta Neuropathol.* **2014**, *127* (3), 441–450. <https://doi.org/10.1007/s00401-013-1211-9>.
- (6) Li, X. L.; Hu, N.; Tan, M. S.; Yu, J. T.; Tan, L. Behavioral and Psychological Symptoms in Alzheimer's Disease. *Biomed Res. Int.* **2014**, *2014*, 1–9.
<https://doi.org/10.1155/2014/927804>.
- (7) Li, X.; Feng, X.; Sun, X.; Hou, N.; Han, F.; Liu, Y. Global, Regional, and National Burden of Alzheimer's Disease and Other Dementias, 1990–2019. *Front. Aging Neurosci.* **2022**, *14* (937486), 1–17. <https://doi.org/10.3389/fnagi.2022.937486>.

- (8) Greenblat, C. World Health Organization <https://www.who.int/news-room/factsheets/detail/dementia> (accessed 2023-06-04).
- (9) Watts, L. T. *Dementia in Canada Cross-Country Report 2022*; Toronto, 2022.
- (10) Chambers, L. W.; Bancej, C.; McDowell, I. *Prevalence and Monetary Costs of Dementia in Canada*; Toronto, 2016. <https://doi.org/10.1201/9780203025314>.
- (11) Mohamed, T.; Hoang, T.; Jelokhani-Niaraki, M.; Rao, P. P. N. Tau-Derived-Hexapeptide 306VQIVYK311 Aggregation Inhibitors: Nitrocatechol Moiety as a Pharmacophore in Drug Design. *ACS Chem. Neurosci.* **2013**, *4* (12), 1559–1570. <https://doi.org/10.1021/cn400151a>.
- (12) Caesar, I.; Jonson, M.; Peter Nilsson, K. R.; Thor, S.; Hammarström, P. Curcumin Promotes A-Beta Fibrillation and Reduces Neurotoxicity in Transgenic Drosophila. *PLoS One.* **2012**, *7* (2), 31424. <https://doi.org/10.1371/journal.pone.0031424>.
- (13) Mohamed, T.; Shakeri, A.; Rao, P. P. N. Amyloid Cascade in Alzheimer's Disease: Recent Advances in Medicinal Chemistry. *Eur. J. Med. Chem.* **2016**, *113*, 258–272. <https://doi.org/10.1016/j.ejmech.2016.02.049>.
- (14) Gendron, T. F. The Role of Tau in Neurodegeneration. *Mol. Neurodegener.* **2009**, *4* (1), 1–19. <https://doi.org/10.1186/1750-1326-4-13>.
- (15) Yang, S.-H.; Lee, D. K.; Shin, J.; Lee, S.; Baek, S.; Kim, J.; Jung, H.; Hah, J.-M.; Kim, Y. Nec-1 Alleviates Cognitive Impairment with Reduction of Ab and Tau Abnormalities in APP/PS1 Mice. *EMBO Mol. Med.* **2017**, *9* (1), 61–77. <https://doi.org/10.15252/emmm.201606566>.

- (16) Caesar-Chavannes, C. R.; MacDonald, S. Cross-Canada Forum-National Population Health Study of Neurological Conditions in Canada. *Chronic Dis. Inj. Can.* **2013**, *33* (3), 188–191.
- (17) Mohamed, T.; P.N. Rao, P. Alzheimer's Disease: Emerging Trends in Small Molecule Therapies. *Curr. Med. Chem.* **2011**, *18* (28), 4299–4320.
<https://doi.org/10.2174/092986711797200435>.
- (18) Jr, A. V. T.; Buccafusco, J. J.; Clinical, P.; Therapeutics, E.; College, G.; Campus, A.; Animal, S. The Cholinergic Hypothesis of Age and Alzheimer's Disease- Related Cognitive Deficits : Recent Challenges and Their Implications for Novel Drug Development. **2003**, *306* (3), 821–827. <https://doi.org/10.1124/jpet.102.041616>.
- (19) Albuquerque, E. X.; Pereira, E. F. R.; Alkondon, M.; Rogers, S. W. Mammalian Nicotinic Acetylcholine Receptors: From Structure to Function. *Physiol. Rev.* **2009**, *89* (1), 73–120.
<https://doi.org/10.1152/physrev.00015.2008>.
- (20) Kudlak, M.; Tadi, P. Physiology, Muscarinic Receptor
<https://www.ncbi.nlm.nih.gov/books/NBK555909/> (accessed 2023-06-04).
- (21) Belluti, F.; Rampa, A.; Piazzzi, L.; Bisi, A.; Gobbi, S.; Bartolini, M.; Andrisano, V.; Cavalli, A.; Recanatini, M.; Valenti, P. Cholinesterase Inhibitors: Xanthostigmine Derivatives Blocking the Acetylcholinesterase-Induced β -Amyloid Aggregation. *J. Med. Chem.* **2005**, *48* (13), 4444–4456. <https://doi.org/10.1021/jm049515h>.
- (22) Inestrosa, N. C.; Alvarez, A.; Pérez, C. A.; Moreno, R. D.; Vicente, M.; Linker, C.; Casanueva, O. I.; Soto, C.; Garrido, J. Acetylcholinesterase Accelerates Assembly of Amyloid- β -Peptides into Alzheimer's Fibrils: Possible Role of the Peripheral Site of the

- Enzyme. *Neuron*. **1996**, *16* (4), 881–891. [https://doi.org/10.1016/S0896-6273\(00\)80108-7](https://doi.org/10.1016/S0896-6273(00)80108-7).
- (23) Inestrosa, N. C.; Dinamarca, M. C.; Alvarez, A. Amyloid-Cholinesterase Interactions: Implications for Alzheimer's Disease. *FEBS J.* **2008**, *275* (4), 625–632. <https://doi.org/10.1111/j.1742-4658.2007.06238.x>.
- (24) Saravanaraman, P.; Chinnadurai, R. K.; Boopathy, R. A New Role for the Nonpathogenic Nonsynonymous Single-Nucleotide Polymorphisms of Acetylcholinesterase in the Treatment of Alzheimer's Disease: A Computational Study. *J. Comput. Biol.* **2014**, *21* (8), 632–647. <https://doi.org/10.1089/cmb.2014.0005>.
- (25) Avila, J.; Lucas, J. J.; Pérez, M.; Hernández, F. Role of Tau Protein in Both Physiological and Pathological Conditions. *Physiol. Rev.* **2004**, *84* (2), 361–384. <https://doi.org/10.1152/physrev.00024.2003>.
- (26) Martin, L.; Latypova, X.; Wilson, C. M.; Magnaudeix, A.; Perrin, M. L.; Terro, F. Tau Protein Phosphatases in Alzheimer's Disease: The Leading Role of PP2A. *Ageing Res. Rev.* **2013**, *12* (1), 39–49. <https://doi.org/10.1016/J.ARR.2012.06.008>.
- (27) Panza, F.; Lozupone, M.; Seripa, D.; Imbimbo, B. P. Amyloid- β Immunotherapy for Alzheimer Disease: Is It Now a Long Shot? *Ann. Neurol.* **2019**, *85* (3), 303–315. <https://doi.org/10.1002/ana.25410>.
- (28) Hardy, J. A.; Higgins, G. A. Alzheimer's Disease: The Amyloid Cascade Hypothesis. *Science*. **1992**, *256* (5054), 184–185. <https://doi.org/10.1126/science.1566067>.
- (29) Bu, X. Le; Rao, P. P. N.; Wang, Y. J. Anti-Amyloid Aggregation Activity of Natural Compounds: Implications for Alzheimer's Drug Discovery. *Mol. Neurobiol.* **2016**, *53* (6),

- 3565–3575. <https://doi.org/10.1007/s12035-015-9301-4>.
- (30) Zhang, Y. W.; Thompson, R.; Zhang, H.; Xu, H. APP Processing in Alzheimer's Disease. *Mol. Brain*. **2011**, *4* (1), 3. <https://doi.org/10.1186/1756-6606-4-3>.
- (31) Zheng, H.; Koo, E. H. The Amyloid Precursor Protein: Beyond Amyloid. *Mol. Neurodegener*. **2006**, *1* (1), 1–12. <https://doi.org/10.1186/1750-1326-1-5>.
- (32) Plummer, S.; Van Den Heuvel, C.; Thornton, E.; Corrigan, F.; Cappai, R. The Neuroprotective Properties of the Amyloid Precursor Protein Following Traumatic Brain Injury. *Aging Dis*. **2016**, *7* (2), 163–179. <https://doi.org/10.14336/AD.2015.0907>.
- (33) Xu, F.; Previti, M. Lou; Nieman, M. T.; Davis, J.; Schmaier, A. H.; Van Nostrand, W. E. A BPP/APLP2 Family of Kunitz Serine Proteinase Inhibitors Regulate Cerebral Thrombosis. *J. Neurosci*. **2009**, *29* (17), 5666–5670. <https://doi.org/10.1523/JNEUROSCI.0095-09.2009>.
- (34) Cheng, F.; Cappai, R.; Lidfeldt, J.; Belting, M.; Fransson, L. Å.; Mani, K. Amyloid Precursor Protein (APP)/APP-like Protein 2 (APLP2) Expression Is Required to Initiate Endosome-Nucleus-Autophagosome Trafficking of Glypican-1-Derived Heparan Sulfate. *J. Biol. Chem*. **2014**, *289* (30), 20871–20878. <https://doi.org/10.1074/jbc.M114.552810>.
- (35) Needham, B. E.; Ciccotosto, G. D.; Cappai, R. Combined Deletions of Amyloid Precursor Protein and Amyloid Precursor-like Protein 2 Reveal Different Effects on Mouse Brain Metal Homeostasis. *Metallomics*. **2014**, *6* (3), 598–603. <https://doi.org/10.1039/c3mt00358b>.
- (36) Tcw, J.; Goate, A. M. Genetics of β -Amyloid Precursor Protein in Alzheimer's Disease.

- Cold Spring Harb. Perspect. Med.* **2017**, 7 (6), 1–12.
<https://doi.org/10.1101/cshperspect.a024539>.
- (37) Hardy, J. Amyloid, the Presenilins and Alzheimer's Disease. *Trends Neurosci.* **1997**, 20 (4), 154–159. [https://doi.org/10.1016/S0166-2236\(96\)01030-2](https://doi.org/10.1016/S0166-2236(96)01030-2).
- (38) Bitan, G.; Kirkitadze, M. D.; Lomakin, A.; Vollers, S. S.; Benedek, G. B.; Teplow, D. B. Amyloid-Beta Protein (Abeta) Assembly : Abeta 40 and Abeta 42 Oligomerize through Distinct Pathways. *Proc. Natl. Acad. Sci. U. S. A.* **2003**, 100 (1), 330–335.
- (39) Shih, Y. H.; Tu, L. H.; Chang, T. Y.; Ganesan, K.; Chang, W. W.; Chang, P. S.; Fang, Y. S.; Lin, Y. T.; Jin, L. W.; Chen, Y. R. TDP-43 Interacts with Amyloid- β , Inhibits Fibrillization, and Worsens Pathology in a Model of Alzheimer's Disease. *Nat. Commun.* **2020**, 11 (1). <https://doi.org/10.1038/s41467-020-19786-7>.
- (40) Dickson, D. W. Apoptotic Mechanisms in Alzheimer Neurofibrillary Degeneration: Cause or Effect? *J. Clin. Invest.* **2004**, 114 (1), 23–27. <https://doi.org/10.1172/JCI22317>.
- (41) Kametani, F.; Hasegawa, M. Reconsideration of Amyloid Hypothesis and Tau Hypothesis in Alzheimer's Disease. *Front. Neurosci.* **2018**, 12 (25), 1–11.
<https://doi.org/10.3389/fnins.2018.00025>.
- (42) Roberts, S. B.; Ripellino, J. A.; Ingalls, K. M.; Robakis, N. K.; Felsenstein, K. M. Non-Amyloidogenic Cleavage of the β -Amyloid Precursor Protein by an Integral Membrane Metalloendopeptidase. *J. Biol. Chem.* **1994**, 269 (4), 3111–3116.
[https://doi.org/10.1016/s0021-9258\(17\)42055-2](https://doi.org/10.1016/s0021-9258(17)42055-2).
- (43) Kuhn, P. H.; Wang, H.; Dislich, B.; Colombo, A.; Zeitschel, U.; Ellwart, J. W.; Kremmer,

- E.; Roßner, S.; Lichtenthaler, S. F. ADAM10 Is the Physiologically Relevant, Constitutive α -Secretase of the Amyloid Precursor Protein in Primary Neurons. *EMBO J.* **2010**, *29* (17), 3020–3032. <https://doi.org/10.1038/emboj.2010.167>.
- (44) Hitschler, L.; Lang, T. The Transmembrane Domain of the Amyloid Precursor Protein Is Required for Antiamyloidogenic Processing by α -Secretase ADAM10. *J. Biol. Chem.* **2022**, *298* (6), 1–14. <https://doi.org/10.1016/j.jbc.2022.101911>.
- (45) Yamazaki, K.; Mizui, Y.; Tanaka, I. Radiation Hybrid Mapping of Human ADAM10 Gene to Chromosome 15. *Genomics.* **1997**, *45* (2), 457–459. <https://doi.org/10.1006/GENO.1997.4910>.
- (46) Skovronsky, D. M.; Moore, D. B.; Milla, M. E.; Doms, R. W.; Lee, V. M. Y. Protein Kinase C-Dependent α -Secretase Competes with β -Secretase for Cleavage of Amyloid- β Precursor Protein in the Trans-Golgi Network. *J. Biol. Chem.* **2000**, *275* (4), 2568–2575. <https://doi.org/10.1074/jbc.275.4.2568>.
- (47) Nhan, H. S.; Chiang, K.; Koo, E. H. The Multifaceted Nature of Amyloid Precursor Protein and Its Proteolytic Fragments: Friends and Foes. *Acta Neuropathol.* **2015**, *129* (1), 1–19. <https://doi.org/10.1007/s00401-014-1347-2>.
- (48) Van Cauwenberghe, C.; Van Broeckhoven, C.; Sleegers, K. The Genetic Landscape of Alzheimer Disease: Clinical Implications and Perspectives. *Genet. Med.* **2016**, *18* (5), 421–430. <https://doi.org/10.1038/gim.2015.117>.
- (49) Mohamed, T.; Gujral, S. S.; Rao, P. P. N. Tau Derived Hexapeptide AcPHF6 Promotes Beta-Amyloid ($A\beta$) Fibrillogenesis. *ACS Chem. Neurosci.* **2018**, *9* (4), 773–782. <https://doi.org/10.1021/acchemneuro.7b00433>.

- (50) Vassar, R.; Bennett, B. D.; Babu-Khan, S.; Kahn, S.; Mendiaz, E. A.; Denis, P.; Teplow, D. B.; Ross, S.; Amarante, P.; Loeloff, R.; Luo, Y.; Fisher, S.; Fuller, J.; Edenson, S.; Lile, J.; Jarosinski, M. A.; Biere, A. L.; Curran, E.; Burgess, T.; Louis, J. C.; Collins, F.; Treanor, J.; Rogers, G.; Citron, M. β -Secretase Cleavage of Alzheimer's Amyloid Precursor Protein by the Transmembrane Aspartic Protease BACE. *Science*. **1999**, *286* (5440), 735–741. <https://doi.org/10.1126/science.286.5440.735>.
- (51) Zhang, X.; Song, W. The Role of APP and BACE1 Trafficking in APP Processing and Amyloid- β Generation. *Alzheimer's Res. Ther.* **2013**, *5* (5), 1–8. <https://doi.org/10.1186/alzrt211>.
- (52) Citron, M. Beta-Secretase: Tissue Culture Studies of Sequence Specificity, Inhibitors, and Candidate Enzymes. In *Methods in Molecular Medicine: Alzheimer's Disease Methods and Protocols*; Hooper, N. M., Ed.; Humana Press Inc.: New Jersey, 2000; Vol. 32, p 229.
- (53) Vassar, R. BACE1: The β -Secretase Enzyme in Alzheimer's Disease. *J. Mol. Neurosci.* **2004**, *23* (1), 105–114. <https://doi.org/10.1385/JMN:23:1-2:105>.
- (54) Shimizu, H.; Tosaki, A.; Kaneko, K.; Hisano, T.; Sakurai, T.; Nukina, N. Crystal Structure of an Active Form of BACE1, an Enzyme Responsible for Amyloid β Protein Production. *Mol. Cell. Biol.* **2008**, *28* (11), 3663–3671. <https://doi.org/10.1128/mcb.02185-07>.
- (55) Touloukhonova, L.; Metzler, W. J.; Witmer, M. R.; Copeland, R. A.; Marcinkeviciene, J. Kinetic Studies on β -Site Amyloid Precursor Protein-Cleaving Enzyme (BACE). *J. Biol. Chem.* **2003**, *278* (7), 4582–4589. <https://doi.org/10.1074/jbc.M210471200>.
- (56) Kimberly, W. T.; LaVoie, M. J.; Ostaszewski, B. L.; Ye, W.; Wolfe, M. S.; Selkoe, D. J. γ -Secretase Is a Membrane Protein Complex Comprised of Presenilin, Nicastrin, Aph-1,

- and Pen-2. *Proc. Natl. Acad. Sci. U. S. A.* **2003**, *100* (11), 6382–6387.
<https://doi.org/10.1073/pnas.1037392100>.
- (57) De Strooper, B. Aph-1, Pen-2, and Nicastrin with Presenilin Generate an Active γ -Secretase Complex. *Neuron*. **2003**, *38* (1), 9–12. [https://doi.org/10.1016/S0896-6273\(03\)00205-8](https://doi.org/10.1016/S0896-6273(03)00205-8).
- (58) Chen, A. C.; Guo, L. Y.; Ostaszewski, B. L.; Selkoe, D. J.; LaVoie, M. J. Aph-1 Associates Directly with Full-Length and C-Terminal Fragments of γ -Secretase Substrates. *J. Biol. Chem.* **2010**, *285* (15), 11378–11391.
<https://doi.org/10.1074/jbc.M109.088815>.
- (59) Zhang, X.; Li, Y.; Xu, H.; Zhang, Y. W. The γ -Secretase Complex: From Structure to Function. *Front. Cell. Neurosci.* **2014**, *8* (427), 1–10.
<https://doi.org/10.3389/fncel.2014.00427>.
- (60) Schellenberg, G. D.; Bird, T. D.; Wijsman, E. M.; Orr, H. T.; Anderson, L.; Nemens, E.; White, J. A.; Bonnycastle, L.; Weber, J. L.; Alonso, M. E.; Potter, H.; Heston, L. L.; Martin, G. M. Genetic Linkage Evidence for a Familial Alzheimer's Disease Locus on Chromosome 14. *Science*. **1992**, *258* (5082), 668–671.
<https://doi.org/10.1126/science.1411576>.
- (61) Levy-Lahad, E.; Wijsman, E. M.; Nemens, E.; Anderson, L.; Goddard, K. A. B.; Weber, J. L.; Bird, T. D.; Schellenberg, G. D. A Familial Alzheimer's Disease Locus on Chromosome 1. *Science*. **1995**, *269* (5226), 970–973.
<https://doi.org/10.1126/science.7638621>.
- (62) De Strooper, B.; Iwatsubo, T.; Wolfe, M. S. Presenilins and γ -Secretase: Structure,

- Function, and Role in Alzheimer Disease. *Cold Spring Harb. Perspect. Med.* **2012**, 2 (1), a006304–a006304. <https://doi.org/10.1101/cshperspect.a006304>.
- (63) Vetrivel, K. S.; Zhang, Y.; Xu, H.; Thinakaran, G. Pathological and Physiological Functions of Presenilins. *Mol. Neurodegener.* **2006**, 1 (4), 1–12. <https://doi.org/10.1186/1750-1326-1-4>.
- (64) Haass, C.; Kaether, C.; Thinakaran, G.; Sisodia, S. Trafficking and Proteolytic Processing of APP. *Cold Spring Harb. Perspect. Med.* **2012**, 2 (5), 1–25. <https://doi.org/10.1101/cshperspect.a006270>.
- (65) Li, X.; Dang, S.; Yan, C.; Gong, X.; Wang, J.; Shi, Y. Structure of a Presenilin Family Intramembrane Aspartate Protease. *Nature.* **2013**, 493 (7430), 56–61. <https://doi.org/10.1038/nature11801>.
- (66) Veeraraghavalu, K.; Choi, S. H.; Zhang, X.; Sisodia, S. S. Endogenous Expression of FAD-Linked PS1 Impairs Proliferation, Neuronal Differentiation and Survival of Adult Hippocampal Progenitors. *Mol. Neurodegener.* **2013**, 8 (1), 1–9. <https://doi.org/10.1186/1750-1326-8-41>.
- (67) Bezprozvanny, I.; Hiesinger, P. The Synaptic Maintenance Problem: Membrane Recycling, Ca²⁺ Homeostasis and Late Onset Degeneration. *Mol. Neurodegener.* **2013**, 8 (1), 1–14. <https://doi.org/10.1186/1750-1326-8-23>.
- (68) Wang, X.; Huang, T.; Bu, G.; Xu, H. Dysregulation of Protein Trafficking in Neurodegeneration. *Mol. Neurodegener.* **2014**, 9 (1), 1–9. <https://doi.org/10.1186/1750-1326-9-31>.

- (69) Yang, D.-S.; Tandon, A.; Chen, F.; Yu, G.; Yu, H.; Arawaka, S.; Hasegawa, H.; Duthie, M.; Schmidt, S. D.; Ramabhadran, T. V.; Nixon, R. A.; Mathews, P. M.; Gandy, S. E.; Mount, H. T. J.; St George-Hyslop, P.; Fraser, P. E. Mature Glycosylation and Trafficking of Nicastrin Modulate Its Binding to Presenilins. *J. Biol. Chem.* **2002**, *277* (31), 28135–28142. <https://doi.org/10.1074/jbc.M110871200>.
- (70) Yu, G.; Nishimura, M.; Arawaka, S.; Levitan, D.; Zhang, L.; Tandon, A.; Song, Y.-Q.; Rogaeva, E.; Chen, F.; Kawarai, T.; Supala, A.; Levesque, L.; Yu, H.; Yang, D.-S.; Holmes, E.; Milman, P.; Liang, Y.; Zhang, D. M.; Xu, D. H.; Sato, C.; Rogaev, E.; Smith, M.; Janus, C.; Zhang, Y.; St. George-Hyslop, P. Nicastrin Modulates Presenilin-Mediated Notch/Glp-1 Signal Transduction and BAPP Processing. *Nature.* **2000**, *407* (6800), 48–54. <https://doi.org/10.1038/35024009>.
- (71) Crystal, A. S.; Morais, V. A.; Pierson, T. C.; Pijak, D. S.; Carlin, D.; Lee, V. M.-Y.; Doms, R. W. Membrane Topology of γ -Secretase Component PEN-2. *J. Biol. Chem.* **2003**, *278* (22), 20117–20123. <https://doi.org/10.1074/jbc.M213107200>.
- (72) Fukumori, A.; Fluhrer, R.; Steiner, H.; Haass, C. Three-Amino Acid Spacing of Presenilin Endoproteolysis Suggests a General Stepwise Cleavage of γ -Secretase-Mediated Intramembrane Proteolysis. *J. Neurosci.* **2010**, *30* (23), 7853–7862. <https://doi.org/10.1523/JNEUROSCI.1443-10.2010>.
- (73) Schemmert, S.; Schartmann, E.; Zafiu, C.; Kass, B.; Hartwig, S.; Lehr, S.; Bannach, O.; Langen, K. J.; Shah, N. J.; Kutzsche, J.; Willuweit, A.; Willbold, D. A β Oligomer Elimination Restores Cognition in Transgenic Alzheimer's Mice with Full-Blown Pathology. *Mol. Neurobiol.* **2019**, *56* (3), 2211–2223. <https://doi.org/10.1007/s12035-018->

1209-3.

- (74) Itoh, S. G.; Yagi-Utsumi, M.; Kato, K.; Okumura, H. Key Residue for Aggregation of Amyloid- β Peptides. *ACS Chem. Neurosci.* **2022**, *13* (22), 3139–3151.
<https://doi.org/10.1021/acchemneuro.2c00358>.
- (75) Chen, G. F.; Xu, T. H.; Yan, Y.; Zhou, Y. R.; Jiang, Y.; Melcher, K.; Xu, H. E. Amyloid Beta: Structure, Biology and Structure-Based Therapeutic Development. *Acta Pharmacol. Sin.* **2017**, *38* (9), 1205–1235. <https://doi.org/10.1038/aps.2017.28>.
- (76) Rao, C. V.; Asch, A. S.; Carr, D. J. J.; Yamada, H. Y. “Amyloid-Beta Accumulation Cycle” as a Prevention and/or Therapy Target for Alzheimer’s Disease. *Aging Cell.* **2020**, *19* (3). <https://doi.org/10.1111/accel.13109>.
- (77) Brown, M. R.; Radford, S. E.; Hewitt, E. W. Modulation of β -Amyloid Fibril Formation in Alzheimer’s Disease by Microglia and Infection. *Front. Mol. Neurosci.* **2020**, *13* (609073), 1–16. <https://doi.org/10.3389/fnmol.2020.609073>.
- (78) Rao, P. P. N.; Mohamed, T.; Teckwani, K.; Tin, G. Curcumin Binding to Beta Amyloid: A Computational Study. *Chem. Biol. Drug Des.* **2012**, *86* (4), 813–820.
<https://doi.org/10.1111/cbdd.12552>.
- (79) Zhang, N.; Yan, C.; Yin, C.; Hu, X.; Guan, P.; Cheng, Y. Structural Remodeling Mechanism of the Toxic Amyloid Fibrillary Mediated by Epigallocatechin-3-Gallate. *ACS Omega.* **2022**, *7* (51), 48047–48058. <https://doi.org/10.1021/acsomega.2c05995>.
- (80) Huang, Y. R.; Liu, R. T. The Toxicity and Polymorphism of β -Amyloid Oligomers. *Int. J. Mol. Sci.* **2020**, *21* (12), 1–19. <https://doi.org/10.3390/ijms21124477>.

- (81) Wei, W.; Nguyen, L. N.; Kessels, H. W.; Hagiwara, H.; Sisodia, S.; Malinow, R. Amyloid Beta from Axons and Dendrites Reduces Local Spine Number and Plasticity. *Nat. Neurosci.* **2010**, *13* (2), 190–196. <https://doi.org/10.1038/nn.2476>.
- (82) Müller, M. K.; Jacobi, E.; Sakimura, K.; Malinow, R.; von Engelhardt, J. NMDA Receptors Mediate Synaptic Depression, but Not Spine Loss in the Dentate Gyrus of Adult Amyloid Beta (A β) Overexpressing Mice. *Acta Neuropathol. Commun.* **2018**, *6* (110), 1–20. <https://doi.org/10.1186/s40478-018-0611-4>.
- (83) Yamamoto, N.; Matsubara, E.; Maeda, S.; Minagawa, H.; Takashima, A.; Maruyama, W.; Michikawa, M.; Yanagisawa, K. A Ganglioside-Induced Toxic Soluble A β Assembly: Its Enhanced Formation from A β Bearing the Arctic Mutation. *J. Biol. Chem.* **2007**, *282* (4), 2646–2655. <https://doi.org/10.1074/jbc.M606202200>.
- (84) Yanagisawa, K. Role of Gangliosides in Alzheimer’s Disease. *Biochim. Biophys. Acta - Biomembr.* **2007**, *1768* (8), 1943–1951. <https://doi.org/10.1016/j.bbamem.2007.01.018>.
- (85) Caesar, I.; Jonson, M.; Peter Nilsson, K. R.; Thor, S.; Hammarström, P. Curcumin Promotes A-Beta Fibrillation and Reduces Neurotoxicity in Transgenic Drosophila. *PLoS One.* **2012**, *7* (2), e31424. <https://doi.org/10.1371/journal.pone.0031424>.
- (86) Inoue, S.; Kisilevsky, R. Beta-Amyloid Fibrils of Alzheimer’s Disease: Pathologically Altered, Basement Membrane-Associated Microfibrils? *Ital. J. Anat. Embryol.* **2001**, *106* (2), 93–102.
- (87) Kuhn, J.; Sharman, T. Cerebral Amyloid Angiopathy <https://www.ncbi.nlm.nih.gov/books/NBK556105/> (accessed 2023-02-20).

- (88) Behl, T.; Kaur, D.; Sehgal, A.; Singh, S.; Sharma, N.; Zengin, G.; Andronie-Cioara, F. L.; Toma, M. M.; Bungau, S.; Bumbu, A. G. Role of Monoamine Oxidase Activity in Alzheimer's Disease: An Insight into the Therapeutic Potential of Inhibitors. *Molecules*. **2021**, *26* (12), 1–21. <https://doi.org/10.3390/molecules26123724>.
- (89) Bhatt, S.; Puli, L.; Patil, C. R. Role of Reactive Oxygen Species in the Progression of Alzheimer's Disease. *Drug Discov. Today*. **2021**, *26* (3), 794–803. <https://doi.org/10.1016/j.drudis.2020.12.004>.
- (90) Kinney, J. W.; Bemiller, S. M.; Murtishaw, A. S.; Leisgang, A. M.; Salazar, A. M.; Lamb, B. T. Inflammation as a Central Mechanism in Alzheimer's Disease. *Alzheimer's Dement. Transl. Res. Clin. Interv.* **2018**, *4* (1), 575–590. <https://doi.org/10.1016/j.trci.2018.06.014>.
- (91) Perkovic, M. N.; Pivac, N. Genetic Markers of Alzheimer's Disease. In *Frontiers in Psychiatry, Advances in Experimental Medicine and Biology*; Yong-Ku, K., Ed.; Springer, Singapore: Bijenicka, 2019; Vol. 1192, pp 27–52. https://doi.org/10.1007/978-981-32-9721-0_25.
- (92) De La Monte, S. M.; Wands, J. R. Alzheimer's Disease Is Type 3 Diabetes—Evidence Reviewed. *J. Diabetes Sci. Technol.* **2008**, *2* (6), 1101–1113. <https://doi.org/10.1177/193229680800200619>.
- (93) Kivipelto, M.; Mangialasche, F.; Ngandu, T. Lifestyle Interventions to Prevent Cognitive Impairment, Dementia and Alzheimer Disease. *Nat. Rev. Neurol.* **2018**, *14* (11), 653–666. <https://doi.org/10.1038/s41582-018-0070-3>.
- (94) Deckers, K.; Van Boxtel, M. P. J.; Schiepers, O. J. G.; De Vugt, M.; Sánchez, J. L. M.; Anstey, K. J.; Brayne, C.; Dartigues, J. F.; Engedal, K.; Kivipelto, M.; Ritchie, K.; Starr,

- J. M.; Yaffe, K.; Irving, K.; Verhey, F. R. J.; Köhler, S. Target Risk Factors for Dementia Prevention: A Systematic Review and Delphi Consensus Study on the Evidence from Observational Studies. *Int. J. Geriatr. Psychiatry* **2015**, *30* (3), 234–246.
<https://doi.org/10.1002/gps.4245>.
- (95) Mendez, M. F. Early-Onset Alzheimer’s Disease: Nonamnestic Subtypes and Type 2 AD. *Arch. Med. Res.* **2012**, *43* (8), 677–685. <https://doi.org/10.1016/j.arcmed.2012.11.009>.
- (96) Serrano-Pozo, A.; Das, S.; Hyman, B. T. APOE and Alzheimer’s Disease: Advances in Genetics, Pathophysiology, and Therapeutic Approaches. *Lancet Neurol.* **2021**, *20* (1), 68–80. [https://doi.org/10.1016/S1474-4422\(20\)30412-9](https://doi.org/10.1016/S1474-4422(20)30412-9).
- (97) McDade, E.; Cummings, J. L.; Dhadda, S.; Swanson, C. J.; Reyderman, L.; Kanekiyo, M.; Koyama, A.; Irizarry, M.; Kramer, L. D.; Bateman, R. J. Lecanemab in Patients with Early Alzheimer’s Disease: Detailed Results on Biomarker, Cognitive, and Clinical Effects from the Randomized and Open-Label Extension of the Phase 2 Proof-of-Concept Study. *Alzheimer’s Res. Ther.* **2022**, *14* (1), 1–17. <https://doi.org/10.1186/s13195-022-01124-2>.
- (98) Dhillon, S. Aducanumab: First Approval. *Drugs.* **2021**, *81* (12), 1437–1443.
<https://doi.org/10.1007/s40265-021-01569-z>.
- (99) ClinicalTrials.gov. A Study to Evaluate Safety and Tolerability of Aducanumab in Participants With Alzheimer’s Disease Who Had Previously Participated in the Aducanumab Studies 221AD103, 221AD301, 221AD302 and 221AD205 2020.
<https://clinicaltrials.gov/ct2/show/NCT04241068> (accessed 2023-02-28).
- (100) Dunn, B.; Stein, P.; Cavazzoni, P. Approval of Aducanumab for Alzheimer’s Disease - The FDA’s Perspective. *JAMA Intern. Med.* **2021**, *181* (10), 1276–1278.

<https://doi.org/doi:10.1001/jamainternmed.2021.4607>.

- (101) Clinicaltrials.gov. A Study to Evaluate Safety, Tolerability, and Efficacy of Lecanemab in Subjects With Early Alzheimer's Disease
<https://clinicaltrials.gov/ct2/show/results/NCT01767311> (accessed 2023-02-28).
- (102) Knowles, J. Donepezil in Alzheimer's Disease: An Evidence-Based Review of Its Impact on Clinical and Economic Outcomes. *Core Evid.* **2006**, *1* (3), 195–219.
- (103) Camps, P.; Formosa, X.; Galdeano, C.; Gómez, T.; Muñoz-Torrero, D.; Scarpellini, M.; Viayna, E.; Badia, A.; Clos, M. V.; Camins, A.; Pallàs, M.; Bartolini, M.; Mancini, F.; Andrisano, V.; Estelrich, J.; Lizondo, M.; Bidon-Chanal, A.; Luque, F. J. Novel Donepezil-Based Inhibitors of Acetyl- and Butyrylcholinesterase and Acetylcholinesterase-Induced β -Amyloid Aggregation. *J. Med. Chem.* **2008**, *51* (12), 3588–3598. <https://doi.org/10.1021/jm8001313>.
- (104) Geerts, H.; Guillaumat, P. O.; Grantham, C.; Bode, W.; Anciaux, K.; Sachak, S. Brain Levels and Acetylcholinesterase Inhibition with Galantamine and Donepezil in Rats, Mice, and Rabbits. *Brain Res.* **2005**, *1033* (2), 186–193.
<https://doi.org/10.1016/J.BRAINRES.2004.11.042>.
- (105) Sharma, K. Cholinesterase Inhibitors as Alzheimer's Therapeutics (Review). *Mol. Med. Rep.* **2019**, *20* (2), 1479–1487. <https://doi.org/10.3892/mmr.2019.10374>.
- (106) Rogawski, M. A.; Wenk, G. L. The Neuropharmacological Basis for the Use of Memantine in the Treatment of Alzheimer's Disease. *CNS Drug Rev.* **2006**, *9* (3), 275–308. <https://doi.org/10.1111/j.1527-3458.2003.tb00254.x>.

- (107) Kuns, B.; Rosani, A.; Varghese, D. Memantine.
<https://www.ncbi.nlm.nih.gov/books/NBK500025/> (accessed 2023-06-04).
- (108) Blanco-Silvente, L.; Capellà, D.; Garre-Olmo, J.; Vilalta-Franch, J.; Castells, X. Predictors of Discontinuation, Efficacy, and Safety of Memantine Treatment for Alzheimer's Disease: Meta-Analysis and Meta-Regression of 18 Randomized Clinical Trials Involving 5004 Patients. *BMC Geriatr.* **2018**, *18* (1), 1–16.
<https://doi.org/10.1186/s12877-018-0857-5>.
- (109) Aloisi, A.; Barca, A.; Romano, A.; Guerrieri, S.; Storelli, C.; Rinaldi, R.; Verri, T. Anti-Aggregating Effect of the Naturally Occurring Dipeptide Carnosine on A β 1-42 Fibril Formation. *PLoS One.* **2013**, *8* (7), e68159. <https://doi.org/10.1371/journal.pone.0068159>.
- (110) Okuda, M.; Hijikuro, I.; Fujita, Y.; Teruya, T.; Kawakami, H.; Takahashi, T.; Sugimoto, H. Design and Synthesis of Curcumin Derivatives as Tau and Amyloid β Dual Aggregation Inhibitors. *Bioorg. Med. Chem. Lett.* **2016**, *26* (20), 5024–5028.
<https://doi.org/10.1016/j.bmcl.2016.08.092>.
- (111) Safura, J.; Saeedeh, K.; Xaniar, E. G.; Mona, K.; Behnam, Y.; Mohammad, S.; Davood, B.; Omid, B. Alzheimer's Disease: Drug Discovery. In *Alzheimer's Disease: Drug Discovery*; X, H., Ed.; Brisbane (AU): Exon Publications: Brisbane, 2020; pp 51–68.
<https://doi.org/10.36255/exonpublications.alzheimersdisease.2020>.
- (112) Tahami Monfared, A. A.; Tafazzoli, A.; Ye, W.; Chavan, A.; Zhang, Q. Long-Term Health Outcomes of Lecanemab in Patients with Early Alzheimer's Disease Using Simulation Modeling. *Neurol. Ther.* **2022**, *11* (2), 863–880.
<https://doi.org/10.1007/s40120-022-00350-y>.

- (113) Beshir, S. A.; Aadithsoorya, A. M.; Parveen, A.; Goh, S. S. L.; Hussain, N.; Menon, V. B. Aducanumab Therapy to Treat Alzheimer's Disease: A Narrative Review. *Int. J. Alzheimers. Dis.* **2022**, 2022 (2090), 1–10. <https://doi.org/10.1155/2022/9343514>.
- (114) Derosa, G.; Maffioli, P.; Sahebkar, A. Piperine and Its Role in Chronic Diseases. In *Anti-inflammatory Nutraceuticals and Chronic Diseases*; Cohen, I. R., Lajtha, N. S. A., Paoletti, R., Lambris, J. D., Eds.; Springer International Publishing Switzerland: Cham, 2016; pp 173–184. https://doi.org/DOI.10.1007/978-3-319-41334-1_8.
- (115) Tiwari, A.; Mahadik, K. R.; Gabhe, S. Y. Piperine: A Comprehensive Review of Methods of Isolation, Purification, and Biological Properties. *Med. Drug Discov.* **2020**, 7 (100027), 1–21. <https://doi.org/10.1016/j.medidd.2020.100027>.
- (116) Ng, Y. P.; Or, T. C. T.; Ip, N. Y. Plant Alkaloids as Drug Leads for Alzheimer's Disease. *Neurochem. Int.* **2015**, 89 (2015), 260–270. <https://doi.org/10.1016/j.neuint.2015.07.018>.
- (117) Ain, Q.-U.-; Khan, H.; Mubarak, M. S.; Pervaiz, A. Plant Alkaloids as Antiplatelet Agent: Drugs of the Future in the Light of Recent Developments. *Front. Pharmacol.* **2016**, 7 (292), 1–9. <https://doi.org/10.3389/fphar.2016.00292>.
- (118) Cui, T.; Wang, Q.; Tian, X.; Zhang, K.; Peng, Y.; Zheng, J. Piperine Is a Mechanism-Based Inactivator of CYP3A S. *Drug Metab. Dispos.* **2020**, 48 (2), 123–134. <https://doi.org/10.1124/DMD.119.088955>.
- (119) Manap, A. S. A.; Tan, A. C. W.; Leong, W. H.; Chia, A. Y. Y.; Vijayabalan, S.; Arya, A.; Wong, E. H.; Rizwan, F.; Bindal, U.; Koshy, S.; Madhavan, P. Synergistic Effects of Curcumin and Piperine as Potent Acetylcholine and Amyloidogenic Inhibitors with Significant Neuroprotective Activity in SH-SY5Y Cells via Computational Molecular

- Modeling and in Vitro Assay. *Front. Aging Neurosci.* **2019**, *11* (206), 1–17.
<https://doi.org/10.3389/fnagi.2019.00206>.
- (120) Aswathy, L.; Jisha, R. S.; Masand, V. H.; Jayant, .; Gajbhiye, M.; Shibi, I. G. Design of Novel Amyloid β Aggregation Inhibitors Using QSAR, Pharmacophore Modeling, Molecular Docking and ADME Prediction. *Silico Pharmacol.* **2018**, *6* (12), 1–19.
<https://doi.org/10.1007/s40203-018-0049-1>.
- (121) Schöffmann, A.; Wimmer, L.; Goldmann, D.; Khom, S.; Hintersteiner, J.; Baburin, I.; Schwarz, T.; Hintersteininger, M.; Pakfeifer, P.; Oufir, M.; Hamburger, M.; Erker, T.; Ecker, G. F.; Mihovilovic, M. D.; Hering, S. Efficient Modulation of γ -Aminobutyric Acid Type a Receptors by Piperine Derivatives. *J. Med. Chem.* **2014**, *57* (13), 5602–5619.
<https://doi.org/10.1021/jm5002277>.
- (122) Zanger, U. M.; Schwab, M. Cytochrome P450 Enzymes in Drug Metabolism: Regulation of Gene Expression, Enzyme Activities, and Impact of Genetic Variation. *Pharmacol. Ther.* **2013**, *138* (1), 103–141. <https://doi.org/10.1016/j.pharmthera.2012.12.007>.
- (123) Ren, T.; Wang, Q.; Li, C.; Yang, M.; Zuo, Z. Efficient Brain Uptake of Piperine and Its Pharmacokinetics Characterization after Oral Administration. *Xenobiotica.* **2018**, *48* (12), 1249–1257. <https://doi.org/10.1080/00498254.2017.1405293>.
- (124) Chonpathompikunlert, P.; Wattanathorn, J.; Muchimapura, S. Piperine, the Main Alkaloid of Thai Black Pepper, Protects against Neurodegeneration and Cognitive Impairment in Animal Model of Cognitive Deficit like Condition of Alzheimer's Disease. *Food Chem. Toxicol.* **2010**, *48* (3), 798–802. <https://doi.org/10.1016/J.FCT.2009.12.009>.
- (125) Yang, X.; Zhi, J.; Leng, H.; Chen, Y.; Gao, H.; Ma, J.; Ji, J.; Hu, Q. The Piperine

- Derivative HJ105 Inhibits A β 1–42-Induced Neuroinflammation and Oxidative Damage via the Keap1-Nrf2-TXNIP Axis. *Phytomedicine*. **2021**, *87* (153571), 1–10.
<https://doi.org/10.1016/j.phymed.2021.153571>.
- (126) Edwards, G. A.; Gamez, N.; Escobedo, G.; Calderon, O.; Moreno-Gonzalez, I. Modifiable Risk Factors for Alzheimer’s Disease. *Front. Aging Neurosci.* **2019**, *11* (146), 1–18.
<https://doi.org/10.3389/fnagi.2019.00146>.
- (127) Wang, C.; Cai, Z.; Wang, W.; Wei, M.; Kou, D.; Li, T.; Yang, Z.; Guo, H.; Le, W.; Li, S. Piperine Attenuates Cognitive Impairment in an Experimental Mouse Model of Sporadic Alzheimer’s Disease. *J. Nutr. Biochem.* **2019**, *70* (2019), 147–155.
<https://doi.org/10.1016/j.jnutbio.2019.05.009>.
- (128) Lipinski, C. A.; Lombardo, F.; Dominy, B. W.; Feeney, P. J. Experimental and Computational Approaches to Estimate Solubility and Permeability in Drug Discovery and Development Settings. *Adv. Drug Deliv. Rev.* **2012**, *64* (2012), 4–17.
<https://doi.org/10.1016/J.ADDR.2012.09.019>.
- (129) Pardridge, W. M. Drug Transport across the Blood-Brain Barrier. *J. Cereb. Blood Flow Metab.* **2012**, *32* (11), 1959–1972. <https://doi.org/10.1038/jcbfm.2012.126>.
- (130) Pajouhesh, H.; Lenz, G. R. Medicinal Chemical Properties of Successful Central Nervous System Drugs. *NeuroRX*. **2005**, *2* (4), 541–553.
<https://doi.org/https://doi.org/10.1602/neurorx.2.4.541>.
- (131) Levin, V. A. Relationship of Octanol/Water Partition Coefficient and Molecular Weight to Rat Brain Capillary Permeability. *J. Med. Chem.* **1980**, *23* (6), 682–684.
<https://doi.org/10.1021/jm00180a022>.

- (132) Hitchcock, S. A.; Pennington, L. D. Structure–Brain Exposure Relationships. *J. Med. Chem.* **2006**, *49* (26), 7559–7583. <https://doi.org/10.1021/jm060642i>.
- (133) Colvin, M. T.; Silvers, R.; Ni, Q. Z.; Can, T. V.; Sergeyev, I.; Rosay, M.; Donovan, K. J.; Michael, B.; Wall, J.; Linse, S.; Griffin, R. G. Atomic Resolution Structure of Monomorphic A β 42 Amyloid Fibrils. *J. Am. Chem. Soc.* **2016**, *138* (30), 9663–9674. <https://doi.org/10.1021/jacs.6b05129>.
- (134) Siódmiak, J.; Beldowski, P.; Augé, W. K.; Ledziński, D.; Śmigiel, S.; Gadomski, A. Molecular Dynamic Analysis of Hyaluronic Acid and Phospholipid Interaction in Tribological Surgical Adjuvant Design for Osteoarthritis. *Molecules.* **2017**, *22* (9). <https://doi.org/10.3390/molecules22091436>.
- (135) Takao, K.; Miyashiro, T.; Sugita, Y. Synthesis and Biological Evaluation of Piperic Acid Amides as Free Radical Scavengers and α -Glucosidase Inhibitors. *Chem. Pharm. Bull. (Tokyo).* **2015**, *63* (5), 326–333. <https://doi.org/10.1248/cpb.c14-00874>.
- (136) Tian, X.; Zhou, M.; Ning, J.; Deng, X.; Feng, L.; Huang, H.; Yao, D.; Ma, X. The Development of Novel Cytochrome P450 2J2 (CYP2J2) Inhibitor and the Underlying Interaction between Inhibitor and CYP2J2. *J. Enzyme Inhib. Med. Chem.* **2021**, *36* (1), 737–748. <https://doi.org/10.1080/14756366.2021.1896500>.
- (137) Shiina, I.; Umezaki, Y.; Murata, T.; Suzuki, K.; Tono, T. Asymmetric Total Synthesis of (+)-Coprophilin. *Synth.* **2018**, *50* (6), 1301–1306. <https://doi.org/10.1055/s-0036-1591866>.
- (138) Bauer, A.; Nam, J. H.; Maulide, N. A Short, Efficient, and Stereoselective Synthesis of Piperine and Its Analogues. *Synlett.* **2019**, *30* (4), 413–416. <https://doi.org/10.1055/s-0037-1611652>.

- (139) Tian, M.; Tian, Z.; Yao, D.; Ning, J.; Deng, S.; Feng, L.; Huo, X.; Tian, X.; Zhang, B.; Wang, C.; Yu, Z.; Ma, X. A NIR Fluorescent Probe for Fatty Acid Amide Hydrolase Bioimaging and Its Application in Development of Inhibitors. *J. Mater. Chem. B*. **2021**, *9* (32), 6460–6465. <https://doi.org/10.1039/d1tb01054a>.
- (140) Hammad, A. S.; Ravindran, S.; Khalil, A.; Munusamy, S. Structure–Activity Relationship of Piperine and Its Synthetic Amide Analogs for Therapeutic Potential to Prevent Experimentally Induced ER Stress in Vitro. *Cell Stress Chaperones*. **2017**, *22* (3), 417–428. <https://doi.org/10.1007/s12192-017-0786-9>.
- (141) Montalbetti, C. A. G. N.; Falque, V. Amide Bond Formation and Peptide Coupling. *Tetrahedron*. **2005**, *61* (46), 10827–10852. <https://doi.org/10.1016/j.tet.2005.08.031>.
- (142) Bhattacharya, A. K.; Thyagarajan, G. The Michaelis-Arbuzov Rearrangement. *Chem. Rev.* **1981**, *81* (4), 415–430. <https://doi.org/https://doi.org/10.1021/cr00044a004>.
- (143) Kobayashi, K.; Tanaka, K.; Kogen, H. Recent Topics of the Natural Product Synthesis by Horner–Wadsworth–Emmons Reaction. *Tetrahedron Lett.* **2018**, *59* (7), 568–582. <https://doi.org/10.1016/J.TETLET.2017.12.076>.
- (144) Mohammadkhani, L.; Heravi, M. M. Oxalyl Chloride: A Versatile Reagent in Organic Transformations. *ChemistrySelect*. **2019**, *4* (20), 6309–6337. <https://doi.org/10.1002/slct.201900120>.
- (145) Wade, L. *Organic Chemistry*, 8th ed.; Pearson, 2006.
- (146) Tian, M.; Tian, Z.; Yao, D.; Ning, J.; Deng, S.; Feng, L.; Huo, X.; Tian, X.; Zhang, B.; Wang, C.; Yu, Z.; Ma, X. Supplementary Information: A NIR Fluorescent Probe for Fatty

- Acid Amide Hydrolase Bioimaging and Its Application in Development of Inhibitors. *J. Mater. Chem. B.* **2021**, *9* (32), 6460–6465. <https://doi.org/10.1039/d1tb01054a>.
- (147) Nargotra, A.; Sharma, S.; Koul, J. L.; Sangwan, P. L.; Khan, I. A.; Kumar, A.; Taneja, S. C.; Koul, S. Quantitative Structure Activity Relationship (QSAR) of Piperine Analogs for Bacterial NorA Efflux Pump Inhibitors. *Eur. J. Med. Chem.* **2009**, *44* (10), 4128–4135. <https://doi.org/10.1016/j.ejmech.2009.05.004>.
- (148) El Shatshat, A.; Pham, A. T.; Rao, P. P. N. Interactions of Polyunsaturated Fatty Acids with Amyloid Peptides A β 40 and A β 42. *Arch. Biochem. Biophys.* **2019**, *663* (2019), 34–43. <https://doi.org/10.1016/j.abb.2018.12.027>.
- (149) Levine, H. Thioflavine T Interaction with Synthetic Alzheimer's Disease β -Amyloid Peptides: Detection of Amyloid Aggregation in Solution. *Protein Sci.* **1993**, *2* (3), 404–410.
- (150) Xue, C.; Lin, T. Y.; Chang, D.; Guo, Z. Thioflavin T as an Amyloid Dye: Fibril Quantification, Optimal Concentration and Effect on Aggregation. *R. Soc. Open Sci.* **2017**, *4* (1), 1–12. <https://doi.org/10.1098/rsos.160696>.
- (151) Von Ardenne, M.; Hawkes, P.; Mulvey, T. On the History of Scanning Electron Microscopy, of the Electron Microprobe, and of Early Contributions to Transmission Electron Microscopy. In *Advances in Imagine and Electron Physics*; Elsevier: Amsterdam, 2021; pp 25–50. <https://doi.org/10.1016/bs.aiep.2021.08.002>.
- (152) Paredes, A. M. *Microscopy: Transmission Electron Microscopy*, Second Edi.; Elsevier, 2014; Vol. 2. <https://doi.org/10.1016/B978-0-12-384730-0.00216-0>.

- (153) Jinschek, J. R.; Helveg, S. Image Resolution and Sensitivity in an Environmental Transmission Electron Microscope. *Micron*. **2012**, *43* (11), 1156–1168.
<https://doi.org/10.1016/j.micron.2012.01.006>.
- (154) Wu, G.; Robertson, D. H.; Brooks, C. L.; Vieth, M. Detailed Analysis of Grid-Based Molecular Docking: A Case Study of CDOCKER - A CHARMM-Based MD Docking Algorithm. *J. Comput. Chem.* **2003**, *24* (13), 1549–1562.
<https://doi.org/10.1002/jcc.10306>.
- (155) Paravastu, A. K.; Leapman, R. D.; Yau, W.-M.; Tycko, R. Molecular Structural Basis for Polymorphism in Alzheimer's β -Amyloid Fibrils. *Proc. Natl. Acad. Sci.* **2008**, *105* (47), 18349–18354. <https://doi.org/10.1073/pnas.0806270105>.
- (156) Rao, P. P. N.; Du, D. In Silico Strategies to Design Small Molecules to Study Beta-Amyloid Aggregation. In *Computational Modeling of Drugs Against Alzheimer's Disease, Neuromethods*; Roy, K., Ed.; Humana Press Inc.: New York, NY, 2018; pp 249–261.
https://doi.org/https://doi.org/10.1007/978-1-4939-7404-7_10.
- (157) Deng, Y.; Roux, B. Computations of Standard Binding Free Energies with Molecular Dynamics Simulations. *J. Phys. Chem. B* **2009**, *113* (8), 2234–2246.
<https://doi.org/10.1021/jp807701h>.
- (158) Sevigny, J.; Chiao, P.; Bussière, T.; Weinreb, P. H.; Williams, L.; Maier, M.; Dunstan, R.; Salloway, S.; Chen, T.; Ling, Y.; O'Gorman, J.; Qian, F.; Arastu, M.; Li, M.; Chollate, S.; Brennan, M. S.; Quintero-Monzon, O.; Scannevin, R. H.; Arnold, H. M.; Engber, T.; Rhodes, K.; Ferrero, J.; Hang, Y.; Mikulskis, A.; Grimm, J.; Hock, C.; Nitsch, R. M.; Sandrock, A. The Antibody Aducanumab Reduces A β Plaques in Alzheimer's Disease.

- Nature*. **2016**, 537 (7618), 50–56. <https://doi.org/10.1038/nature19323>.
- (159) Capetillo-Zarate, E.; Gracia, L.; Yu, F.; Banfelder, J. R.; Lin, M. T.; Tampellini, D.; Gouras, G. K. High-Resolution 3D Reconstruction Reveals Intra-Synaptic Amyloid Fibrils. *Am. J. Pathol.* **2011**, 179 (5), 2551–2558. <https://doi.org/10.1016/j.ajpath.2011.07.045>.
- (160) Kim, H. Y.; Kim, H. V.; Jo, S.; Lee, C. J.; Choi, S. Y.; Kim, D. J.; Kim, Y. EPPS Rescues Hippocampus-Dependent Cognitive Deficits in APP/PS1 Mice by Disaggregation of Amyloid- β Oligomers and Plaques. *Nat. Commun.* **2015**, 6 (8997), 1–12. <https://doi.org/10.1038/ncomms9997>.
- (161) Mosmann, T. Rapid Colorimetric Assay for Cellular Growth and Survival: Application to Proliferation and Cytotoxicity Assays. *J. Immunol. Methods.* **1983**, 65 (1–2), 55–63. [https://doi.org/10.1016/0022-1759\(83\)90303-4](https://doi.org/10.1016/0022-1759(83)90303-4).
- (162) Chamchoy, K.; Pakotiprapha, D.; Pumirat, P.; Leartsakulpanich, U.; Boonyuen, U. Application of WST-8 Based Colorimetric NAD(P)H Detection for Quantitative Dehydrogenase Assays. *BMC Biochem.* **2019**, 20 (4), 1–14. <https://doi.org/https://doi.org/10.1186/s12858-019-0108-1>.
- (163) Held, P. *An Absorbance-Based Cytotoxicity Assay Using High Absorptivity, Water-Soluble Tetrazolium Salts Cell*; Vermont, 2015.
- (164) Walsh, D. M.; Klyubin, I.; Fadeeva, J. V.; Cullen, W. K.; Anwyl, R.; Wolfe, M. S.; Rowan, M. J.; Selkoe, D. J. Naturally Secreted Oligomers of Amyloid β Protein Potently Inhibit Hippocampal Long-Term Potentiation in Vivo. *Nature*. **2002**, 416 (6880), 535–539. <https://doi.org/10.1038/416535a>.

- (165) Cong, L.; Dong, X.; Wang, Y.; Deng, Y.; Li, B.; Dai, R. On the Role of Synthesized Hydroxylated Chalcones as Dual Functional Amyloid- β Aggregation and Ferroptosis Inhibitors for Potential Treatment of Alzheimer's Disease. *Eur. J. Med. Chem.* **2019**, *166* (2019), 11–21. <https://doi.org/10.1016/J.EJMECH.2019.01.039>.
- (166) Schöffmann, A.; Wimmer, L.; Goldmann, D.; Khom, S.; Hintersteiner, J.; Baburin, I.; Schwarz, T.; Hintersteininger, M.; Pakfeifer, P.; Oufir, M.; Hamburger, M.; Erker, T.; Ecker, G. F.; Mihovilovic, M. D.; Hering, S. Efficient Modulation of γ -Aminobutyric Acid Type A Receptors by Piperine Derivatives. *J. Med. Chem.* **2014**, *57* (13), 5602–5619. <https://doi.org/10.1021/jm5002277>.
- (167) Wahab, A.; Sultana, A.; Khan, K. M.; Sherwani, S. K. .; Perveen, Z.; Taha, M.; Karim, A. Synthesis, Antimicrobial, Antioxidant and Nematicidal Activity of (2E,4E)-5-(Benzo[d][1,3]Dioxol-5yl)Penta-2,4-Dienamides. *J. Chem. Soc. Pakistan.* **2015**, *37* (5), 1008–1014.
- (168) Sangwan, P. L.; Koul, J. L.; Koul, S.; Reddy, M. V.; Thota, N.; Khan, I. A.; Kumar, A.; Kalia, N. P.; Qazi, G. N. Piperine Analogs as Potent Staphylococcus Aureus NorA Efflux Pump Inhibitors. *Bioorganic Med. Chem.* **2008**, *16* (22), 9847–9857. <https://doi.org/10.1016/j.bmc.2008.09.042>.
- (169) Fukui, M.; Song, J.-H.; Choi, J.; Choi, H. J.; Zhu, B. T. Mechanism of Glutamate-Induced Neurotoxicity in HT22 Mouse Hippocampal Cells. *Eur. J. Pharmacol.* **2009**, *617* (1–3), 1–11. <https://doi.org/10.1016/j.ejphar.2009.06.059>.
- (170) St. Jean, J.; Slavcev, R.; Rao, P. N. The Effects of Amyloid Beta Aggregation on Neuronal Transcription. *IBRO Neurosci. Rep.* **2023**, *14*, 375–379. <https://doi.org/10.1016/j.ibneur.2023.03.009>.

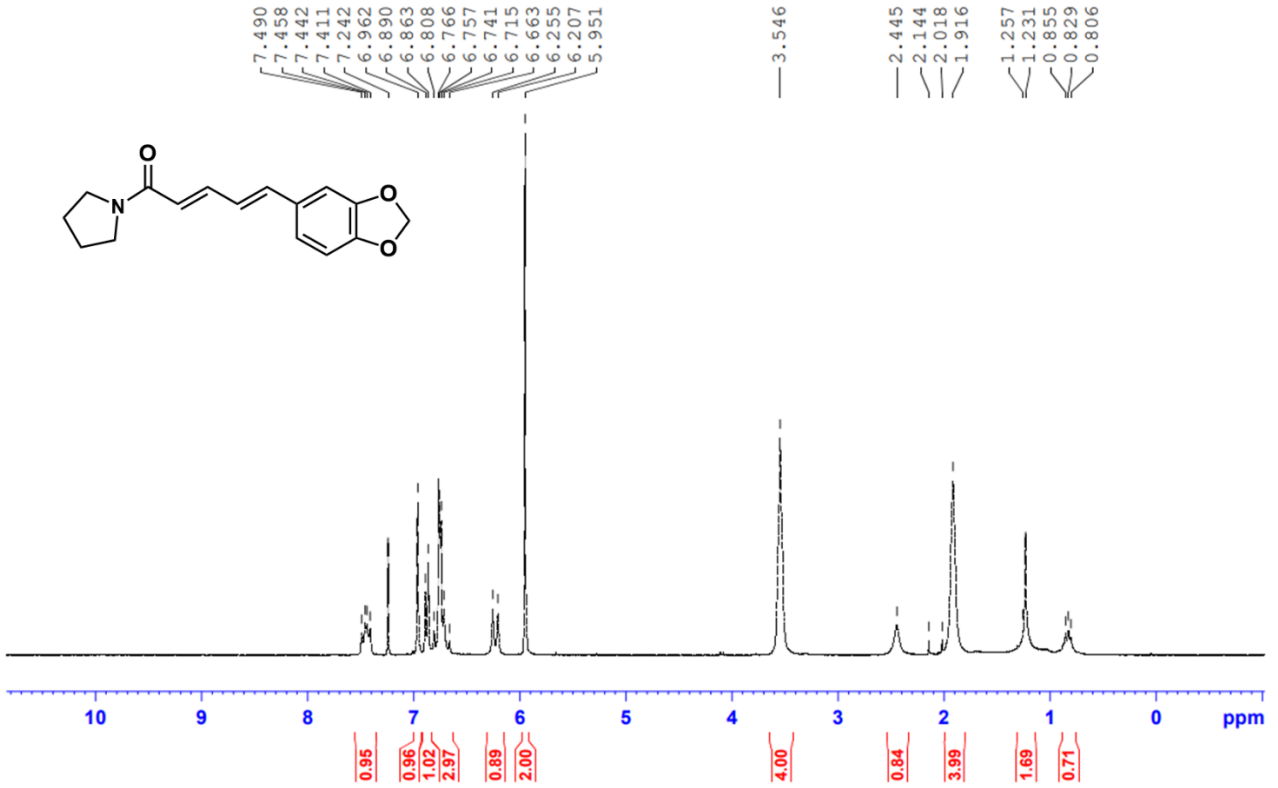
- (171) Seluanov, A.; Hine, C.; Azpurua, J.; Feigenson, M.; Bozzella, M.; Mao, Z.; Catania, K. C.; Gorbunova, V. Hypersensitivity to Contact Inhibition Provides a Clue to Cancer Resistance of Naked Mole-Rat. *Proc. Natl. Acad. Sci. U. S. A.* **2009**, *106* (46), 19352–19357. <https://doi.org/10.1073/pnas.0905252106>.
- (172) Abercrombie, M. Contact Inhibition and Malignancy. *Nature.* **1979**, *281* (5729), 259–262. <https://doi.org/10.1177/1461444810365020>.
- (173) Liu, S. How Cells Grow. In *Bioprocess Engineering*; Liu, S., Ed.; Elsevier: New York, 2017; pp 629–697. <https://doi.org/https://doi.org/10.1016/B978-0-444-63783-3.00011-3>.
- (174) Abcam. Counting cells using a hemocytometer. <https://www.abcam.com/protocols/counting-cells-using-a-hemocytometer#:~:text=To calculate the cell concentration,from the trypan blue addition.> (accessed 2023-04-22).
- (175) Lundholt, B. K.; Scudder, K. M.; Pagliaro, L. Technical Notes: A Simple Technique for Reducing Edge Effect in Cell-Based Assays. *SLAS Discov.* **2003**, *8* (5), 566–570. <https://doi.org/10.1177/1087057103256465>.

Appendix A

A1. NMR spectra for compounds 4a-m

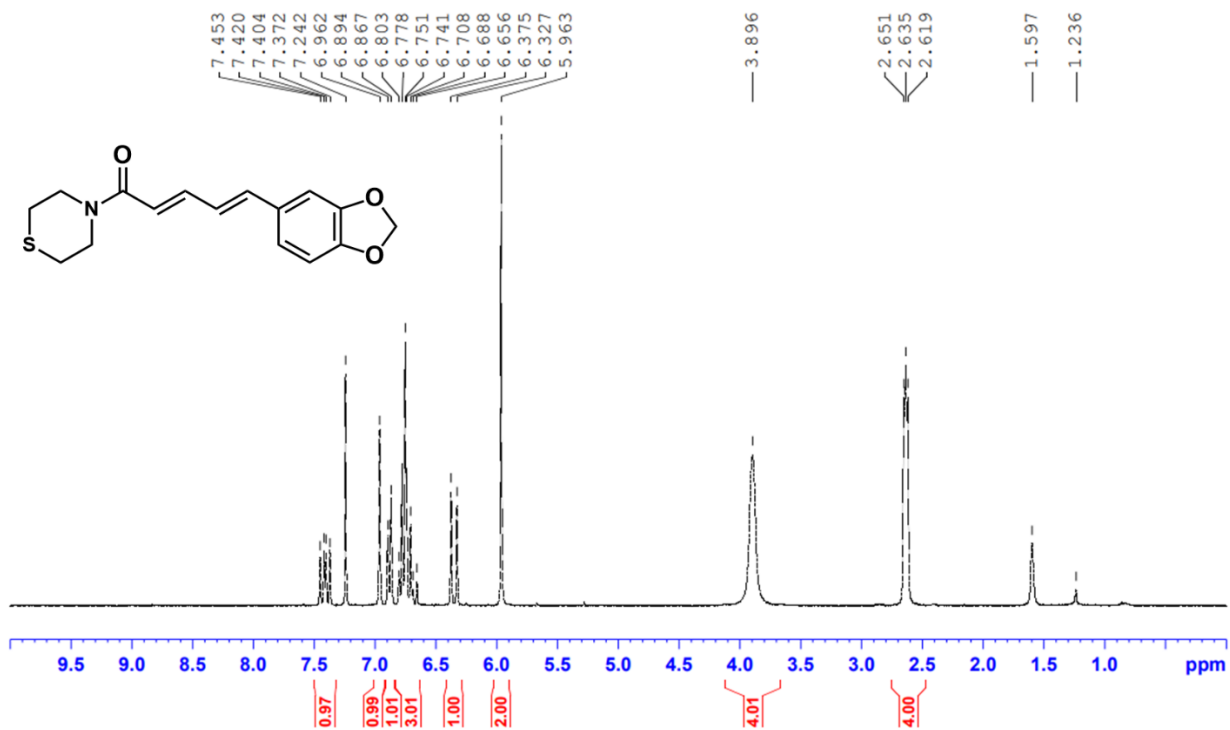
Piperyline (4a)

SW-03-03 F36-53 1H CDC13 300MHz July 20-2021
1d_proton CDC13 /opt/nmrdata nekkar 14



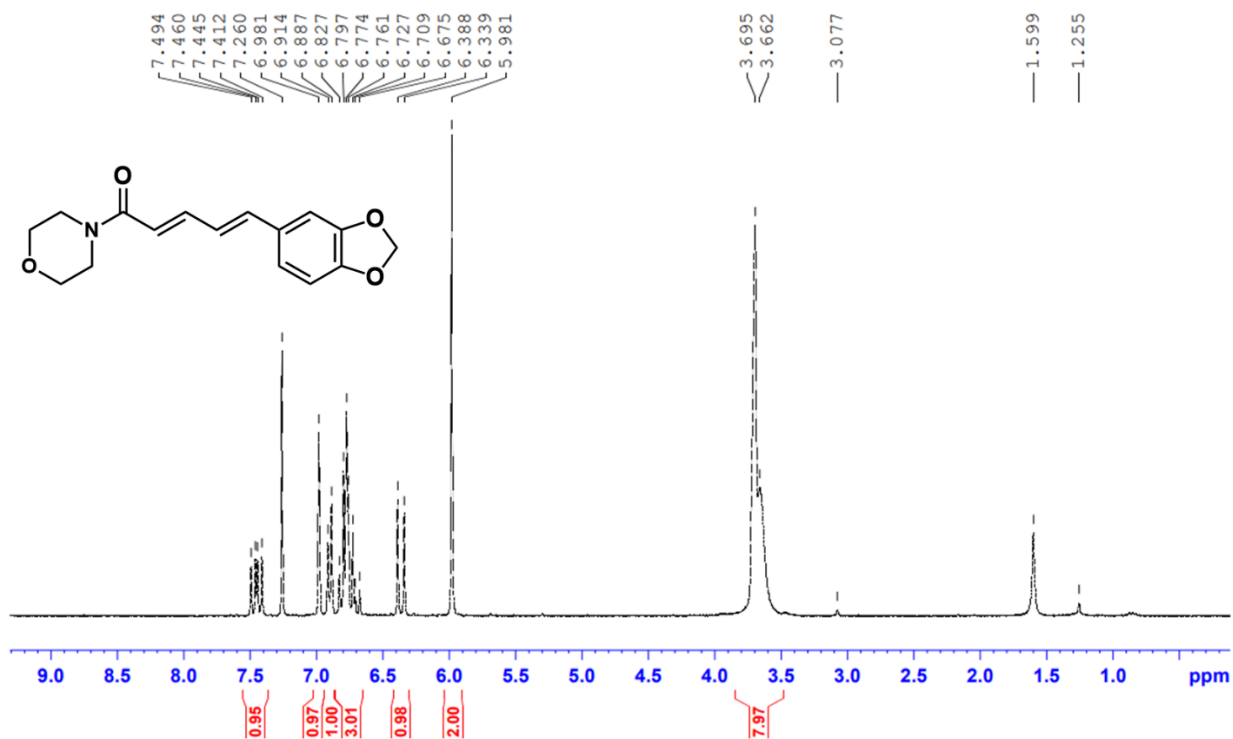
(2E,4E)-5-(Benzo[d][1,3]dioxol-5-yl)-1-thiomorpholinopenta-2,4-dien-1-one (4b)

Instrument 300B
1d_proton CDCl3 /opt/nmrdata nekkar 3
SW-04-03 F22-32 (Product) Aug-24-2021



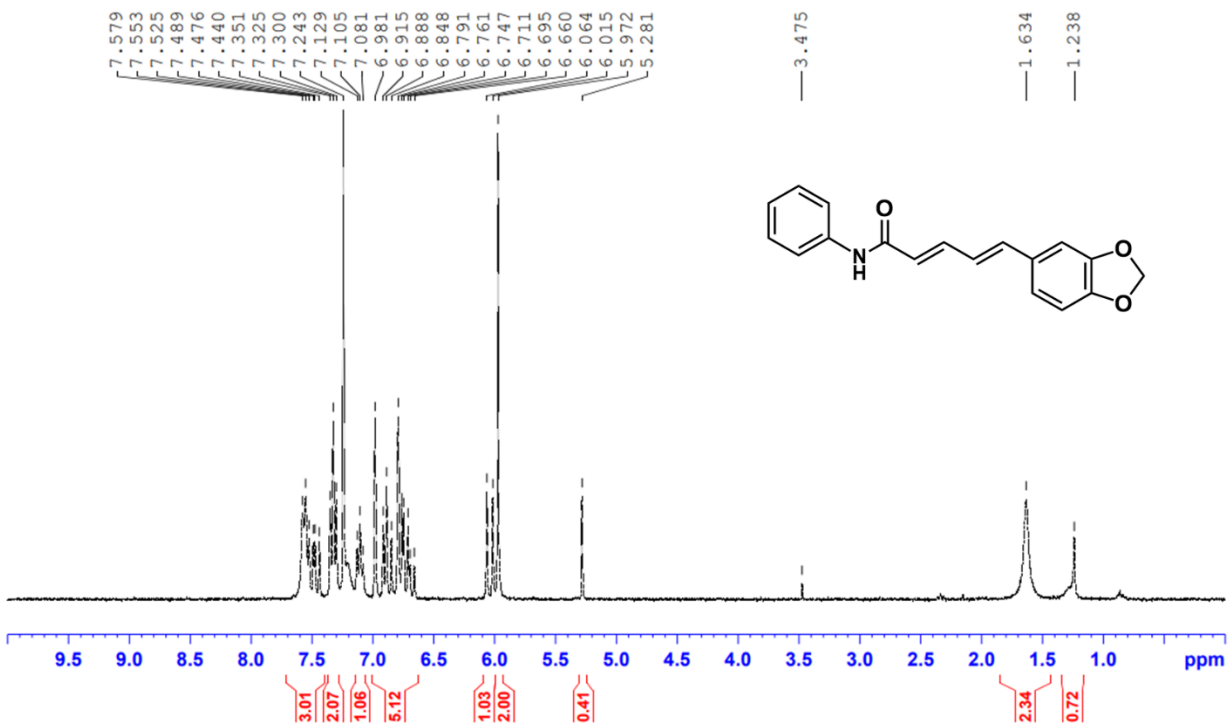
(2E,4E)-5-(Benzo[d][1,3]dioxol-5-yl)-1-morpholinopenta-2,4-dien-1-one (4c)

Instrument 300B
1d_proton CDC13 /opt/nmrdata nekkar 6
SW-05-02 F42-60 1H Aug-24-2021



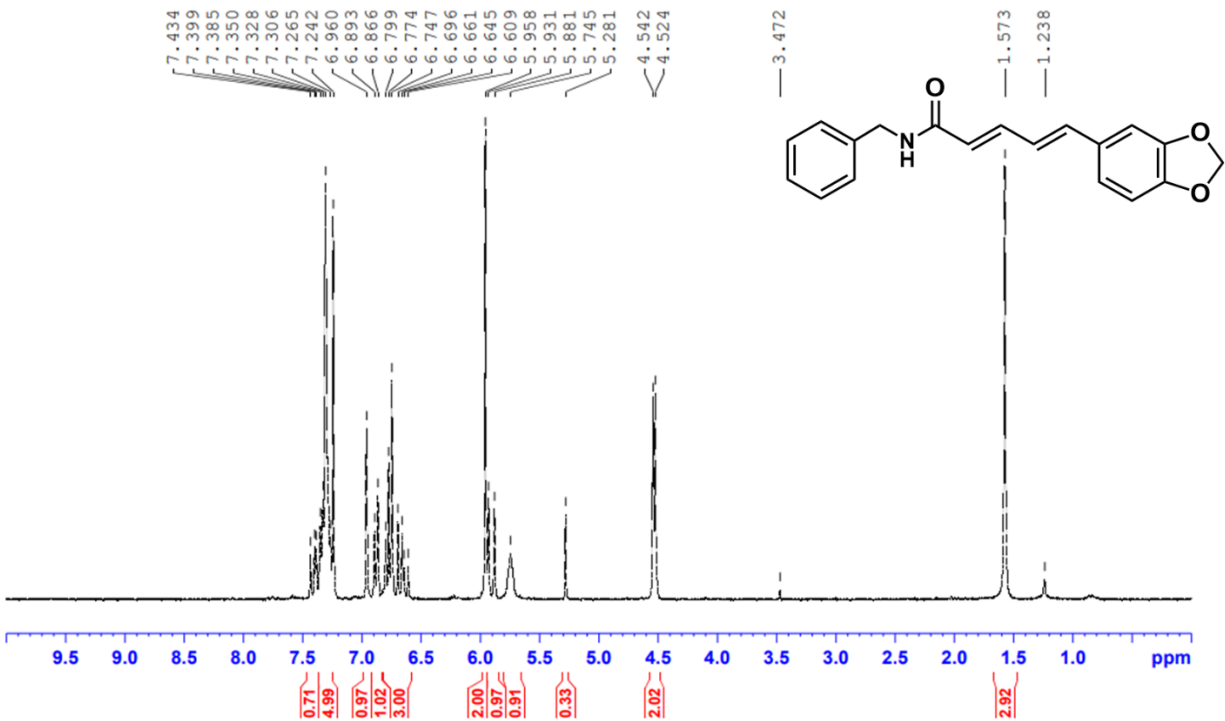
(2E,4E)-5-(Benzo[d][1,3]dioxol-5-yl)-N-phenylpenta-2,4-dienamide (4d)

Instrument 300B
1d_proton CDC13 /opt/nmrdata nekkar 4
SW-06-02 F14-17 1H CDC13



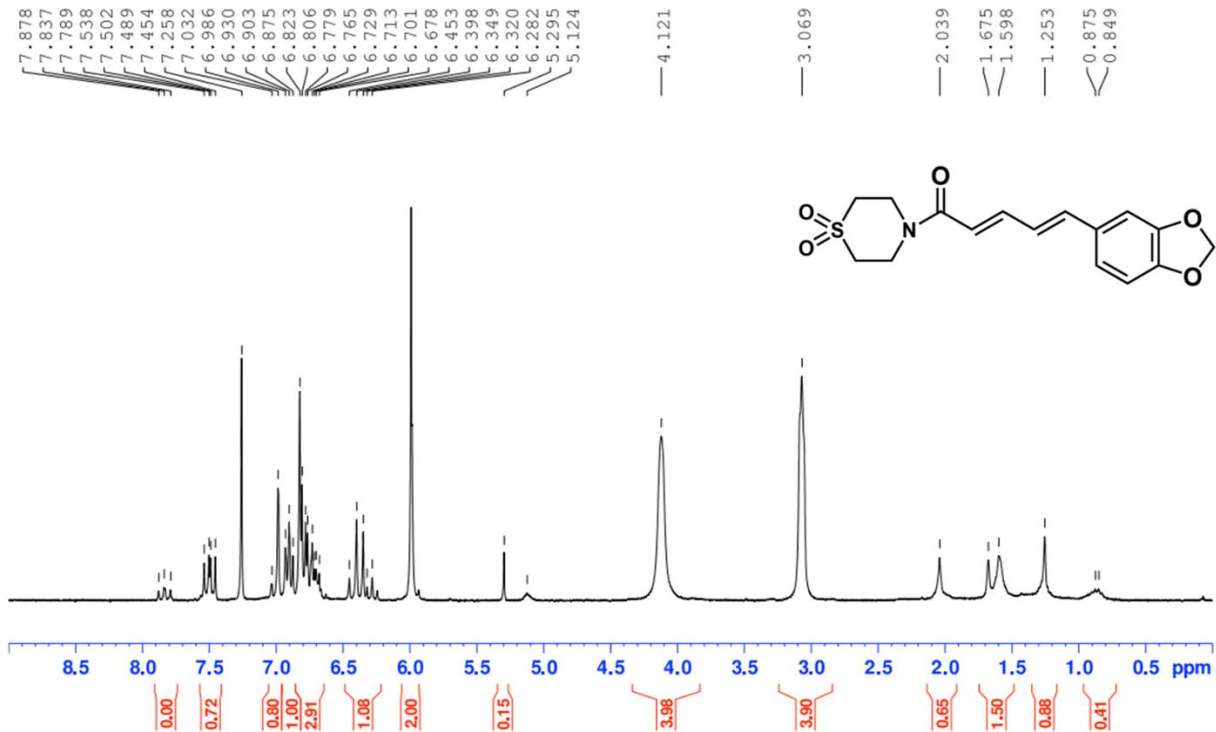
(2E,4E)-5-(Benzo[d][1,3]dioxol-5-yl)-N-benzylpenta-2,4-dienamide (4e)

Instrument 300B
1d_proton CDCl3 /opt/nmrdata nekkar 1
SW-08-01 F18-25 1H CDCl3



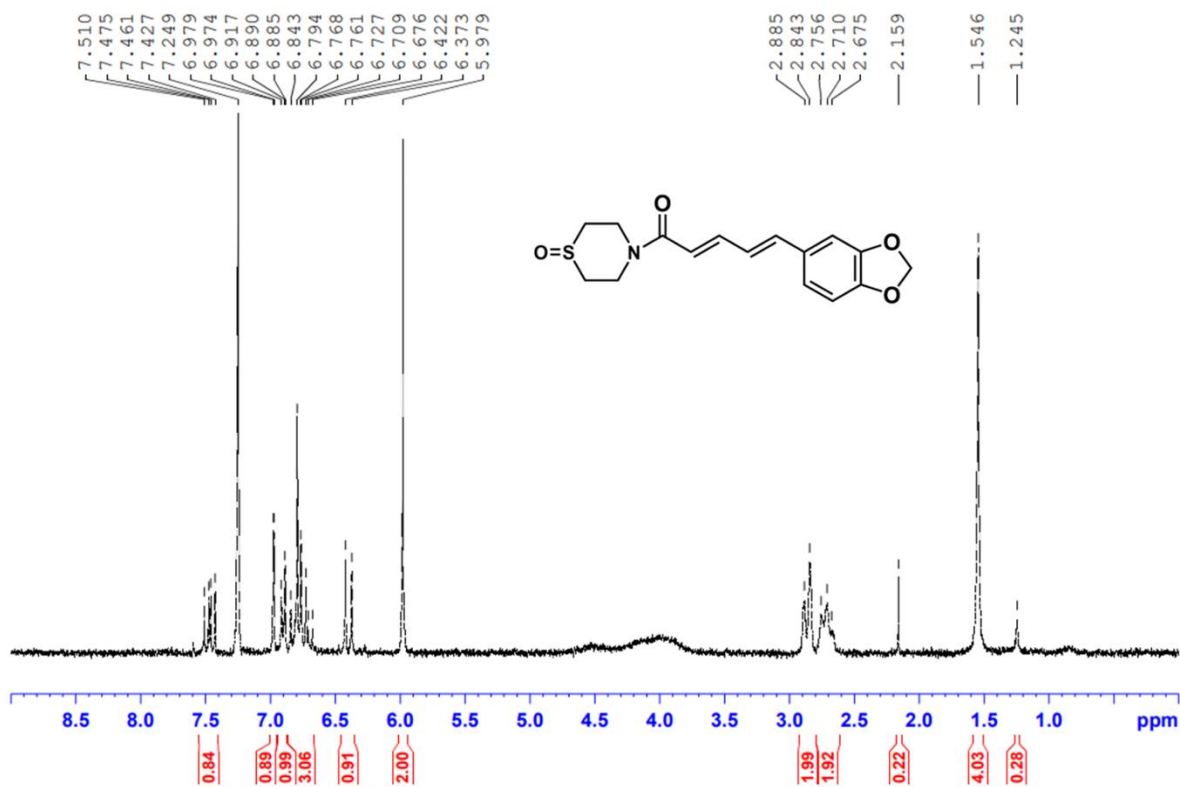
**(2E,4E)-5-(benzo[d][1,3]dioxol-5-yl)-1-(1,1-dioxidothiomorpholino)penta-2,4-dien-1-one
(4f)**

Instrument 300B
ld_proton CDCl3 /opt/nmrdata nekkar 13

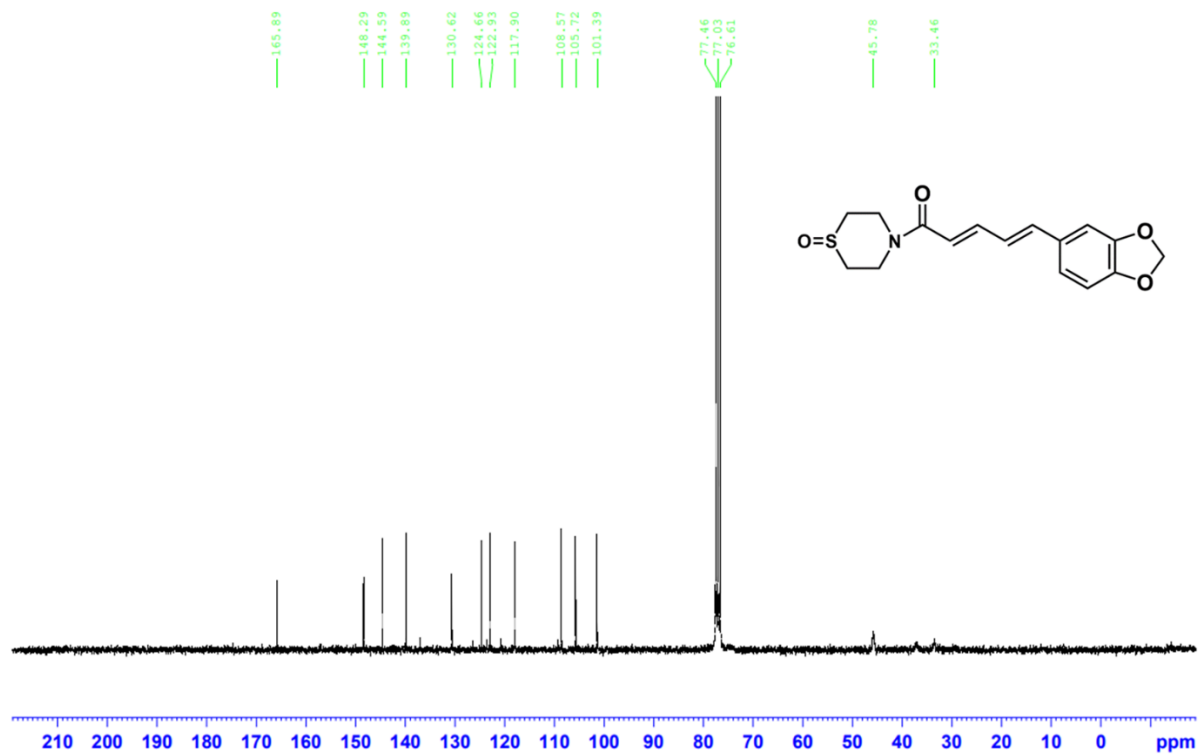


(2E,4E)-5-(benzo[d][1,3]dioxol-5-yl)-1-(1-oxidothiomorpholino)penta-2,4-dien-1-one (4g)

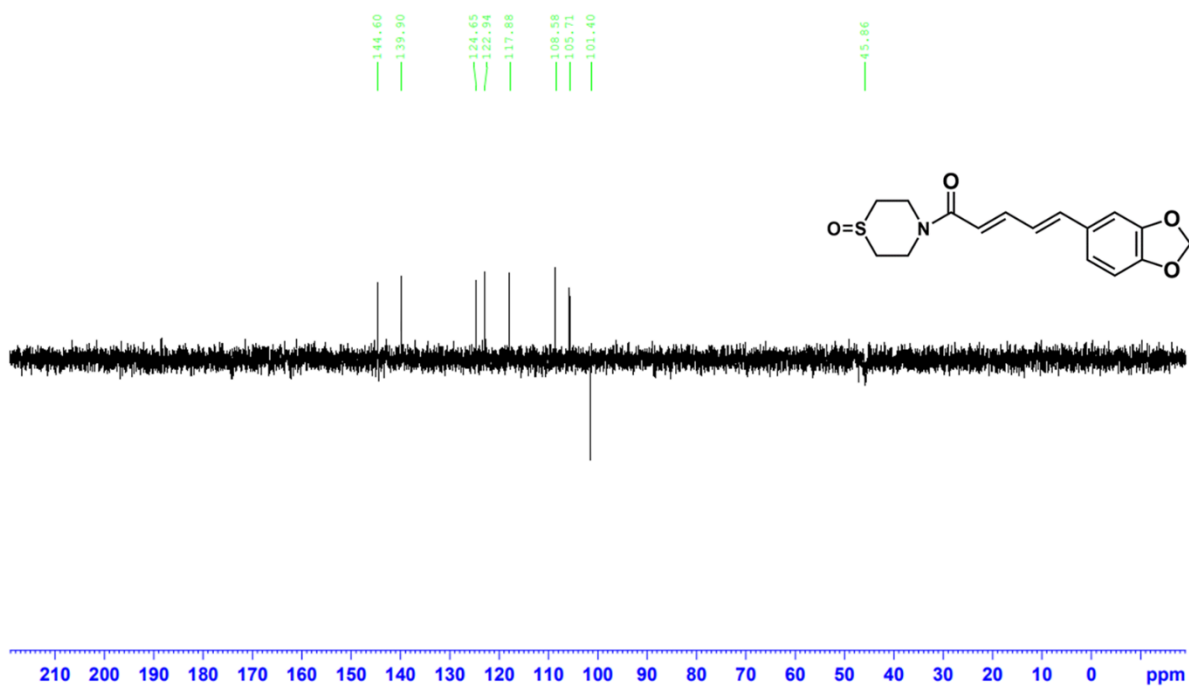
1d_proton CDC13 - SW-10-01 F4-9 Thiomorpholine Monoxide



Instrument 300B
1D_C13_8Hours CDCl3 /opt/nmrdata nekkar 5
SW-10B 13C CDCl3

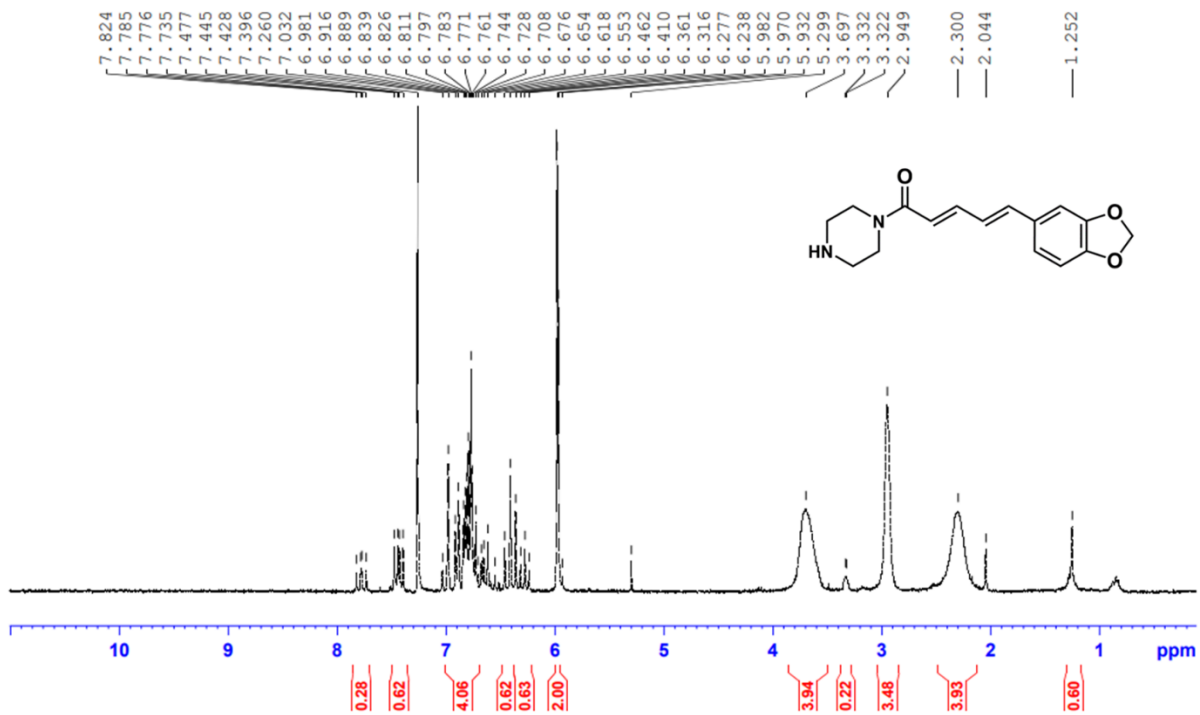


Instrument 300B
C13DEPT135 CDCl3 /opt/nmrdata nekkar 5



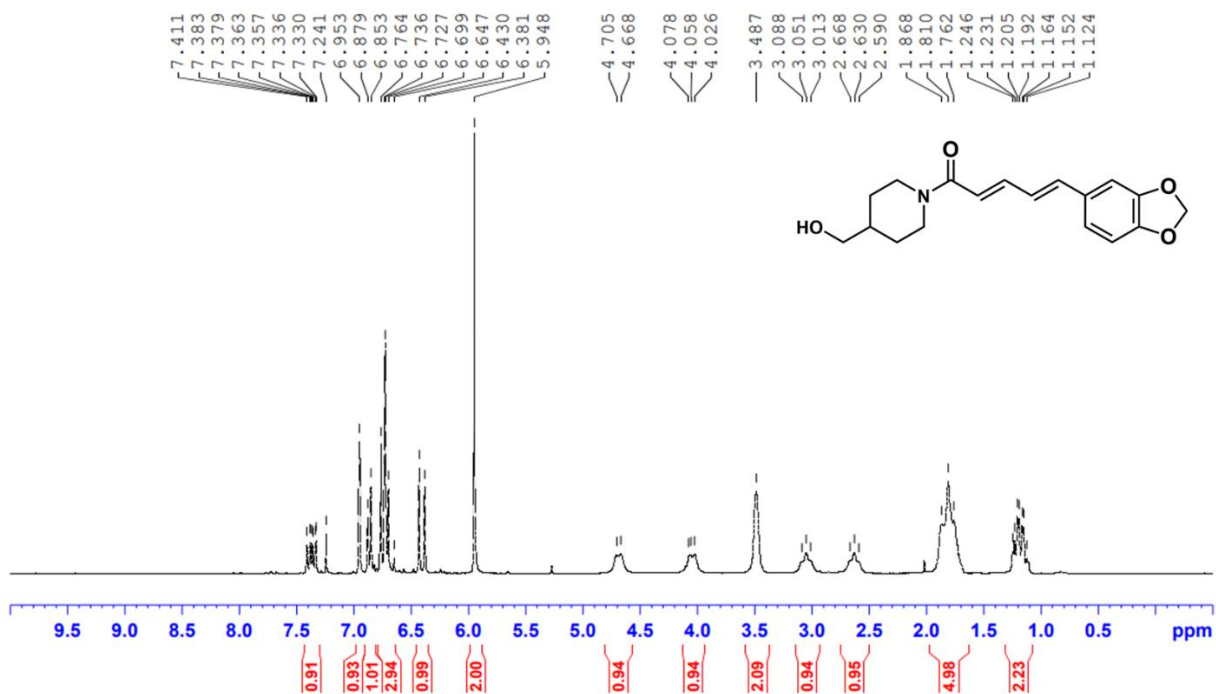
(2E,4E)-5-(benzo[d][1,3]dioxol-5-yl)-1-(piperazin-1-yl)penta-2,4-dien-1-one (4h)

Instrument 300B
1d_proton CDC13 /opt/nmrdata nekkar 2
SW-11-01 1H CdCl3 F8-18

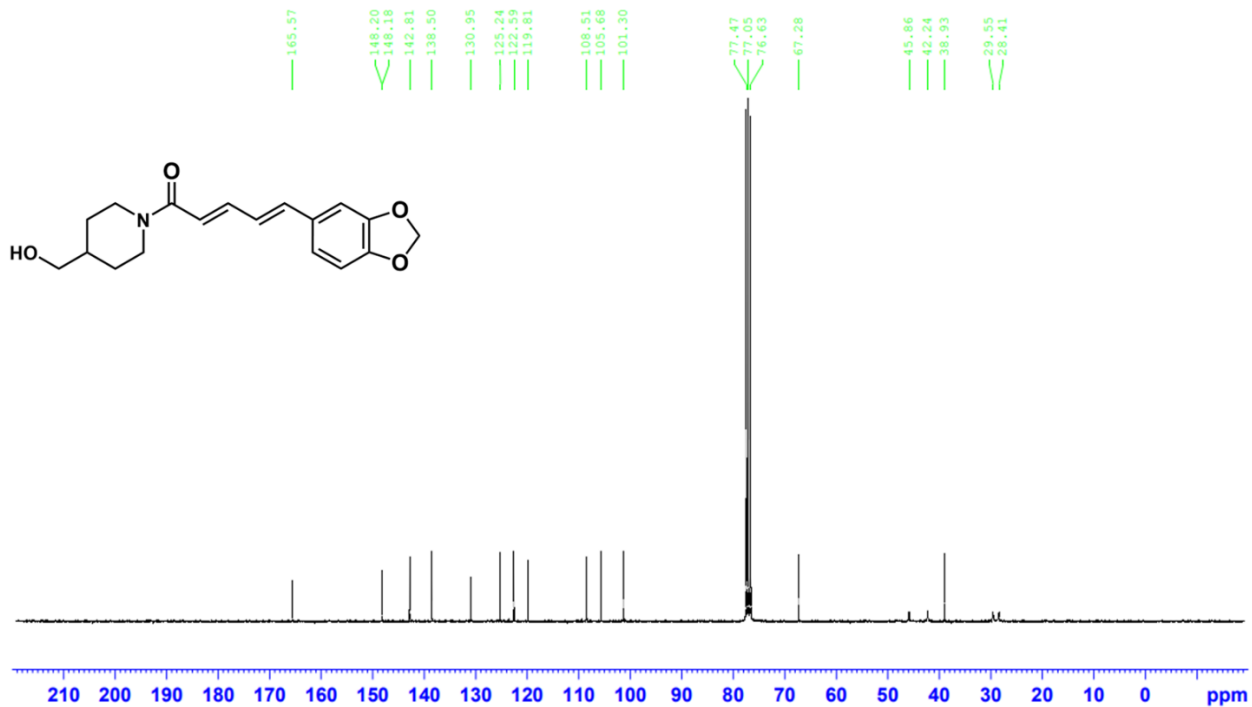


(2E,4E)-5-(benzo[d][1,3]dioxol-5-yl)-1-(4-(hydroxymethyl)piperidin-1-yl)penta-2,4-dien-1-one (4i)

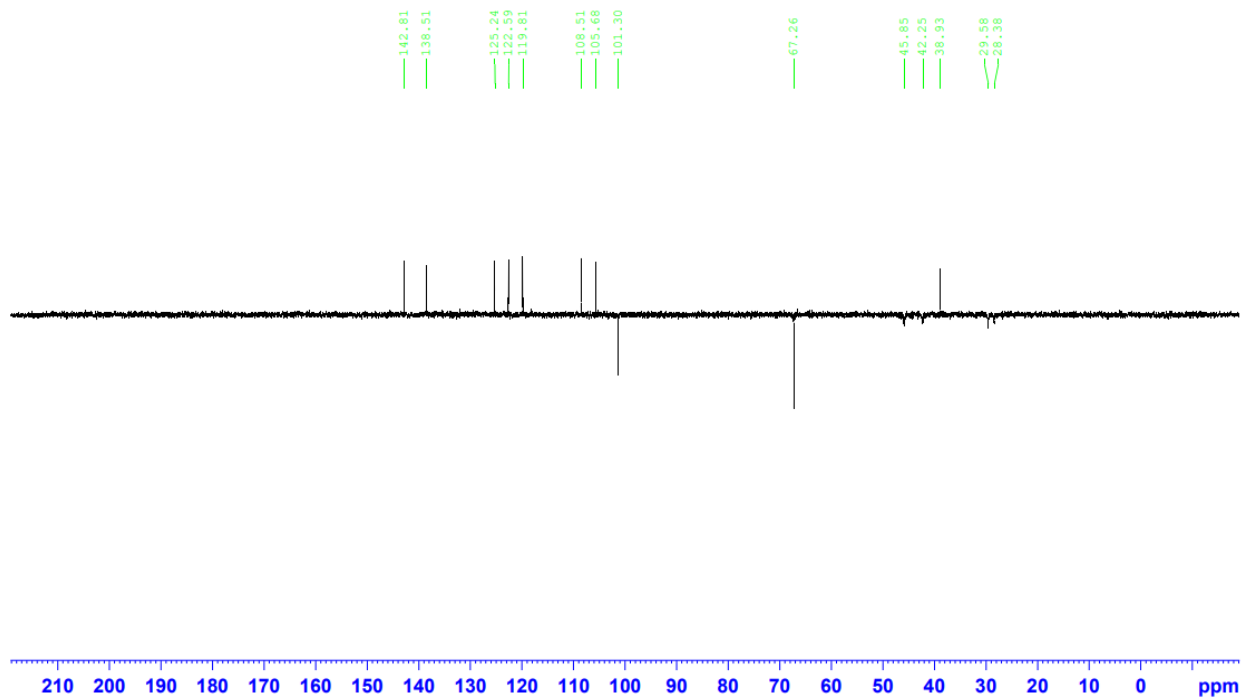
Instrument 300B
1d_proton CDCl3 /opt/nmrdata nekkar 1
SW-12-01 RBF Nov-03-2022



Instrument 300B
1D_C13_8Hours CDC13 /opt/nmrdata nekkar 1
SW-12-01 13CNMR

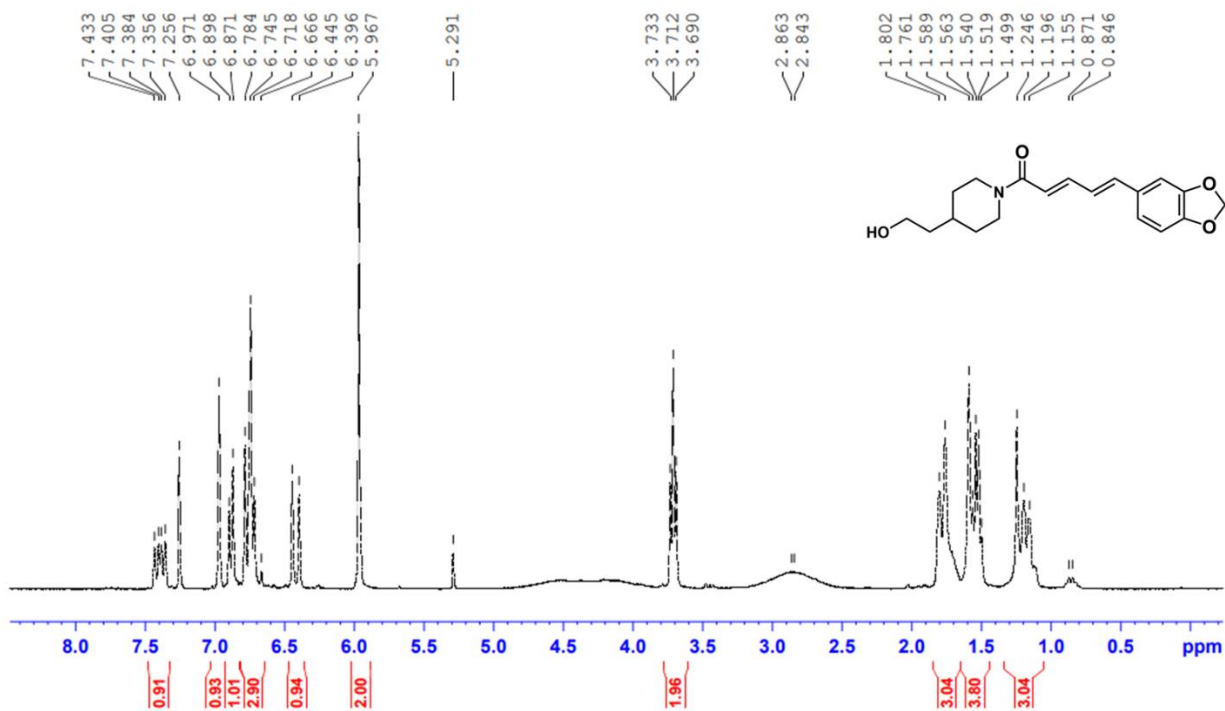


Instrument 300B
C13DEPT135 CDC13 /opt/nmrdata nekkar 2
SW-12-01 Piperidine Methanol Derivative DEPT 135

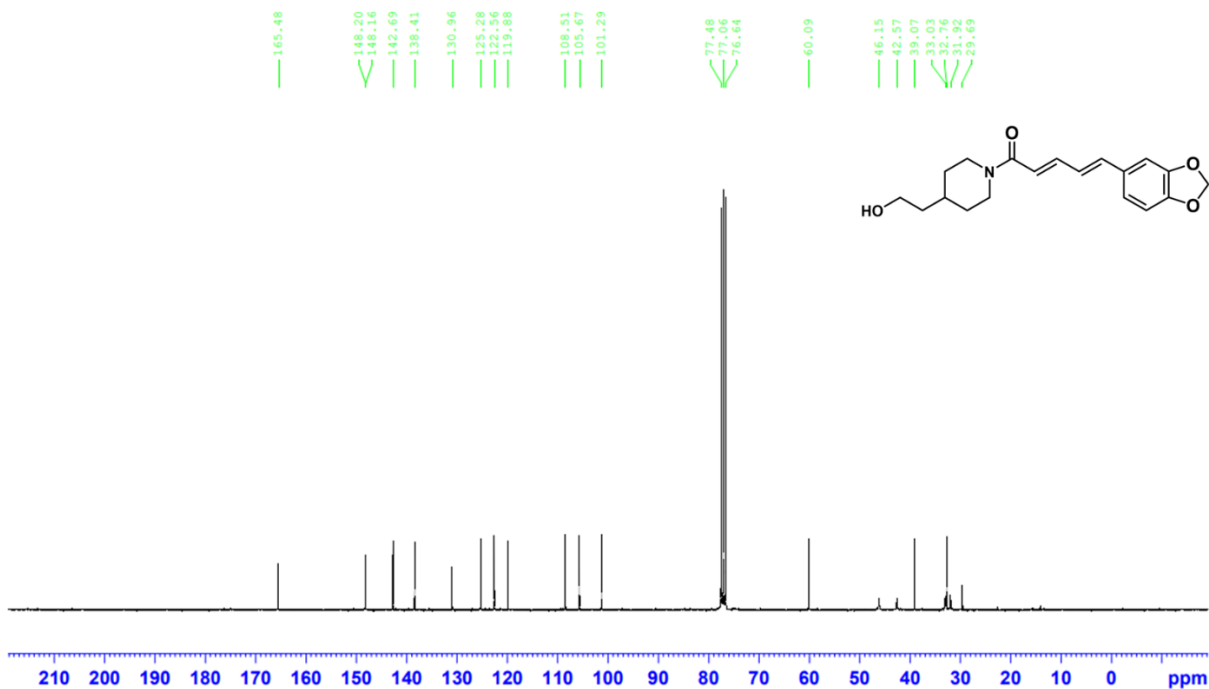


(2E,4E)-5-(benzo[d][1,3]dioxol-5-yl)-1-(4-(2-hydroxyethyl)piperidin-1-yl)penta-2,4-dien-1-one (4j)

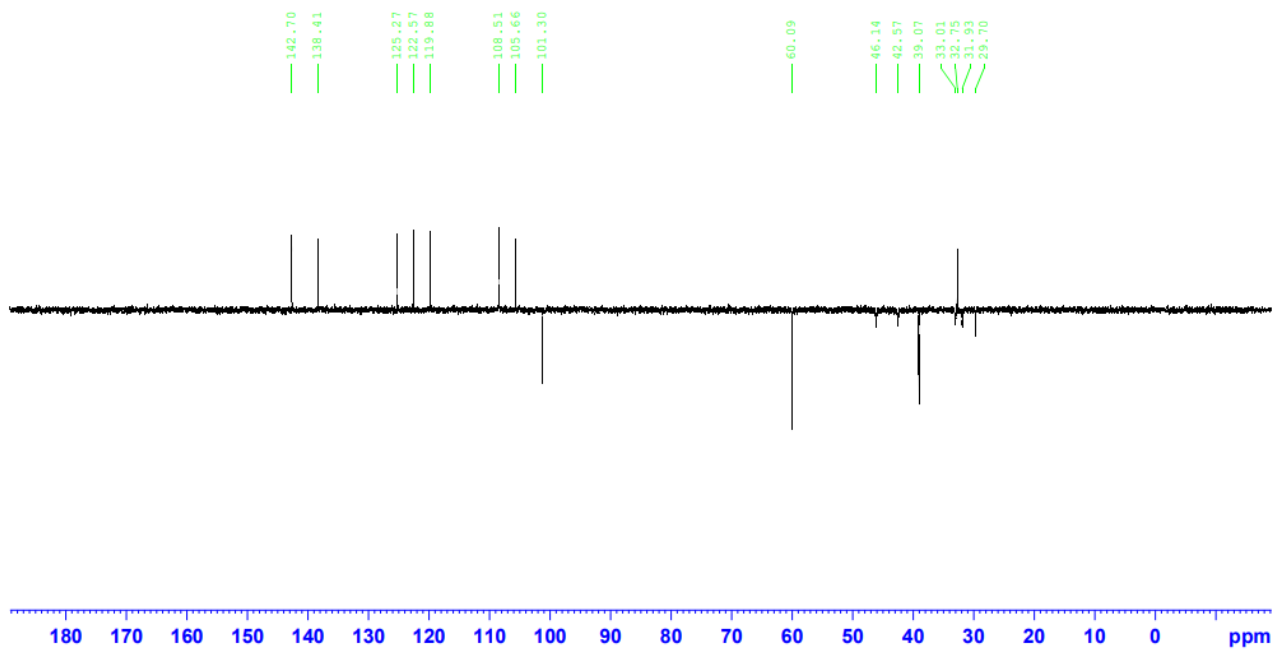
Instrument 300B
1d_proton CDCl3 /opt/nmrdata nekkar 5
SW-13-01 F32-42 1H CDCl3 Oct 29-2021



Instrument 300B
1D_C13_8Hours CDCl3 /opt/nmrdata nekkar 3
SW-13-01 F32-42 13C NMR

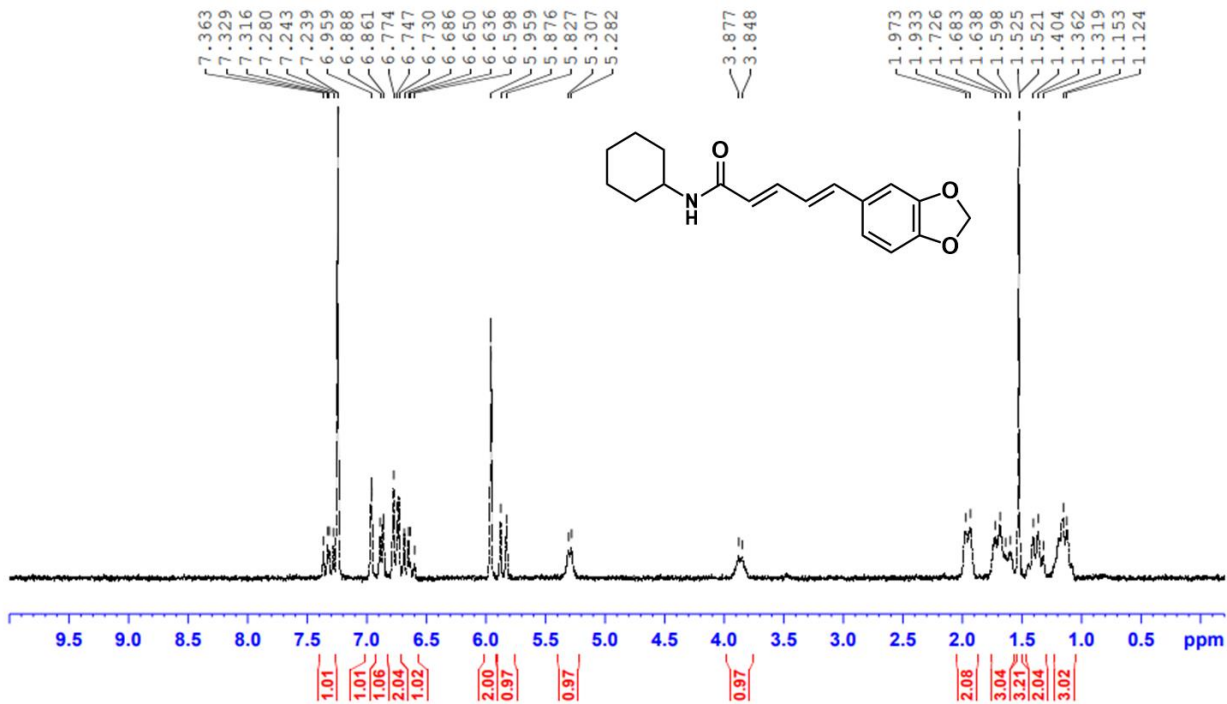


Instrument 300B
C13DEPT135 CDCl3 /opt/nmrdata nekkar 3
SW-13-01 F32-42 DEPT135



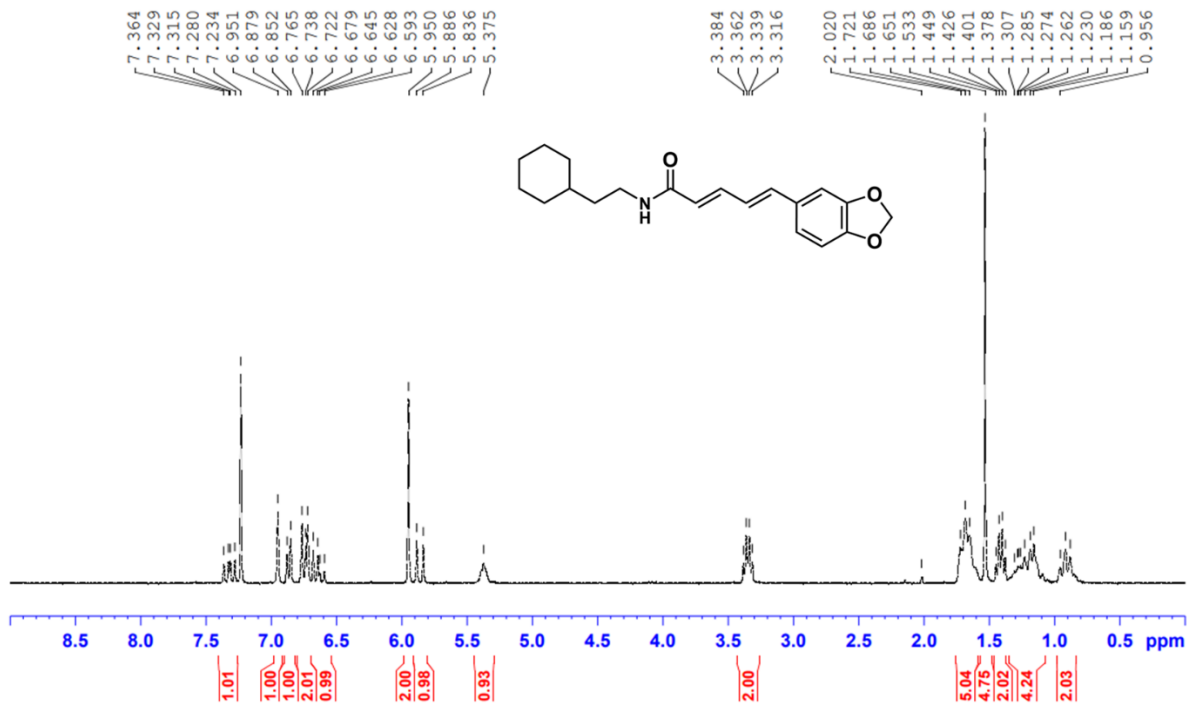
(2E,4E)-5-(benzo[d][1,3]dioxol-5-yl)-1-(piperidin-1-yl)penta-2,4-dien-1-one (4k)

Instrument 300B
1d_proton CDCl3 /opt/nmrdata nekkar 15
SW-14-01 Col 5 F24-28 (CDCl3 has water peak in it)

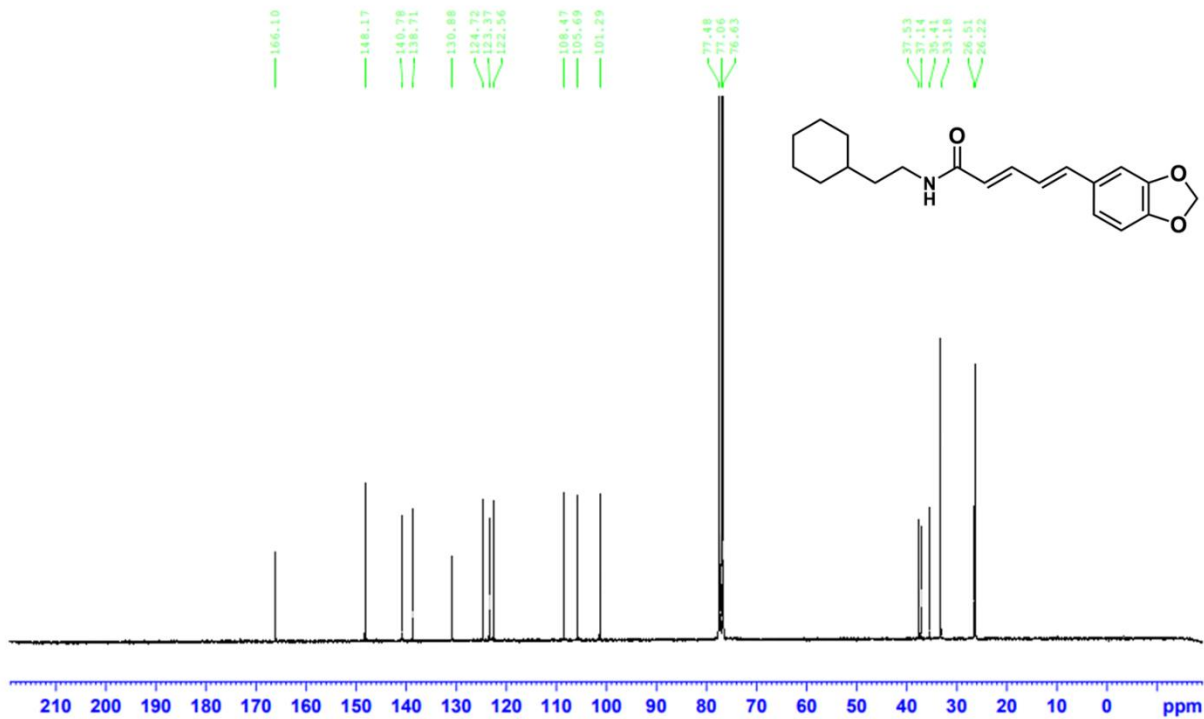


(2E,4E)-5-(benzo[d][1,3]dioxol-5-yl)-N-(2-cyclohexylethyl)penta-2,4-dienamide (4l)

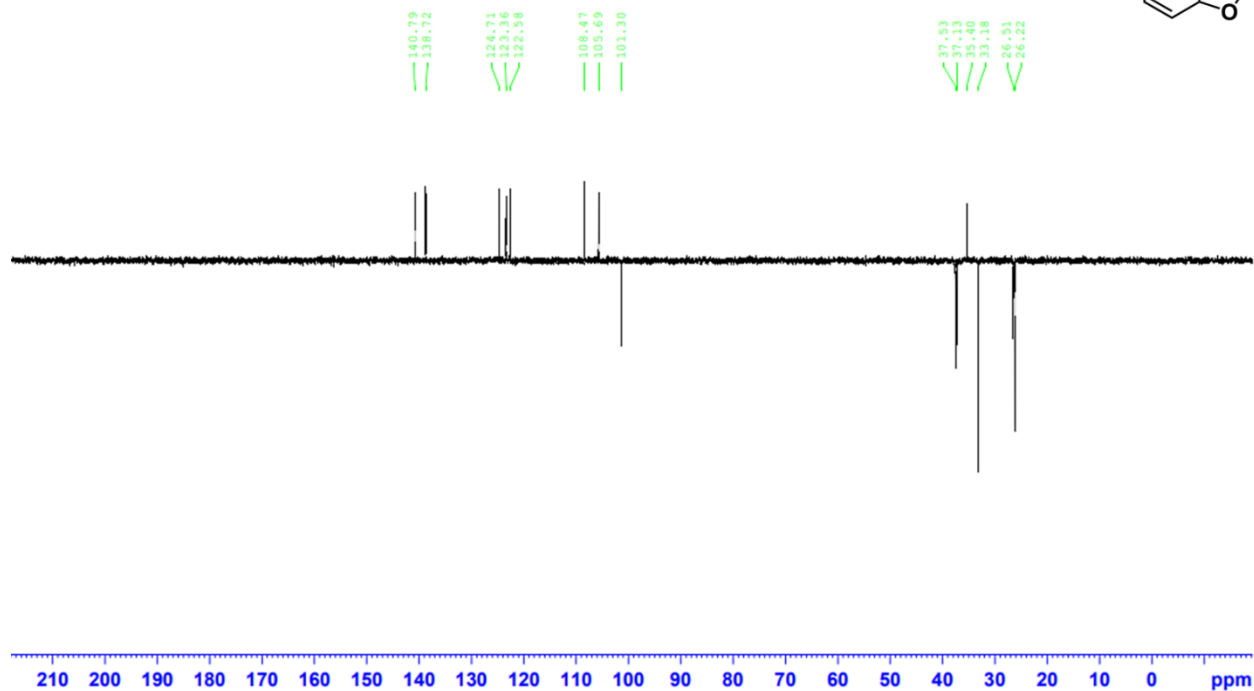
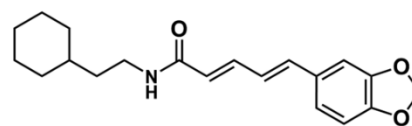
Instrument 300B
ld_proton CDCl3 /opt/nmrdata nekkar 5
SW-15-01 Post Recrystallization 1H



Sw-15-01 13CNMR CDCl3 2022-11-10

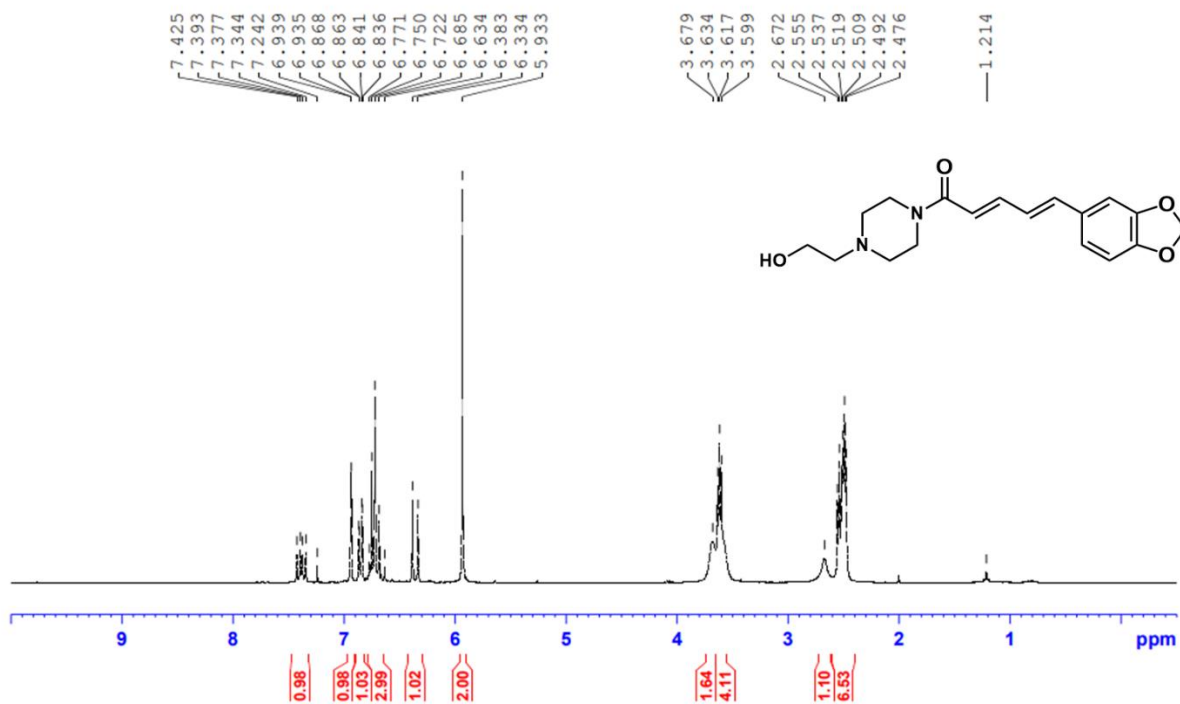


Instrument 300B
C13DEPT135 CDC13 /opt/nmrdata nekkar 4
SW-15-01 F22 DEPT135

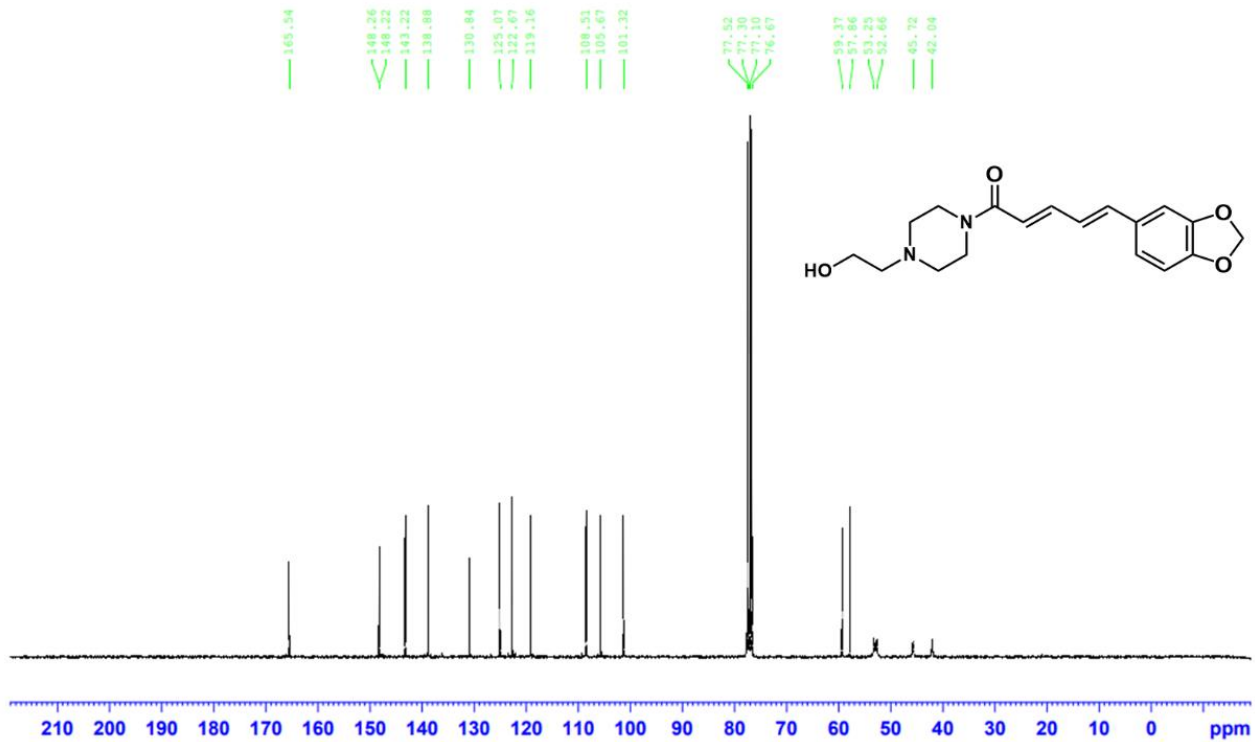


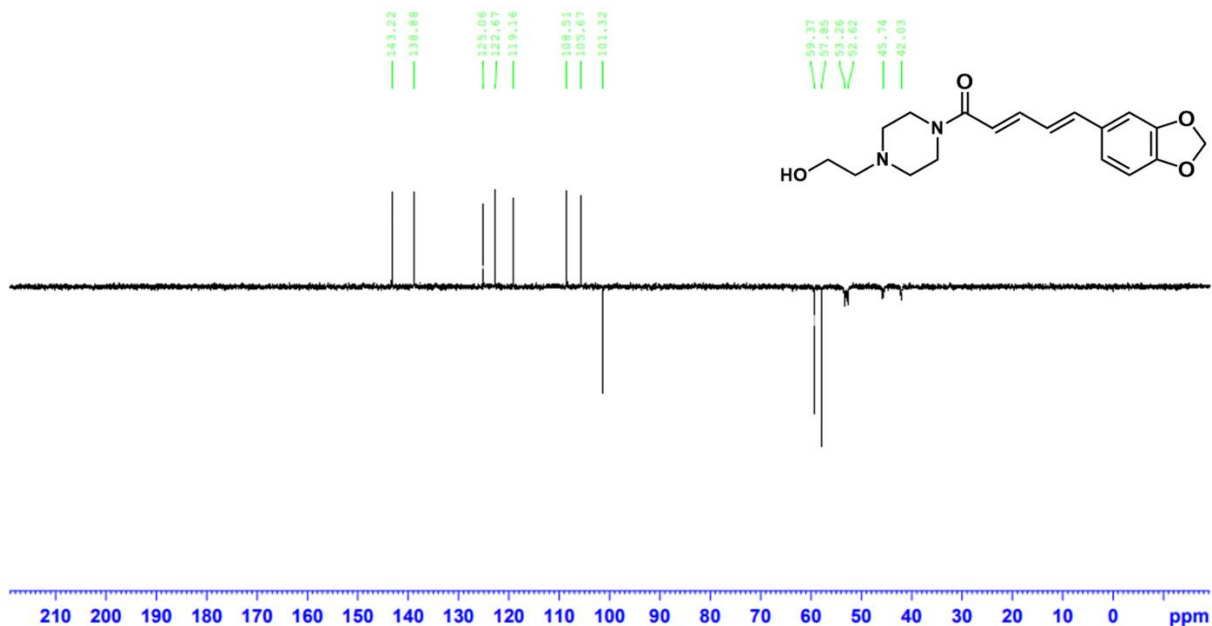
(2E,4E)-5-(benzo[d][1,3]dioxol-5-yl)-1-(4-(2-hydroxyethyl)piperazin-1-yl)penta-2,4-dien-1-one (4m)

SW-16-01 1H Jan-06-2023



SW-16-01 13C NMR CDC13 Jan-06-2023

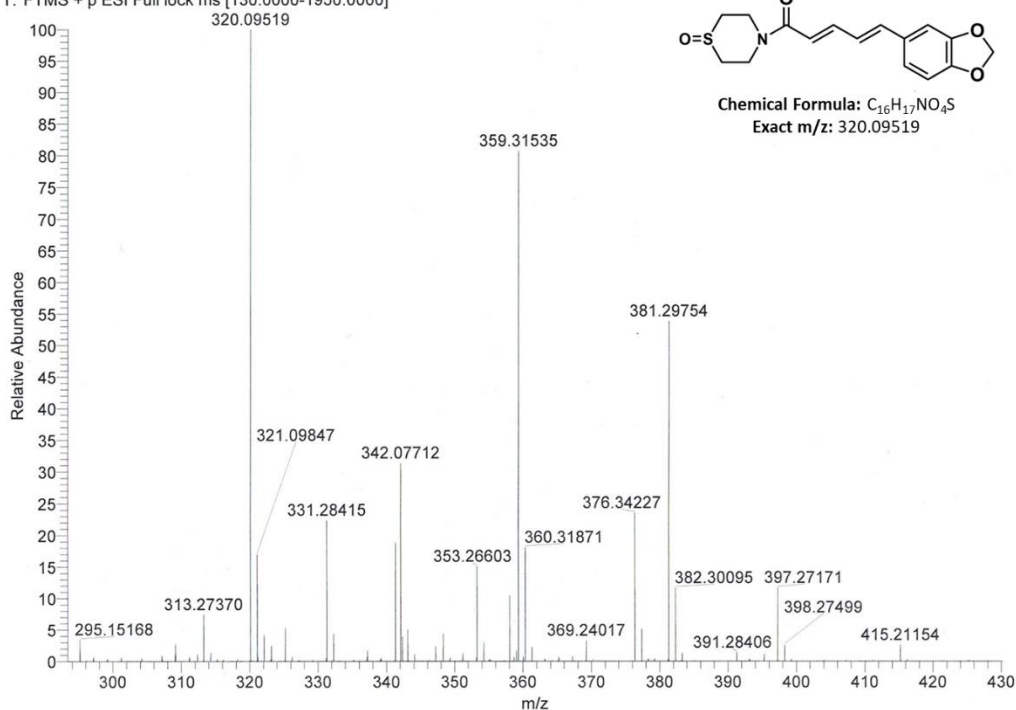




A2. HR-MS data for compounds 4g, 4i, 4j, 4l, and 4m

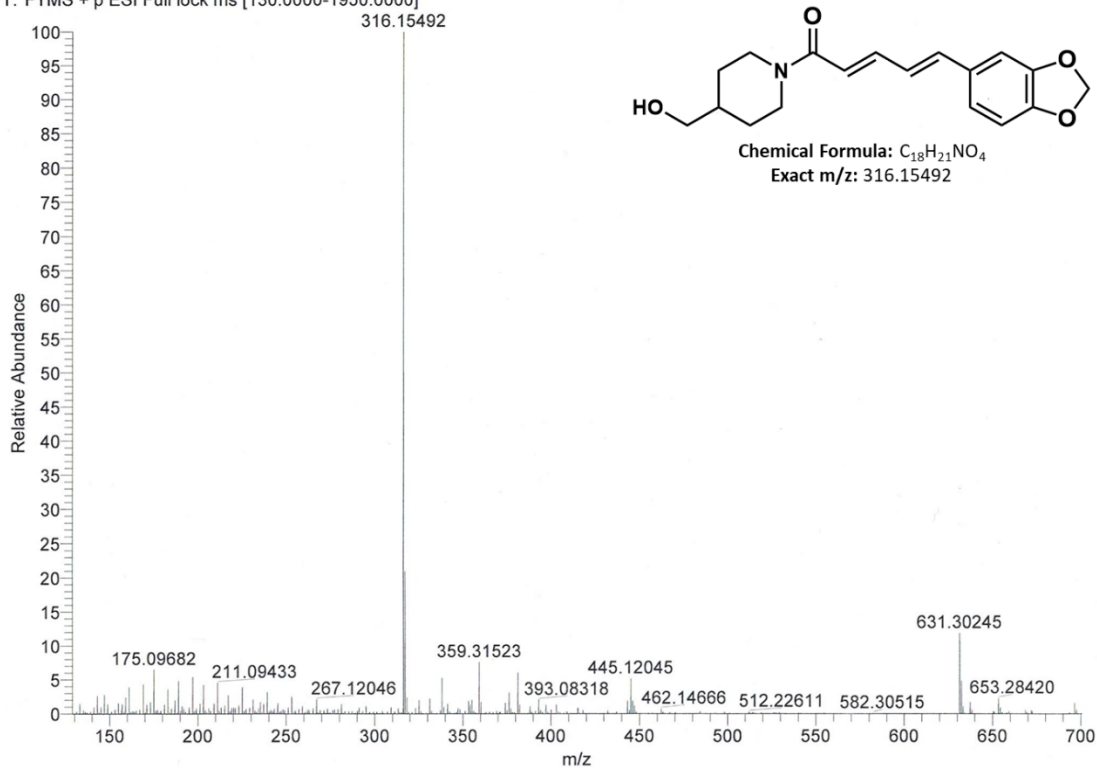
(2E,4E)-5-(benzo[d][1,3]dioxol-5-yl)-1-(1-oxidomorpholino)penta-2,4-dien-1-one (4g)

+ESI in 1:1 MeOH/H₂O+0.1 FA
 Jan5SW2 #279-430 RT: 1.24-1.92 AV: 152 NL: 1.24E8
 T: FTMS + p ESI Full lock ms [130.0000-1950.0000]



(2E,4E)-5-(benzo[d][1,3]dioxol-5-yl)-1-(4-(hydroxymethyl)piperidin-1-yl)penta-2,4-dien-1-one (4i)

+ESI in 1:1 MeOH/H2O+0.1 FA
Jan5SW1 #415-438 RT: 1.85-1.95 AV: 24 NL: 3.56E8
T: FTMS + p ESI Full lock ms [130.0000-1950.0000]

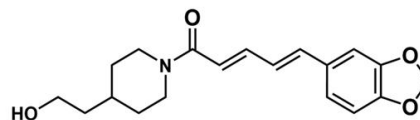
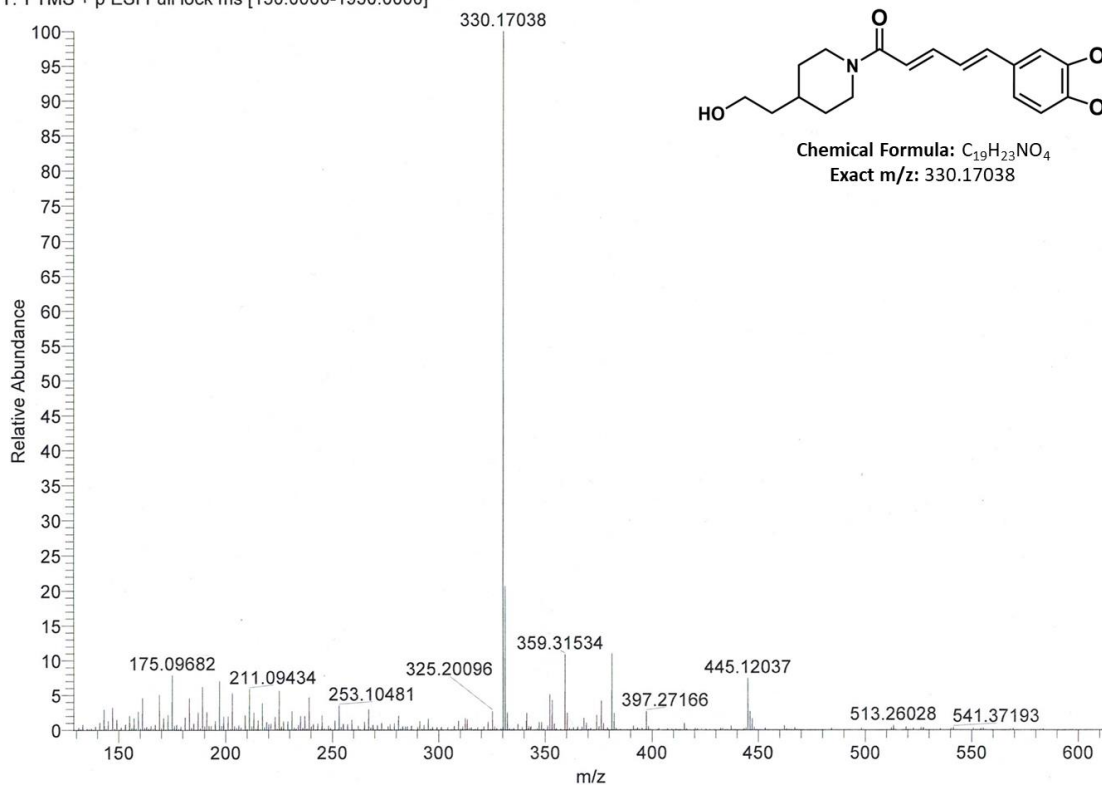


(2E,4E)-5-(benzo[d][1,3]dioxol-5-yl)-1-(4-(2-hydroxyethyl)piperidin-1-yl)penta-2,4-dien-1-one (4j)

+ESI in 1:1 MeOH/H2O+0.1 FA

Jan5SW4 #3-160 RT: 0.01-0.71 AV: 158 NL: 3.33E8

T: FTMS + p ESI Full lock ms [130.0000-1950.0000]



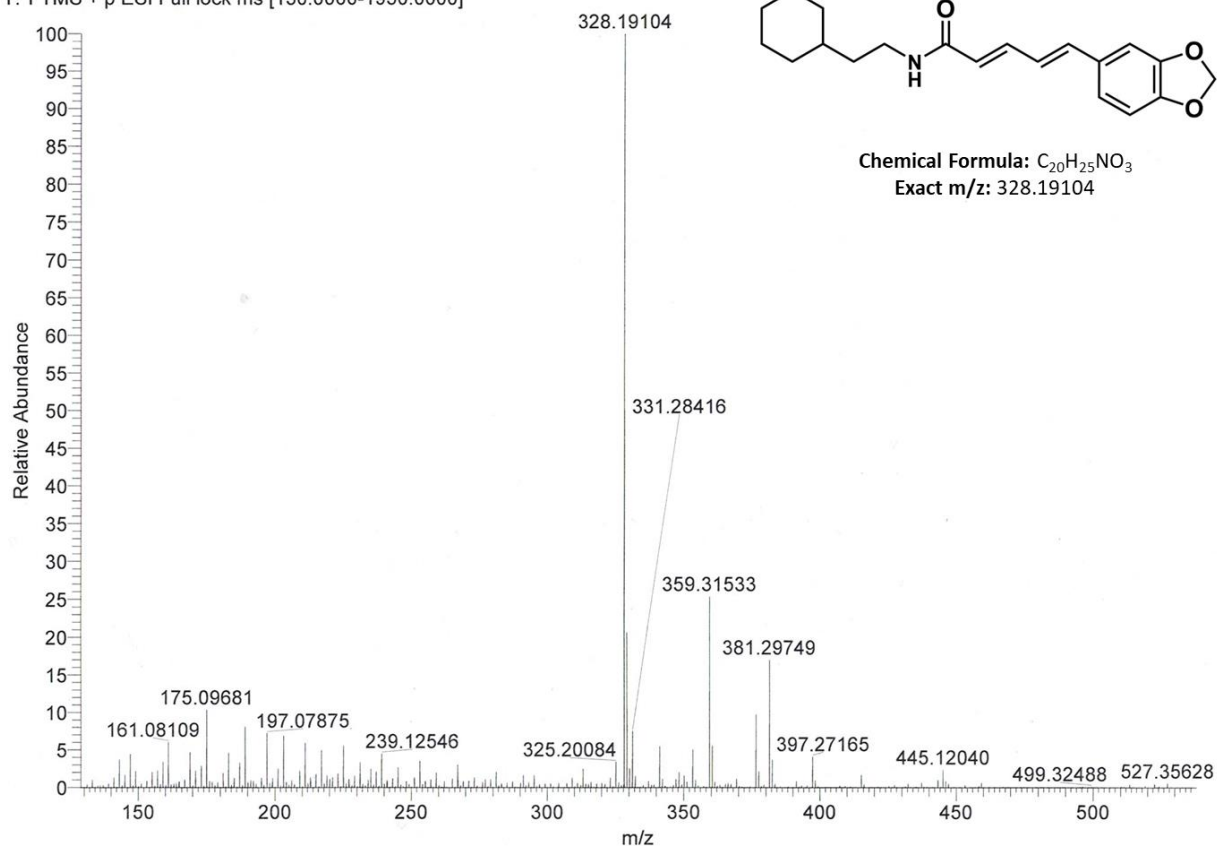
Chemical Formula: C₁₉H₂₃NO₄
Exact m/z: 330.17038

(2E,4E)-5-(benzo[d][1,3]dioxol-5-yl)-N-(2-cyclohexylethyl)penta-2,4-dienamide (4l)

+ESI in 1:1 MeOH/H2O+0.1 FA

Jan5SW3 #164-298 RT: 0.73-1.33 AV: 135 NL: 2.68E8

T: FTMS + p ESI Full lock ms [130.0000-1950.0000]

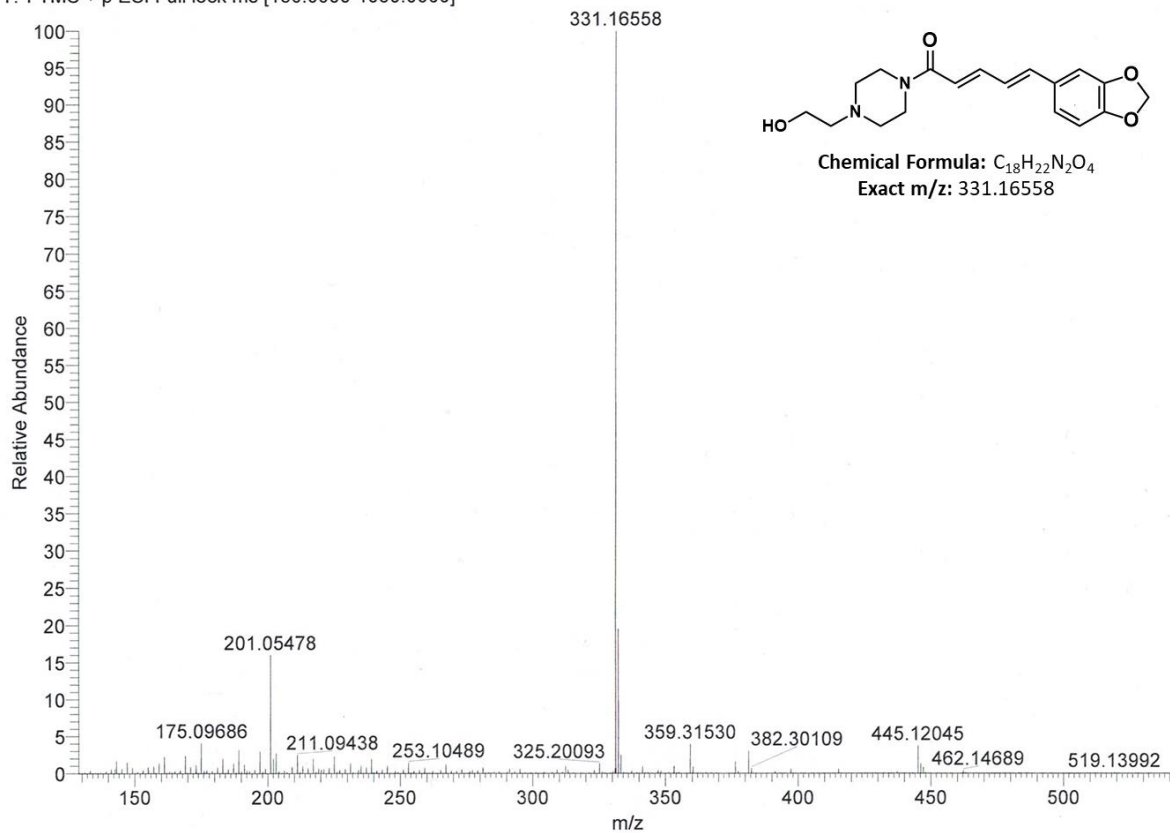


(2E,4E)-5-(benzo[d][1,3]dioxol-5-yl)-1-(4-(2-hydroxyethyl)piperazin-1-yl)penta-2,4-dien-1-one (4m)

+ESI in 1:1 MeOH/H2O+0.1 FA

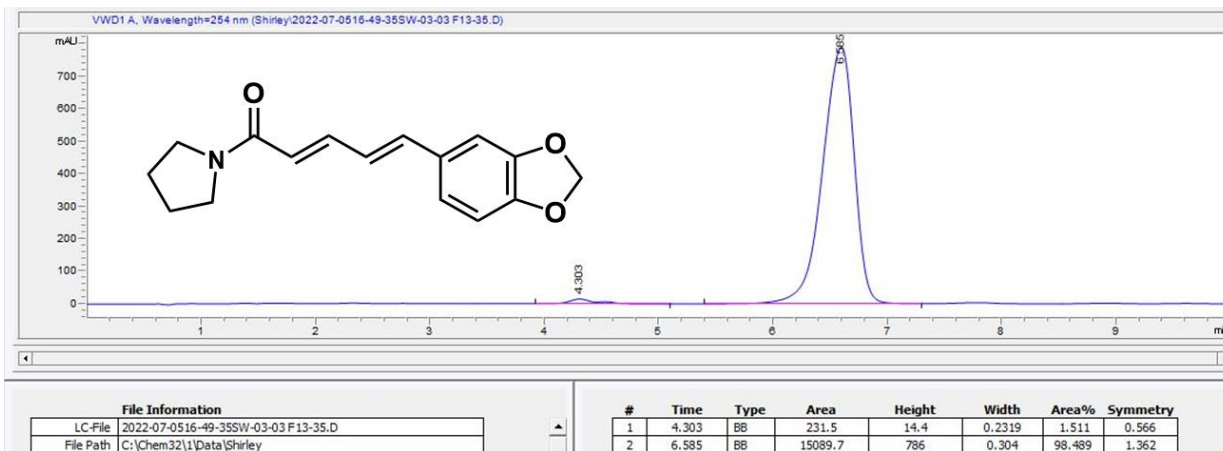
Jan5SW5 #187-282 RT: 0.83-1.26 AV: 96 NL: 5.47E8

T: FTMS + p ESI Full lock ms [130.0000-1950.0000]

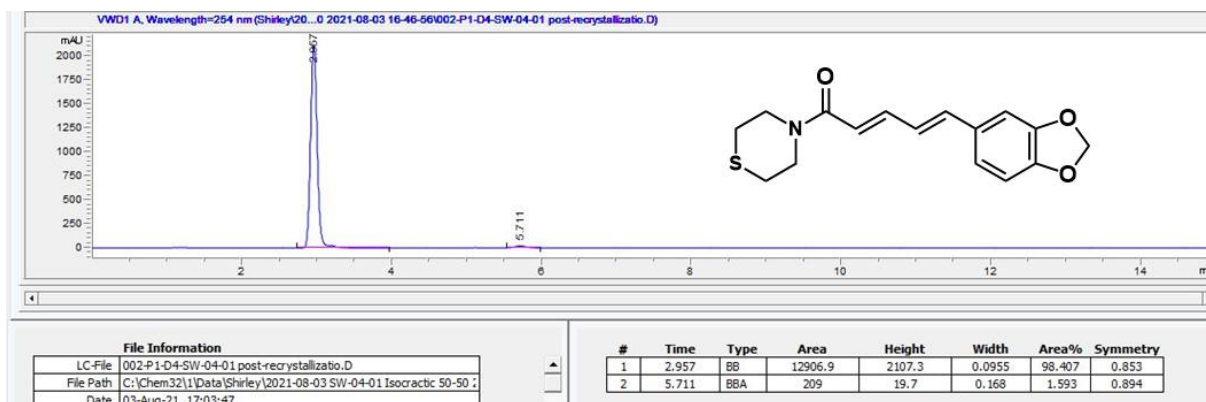


A3. LC-MS trace for compounds 4a-m

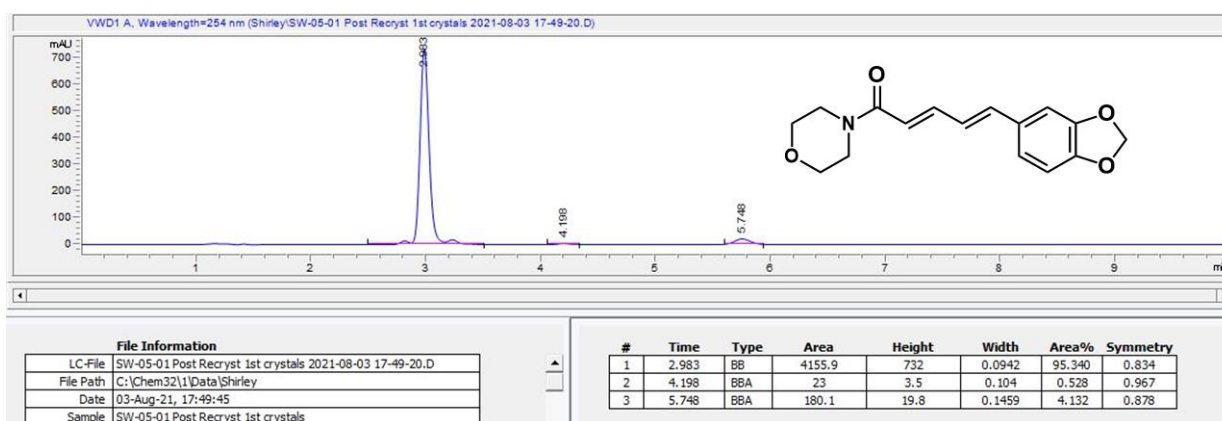
Piperyline (4a)



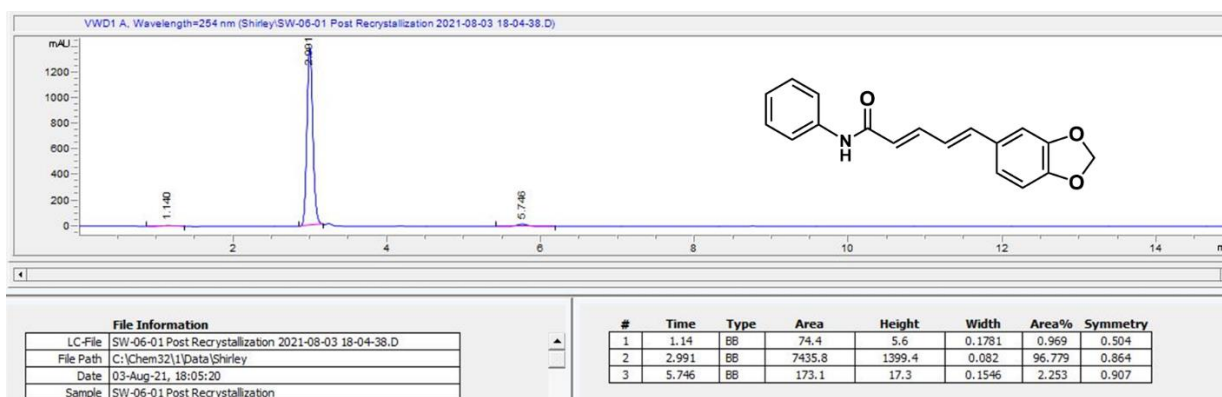
(2E,4E)-5-(Benzo[d][1,3]dioxol-5-yl)-1-thiomorpholinopenta-2,4-dien-1-one (4b)



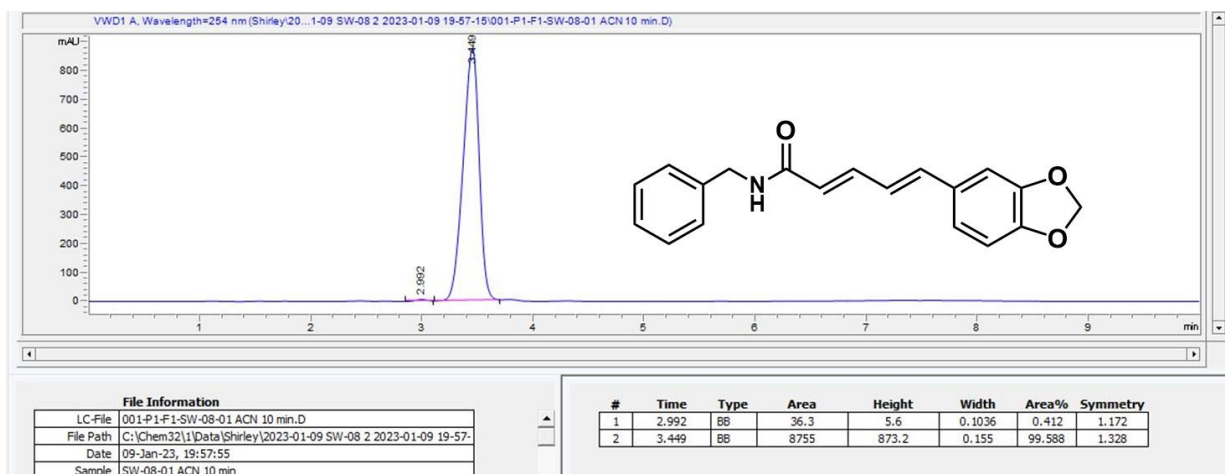
(2E,4E)-5-(Benzo[d][1,3]dioxol-5-yl)-1-morpholinopenta-2,4-dien-1-one (4c)



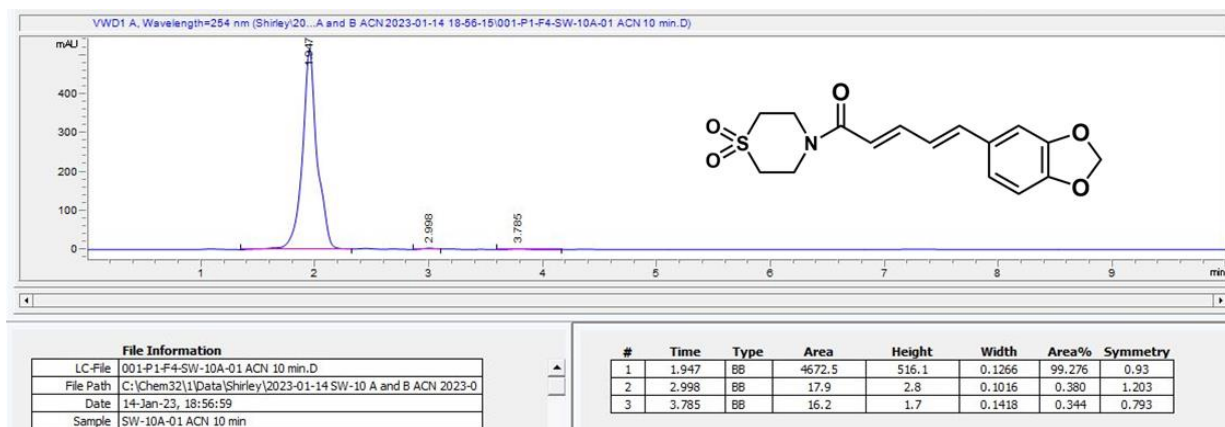
(2E,4E)-5-(Benzo[d][1,3]dioxol-5-yl)-N-phenylpenta-2,4-dienamide (4d)



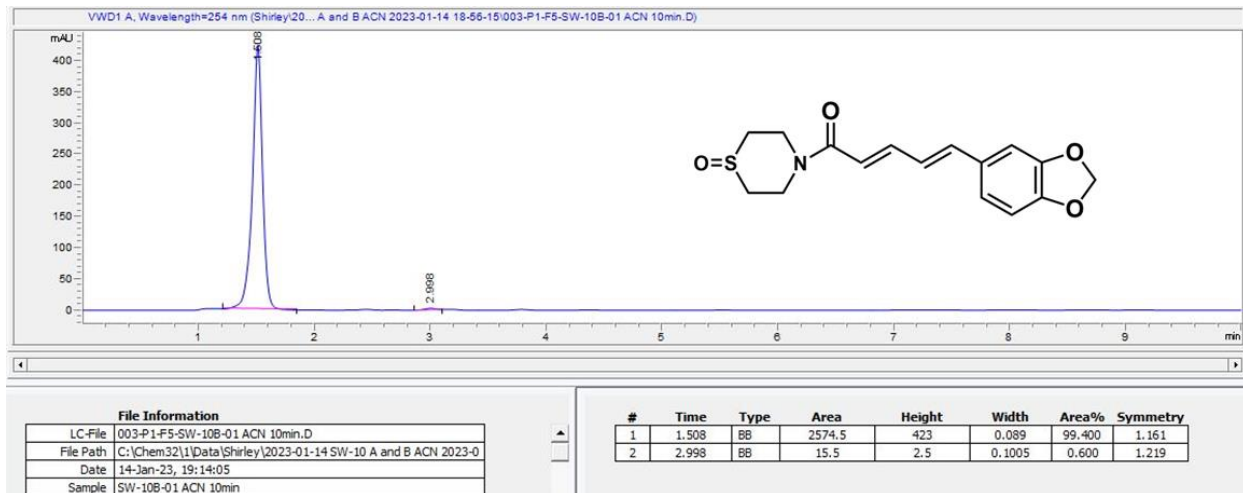
(2E,4E)-5-(Benzo[d][1,3]dioxol-5-yl)-N-benzylpenta-2,4-dienamide (4e)



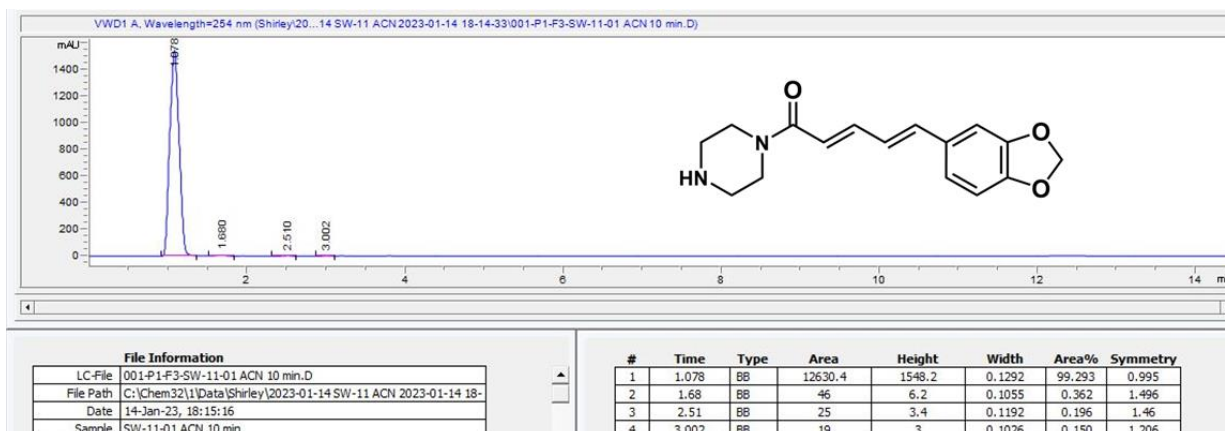
(2E,4E)-5-(benzo[d][1,3]dioxol-5-yl)-1-(1,1-dioxidothiomorpholino)penta-2,4-dien-1-one (4f)



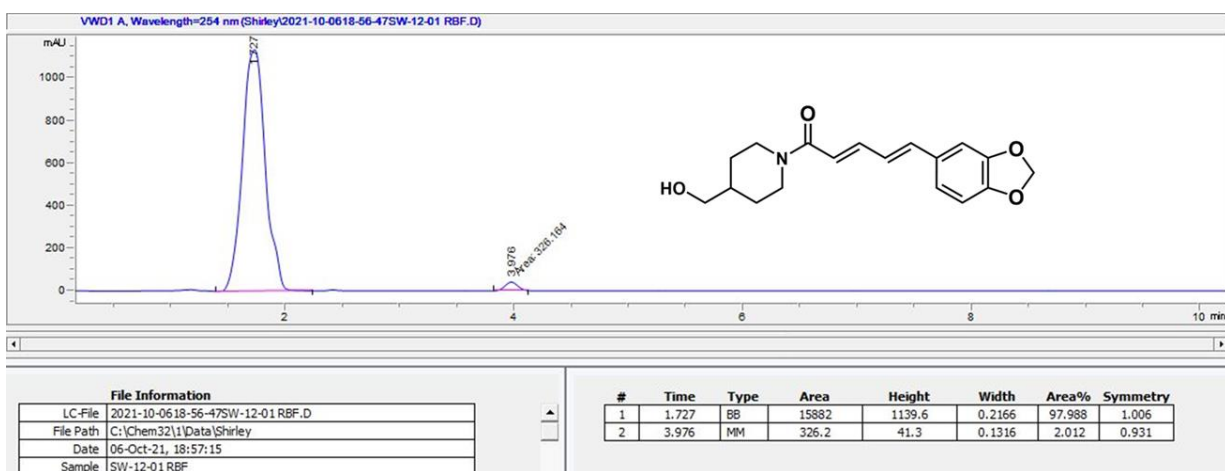
(2E,4E)-5-(benzo[d][1,3]dioxol-5-yl)-1-(1-oxidothiomorpholino)penta-2,4-dien-1-one (4g)



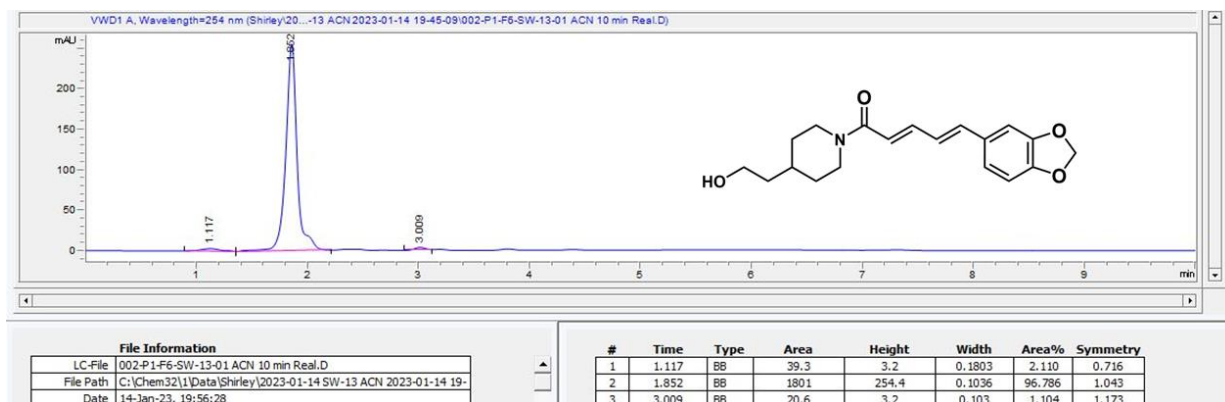
(2E,4E)-5-(benzo[d][1,3]dioxol-5-yl)-1-(piperazin-1-yl)penta-2,4-dien-1-one (4h)



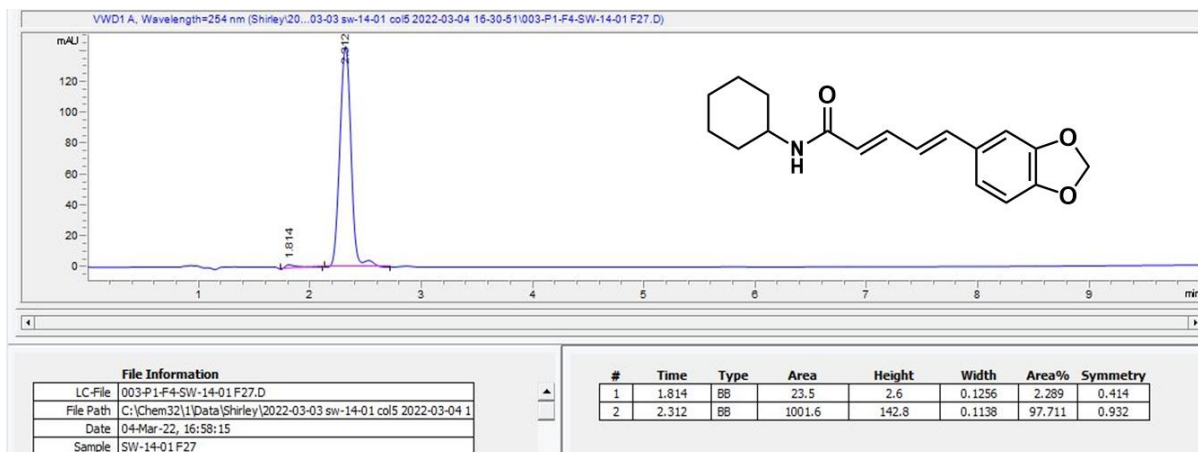
(2E,4E)-5-(benzo[d][1,3]dioxol-5-yl)-1-(4-(hydroxymethyl)piperidin-1-yl)penta-2,4-dien-1-one (4i)



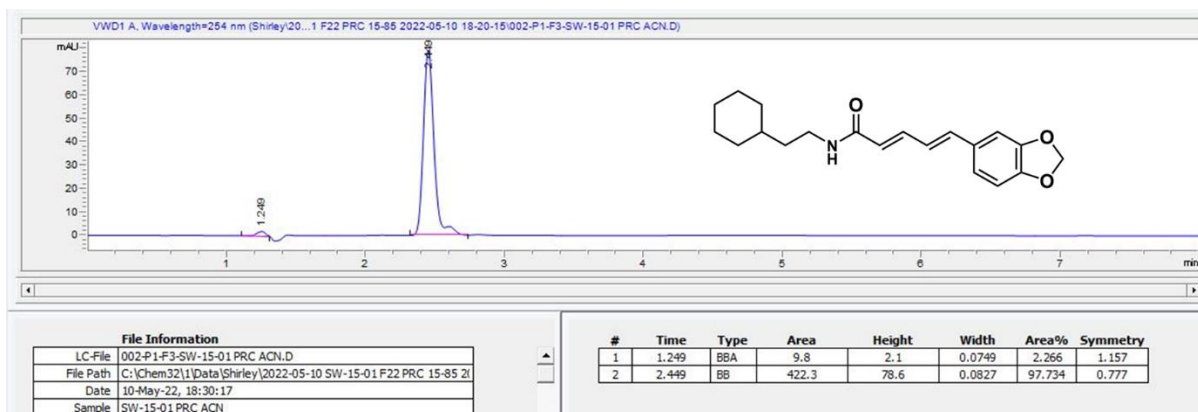
(2E,4E)-5-(benzo[d][1,3]dioxol-5-yl)-1-(4-(2-hydroxyethyl)piperidin-1-yl)penta-2,4-dien-1-one (4j)



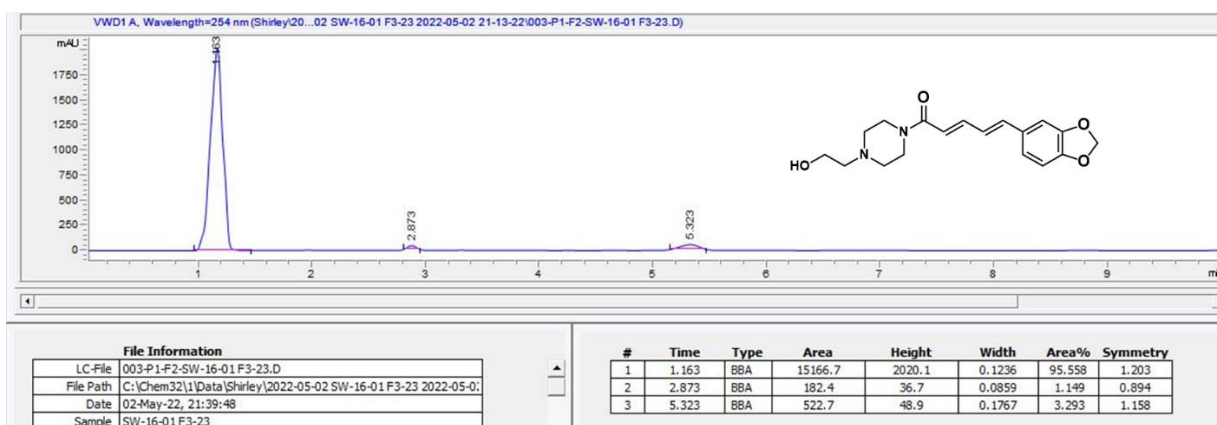
(2E,4E)-5-(benzo[d][1,3]dioxol-5-yl)-1-(piperidin-1-yl)penta-2,4-dien-1-one (4k)



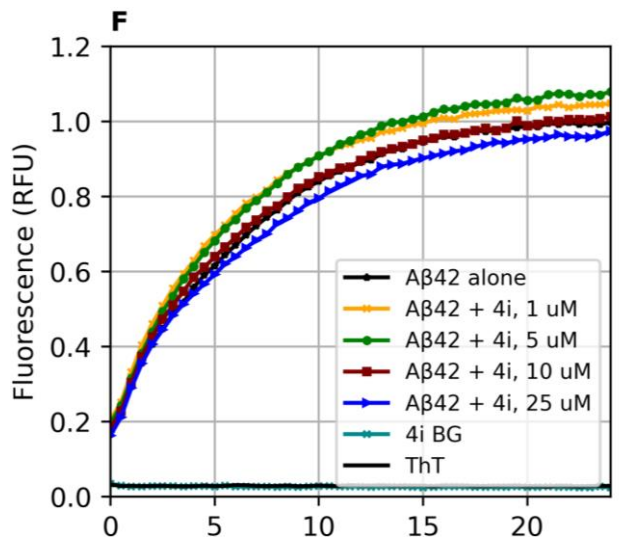
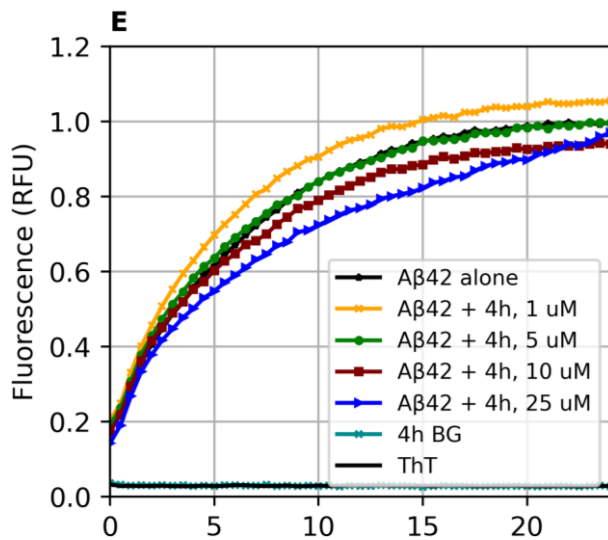
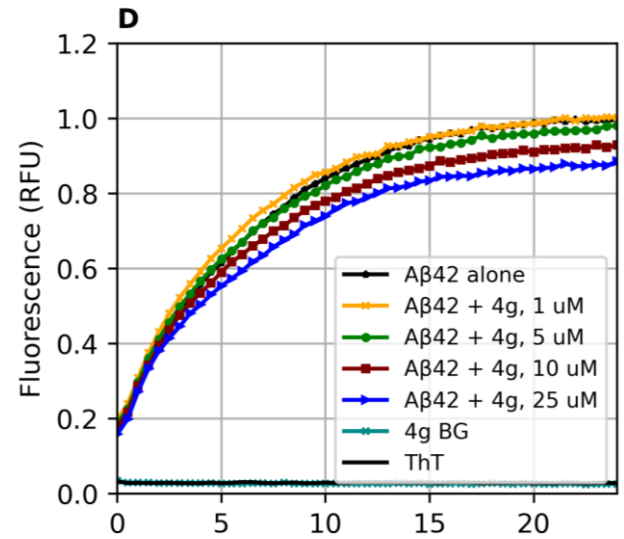
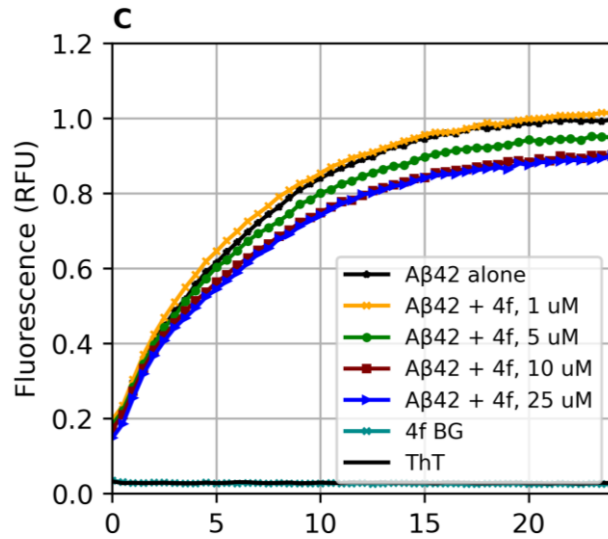
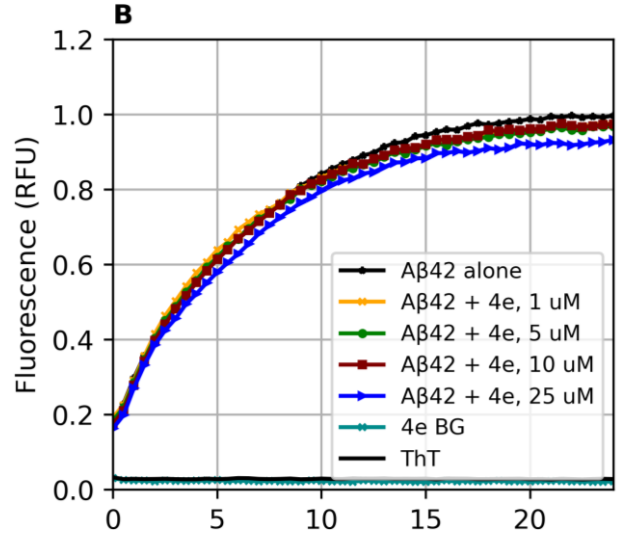
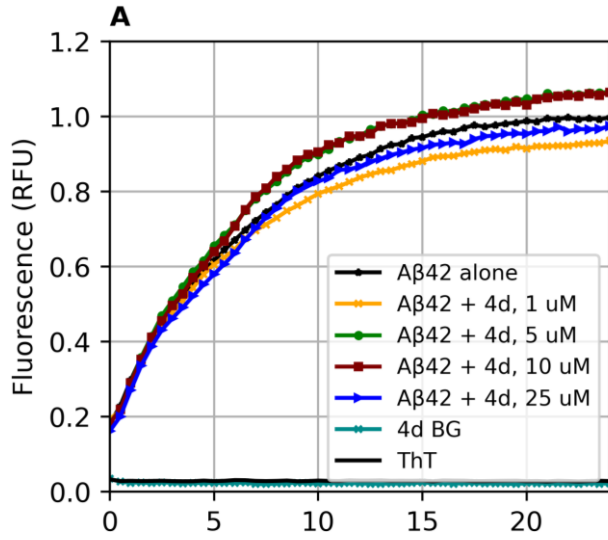
(2E,4E)-5-(benzo[d][1,3]dioxol-5-yl)-N-(2-cyclohexylethyl)penta-2,4-dienamide (4l)



(2E,4E)-5-(benzo[d][1,3]dioxol-5-yl)-1-(4-(2-hydroxyethyl)piperazin-1-yl)penta-2,4-dien-1-one (4m)



A4. Additional aggregation kinetics plots for piperine derivatives 4d-m and 3



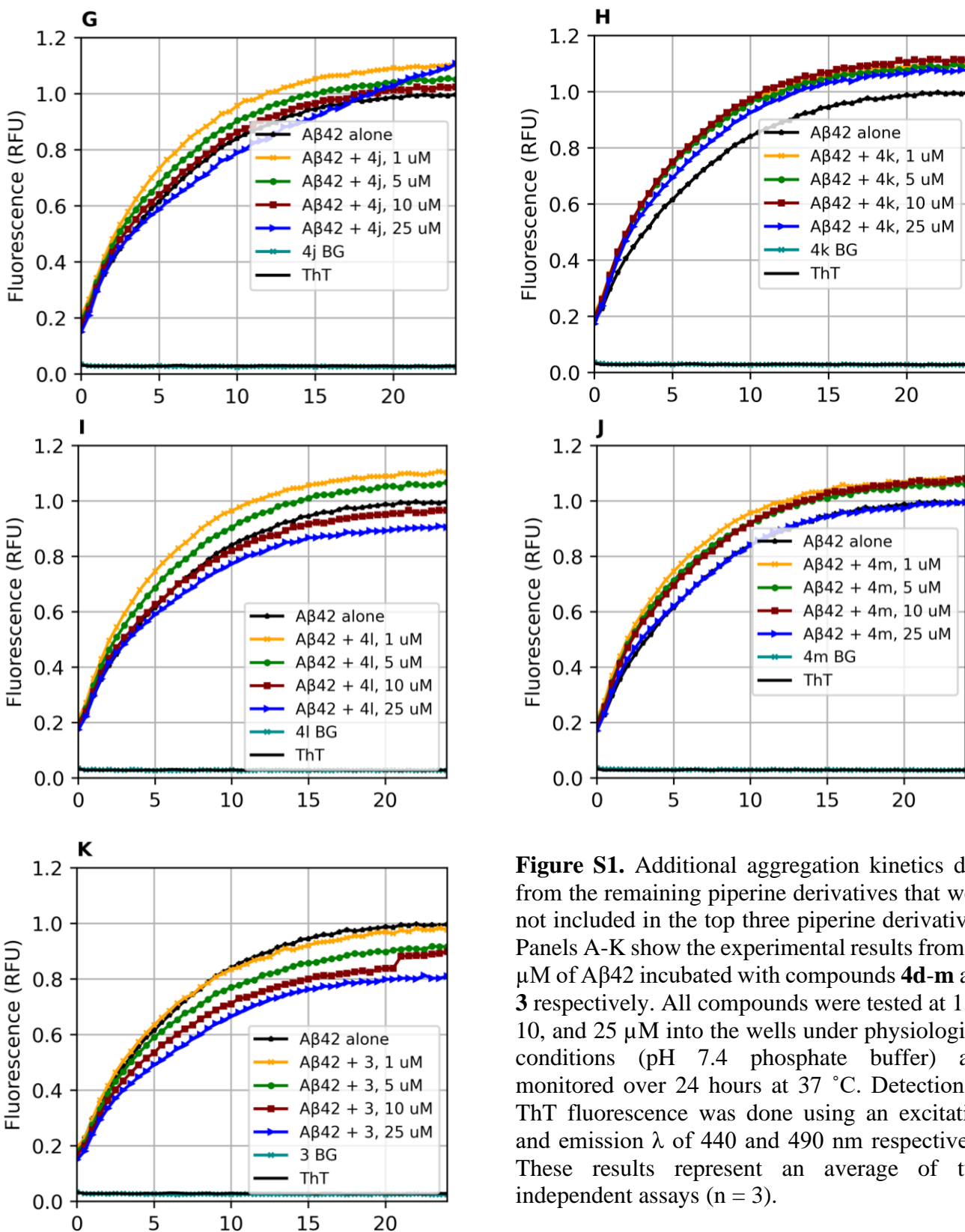


Figure S1. Additional aggregation kinetics data from the remaining piperine derivatives that were not included in the top three piperine derivatives. Panels A-K show the experimental results from 10 μ M of A β 42 incubated with compounds **4d-m** and **3** respectively. All compounds were tested at 1, 5, 10, and 25 μ M into the wells under physiological conditions (pH 7.4 phosphate buffer) and monitored over 24 hours at 37 $^{\circ}$ C. Detection of ThT fluorescence was done using an excitation and emission λ of 440 and 490 nm respectively. These results represent an average of two independent assays (n = 3).